A Warm Atomic Vapour Quantum Memory in the Context of Space Research

vorgelegt von

M. Sc.
Luisa Esguerra Rodríguez
ORCID: 0009-0003-2647-6349

an der Fakultät II – Mathematik und Naturwissenschaften
der Technischen Universität Berlin
zur Erlangung des akademischen Grades

Doktor der Naturwissenschaften
- Dr. rer. nat. -

genehmigte Dissertation

Promotionsausschuss:

Vorsitzende: Prof. Dr. Sabine Klapp
1. Gutachter: Prof. Dr. Janik Wolters
2. Gutachterin: Prof. Dr. Jasmin Meinecke
3. Gutachter: Prof. Dr. Philipp Treutlein

Tag der wissenschaftlichen Aussprache: 26. Juni 2024

Berlin 2024

Abstract

Quantum memories serve as indispensable enabling components for possible satellite-based quantum repeaters in future intercontinental and global quantum communication networks. These memories play a crucial role in synchronising and buffering incoming photons at network nodes. Additionally, they have wide-ranging applications in distributed quantum computing, optical machine learning, testing of fundamental physics in space, and storage of quantum tokens for secure online authentication, etc. The landscape of possible platforms and implementation protocols for quantum storage is vast. We choose a simple and scalable storage platform: a warm atomic vapour cell. This choice eliminates the need for large technical overhead and can be operated without the need for cryogenics, strong magnetic fields, or vacuum chambers, making it highly suitable for space deployment.

In this thesis, we experimentally realise a warm vapour quantum memory based on electromagnetically induced transparency (EIT) on the Cs D_1 line and focus on simultaneously optimising two key parameters crucial for various applications: the end-to-end efficiency, η_{e2e}, and the signal-to-noise ratio (SNR). For the storage and retrieval of attenuated coherent pulses containing $|\alpha|^2 = 1.0(1)$ photons on average, our memory achieves an end-to-end efficiency of $\eta_{\mathrm{e2e}} = 13(2)\%$ and an internal memory efficiency of $\eta_{\mathrm{mem}} = 33(1)\%$. We simultaneously obtain an SNR $= 14(2)$, equivalent to a noise level corresponding to $\mu_1 = 0.07(2)$ signal photons. The $1/e$ memory lifetime is approximately $1\,\mu$s, as determined using macroscopic pulses. Through a comprehensive noise analysis, we identify spontaneous Raman scattering and fluorescence as the primary limiting noise sources, while four-wave mixing noise, often problematic in warm vapour memories, has negligible contributions in our experiment.

Moreover, we leverage our memory to realise a random-access spatially multimode memory for coherent macroscopic pulses. Additionally, we implement control pulse optimisation using a genetic algorithm, offering a novel technique for in-experiment optimisations to enhance performance metrics. Furthermore, we propose an experiment to demonstrate, for the first time quantum token storage in a warm vapour memory using time-bin encoding and coherent single-photon pulses, and perform preliminary experiments in this direction. Operating within a technologically relevant regime for future applications, our simple and scalable system has proven to be a promising candidate for satellite deployment and integration into quantum repeaters for future quantum networks.

Zusammenfassung

Quantenspeicher dienen als unverzichtbare Komponenten für die Entwicklung satellitengestützter Quantenrepeater in zukünftigen interkontinentalen und globalen Quantenkommunikationsnetzwerken. Sie synchronisieren und puffern eingehende Photonen an Netzwerkknoten und haben darüber hinaus vielfältige Anwendungen in verteiltem Quantencomputing, im optischen Maschinenlernen, beim Nachweis von Grundlagenphysik im Weltraum und in der Speicherung von Quantentoken für die sichere Online-Authentifizierung. Die Landschaft möglicher Plattformen und Implementierungsprotokolle für Quantenspeicher ist umfangreich. Wir wählen eine einfache und skalierbare Speicherplattform: eine warme atomare Dampfzelle. Diese erfordert keinen großen technischen Aufwand und kann ohne Kryostate, starke Magnetfelder oder Vakuumkammern betrieben werden, was sie für den Weltraumeinsatz besonders geeignet macht.

In dieser Arbeit realisieren wir experimentell einen Quantenspeicher in warmem Alkalidampf, basierend auf der Elektromagnetischen Induzierten Transparenz (EIT) auf der Cs D_1-Linie. Dabei konzentrieren wir uns auf die gleichzeitige Optimierung zweier entscheidender Parameter: die Ende-zu-Ende-Effizienz η_{e2e} und das Signal-Rausch-Verhältnis (SRV). Für die Speicherung und Wiedergabe gedämpfter kohärenter Pulse, die im Durchschnitt $|\alpha|^2 = 1.0(1)$ Photonen enthalten, erreicht unser Speicher eine Ende-zu-Ende-Effizienz von $\eta_{\mathrm{e2e}} = 13(2)\%$ und dementsprechend eine interne Speichereffizienz von $\eta_{\mathrm{mem}} = 33(1)\%$. Gleichzeitig erzielen wir ein SRV von 14(2), was einem Rauschniveau von $\mu_1 = 0.07(2)$ Signalphotonen entspricht. Die $1/e$ - Speicherlebensdauer beträgt etwa $1\,\mu$s und wurde mithilfe makroskopischer Pulse bestimmt. Durch eine umfassende Rauschanalyse identifizieren wir spontane Raman-Streuung und Fluoreszenz als hauptsächliche Rauschquellen. Das oft problematische Rauschen durch Vierwellenmischen in warmen Dampfspeichern hat in unserem Experiment vernachlässigbare Beiträge.

Darüber hinaus realisieren wir einen räumlich multimodalen Speicher mit zufälligem Zugriff für kohärente makroskopische Pulse und implementieren eine Kontrollpulsoptimierung mittels eines genetischen Algorithmus, der eine neuartige Technik für in-Experiment-Optimierungen zur Verbesserung der Leistungsmetriken bietet. Schließlich schlagen wir ein Experiment vor, um erstmals die Speicherung von Quantentoken in einem warmen Dampf-Speicher unter Verwendung der Zeitbin-Codierung und kohärenter Einzelphotonenpulse zu demonstrieren, und führen vorläufige Experimente in diese Richtung durch. Da unser einfaches und skalierbares System in einem technologisch relevanten Bereich für zukünftige

Anwendungen betrieben wird, bleibt es ein vielversprechender Kandidat für den Einsatz auf Satelliten und für die Integration in Quantenrepeater für zukünftige Quantennetzwerke.

Acknowledgements

I cannot believe the day I am writing these words has finally arrived. This thesis, with unofficial title “LaserLuisa and the Quest for the Lost Photons” would not have been possible without the help of so many important people. The list is so long that it could fill another 100 pages, but I promise I will try to keep it as short as I can.
First and foremost I would like to thank my supervisor Janik Wolters, for giving me the chance to come back to science after a long break, and for taking me on as his first PhD student in the newly founded FITS group. You have always trusted me, pushed me, and motivated me to continue, even when it was hard. Moreover, you always provided me with many great opportunities to take part in scientific outreach. I very much admire your drive and how you do science, always treating everyone as an equal. I further thank you for thoroughly proofreading the manuscript. It has truly been an honour to be your first PhD student. I also want to thank the remaining members of the committee, Prof. Jasmin Meinecke and Prof. Phillipp Treutlein for agreeing to review this thesis, and Prof. Sabine Klapp for acting as the chair.
To all my colleagues at DLR in OS and TLS, I sincerely thank for your collaboration, help, excursions, and the great atmosphere these last few years. Special mentions go to the dear secretaries, especially Ute Dombrowski and Michaela George; the IT people, Eilke Santjer and Andreas Barthold; and Daniela Steinweg at the Warenannahme for making our work and life at DLR so much easier.
I also want to thank all our collaborators from the LUH, the PTB, the HU, the FU, the TU, etc., for all the great work we have done together. A very special thank you goes, of course, to all the members of the FITS group, former and present. It has (mostly ;)) been a blast to work with all of you. Of course, I have many special mentions. In order of appearance: Leon, thank you for putting up with me from day one and ‘patiently’ teaching me all the names of cables and connectors used in the lab. I have learned so much from you and I think we have had some fun ;) Also, thank you for our drives from and to Adlershof over the years. Mingwei, thank you for always being so incredibly sweet! Lizzy, there are no words to express the amount of help you have given me, and everyone else, over the past years. Thank you for taking care of automatising our experiments and for always being there to aid when I had coding issues. I have loved sharing an office and the lab with you. You are an amazing scientist and I am sure you will do great things. Benni, the award to the best comforting hugs goes to you without a doubt. I am so happy to have had you as a colleague and a friend, and I thank you for always being there for any kind of support I needed. I really cherished all the times we spent in and out of the

lab. I will always be there when you need to rant, you know how much I enjoy a good one! Inna, although we only worked together for a short time, it was a lot of fun, and I am very happy that we have become friends. Thank you so much for your support in the last year! Helen, I cannot thank you enough for how much you have been there for me this last year, both scientifically and personally. Thank you for very carefully reading my thesis, giving me great input and positive feedback, teaching me so much, and making me laugh a great deal. You are one of the smartest people I have ever encountered, but you are also incredibly kind, thank you. Alex, thank you for your help and for coming to me with questions, I am sure you will be a fantastic successor and I look forward to seeing what comes out of your experiments. To Jinglan and David, thank you for putting up with me as your supervisor, and for all we learned together. Special thanks naturally also go to out dear lab ghost, Lord Etalon Eric, who always kept things fun and confusing ;).
Outside of DLR, I want to thank Mustafa Gündoğan for reading parts of the thesis and for all your help and support during my PhD. To Esteban Gómez, Martin Jutisz and all others with whom I have discussed about memories, shared labs, problems, and optics over the years, thank you for everything. To Franz Sitzmann and the Jünge Tüftler, thank you for all the fun we had. I hope to work together again many times! Marty, also special thanks for proofreading and hopefully for more Vabali days to come! All the people I met through BOS.QT, Gabi, Robert, alias Mr. President, and everyone else, thank you for all the great times. Gabi, I will always still be here for any revolution we want to start together. I thank the BOS.QT itself for giving me two of the best people I could ever have met in physics and in life: Daniel Lechner, aka LightJesus, thank you for your friendship in and out of Adlershof and the Mensa, for constantly showing us all the beauty there is in light, and for being the diffraction to my laser. To Chris Liedl, thank you for being you, for your friendship, for all your support, hugs, good times, and your wise words. Also, thank you so much for reading the manuscript in such detail, and for solving some of the big memory questions with me two days before submission. You two are among the best things this PhD has given me. To all of the above (and below), thank you for being avid subscriptors of my 'podcast': *Evening (and Morning, and Afternoon) Rants with Luisa Esguerra*. Thank you, and I truly am sorry!
To the rest of my friends, you know who you are. Thank you for always being there and for all the fun. You are my dearest possession, for a lack of a better word. María (amigaaah), Marisa, Gustavo, Claudia, Sof, Keller, Danilo, Andrea, Bea, Jona, thank you for supporting me and always listening so much in this last year, and always. I would really not have made it without you. To my Berlin gang, thank you all for always believing in me and for coming up with the awesome nickname of LaserLuisa.
To my Horvath family, Coco, Chris, Moriti, Freddie, Vicky and newly added David, thank

you for bearing with me all these years and for all you have done for me these last months: feeding me, hugging me, motivating me. I am so lucky to share or have shared a life and a house with each and every one of you. To my brother, Alejandro, thank you for always being there for me and believing in me, and for giving me the best nephews I could ever ask for. To my parents, Cristina and Miguel, all of this would never have been possible without your support in every sense. Nigel, thank you again also for proofreading. I love you all so much. To Catalina, my psychologist, thank you for embarking with me in this crazy ride the last two years, for your always so accurate metaphors, and for teaching me to always do my pliés in the lab and everywhere. To this very thesis, thank you for giving me a reason to leave when I could no longer continue, and for helping me find my passion for physics again.
And finally, I want to thank me. For finding the strength and pushing through, for not giving up, for getting up every morning, for never stopping to dance and to science. As a famous actress once said: "There are days when I myself feel overrated. Today is definitely not one of them." If anyone reading this needs to hear this: There are always some photons to be found, if you are willing to put in the work, and ask for help when you need it!
Love,
LaserLuisa

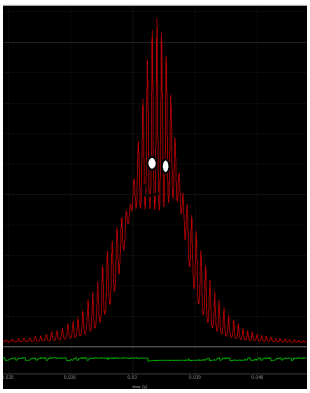

Here I leave a photo of our dear lab ghost, Lord Etalon Eric.

para Invencible,
que en este caso también fui yo.

para Mamá,
porque a nosotros solo nos puede ir... ¡MEJOR!

Contents

List of publications

In the process of working on this thesis, the following articles have been published or are currently under review in peer-reviewed journals:

- **L. Esguerra**, L. Meßner, E. Robertson, N. V. Ewald, M. Gündoğan, and J. Wolters, Optimization and readout-noise analysis of a warm-vapor electromagnetically-induced-transparency memory on the Cs D_1 line. *Phys. Rev. A*, 107, 042607, 2023, [1].
- J.-M. Mol, **L. Esguerra**, M. Meister, D. E. Bruschi, A. W. Schell, J. Wolters, and L. Wörner, Quantum memories for fundamental science in space. *Quantum Sci. Technol.*, 8, 024006, 2023, [2].
- L. Meßner, E. Robertson, **L. Esguerra**, K. Lüdge, and J. Wolters, Multiplexed random-access optical memory in warm cesium vapor. *Opt. Express*, 31, 10150-10158 2023, [3].
- E. Robertson, **L. Esguerra**, L. Meßner, G. Gallego, and J. Wolters, Machine learning optimal control pulses in an optical quantum memory experiment. *arXiv*.2401.05077, 2024, [4].
- M. Yang, E. Robertson, **L. Esguerra**, K. Busch, and J. Wolters, Optical convolutional neural network with atomic nonlinearity. *Opt. Express*, 31, 16451-16459, 2023, [5].

Further contributions

In the process of working on this thesis, I have further been involved in the following (selected) contributions:

Conference contributions and invited talks:

- Poster Presentation: *"Quantum Memories suited for Space"*, **L. Esguerra**, L. Meßner, and J. Wolters, QTech Conference (online), Abstract ID: 246, 2020

- Contributed Talk: *"Quantum Memories for Space - Path to a Noise-Free Memory"*, **L. Esguerra**, L. Meßner, M. Gündoğan, and J. Wolters, BOS.QT[1] Retreat, Berlin, 2020

- Poster Presentation: *"Towards satellite-suited noise-free quantum memories"*, **L. Esguerra**, L. Meßner, E. Robertson, M. Gündoğan, and J. Wolters, CLEO Conference (online), Joint Poster Session III (JTh3A) [6], 2021

- Contributed Talk: *"Towards satellite-suited noise-free quantum memories"*, **L. Esguerra**, L. Meßner, E. Robertson, M. Gündoğan, and J. Wolters, CLEO EU (online), Integrated Devices and Memories (eb_2) [7], 2021

- Contributed Talk: *"Quantum Memories for Space - Path to a Noise-Free Memory"*, **L. Esguerra**, L. Meßner, E. Robertson, M. Gündoğan, and J. Wolters, DPG Conference (online), 2021

- Contributed Talk: *"Readout-noise analysis and optimization of a warm vapour EIT memory on the Cs D1 line"*, **L. Esguerra**, L. Meßner, E. Robertson, N. V. Ewald, M. Gündoğan, and J. Wolters, SPIE Conference, [12133 – 34] [8], Strasbourg, 2022

- Poster Presentation: *"Quantum memories for quantum communication"*, **L. Esguerra**, N. V. Ewald, B. Maaß, E. Robertson, L. Meßner, D. Becker, F. Günther, and J. Wolters, Adlershofer Forschungstage, Berlin, 2022

- Contributed Talk: *"Readout-noise analysis and optimization of a warm vapour EIT memory on the Cs D1 line"*, **L. Esguerra**, L. Meßner, E. Robertson, N. V. Ewald, M. Gündoğan, and J. Wolters, DPG Conference (online), 2022

[1] Berlin School of Optical Sciences and Quantum Technologies

- Poster Presentation: *"Towards a noise-free EIT quantum memory on the Cs D1 line"*, **L. Esguerra**, L. Meßner, E. Robertson, N. V. Ewald, M. Gündoğan, and J. Wolters, BOS.QT Retreat, Berlin, 2021

- Poster Presentation: *"Optimisation and readout-noise analysis of a hot vapor EIT memory on the Cs D1 line"*, **L. Esguerra**, L. Meßner, E. Robertson, N. V. Ewald, M. Gündoğan, and J. Wolters, Quantum Information Summer School, Les Houches, 2022

- Poster Presentation: *"Quantum Memories for Quantum Communication"*, **L. Esguerra**, N. V. Ewald, B. Maaß, E. Robertson, L. Meßner, D. Becker, F. Günther, and J. Wolters, BOS.QT Retreat, Gut Gremmelin, 2022

- Contributed Talk: *"Readout-noise analysis and optimization of a warm vapor EIT memory on the Cs D1 line"*, **L. Esguerra**, L. Meßner, E. Robertson, N. V. Ewald, M. Gündoğan, and J. Wolters, DPG Conference, Hannover, 2023

- Invited Talk: *"Quantentechnologien in der Raumfahrt am Beispiel von Quantenspeichern"*, **L. Esguerra**, L. Meßner, E. Robertson, N. V. Ewald, M. Gündoğan, and J. Wolters, Deutsche Raumfahrtagentur im DLR (online), 2023

- Invited Talk: *"Quantum Memories for Space Applications"*, Technical Talks of the *DLR Women+ in Science & Technology Network* (online), 2024

Student (co)-supervision, mentoring, and collaboration:

- Jinglan Wu (Bachelor thesis [9])

- David Becker (Bachelor thesis [10])

- Alexander Erl (Bachelor and Master thesis [11], co-supervision)

- Leon Meßner (Master thesis [12], collaboration)

- Mingwei Yang (Master thesis [13], collaboration, mentoring)

Outreach activities:

- Scientific consultancy in the project Quantum 1×1 for the realisation of games and informative videos for young students concerning the topic of quantum technologies

  - Assessment of the correctness of the scientific content for the videos
  - Participation in informative events
  - Interview as an expert on quantum communication
  - Participation in explanatory videos: Quantum Coin Toss
- Creation of scientific outreach videos for the *Girls day* 2021
- Motivational Talks about life in STEM for school children, Deutsche Schule Madrid, Colegio Internacional Santo Tomás de Aquino, Madrid, 2021, 2022
- Participation in the implementation of the Quantum Escape Game realised in the *EsCQuTe* project at the Freiland Festival, Alt Tellin, 2022
- Invited Talk: *"LaserLuisa & the Quest for the Lost Photons"*, Friday Light Talks, HU Berlin, 2022
- Activities for the *Girls day* 2023 with the Junge Tüftler∗innen
- Science Slam presentation at the BMBF (2nd prize), *Konferenz für IT-Sicherheit* 2023
- Organisation of the *Psychological Struggles of PhDs and Postdocs* event concerning mental health in academia together with Friday Light Talks and Scholar Minds at the HU Berlin, 2023
- Science Slam winner at the Zeiss Planetarium Berlin 2024
- Participation in the DPG Careerdays 2024 (to come)

Prizes and Recognitions:

- Best poster award at the BOS.QT Retreat 2022
- Scientist of the Month of January 2023 named by the *DLR Women+ in Science & Technology Network*
- Science Slam at the Zeiss Planetarium Berlin 2024, 1st prize

List of Figures

List of Tables

Abbreviations

Here I present a list of the most important abbreviations used in the following thesis:

- **AFC:** atomic frequency comb
- **AFG/AWG:** arbitrary function/waveform generator
- **AMZI:** asymmetric Mach-Zehnder interferometer
- **AOM/AOD:** acousto-optic modulator/deflector
- **APD:** avalanche photodiode
- **Ar:** argon
- **AR:** anti-reflection
- **AS photon:** anti-Stokes photon
- **ASE:** amplified spontaneous emission
- **ATS:** 'Autler-Townes' splitting
- **ATT:** attenuator
- **BB84:** Bennett and Brassard quantum key distribution protocol (1984)
- **BBM92:** Bennett, Brassard and Mermin quantum key distribution protocol (1992)
- **BBO:** β-barium borate
- **BEC:** Bose-Einstein condensate
- **BECCAL:** Bose-Einstein Condensate and Cold Atom Laboratory project
- **BMBF:** German Federal Ministry of Education and Research (Bundesministerium für Bildung und Forschung)
- **BOS.QT:** Berlin School of Optical Sciences and Quantum Technologies
- **BSM:** Bell-state measurement
- **BS:** beam splitter
- **CAL:** Cold Atom Laboratory project

- **CP:** calcite prism
- **CPT:** coherent population trapping
- **CQM:** cyclical quantum memory
- **CRIB:** controlled reversible inhomogeneous broadening
- **Cs:** caesium
- **CV:** continuous variable
- **cw:** continuous wave
- **DC:** direct current
- **DET:** detector
- **DIY:** do it yourself
- **DI-QKD:** device-independent quantum key distribution
- **DLCZ:** Duan-Lukin-Cirac-Zoller quantum repeater protocol (2001)
- **DLR**: German Aerospace Center (Deutsches Zentrum für Luft- und Raumfahrt)
- **DPG:** Deutsche Physikalische Gesellschaft
- **E91:** Ekert 91 quantum cryptography protocol (1991)
- **EIT:** electromagnetically induced transparency
- **EOM:** electro-optic modulator
- **EPR:** Einstein-Podolski-Rosen
- **EsCQuTe:** Escape Game on Quantum Technologies project
- **FFT:** fast Fourier transform
- **FITS:** (physical) foundations of IT security
- **FLAME:** fast-ladder memory
- **FPGA:** field programmable gate array
- **FSR:** free spectral range

- **FU:** Freie Universität Berlin
- **FWHM:** full width at half maximum
- **FWM:** four-wave mixing
- **GA:** genetic algorithm
- **GaAs:** gallium arsenide
- **GEM:** gradient-echo memory
- **GPS:** global positioning system
- **He:** helium
- **HU:** Humboldt University Berlin
- **HWP:** half-wave ($\frac{\lambda}{2}$) plate
- **InAs:** indium arsenide
- **InGaAs:** indium gallium arsenide
- **ISS:** international space station
- **IT:** information technology
- **Kr:** krypton
- **KTP:** potassium titanyl phosphate
- **L:** lens
- **LEO:** low Earth orbit
- **LiNbO3/LN:** lithium niobate
- **LOQC:** linear optical quantum computing
- **LUH:** Leibniz-Unversität Hannover
- **MA-QKD:** memory-assisted quantum key distribution
- **MDI-QKD:** measurement-device-independent quantum key distribution
- **MON:** monitor

- **MOT:** magneto-optical trap
- **N_2:** nitrogen molecule
- **ND:** neutral density
- **NMR:** nuclear-magnetic resonance
- **NPBS:** non-polarising beam splitter
- **NTC:** negative temperature coefficient
- **NV:** nitrogen-vacancy
- **OAM:** orbital angular momentum
- **OD:** optical depth
- **OFHC:** oxygen-free-high-thermal-conductivity
- **OI:** optical isolator
- **OS:** Institute of Optical Sensor Systems (DLR)
- **ORCA:** off-resonant cascaded absorption
- **PBS:** polarising beam splitter
- **PCB:** printed circuit boards
- **PD:** photodiode
- **PDE:** partial differential equation
- **PEEK:** Polyether ether ketone
- **PhD:** Doctor of Philosophy[1]
- **PID:** proportional-integral-derivative
- **PM:** polarisation-maintaining
- **PTB:** Physikalisch-Technische Bundesanstalt
- **QC:** quantum computing
- **QD:** quantum dot

[1] Alternatively, pretty hard degree.

- **QDYN:** quantum dynamics and control (Fortran library)
- **QIS/QIP:** quantum information science/processing
- **QKD:** quantum key distribution
- **QM:** quantum memory
- **QND:** quantum-non-demolition measurement
- **QR:** quantum repeater
- **QToRX:** Quantum Token Based on Rubidium and Xenon project
- **QUESS:** Quantum Experiments at Space Scale project
- **QuMSeC:** Quantum Memories for Secure Communication in Tomorrow's Society project
- **QWP:** quarter-wave ($\frac{\lambda}{4}$) plate
- **Rb:** rubidium
- **RC:** reservoir computing
- **RSA:** Rivest, Shamir, and Adleman cryptographic protocol (1977)
- **REIDs:** rare-earth ion-doped solids
- **RF:** radio frequency
- **RP:** Red Pitaya
- **RWA:** rotating wave approximation
- **S photon:** Stokes photon
- **SatQKD:** satellite-based free-space QKD
- **SDP:** semidefinite programming
- **SE:** spin exchange
- **SEOP:** spin exchange optical pumping
- **SERF:** spin exchange relaxation free
- **SI:** international system of units (french abbreviation)

- **SiV:** silicon-vacancy
- **SNSPD:** superconducting nanowire single-photon detector
- **SNR:** signal-to-noise ratio
- **SnV:** tin-vacancy
- **SOA:** semiconductor optical amplifier
- **SPD:** single-photon detector
- **SPDC:** spontaneous-parametric down-conversion
- **SPL:** single-photon level
- **SPS:** single-photon source
- **SRS:** spontaneous Raman scattering
- **SRV:** Signal-Rausch-Verhältnis
- **STEM:** science, technology, engineering and mathematics
- **SWaP budget:** size, weight, and power budget
- **TA:** tapered amplifier
- **TBP:** time-bandwidth product
- **TLS:** Department Terahertz and Laser Spectroscopy (DLR)
- **TU:** Technical University Berlin
- **TEC:** thermoelectric cooler
- **UUL:** ultra-long-lifetime
- **Xe:** xenon

1 Introduction

"Derrotado por aquellas prácticas de consolación, José Arcadio Buendía decidió entonces construir la máquina de la memoria que una vez había deseado para acordarse de los maravillosos inventos de los gitanos. El artefacto se fundaba en la posibilidad de repasar todas las mañanas, y desde el principio hasta el fin, la totalidad de los conocimientos adquiridos en la vida. Lo imaginaba como un diccionario giratorio que un individuo situado en el eje pudiera operar mediante una manivela, de modo que en pocas horas pasaran frente a sus ojos las nociones más necesarias para vivir."

Cien Años de Soledad,
Gabriel García Márquez.

"Defeated by those practices of consolation, José Arcadio Buendía then decided to build the memory machine that he had desired once in order to remember the marvelous inventions of the gypsies. The artifact was based on the possibility of reviewing every morning, from beginning to end, the totality of knowledge acquired during one's life. He conceived of it as a spinning dictionary that a person placed on the axis could operate by means of a lever, so that in a very few hours there would pass before his eyes the notions most necessary for life."

One Hundred Years of Solitude,
Gabriel García Márquez.

One might argue that our capacity to remember and learn from our memories is the reason human civilisation has made tremendous leaps forward. However, in contrast to this ability lies our ominous inclination to forget. As history has taught us, those who fail to remember the past are condemned to repeat it. A 'memory machine', as García Márquez describes it, has always been a target of relentless pursuit. Humans learned to write and draw to record their thoughts, first in caves, later on clay tablets and parchment. The invention of books as a means for remembrance marked a defining moment for humankind. From Gutenberg's press we have come a long way, now arriving

at ChatGPT[1] [14], which can be seen more akin to a vast repository of memory rather than genuine intelligence. It even makes up nonexistent memories, hallucinations, as they are generally referred to, just as humans do. In the information age we live in, when we speak of memory, we often refer to computer memory, the physical devices used to store data or instructions for use by a computer's central processing unit (CPU). Computer memory encompasses various types, each tailored to meet distinct demands. These memories store classical information encoded in bits. In this thesis however, the focus lies on the concept of a quantum memory, that is, a device able to store quantum information, i.e., qubits, for a sufficient amount of time, generally dependent on the specific application. Quantum information tends to be more volatile than its classical counterpart, hence the need for this clarification.

I will start the thesis with an introduction to the so-called second quantum revolution, driven by the field of quantum information processing, and one of its fundamental building blocks, the famous no-cloning theorem. I have chosen to deliver a detailed introduction with some historical accounts because I really enjoyed the process of investigating and summarising the field, and hope that it will serve as a gentle initiation that can be of use to colleagues and the interested reader. Thereafter, the topics of quantum cryptography and quantum repeaters and their components will be presented, followed by an introduction into quantum light sources, essential components of these repeaters. To conclude the introduction, I will give a short definition of what constitutes a quantum memory in general terms. Chapter 2 will yield a thorough review of the field of quantum memories, from the figures of merit used to characterise them, through the different memory platforms, to the variety of existing storage protocols. Chapter 3 contains the theoretical backbone of the thesis and describes the relevant concepts in order to understand light storage in atomic vapours. In Chapter 4, the group's first experimental realisation of the hyperfine Λ-memory in warm atomic caesium is described in detail, and the main results of this thesis are presented, along with further experiments conducted on the setup. Moreover, this chapter contains theoretical simulations of the memory that serve for comparison with the experiment. Thereafter, in Chapter 5, several possible applications and developments of our system, in which the group is involved, are described in form of a detailed outlook, ranging from more speculative proposals to imminent experiments, delivering a roadmap for current and future implementations and endeavours. Finally, I will end with a summary of the achieved results and some conclusions about the field of quantum memories in the context of space research in Chapter 6.

[1] I hereby genuinely thank ChatGPT for its contributions to this thesis.

1.1 The second quantum revolution

After having collected the work of several physicists and scientists before him, among them Ampère, Gauß and Faraday, in the 1860s James Clerk Maxwell set out to write his famous equations of electromagnetism, which together explain the existence of light and its nature as an electromagnetic wave. Originally, these consisted of a set of about 20 equations in scalar form (or about 12 in form of quaternions) [15]. It was actually Heaviside who granted physicists the great favour of summarising these into the four famous equations we know today, by introducing vector calculus [16]. Even though the corpuscular hypothesis of light, enforced by Newton himself, had been mostly relinquished by then, time would show that Maxwell's equations would survive the birth of quantum mechanics at the beginning of the 20th century, and the complete change of paradigm that this implied. The photoelectric effect and the ultraviolet catastrophe led Einstein and Planck to suggest that light and energy were quantised, thus giving birth to quantum mechanics. The latter stated that photons, as these light quanta were later on called by Lewis in 1926 [17], showed a wave-particle duality themselves, just as other subatomic particles, like the electron and the proton, had. Quantum mechanics and electrodynamics were afterwards combined to form quantum electrodynamics by Dirac, Heisenberg and later on Feynman, among others. Another revolutionary theory born in the same era was relativity. Maxwell's equations also survived this upheaval admirably as they are relativistically covariant, the only addition to them being the fundamental limit of achievable velocities posed by the speed of light, c. Thus, Maxwell's equations might be the longest standing correct equations in physics [18]. In other words, light is powerful, and the amount of possibilities it gives us is incredibly vast. Let us however momentarily set aside the topic of light. We will later return to it.

The invention and development of quantum mechanics, as mentioned before, is generally known as the first quantum revolution. It brought us a deep understanding of the world on a microscopic level and confronted humanity with its weirdness and complete counterintuitiveness, as I will dwell on a bit more later on. Concepts like superposition and entanglement still are a source of headache for many physicists, and not less so for the general public. We have learned to accept them and work with them, but as Feynman or Bohr themselves argued, nobody in their right mind could claim that they really understand their meaning, or are not disturbed by it. However, this first revolution was the source of later technical milestones of humanity, the transistor invented by W. Shockley, J. Bardeen, W. Brattain in 1948 [19], and the laser by T. H. Maiman in 1960 [20], which both gave rise to a great technological revolution and to the information age we live in now.

Nonetheless, returning to the headaches, in the 1920s-1940s, quantum mechanics led to intense philosophical discussions regarding its possible interpretations and its correctness. The Bohr-Einstein debate at the Solvay conference of 1927 remains famous to this day [21]. Even though Einstein played a major role in the development of quantum physics, he never came to peace with the idea of uncertainty and the role of the measurement process, as described in the Copenhagen interpretation, pushed forward by Niels Bohr, Heisenberg and others. Hence his famous phrase: "God does not play dice". Nevertheless, quantum theory was able to correctly predict the outcomes of measurements, something Einstein never questioned. The debate was rather about the profound implications of this new theory. In 1935, Einstein, Podolski and Rosen presented an apparent paradox of faster-than-light signalling in their famous EPR paper [22], and claimed that quantum theory must be incomplete, a statement with which Bohr did not agree [23]. Einstein (and others) concluded that there must be some sort of underlying structure to quantum mechanics, some hidden variable that would explain this apparent paradox. It was not until John Stuart Bell presented his famous Bell inequality in 1964 [24], which formulates a mathematical description of the problem by posing an upper bound for correlations between measurement outcomes of distant particles obeying local realism, that a possibility for solving this debate was unveiled. This groundbreaking paper's result is that quantum mechanics is in conflict with our intuitive local-realist world view. This discovery shifted the longstanding debate between Einstein and Bohr from epistemology into the realm of experimental physics [25].

By realism, we understand that physical systems have objective states and characteristics with definite values inherent to them, and not determined by observation. Although consistent with our every-day experience, this turns out to be problematic under quantum theory, if simultaneously subjected to locality. Locality meaning that physical interactions between objects or events can only occur if these are located within each other's light cones. Correlations exceeding the speed of light, such as entanglement or, as Einstein called it "spooky action at a distance", are therefore non-local.

In the last decades, several quantum physical experiments have been proposed and realised, which have shown to violate Bell's inequality. First pioneering experiments were performed in the 70s by S. Freedman and J. F. Clauser [26] (see also [27, 28]). Later on in 1982, Alain Aspect and colleagues were the first to close the locality loophole [29]. These major achievements won Aspect and Clauser the 2022 Nobel Prize, together with Anton Zeilinger.

These abstract discussions that Bell was able to bring into the realm of the experimentally provable led to the realisation of the relevance and benefits of entanglement, essentially

planting the seed of what has been coined the second quantum revolution [21, 30, 31], in the midst of which we are today. It is not only the understanding of superposition and entanglement, as far as this is possible, but the harnessing of exactly these puzzling characteristics that led to the development of quantum information science (or processing) (QIS/QIP). One can consider Feynman's 1982 lecture on computation at Caltech [32], where he firstly introduced the concept of a universal quantum computer, as the origin of QIS, followed shortly after by Wiesner's conjugate coding paper [33], and by Bennet and Brassard's BB84 quantum communication and teleportation protocols [34, 35]. The three big pillars of QIS are quantum computing (QC) [36–39] and simulation [40], quantum communication [41], and quantum metrology and sensing [42, 43].

But what is the essence of QIS in a nutshell? Classical information is encoded in bits, strings of zeros and ones. These can have different physical implementations, a switch being off or on, two different voltage levels, etc. When 'going quantum', information is encoded in quantum bits or qubits[1] [44]. Qubits do not only take the two mutually exclusive states 0 and 1, but all possible combinations thereof. They thus can be in a superposition state, written in Dirac notation as

$$|\psi\rangle = \alpha\,|0\rangle + \beta\,|1\rangle\,, \tag{1.1}$$

where $|\psi\rangle$ represents the state vector, and α and β are complex numbers that can take on any value, provided $|\alpha|^2 + |\beta|^2 = 1$.
The remaining weird quantum mechanical property needed to understand QIP is entanglement, a name we owe to Schrödinger[2] [46]. An entangled state of two particles is a state that can only be described as a whole, and not through its constituents. Mathematically this is equal to saying the state cannot be factorised into a product of its component states [39]. As a result, two entangled particles have correlations that cannot be explained classically, and that persist even when the particles are *infinitely* separated. Infinite here meaning even when they are outside of each other's light cones.
A joint quantum state of two particles with two distinct possible states, i.e., two spin-$\frac{1}{2}$ particles, can be written as

$$|\Phi^{\pm}_{12}\rangle = \frac{1}{\sqrt{2}}\Big\{|\uparrow_1\uparrow_2\rangle \pm |\downarrow_1\downarrow_2\rangle\Big\}, \tag{1.2}$$

[1] Other encodings like qudits, qumodes, etc. exist.
[2] It has come to my attention recently that Schrödinger was actually a horrible human being and a paedophile [45]. Unfortunately, it is very often the case that many great thinkers in history were not the nicest people, to put it softly. However, this case is in my opinion extreme. Although this does not undermine the contributions Schrödinger made to physics, one should not separate author and work completely, and I definitely consider this issue worth mentioning.

in the case of perfect correlation, or

$$|\Psi_{12}^{\pm}\rangle = \frac{1}{\sqrt{2}}\Big\{|\uparrow_1\downarrow_2\rangle \pm |\downarrow_1\uparrow_2\rangle\Big\}, \tag{1.3}$$

for perfect anticorrelation. The notation signifies that, e.g., for the state $|\uparrow_1\downarrow_2\rangle$ the first particle (1) has a spin projection of $+\frac{1}{2}$ with respect to the quantisation axis, while the second (2) particle's projection equals $-\frac{1}{2}$. These states in Eqs. (1.2) and (1.3) represent maximally entangled states and are known as the Bell states. The measurement of one individual particle directly determines the state of its partner. Moreover, a measurement that projects the state of two particles into either one of these Bell states is called a Bell-state measurement (BSM), essential for, i.e., quantum teleportation [35]. For more details on the fundamentals of quantum mechanics for QIP, especially regarding the measurement process, I refer the reader to [39].

Returning to light, photons can be considered ideal qubits. Information can be encoded in, i.e., their polarisation states (horizontal $|H\rangle$ and vertical $|V\rangle$), and superpositions of these (diagonal $|D\rangle$ and anti-diagonal $|A\rangle$) can be straightforwardly prepared in the lab by means of waveplates. Further discrete degrees of freedom such as time-bin, frequency, path, etc. [39] are also feasible. Photons are weakly interacting but easily manipulated in the lab via linear optical elements like beamsplitters, mirrors, and filters, and they can travel long distances, famously very fast, making them perfect flying qubits that can transmit quantum information over long distances. However, their reluctance to be stopped or trapped renders them problematic as stationary qubits.
Many applications for photons in QIP exist. Universal quantum computation, for instance, requires two type of operations or gates [38, 39], namely single-qubit rotations and two-qubit entangling gates. The first kind are, as explained above, very easily performed with photons. However, it is the second kind that is not straightforward, due to the non-interacting nature of photons. Nevertheless, proposals for overcoming this issue through careful use of the measurement process have emerged in the last decades, and thus shown that universal computation with linear optics is possible [47–50]. This field is now known a linear optical quantum computing (LOQC). Another widely inverstigated field of QIS using photons is photonic quantum simulation [51].

Even if photons do not turn out to be the ideal qubit for quantum computing, they surely are for quantum communication. Because of their quantum nature, they offer the possibility of inherently secure communication, resulting from the no-cloning theorem, which will be introduced below. This means, security is guaranteed by the laws of

physics. Future quantum networks consisting of nodes connected locally or globally via communication networks operating with quantum information are currently envisioned. These networks will definitely require the transmission of entangled flying qubits, i.e., photons, over long distances. Moreover, the ability to convert them into stationary qubits with the help of some type of quantum interface will be fundamental[1] [52]. This point is were quantum memories enter the equation. They are an essential building block for these networks and for the rather science-fiction sounding proposal of a global quantum internet [53, 54]. Notwithstanding, the idea that we would all have a small computer, the size of our hand in our pockets that would allow us to communicate instantaneously with people all over the world, also seemed like science fiction 50-60 years ago. So we will have to let the future surprise us[2]. Before we go into quantum memories in depth, let me present the essential no-cloning theorem and introduce (a fraction of) the field of quantum cryptography in more detail.

1.1.1 No-cloning theorem

The basis of most quantum communication protocols is a relatively simple, but highly important result in quantum mechanics arising from its linearity, namely the no-cloning theorem [55]. It states the impossibility of perfectly copying an arbitrary unknown quantum state. The proof of this fact is very straightforward [39]. Suppose we have a machine capable of making a perfect copy of an unknown pure quantum state $|\psi\rangle$. The machine receives this state $|\psi\rangle$ as input, and is supposed to copy this state into some target state, given by some general, also pure, quantum state $|t\rangle$. As we are dealing with quantum mechanics, our machine ideally performs some unitary transformation U, such that it is reversible and length-preserving [39], onto the initial composite state $|\psi\rangle \otimes |t\rangle$, and thus produces a copy of it. Mathematically, one has

$$|\psi\rangle \otimes |t\rangle \xrightarrow{U} U(|\psi\rangle \otimes |t\rangle) = |\psi\rangle \otimes |\psi\rangle \,. \tag{1.4}$$

Supposing this procedure works for two different pure quantum states $|\psi\rangle$ and $|\varphi\rangle$, one obtains

[1] I will here, I hope for obvious reasons, overlook memoryless repeater proposals.
[2] Here I feel obliged to paraphrase my colleague Helen Chrzanowski: That is, if we sort out climate change first.

$$U(|\psi\rangle \otimes |t\rangle) = |\psi\rangle \otimes |\psi\rangle \tag{1.5}$$
$$U(|\varphi\rangle \otimes |t\rangle) = |\varphi\rangle \otimes |\varphi\rangle \,. \tag{1.6}$$

The scalar product of the equations above yields

$$(\langle\psi| \otimes \langle t| U^\dagger)\,(U\,|\varphi\rangle \otimes |t\rangle) = \langle\psi| \otimes \langle\psi|\,|\varphi\rangle \otimes |\varphi\rangle \,. \tag{1.7}$$

and thus

$$\langle\psi|\varphi\rangle = \langle\psi|\varphi\rangle^2 \,. \tag{1.8}$$

Since the equation above has only two possible solutions, $\langle\psi|\varphi\rangle = 0$ or $\langle\psi|\varphi\rangle = 1$, either $|\psi\rangle = |\varphi\rangle$, or they are orthogonal. Thus, the unitary machine we envisioned is only able to clone either a fixed predetermined state or states which are mutually exclusive, such as a classical computer when copying the bits 0 and 1. Therefore, cloning any arbitrary unknown quantum state is impossible.
This result has various important consequences. It means that if two parties are communicating via a quantum channel, i.e., a communication channel which can transmit quantum information, as well as classical information, and the parties are sending information encoded in quantum states, then an eavesdropper will not be able to intercept the information and copy it without destroying it. Several quantum communication protocols, specifically those involving an adversary (like the eavesdropper from above), rely on this simple fact. With respect to the field of quantum storage, no-cloning implies that the quantum state cannot be copied and thus will have to be fully transferred onto the memory, while the original state will be lost. How this is explicitly done will be discussed in Chapter 2.

1.2 Quantum cryptography

The encryption of secret messages has been a problem concerning humanity for thousands of years. Classical cryptography, today still used in many different areas such as the finance world, internet communications, online banking, and the security of state affairs among many others, is still an active area of research. One of the simplest cryptographic protocols is the *one-time pad*. Here, a message is paired with a secret key, generally via modular addition. As long as the key is randomly generated, at least as long as the

message itself, is only used once without repeated use of even a fraction of it, and is secretly shared by the two communicating parties, usually referred to as Alice and Bob, then the protocol is provably secure. In fact, it is considered the only provably secure encryption algorithm. If Alice uses the key to encrypt the message, then Bob can use the same key to decrypt it later on. Generally, Alice and Bob are assumed to trust each other. The problem of this technique arises in the sharing of the secret key. Historically, these keys were transmitted in secret meetings and were always destroyed after use. This type of protocol is also known as symmetric encryption, as both parties make use of the same key. However, in the information world we live in we cannot be subject to such conditions.

In order to solve the problem of secure key transmission, around the 1970s, another type of protocol was developed, known as asymmetric or public-key cryptography. Here, a pair of keys, a private and a public one are generated, and only the latter is transmitted via a public channel. Thus, anyone is able to use the public key to encrypt a message, but only the person in possession of the private key can use it to decrypt it. The generation of these keys relies on so-called directional mathematical functions, which are simple to calculate in one direction, but whose inverse is very hard to calculate. Among these functions we find the factorisation of very large numbers. Multiplying two large prime numbers is not computationally hard, while determining the prime factors of very large numbers becomes exponentially more complicated as they grow. If the prime factors of a number n are p and q, such that $n = pq$, the fastest algorithm to find p and q when only n is known, is the *number field sieve*, which can find the factors in n in about $e^{N^{1/3}\log_2^{2/3} N}$ computational steps, where N is the number of bits needed to encode n [18]. The most famous public key algorithm is known as RSA, and was developed by Rivest, Shamir, and Adleman in 1977 [56]. As opposed to the case of the *one-time pad*, the security of RSA or similar protocols has to date not been proven, it is assumed to be secure as long as the premise that it remains a NP hard problem is not disproved. In other words, security is based on the arguably rather bold assumption that our opponent does not have better resources than we do.
Nonetheless, with the quest for developing a universal quantum computer being currently pursued all around the world, the generalised use of such algorithms renders the security of private and secret data in *great danger*. It makes our information vulnerable to present but also future attacks. It seems, regrettably or not, since the realisation of a quantum computer does represent the holy grail of QIP, only a matter of time (however long) until RSA systems are cracked. Specifically, in 1994 Peter Shor's famous algorithm for factorisation of prime numbers appeared for the first time and was published later in 1997 [57]. It shows how a quantum computer can be used to increase the speed of prime

factorisation. The number of steps needed in this case is given by $N^2(\log_2 N)\log_2(\log_2 N)$, which corresponds to an exponential improvement over classical algorithms. Nevertheless, as it does happen rather often in physics, quantum information science has not only created new problems but also new solutions. It has provided us with a way of securely sharing an encryption key with security ensured by the laws of physics, namely quantum key distribution (QKD).

1.2.1 The BB84 protocol

The field of quantum cryptography originated from Bennett and Brassard in 1984 with the publication of the original QKD protocol [34], now known as the BB84 protocol. This protocol makes use of the quantum characteristics of photons in order to securely transmit a secret key, which can be used as a one-time pad. Here, photons act as qubits which are sent from Alice to Bob in order to generate a qubit string, from which the secret key can be extracted. The principle works as follows: In the original proposal, the polarisation degree of freedom is used to encode the bit value, although there exist many other realisations using different encodings. Specifically, two conjugate bases are used, namely the rectilinear basis consisting of the states $|H\rangle$ and $|V\rangle$ (horizontal and vertical), and the diagonal basis made out of the states $|D\rangle$ and $|A\rangle$ (diagonal and anti-diagonal), which is obtained from the previous basis by rotating it by $\pi/2$. Due to the Heisenberg uncertainty principle, the measurement process will affect the state of the qubit if it is not prepared in the correct basis. Thus, if the photon is prepared, e.g., in the rectilinear basis, a measurement in exactly that basis will yield the correct result with 100% probability, while a measurement in the diagonal basis will yield a random result, either $|D\rangle$ or $|A\rangle$, each with 50% probability. Thus, if the measurement is performed in the wrong basis, the result becomes useless.
For the transmission of the key, Alice sends a string of photons, each prepared in a basis which she randomly chooses at the time of sending. She records the bit value ($|H\rangle, |D\rangle = 0$ and $|V\rangle, |A\rangle = 1$) and the chosen basis each time. Bob, in turn, as he does not know which basis Alice has used for preparation, randomly chooses the measurement basis of his detector for each photon, and also records the basis choice and his measurement result. In a second step, Alice then shares a bit string with only the information of the used bases, but not the encoded values, with Bob over a public classical channel. As no information about the actual key is included in this transmission, there is no concern about security. Bob then compares his basis choices with Alice's basis choices and both discard all bits where these do not match, as they contain no

information. The remaining bit string of values shared by Alice and Bob should then match perfectly up to some transmission errors which can be calculated.
There exists the possibility that an eavesdropper, the famous Eve[1], will try to intercept the quantum key. Since Alice's choice of basis is secret, Eve can only either try to intercept the information about the used bases, which is sent after the transmission of the photons and contains no relevant information about the actual key, or she can try to measure the photons Alice has sent to Bob before they reach their destination. Since she does not know which basis Alice has used for preparation, she can only randomly choose her measurement basis and then send the photons to Bob, encoded, i.e., in the same basis. As the measurement process affects the state of the photons, this will introduce more errors into the resulting bit string. In order to determine if Eve has tried to interfere, Alice and Bob can take a small part of the actual key string and compare the measured values. This process is known as key sifting. If the error rate is larger than the transmission error rate mentioned before, it means that someone has meddled in the transmission process and the key will be discarded. Thus, Alice and Bob can always determine if someone has tried to intercept the information, which makes the protocol secure by the laws of quantum mechanics.

1.2.2 The Ekert protocol

A further relevant QKD protocol, this time relying on entanglement, was developed by Ekert in 1991 [58], some years after the introduction of BB84. In this case, the used photons are not transmitted from Alice to Bob, but they both share a pair of entangled photons generated by a photon-pair source (originally spin-1/2 particles), typically in a singlet state $|\Psi^-\rangle = \frac{1}{\sqrt{2}}\{|\uparrow\downarrow\rangle - |\downarrow\uparrow\rangle\}$[2] (where I have dropped the subscripts $1, 2$ for simplicity). Upon arrival of the photons, one at Alice's and one at Bob's end, they both perform randomly chosen measurements of the spin (polarisation) component on a plane perpendicular to the photons, each using a set of three azimuthal angles, $a_i \in \{0, \pi/4, \pi/2\}$ for Alice and $b_j \in \{\pi/4, \pi/2, 3\pi/2\}$ for Bob. Each measurement will yield either ± 1 in units of $\hbar/2$ and maximally one bit of information. Note that among the possible measurement angles, some of them belong to the same orientation and some do not. Alice and Bob divide their measurements into the ones where they used the same orientation and the ones were they used different orientations of the analysers, while they discard any measurements where either one or both of them did not measure a photon.

[1] Naturally, a woman who, like in the Bible, merely sought wisdom by taking the apple from the tree, yet was condemned as evil for all eternity.
[2] $|\Psi^-\rangle = \frac{1}{\sqrt{2}}\{|H, V\rangle - |V, H\rangle\}$ in polarisation basis.

As a next step, Alice and Bob perform a Bell test on their measured results, meaning they check their results and calculate the so-called CSHS quantity S (see Ref. [27]) for the measurements where different orientations were used. S is a composed quantity consisting of the different probabilities of measuring the result ± 1 along a_i, when the orientation along b_j is given by ± 1 [58]. Quantum mechanics requires $|S| = 2\sqrt{2}$. Because of unavoidable measurement errors in real applications, S will not reach exactly this value but will be very close to it. Alice and Bob now can use the measurement results obtained with the same orientation as the shared secret key. If the singlet state has been used, one of them will need to perform bit flips on every bit to obtain the key, as the results will be perfectly anticorrelated.
Intercepting the photons by Eve before they are analysed by Alice and Bob will yield no information whatsoever, as the information only 'comes into existence' when the measurements are performed by both parties. It can be shown that if Eve has tried to perform some other type of eavesdropping, such as meddling with the used photon pair source, the quantum correlations of the entangled pair will be destroyed and the photons will behave classically. This will yield a result of $|S| \leq \sqrt{2}$. Thus, if the resulting value is $S \ll 2\sqrt{2}$, Alice and Bob will again know someone has tampered with their photons and they will discard the resulting key. This method constitutes a real application of the Bell inequalities and allows for QKD with untrusted nodes, e.g., for application on satellite-based QKD, as will be discussed in more detail in Ch. 5. This stems from the above mentioned fact that the information is only created at the time of measurement. Therefore, this protocol is sometimes referred to as quantum key generation [39].

1.2.3 Further protocols

The two protocols described in the previous section constitute the most widespread and studied quantum communication protocols. Implementations of the BB84 protocol have been realised with single photons using practically all imaginable encodings, including polarisation, time-bin, amplitude and phase, etc.; and also with the same discrete degrees-of-freedom but using coherent states of light [59, 60]. Another worth-mentioning protocol is continuous-variable (CV) QKD [61], where the information is encoded in the continuous degrees of freedom of the electromagnetic field, i.e., the field quadratures.
Another protocol developped by Bennet, Brassard and Mermin in 1992 [62], which we will refer to as BBM92, is a simpler version of Ekert's protocol, that was shown to be secure against more general attacks such as the substitution of a fake EPR source, and is now widely used alongside BB84.

Concerning this last point, even though theoretically QKD proves to be secure against eavesdropping, practical implementations will never be perfect and will possess loopholes sensitive to many different types of attacks of motivated hackers. Typical security loopholes in experimental systems rely on source- and detector imperfections. Thorough reviews of possible existing attacks to QKD systems are given in Refs. [63, 64].
Secure QKD systems can be attained, e.g., by implementing (full) device-independent QKD (DI-QKD) [65]. However, DI-QKD turns out to be very complicated to achieve experimentally, stemming from the necessary near-unity detector efficiencies, quantum nondemolition measurements or qubit amplification. Therefore, it amounts to a loophole-free Bell violation. Moreover, it yields extremely low key-rates [41]. A simpler approach to the problem is given by measurement-device-independent (MDI)-QKD [66, 67]. In this case, the focus lies in overcoming the generally most problematic part of QKD by removing the requirement to trust your measurement devices. The aforementioned requirements are relaxed in these implementations. Further, they achieve many orders of magnitude higher key rates when compared to full DI-QKD.
The development of novel protocols for quantum communication is an ongoing effort and this section only aims to give a small introduction. For thorough reviews on the topic I recommend Refs. [68–70].

1.3 The quantum repeater

QKD is a widely advanced field that has been developing incredibly since its birth in the 80s. It arguably is the fastest growing area of QIP that has produced functioning commercial devices. There exist several companies offering commercial systems and the number of quantum startups like MagiQ, ID Quantique (IDQ), QXchange, Quintessence Labs, QNu Labs, QEYnet, to name a few [71], seems to be ever growing. However, overcoming exponential losses in the transmission rates and the sharing of entanglement over large distances remains a Sisyphean endeavour both in fibre and free-space operation due to fundamental bounds [72–74]. In other words, photons do not survive longer than about 1 ms in optical fibres (depending highly on the wavelength). As a result, Alice and Bob should not be further than ~ 200 km apart for Alice's photons to reach Bob with non-vanishing probability.
Entanglement purification techniques can be used in order to regain a better fidelity [75, 76], but this requires a large number of partially entangled states and the scaling is again exponential, which clearly does not solve the issue.
The quantum repeater (QR) was proposed in Ref. [77], and shortly after also investigated

in Ref. [78], as a general solution to this problem. The underlying principle consists in dividing a long distance L between two nodes that are too far away for point-to-point entanglement distribution into smaller segments or elementary links. First, entanglement is established between neighbouring nodes connecting these smaller segments, which are close enough to each other to allow for effective and efficient entanglement distribution. When all pairs of neighbouring links have successfully established entanglement, recursive entanglement swapping operations [79, 80] are performed until the two outermost nodes share the entanglement. The entanglement swapping operation consists of a joint Bell-state measurement. Optically this simply means sending two photons arriving from distinct locations, each belonging to its respective entangled pair, through a beamsplitter and detecting coincidence counts on two detectors placed behind the two output ports. This procedure effectively erases the 'which-way' information and entangles the two measured photons. Therefore, the former partners of the measured photons, now at double the original distance, are immediately entangled as well, despite never having encountered each other. This procedure was first demonstrated experimentally in Ref. [81]. A very informative description of the principles behind Bell-state measurements and simple entanglement swapping is given in [18]. The scheme in Refs. [77, 78] further makes use of entanglement purification with imperfect means and a 'nested purification' protocol, where the time required for creating entanglement now scales polynomially with distance, but the required resources scale only logarithmically.
In order for the distribution of entanglement to succeed, it needs to occur simultaneously across all elementary links. This being a probabilistic process makes this joint probability rather low. Quantum memories can aid to synchronise this process, by storing the arriving photons until all have arrived, before performing the swapping. Exactly this fact is what ensures the polynomial scaling of communication efficiency. The working principle of entanglement swapping is represented in Fig. 1.1.

1.3.1 Repeater architectures

A highly prominent proposal for the realisation of a QR is the DLCZ protocol, brought forward by Duan, Lukin, Cirac and Zoller in 2001 [82]. The scheme relies on manipulation of atomic ensembles, linear optics, and single photon detectors, making it dependent only on currently (and at the time) available technology. The resulting communication efficiency scales polynomially with channel distance, a considerable improvement to the exponential case. Furthermore, the scheme includes built-in entanglement purification [76, 83], making it robust against noise and allowing for high entanglement fidelities over

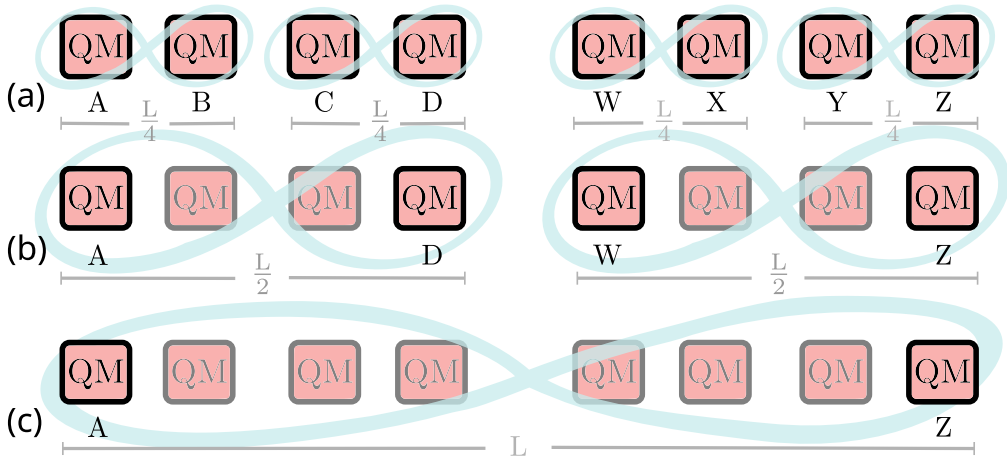

Figure 1.1: Working principle of a quantum repeater network. A distance L is divided into several sections of length $L_0 = \frac{L}{N}$, where $2N$ is the number of nodes. The nodes, here each represented by a quantum memory (QM), are pairwise entangled in a first step (a). Thus, entanglement (light blue) is created between A & B, C & D, W & X, and Y & Z. In a second step (b), neighbouring links are entangled via entanglement swapping by performing a Bell-state measurement on B & C and X & Y, such that now A & D and W & Z are entangled. Third, entanglement swapping is performed again. As a result, now A & Z are entangled and the information is shared over the whole distance L.

long distances. The general principle consists in the creation of a long-lived collective spin excitation in two atomic ensembles acting as read-only memories (see Sec. 1.5), called a spinwave, as we will see later on. This excitation is generated via a stimulated Raman transition of one atom, which generates a forward scattered Stokes photon. As it is not known which atom in the ensemble has been excited, the resulting state is a coherent superposition of all possibilities. Via coincident detection of the generated Stokes photons after passing a beam splitter, i.e., after a Bell-state measurement, both memories can be entangled. In order to extend the quantum communication distance, entanglement swapping between pairs of entangled memories distributed across three nodes is performed by reading out the two memories of each pair located in the central node. The readout again occurs via a stimulated Raman transition. The included purification scheme relies on the fact that noise corresponding to vacuum components of photons that have been lost in transmission are inherently discarded, as they do not yield coincidence clicks at detection. The ensembles, generally consisting of alkali vapours, used in this protocol serve both as memories and as photon sources (see Sec. 1.4.2). Resulting from the wavelength of the generated photons ($\approx 800 - 900\,\mathrm{nm}$), losses in fibre are relatively high. Furthermore, since the verification that the entanglement has been created in the

elementary link can only be communicated through a classical channel, as occurs in the Ekert protocol [58], the time between entanglement generation attempts is limited to $\frac{L_0}{c}$.

Further QR schemes were proposed in 2007 by C. Simon et al. [84] and by N. Sangouard et al. [85] aiming to overcome the classical information transmission issue by developing the DLCZ scheme to include photon pair sources and multimode memories, or a single photon source, respectively. The latter protocol [85] additionally yields enhanced transmission rates, limited in Ref. [84] by the intrinsic two-photon pair emission probability (see Sec. 1.4.3). This is accomplished by using an ideal single photon source and a beam splitter in order to separate the photon going to the memory and the one going to the intermediate link. A schematic of the repeater scheme of Ref. [84] is depicted in Figure 1.2.

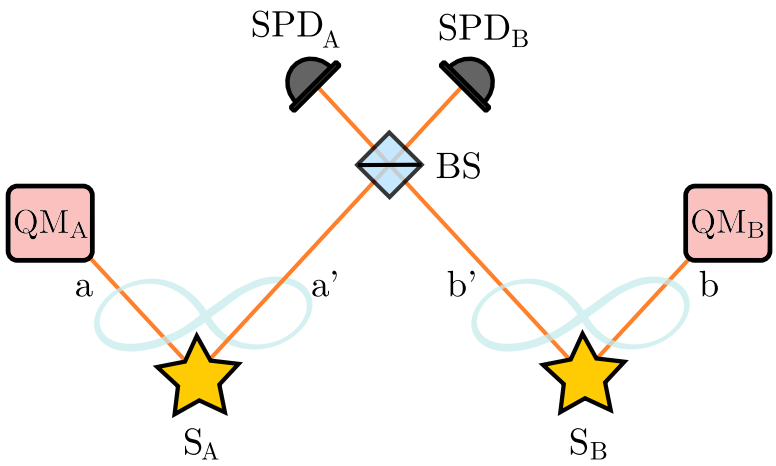

Figure 1.2: Schematic of a basic quantum repeater segment as proposed in Ref. [84]. Two photon-pair sources $S_{A,B}$ emit pairs of entangled photons a and a' & b and b'. The distant memories QM_A and QM_B can be entangled via a Bell-state measurement performed with the beamsplitter (BS) and the single photon detectors $SPD_{A,B}$. Several of these segments can be entangled via entanglement swapping (not shown).

The field of quantum repeaters is a large area of research on its own, and implementations can be divided into three big categories according to the scheme employed for the correction of propagation errors, as described in detail in Ref. [86]. For more information about details and further schemes I refer the reader to several review papers [68, 87, 88]. The type of repeaters that mostly interest us though, are the ones which make use of quantum light sources and quantum memories plus entanglement swapping operations to extend the communication lengths. As these components are highly relevant, a

short introduction on quantum light sources is given in the following section. Quantum memories will be introduced in Sec. 1.5. Several proposals exist for the realisation of QRs in space, this being a large field of its own. Therefore, repeaters for long-distance satellite-based quantum communication and various other ground- and space-borne applications will be discussed in detail in Ch. 5.

1.4 Quantum light sources

As we have seen, single photons are indispensable for QIP protocols, if we leave continuous-variable primitives out of the discussion. However, the definition of a single photon is not straightforward, and as always, has led to many discussions in the quantum optics community. As a matter of fact, there are several possible definitions [89], and even denial of their existence [90].
Assuming photons do exist, since we do need them for this work, we will mainly adopt the experimentalist's practical point of view, where a photon is understood as a click on a detector. Yet, we will also keep in mind that a photon can be seen as the elementary excitation of a single mode of the quantised electromagnetic field, as Dirac understood it [91]. The latter is what theorist's would understand a photon to be. Notwithstanding, if we are going to discuss quantum or single-photon sources (SPS), our photons will have to be 'created' somewhere, and therefore exist before they arrive at the detector[1]. We can thus imagine the photon as a discrete travelling wave-packet mode propagating from source to detector [89].

Turning to the description of the sources, or so-called 'photon-guns' [92] where the photons are 'created', it is important to summarise what makes an ideal SPS. First, it should be on-demand or deterministic, meaning that the user can define the emission time of the photon with 100% probability, just as if pressing a button on a photon-creating black box. Further, the probability of multi-photon emission should vanish. Second, subsequently emitted photons should be indistinguishable, that is, have exactly the same frequency, polarisation, duration of the temporal pulse, etc. Third, the repetition rate or brightness of the source should be arbitrarily high [93]. Naturally, no such perfect source exists to date, and will probably ever exist. Yet, the development of near-to-ideal SPS has become a large, steadily-growing field of its own. Real SPS can de divided into two different types: deterministic and probabilistic ones. The first kind are semiconductor sources such as quantum dots (QDs) and nitrogen-vacancy (NV) centres, but also single emitters in

[1] Although this fact also is a matter of taste.

cavities. The second kind are *heralded* pair sources based on spontaneous-parametric down-conversion (SPDC) or four-wave mixing (FWM), where the detection of an idler photon heralds the creation of a signal photon. Ensemble-type emitters like read-only memories also belong to this category. In the following, I will shortly describe these types of sources. For more detailed information I refer the reader to Refs. [92–95].

1.4.1 Single emitters

Single-emitter-based photon sources comprise a broad variety of systems. Among these there exist single atoms, ions, and molecules, and semiconductor based systems such as quantum dots (QD) and NV- and other colour centres. Here I will focus mainly on QDs, and leave out the discussion of the rest (see again [93]). In Ch. 2, some of these remaining systems are described in the context of their use as possible memory platforms. The operational principle of all of these types of systems is similar, even though the material systems are different. They are externally excited by some sort of control, and emit a photon upon relaxation to a lower level. Generally, optical cavities are employed to engineer the emission characteristics and achieve higher efficiencies.
Semiconductor QDs are engineered 'artificial atoms', islands of a smaller-bandgap semiconductor material embedded in a host semiconductor material with a larger bandgap. Common material combinations are InAs or InGaAs on GaAs. Due to the small size of the dots, the resulting energy structure for the involved electrons and holes is discrete. In a weak-excitation regime, excitons (electron-hole pairs) can be produced on demand. Their recombination results in photon emission with a radiative lifetime of about 1 ns. Quantum dots thus emit deterministically, with a high brightness and a low multiphoton contribution [96]. They are very well suited for use in quantum information processing [97, 98]. There have been several approaches to interface these systems with warm alkali vapours [99], as a first step to build heterogeneous quantum systems. A drawback of these systems is that they require cryogenic cooling and suffer from inhomogeneity of the source [100]. An ongoing issue is the difficulty of achieving high collection efficiencies of the emitted photons into optical fibres. A detailed review of QD sources for quantum communication can be found in [97].

1.4.2 Ensemble-based sources

Ensemble-based sources are a very good alternative SPS compared to single emitters, showing satisfactory rates and efficiencies, albeit with a lower photon state accuracy,

hereby meaning its closeness to a single photon Fock state [94]. A significant example are sources based on spontaneous four-wave mixing (FWM) [101, 102]. These types of sources can be seen as the atomic ensemble analogy to SPDC sources in non-linear crystals and achieve comparable results when operated in a cavity [94]. A huge benefit of ensemble-based sources is the innate compatibility with ensemble-based memories, facilitating interfacing between these systems. Another candidate in this context are so-called 'read-only' memories [103], as the ones used in the DLCZ repeater scheme introduced above. Here the single photons are generated via Raman scattering using a write-read pulse sequence, in which the first photon heralds the existence of a spinwave (see Fig. 1.3) in the atomic ensemble, which is later converted into a second photon. For more details I refer the reader to Chapter 2. Examples of these sources in cold and warm atomic ensembles can be found in Refs. [104–109].

1.4.3 Spontaneous parametric down-conversion sources

Spontaneous parametric down-conversion (SPDC) is the name given to a process occurring in a nonlinear crystal, in which a high-frequency photon of a strong pump laser is downconverted into a pair of photons with lower frequency. The process allows for tunability over a broad wavelength range. It relies on a $\chi^{(2)}$ optical nonlinearity in the material, which gives rise to a three-wave mixing process [94, 110]. Common materials are LN, BBO and KTP [95]. The process can be degenerate, where the two resulting photons have equal frequency, and it can also be non-degenerate, producing two photons with different frequencies. These are called the signal and the idler, and $\omega_{\text{pump}} = \omega_{\text{signal}} + \omega_{\text{idler}}$ is required for the resulting frequencies. The possible frequency and wavevector relations between signal and idler are given by the phase-matching conditions, stemming from energy and momentum conservation. As a result, the emission in these sources is highly directional. However, due to reduced control over the dispersion of the material, phase matching is only attainable for some sets of wavelengths [95]. Regarding experimental complexity, SPDC sources are relatively simple when compared to deterministic sources, since they work at room temperature. They behave as probabilistic sources. Specifically, the detection of the idler photon heralds the presence of the signal photon. The ideal state emitted by a (non-degenerate) downconversion source is a two-mode squeezed state. The emitted photons in such a process are exclusively generated in pairs [95]. Even for a small generation probability, there is a non-vanishing probability of higher order multi-photon events. For a mean photon-pair number μ, the generation probability $p_\mu(k)$ of k photon pairs is given as [100]

$$p_\mu(k) = \frac{\mu^k}{(\mu+1)^{k+1}}. \tag{1.9}$$

This implies that the generation probability of a single photon pair reaches a maximum at 25%, resulting from the non-vanishing likelihood $\sim \mu^k$ of undesired zero-pair and multiple-pair outcomes. In other words, for the generation of heralded single photons, SPDC sources have to be operated far below threshold [95]. This leads to low generation rates, posing a problem for applications in, i.e., QIP.
The generated photons in bulk SPDC have typical spectral widths on the order of hundreds of GHz to THz [111]. In order to make the output of such a source compatible with atomic quantum memories, the output can either be filtered, leading to even lower brightness, or the crystal can be placed in a cavity that leads to narrowing of the emission of the cavity decay rate [95] and what is more, to enhanced brightness. Examples of such sources are presented in [112, 113].

1.5 Quantum memory

This section aims to give an introduction to the concept of a quantum memory, which will be later on reviewed in detail in Chapter 2.
In its most general definition, a quantum memory [114] is a device able to store quantum information, allowing for its on-demand read-out when the information is needed for further manipulation, processing or detection. We have learned that due to no-cloning quantum information can in general not be copied, meaning, as mentioned, that the storage procedure of a quantum memory cannot be the same as the one used in the memory, of, e.g., a classical computer. Here, the information, encoded in bits, is simply copied onto the storage system, while it remains existent in its original form. In the quantum realm however, the storage process must consist of a physical interaction of the storage system with the information carriers, resulting in the coherent transfer of the quantum state of the latter onto the memory. Unless, of course, we are thinking of storing a photon in a delay loop.

Apart from this last case, a quantum memory therefore is an interface between flying information carriers, typically photonic qubits, and stationary matter qubits. These matter qubits can encompass various physical systems, ranging from single particles to ensembles, spanning warm and cold atoms, solid-state systems, and optical fibres or delay lines. An essential attribute of a quantum memory is its ability to preserve the quantum state as faithfully as possible until it's needed again. Hence, the physical system

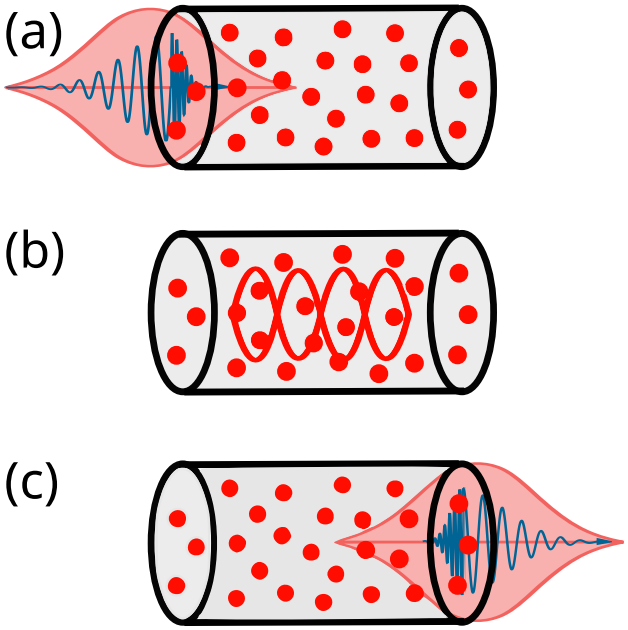

Figure 1.3: Sketch of the working principle of an optical warm vapour quantum memory. The signal pulse (blue wiggly pulse) enters the memory cell filled with atoms simultaneously to the strong control pulse (light red) that serves as a switch to write (a) into and read (c) from the memory. The red wave in (b) represents the so-called spinwave, the long-lived atomic coherence into which the photonic information is transferred to and stored for a given time.

should ideally be well-shielded from noise and decoherence processes, or if this is the case, suitable for quantum error correction [115]. However, a memory will never be perfect and will therefore eventually forget.

Furthermore, simplicity in manipulation is desirable. Unfortunately, this often conflicts with noise susceptibility. Easily controlled systems tend to be more susceptible to noise from the very sources used to manipulate them, while highly isolated systems with minimal noise susceptibility are usually less amenable to manipulation. As a result, the former are much more short-lived than the latter, there always seems to be a trade-off.

One has to differentiate between two kinds of memories; read-only memories, which emit a photon entangled with them upon excitation; and write-read memories, where the information from an incoming photon is transferred into the material excitation, and can be converted back to light upon read-out. The first kind of memories are the protagonists of, e.g., the DLCZ protocol introduced already [82]. We are however more interested in the second kind, as schematically represented in Fig. 1.3.

The field of quantum storage has witnessed significant growth in recent decades, with a wide range of potential applications [114]. Quantum memories are not limited to

synchronising and buffering information at network nodes in long-distance quantum communication and quantum computing. They also find use in single photon generation, tests of fundamental physics in space, secure authentication through quantum tokens, distributed quantum computing architectures, and many other areas. As a result, the study of quantum memories is a captivating and expanding field, in which I have been fortunate to work for the past few years. In the following chapter, I will deliver a detailed review of the field.

2 Quantum Memory Review

"The problem is not making up the steps, but deciding which ones to keep..."

Mikhail Baryshnikov

2.1 General considerations

As was described in the introduction, quantum memories are physical systems that serve as an interface between flying photonic qubits and stationary matter qubits or atomic excitations. They allow one to store photonic quantum information and retrieve it, favourably on demand. This chapter will offer a broad review of the field of quantum memories, covering relevant figures of merit, several different memory platforms, and existing protocols. The discussion is inspired mainly by Refs. [2, 18, 94, 116].

Apart from the possibility of on-demand retrieval, one can impose many different conditions on a memory system and protocol. This memory 'wish-list' will highly depend on the envisioned application. The figures of merit used to describe the performance of a given memory system, which will be introduced in Section 2.2, are a means to compare the far reaching landscape of different platforms and protocols. Some systems yield very long storage times, others high efficiencies, large bandwidths, or low noise, but not a single one shows ideal performance with respect to all of these parameters. In general, trade-offs between these parameters have to be made, depending substantially on the application.

The realm of different physical systems in which quantum memories of light have been realised is vast. It spans from single emitters, such as single atoms in cavities or color centres in diamond, to large atomic ensembles containing $10^4 - 10^{12}$ atoms, both (ultra)-cold and warm (room temperature or higher); and also to solid-state systems. As mentioned in the introduction, also fibre delay lines or storage rings can be considered memories. Each of these platforms, which will be introduced in detail in Section 2.3, has its benefits and its drawbacks, and no single one has yet been found to be the ideal quantum memory.

In order to understand light storage, it is useful to think of the simplest imaginable memory system: a single atom in free space interacting with a single mode of the electromagnetic field, i.e., absorbing one single photon. Describing the atom as an ideal two-level system (see Fig. 2.1(a)), if the energy difference of the photon matches the energy difference between the states, absorption of the photon will transfer the atom from its ground state $|g\rangle$ to the excited state $|e\rangle$.
Ideally, the atom would then reemit the photon after a given time, making the storage process reversible. Naturally, it is not as simple as that. An atom interacting with an electromagnetic field via an electric dipole interaction in, e.g., the strong coupling regime, undergoes Rabi flopping. As a result of the time reversibility of quantum mechanics, in the case of no losses, e.g., due to spontaneous emission, the atom oscillates between $|g\rangle$ and $|e\rangle$ with a frequency given by the Rabi frequency Ω, a measure for the coupling strength between the atom and the electromagnetic field. Hence, such a simple memory would not abide to the condition of on-demand retrieval of the photonic information.

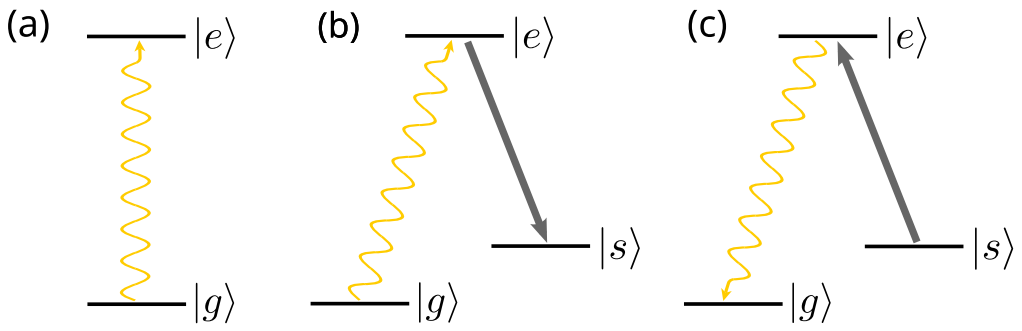

Figure 2.1: Two- and three-level atomic systems. (a) A two level atom becomes excited from its ground state $|g\rangle$ to the excited state $|e\rangle$ by a photon (yellow wiggly arrow). In order to obtain controllability, a third (storage) state $|s\rangle$ becomes necessary. In (b) the atom is transferred from $|g\rangle$ to $|s\rangle$ via $|e\rangle$ with the aid of the control pulse (grey arrow). In (c) the reverse process is shown.

It is thus necessary to include some type of controllability in the system. For this, one must add a third state $|s\rangle$ to the system, which does not interact with the mode of the field to be stored, and is therefore a 'dark state'. There are several possible choices for this state $|s\rangle$ and thus also for the atomic configuration. Depending on the energy of this

state relative to the other two, one can describe the atom as a three-level Λ- (lambda), Ξ- (ladder) or V- (vee) system (see Fig. 2.2). There exist also more complex configurations including even more states [117, 118] but these will be ignored here for simplicity.
The controllability arises from the transfer of the photonic information from $|e\rangle$ to the dark state $|s\rangle$ via an auxiliary control field (grey, see Fig. 2.1(b)), which stops or 'freezes' the Rabi oscillations. In this manner, the photon ideally remains trapped in this storage state for as long as needed, provided the atom is well isolated from the environment.
In order to read the information out from the memory, the same control field reverses the mapping, transferring the photon from $|s\rangle$ back to $|e\rangle$, where the Rabi oscillations lead to reemission of the photon, as depicted in Figure 2.1(c).

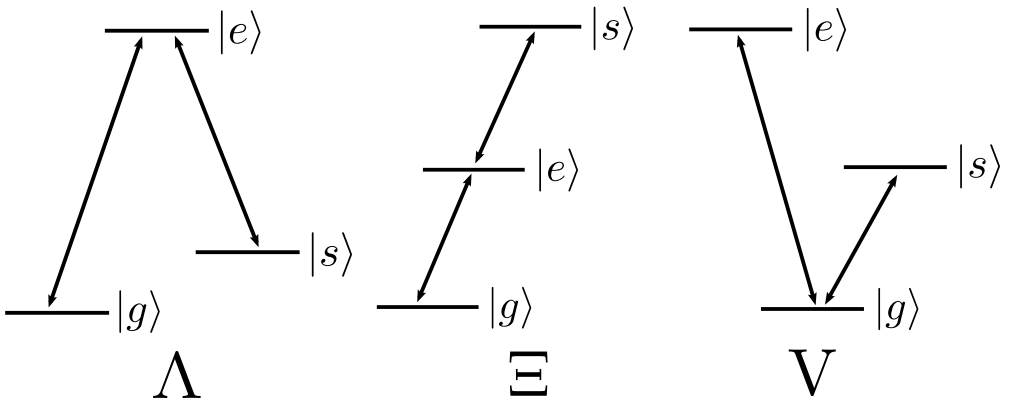

Figure 2.2: Different types of three-level systems. From left to right Λ-system, (ladder) Ξ-system, and V-system. The arrows represent the present laser fields.

The description given above assumes, of course, ideal conditions. When considering real systems, neither the atom can be described as an ideal two- or three- level system, nor the electromagnetic field consists of only one single mode, but actually spans a continuum of modes in all of space. For an atom in free space is it actually rather improbable to undergo Rabi oscillations, as the emitted photon will probably escape before coupling back to the atom. Thus, instead of Rabi flopping, we will see spontaneous emission, an exponential decay of the coupling with a lifetime inversely proportional to its strength. As a result, a real atom in free space will not serve as a quantum memory, alas not a very good one.
However, there are several ways to circumvent this problem. Single atoms or other single emitters have indeed been used for quantum storage. As the coupling of a single atom to light is very weak, one trick is to enclose it in a high-finesse cavity that will restrain

the interaction with unwanted field modes and enhance the coupling to the relevant ones. Another possible option is to increase the probability of light-atom interaction by using not only one, but many atoms. Ensembles of cold or warm atoms in the gas phase with high optical depth, and also solids are thus common storage platforms.
In an ensemble of N atoms, as it is not known exactly which atom experiences the excitation into the storage state $|s\rangle$, the storage process results in a long-lived collective superposition of all but one of the atoms being in the state $|g\rangle$ and one (unknown) atom being in the state $|s\rangle$. Such a superposition is called a spinwave. Mathematically it takes the form [119]

$$|\psi\rangle = \frac{1}{\sqrt{N}} \sum_j e^{i\Delta \boldsymbol{k}\cdot \boldsymbol{r}_j} |g...s_j...g\rangle \,, \tag{2.1}$$

where $\Delta \boldsymbol{k}$ is the wavevector of the spinwave, and $\boldsymbol{r}_j$ corresponds to the spatial coordinate of the jth atom, which is excited to $|s\rangle$.
As extensive as the different memory systems are also the various protocols known to achieve light storage in these systems, which will be described in Section 2.4. The general working principle of optically controlled memories described above applies to all protocols based on light-matter interaction, although the specific details are widely different. In this chapter only an simplified explanation will be given. More detailed calculations will be left to Chapter 3.

2.2 Memory characterisation

We will start our discussion by revisiting the most important figures of merit used to characterise a specific quantum memory. As mentioned before, no single platform and protocol have been found to date to yield an optimum in all of these following parameters simultaneously. Much effort is being put into exactly this, notably in our experiments presented in Chapter 4. For simplicity, we will focus on the case of storage of a single photon, or of coherent light at the single-photon level for the following definitions, although they are also valid in the case of storage of macroscopic light pulses, with some slight modifications. The definitions presented here are mainly based on Refs. [39, 94, 120–122].

2.2.1 Efficiency

The memory efficiency is a measure of the probability of retrieving a light pulse or a photon after having stored it in a memory. Realistic memories will never reemit the stored light perfectly without any losses. As most of the loss mechanisms in a memory platform are time dependent, i.e., the longer a photon is stored, the less probable it is to retrieve it back, the memory efficiency is normally defined as the efficiency at zero storage time $\eta_{\text{mem}} = \eta_{\text{mem}}(t = 0)$. Naturally, this is not a realistic value for applications, but it yields a baseline with respect to which very different systems can easily be compared.

When storing single photons, the external (end-to-end) memory efficiency can be determined from a photon arrival time histogram and is given by

$$\eta_{\text{e2e}} = \frac{N_{\text{out}} - N_{\text{noise}}}{N_{\text{in}}}, \tag{2.2}$$

where $N_{\text{out(in)}}$ stands for the counts measured at the output time bin (input time bin) and N_{noise} is a measure for the photons the memory emits even when no photon has been stored in it (and also on top of the retrieved photon when storage has indeed taken place). This is due to spurious unwanted physical processes such as the ones described in Section 3.4.
This end-to-end efficiency includes all transmission losses η_{transm} of the experimental setup and is related to the internal memory efficiency of only the physical storage and retrieval process as $\eta_{\text{e2e}} = \eta_{\text{transm}}\eta_{\text{mem}}$. Such transmission losses can be seen as technical losses and can theoretically be improved by better optics or better fibre coupling of light. For real applications, naturally the resulting end-to-end efficiency is the relevant one, and the one that should be used to compare different memory systems. Further theoretical definitions of the efficiency, that are of aid in simulations or theoretical work, are given Ch. 3 and in Refs. [123–125].

2.2.2 Signal-to-noise ratio and measures of noise

As stated above, realistic physical systems are not ideal. Spurious physical processes that produce unwanted counts at the detector when nothing has actually been stored in the memory are inherent to quantum storage. These unwanted photons that are added to the retrieved photon counts generate errors in storage, which can, e.g., lead to loopholes in some quantum cryptographic protocols and thus compromise security (see Sec. 1.2.3 and Ref. [126]). Therefore, it is essential to have a measure of the quality of the

retrieved information. As the fidelity, which will be introduced below, is not always easily experimentally accessible, the signal-to-noise ratio (SNR) given as

$$\mathrm{SNR} = \frac{N_{\mathrm{out}} - N_{\mathrm{noise}}}{N_{\mathrm{noise}}} \tag{2.3}$$

is typically used as a measure. The time window for which the SNR is defined can be adjusted to include more or less noise, since in practical implementations time gating can be implemented via hardware. This is useful for memories, such as the EIT Λ-memory, where the highest amount of noise typically is found in the later part of the optical pulse. A further relevant parameter commonly used to describe the noise level or unconditional noise floor is the μ_1 parameter, firstly introduced in Ref. [127] and defined as the ratio of the average noise counts to the end-to-end efficiency scaled by the detector efficiency [120, 128]

$$\mu_1 = \frac{\langle N_{\mathrm{noise}} \rangle}{\eta_{e2e}\eta_{\mathrm{det}}}. \tag{2.4}$$

It provides a measure for the number of input photons into a memory, for which the SNR is exactly one.

2.2.3 Storage time

The storage time t_{storage} of a memory system refers to the time until which it is still possible to retrieve the stored information or some fraction of it. Due to several decoherence mechanisms [129], no memory will have infinite storage time and will thus eventually forget. The definition of the storage time varies, as most of these figures of merit do, with the application. Mostly, one refers to the coherence time of the physical system τ_c, more specifically of the used storage state. Other values, generally extracted experimentally, give a measure of how long it takes for the efficiency or the fidelity (or some other measure) to fall below a specific threshold, generally $1/e$. The latter measure for the decay time of the efficiency will be the benchmark used throughout this thesis. I will generally refer[1] to the actual storage time of the memory as t_{storage}, and the $1/e$ time as τ_{mem}.

For applications, such as long-distance quantum communication, the storage time is clearly of high importance, as it must exceed the time of flight between distant nodes, and be of the order of entanglement creation times. Corresponding estimated values are of the

[1] Although I have done my best to avoid it, I cannot completely guarantee that there will not be some symbol confusion along the thesis. I hereby sincerely apologise for this.

order of $1 - 100\,\mathrm{ms}$ [130, 131]. Other more local applications, such as synchronisation, require significantly lower storage times [94].

2.2.4 Fidelity

The fidelity in quantum mechanics is a measure of distance between two quantum states. In quantum memory applications, it is crucial to determine how much the retrieved state resembles the initially stored state, e.g., if the storage process was coherent. The fidelity is calculated as the overlap between the output and the input state of the memory [39, 121], conditioned on the fact that the memory produces a non-vacuum output. For pure states characterised by a state vector $|\psi\rangle$, the conditional fidelity is thus given as

$$\mathcal{F} = |\,\langle\psi_{\mathrm{out}}|\psi_{\mathrm{in}}\rangle\,|. \tag{2.5}$$

In the case of a mixed state characterised by a density matrix ρ [39], this converts to

$$\mathcal{F} = \mathrm{Tr}\left(\sqrt{\sqrt{\rho_{\mathrm{out}}}\rho_{\mathrm{in}}\sqrt{\rho_{\mathrm{out}}}}\right). \tag{2.6}$$

When considering a quantum memory, its quantum character needs to be certified. This translates to the fact that its fidelity must surpass the 'fidelity' achievable by a classical memory. Such a device would be able to measure an input state and prepare a new state as close as possible to the input state upon retrieval. It has been shown [132] that the maximal achievable fidelity of such a device, assuming perfect efficiency, is given as $\mathcal{F} = \frac{N+1}{N+2}$, where N is the photon number. In the case of a one-photon Fock state $|1\rangle$ this bound equals 2/3. In the case of coherent states and non-unity memory efficiency η_{mem}, the Poissonian statistics and η_{mem} have to be taken into account, yielding higher classical bounds [128, 133, 134]. From these considerations, in Ref. [135] the following relation between the conditional fidelity $\mathcal{F}$ and the SNR, and/or μ_1 is derived:

$$\mathcal{F} = \frac{\mathrm{SNR}+1}{\mathrm{SNR}+2} = \frac{|\alpha|^2+\mu_1}{|\alpha|^2+2\mu_1}, \tag{2.7}$$

which allows to determine the fidelity of a quantum memory via easily attainable experimental parameters without having to reconstruct the density matrix of the state via quantum state tomography or similar techniques.
There is controversy around the question if it makes sense to define a fidelity for a

coherent-state input in a quantum memory, even at single photon level, hence the name 'conditional fidelity' used above. The definition of this fidelity requires the measurement record to be post selected to neglect all 'null' results, where the memory produced no output. Therefore, this fidelity, calculated for coherent states, should be taken with care and understood as the maximal bound on the fidelity achievable by a quantum memory, if it were to store a single photon.

2.2.5 Further figures of merit

Bandwidth

This parameter determines the spectral and temporal size of the photonic wavepacket that can be stored in the memory. As we have seen in the discussion of the different memory protocols, this parameter depends not only on the used platform, but specially on the method used for storage. This is specially important when interfacing quantum memories with, e.g., single photon sources, such as semiconductor quantum dots or parametric down-conversion sources. A formal definition of the bandwidth of a memory is tricky, as it is highly dependent on the protocol. Notwithstanding, one could define the bandwidth $\Delta\omega_{\text{mem}}$ of the memory as the full width at half maximum (FWHM) of the Fourier transform $\mathcal{F}$ of an input pulse $\mathcal{E}_{\text{in,opt}}$ (in time domain) optimised to give the best attainable efficiency of a given memory system as [136]

$$\Delta\omega_{\text{mem}} = \mathcal{F}(\mathcal{E}_{\text{in,opt}}(t)). \tag{2.8}$$

The bandwidth of the memory also gives information about the repetition rate and the multiplexing potential, when thinking about time or frequency multiplexing, as will be treated below. Again, the importance of this parameter depends highly on the application.

Time-bandwidth product

The repetition rate of a memory, and thus of a quantum-information protocol involving such a memory, depends not only on its bandwidth $\Delta\omega_{\text{mem}}$, but also on the amount of time that pulses can be stored in it. In order to store temporally short pulses, the bandwidth of the memory needs to be large. Furthermore, the storage time of the memory should exceed the pulse duration by a large factor, to perform operations while the qubit is stored. This is why the time-bandwidth product (TBP) is commonly used as a metric in some specific quantum memory applications. It is given as

$$\mathrm{TBP} = \Delta\omega_{\mathrm{mem}} \cdot \tau_{\mathrm{mem}}. \tag{2.9}$$

The TBP gives a measure for the number of clock cycles spanned by the storage time of the memory. For synchronisation tasks specifically, a large TBP is required [120, 137, 138].

Multimode capacity

For realistic quantum information protocols to succeed, the transmitted bit rate needs to reach high values in the kHz-MHz range. For this, it is crucial to be able to store more than one mode simultaneously in the memory [130, 131]. This is referred to as multiplexing. It allows to reduce the amount of entanglement swapping trials and enhance the speed with which the quantum channel is established.
There are many possibilities for multiplexing in a quantum system, such as time-, frequency- or spatial multiplexing, and the best suited one depends again on the specific memory system and the application. For completeness it should be noted that storage in continuous variables inherently realises higher bit per symbol possibilities, but I will set aside CV encoding in this thesis. Another approach to multiplexing would be to use N copies of the same quantum memory. As long as quantum memory systems are not so easily scalable, this will be much more cost intensive than trying to implement some multimode storage in a single memory.

Scalability, compatibility and technical simplicity

When thinking of practical applications, another relevant aspect about a quantum memory is how easy to implement and how scalable or integrable it is. Quantitatively, this may be seen also in terms of the cost of implementation. As discussed above, highly multimode memories are desirable for many applications, but if the memory itself is cheap, one can also think of simply implementing a large number of memories in a system. If the goal is to implement memories on a satellite, large cryogenic systems or magneto-optical traps are complicated setups that are hard to implement. However, much progress is being made in this area, and currently there exist many experiments (already active) or proposals planning to implement, e.g., cold atomic experiments in space [139–141]. Nevertheless, it is generally desirable to have a memory which can be operated at ambient conditions, such as room temperature and pressure. Independently of space operation or not, a goal for quantum memories is their implementation in photonic networks based on fibres or in optical circuits. For this, compatibility is a key aspect. Different features

may fall under this requirement, such as the operational wavelength, the possibility for fibre-based operation or even (micro-)integration.
Another measure for the applicability of a memory system is the SWaP (size, weight, and power) budget, as generally resources in these areas are limited in the context of space applications [11].

2.3 Memory platforms

This section will introduce the variety of storage platforms that are commonly used for quantum storage and shortly compare their advantages and drawbacks. The state-of-the-art experimental realisations of quantum memories in these systems will also be mentioned. The focus of this section will be on optically active systems, as they serve as great candidates due to the already very advanced technology of photonic quantum information distribution. Platforms currently lacking optical interfaces, such as those based on semiconductor technology [142], will not be included here. Figure 2.3 shows schematic depictions of the different memory platforms covered in this section. Table 2.1 (at the end of the chapter) presents a comparison of the different platforms regarding experimental parameters such as operational temperatures and magnetic fields, and regarding the technical effort required for their implementation.

2.3.1 Single emitters

Single atoms/ions in a cavity

Among the first systems to be studied for light storage were single atoms or ions in cavities [53, 133, 143, 144]. These can be understood as a slightly different type of memory. Experiments in these types of systems generally do not see the memory as designed to absorb and then emit a photon, but more as a memory emitting photons that are entangled with it, resembling more a DLCZ memory [82], but using single atoms/ions instead of an ensemble. The measurement of two emitted photons from two of these trapped particles allows us to entangle distant memories. They have also been used for teleporting quantum states between nodes [145].
These memories can be integrated with efficient optical interfaces and possess excellent coherence properties. Combining them with efficient high-finesse cavities permits boosting the optical interaction via the Purcell effect and/or strong coupling to cavity modes [146–149]. In these systems, entanglement swapping between network nodes has been

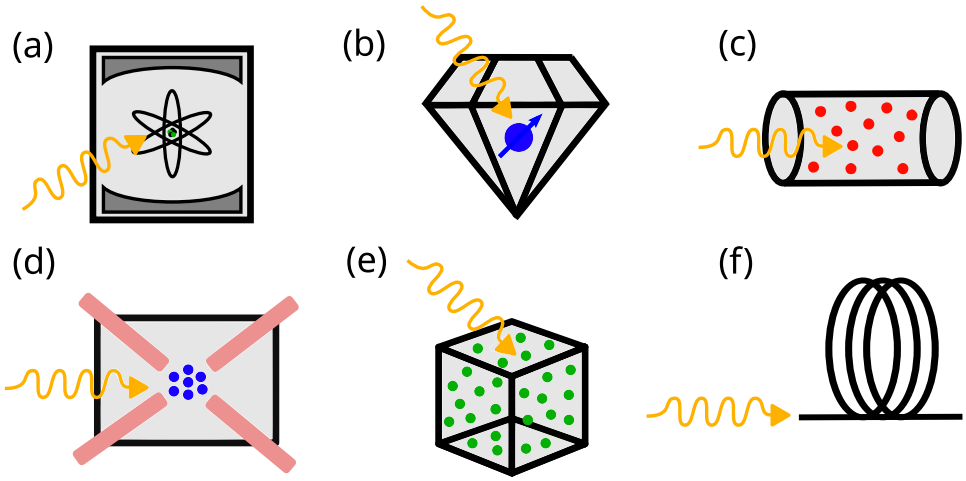

Figure 2.3: Quantum memory platforms. Using single emitters, we find (a) single atoms/ions in a cavity and (b) colour centres in diamond. Among ensemble-based photon storage systems, relevant examples are (c) warm vapour cells, (d) cold atomic gases in magneto-optical traps, and (e) rare-earth-ion-doped crystals (REIDs). Furthermore, we include (f) delay lines and storage loops.

extensively studied and demonstrated [150–154].
In Ref. [155], a single ion used as a memory achieved close to 70% efficiency. Using a single atom in Ref. [156], an efficiency of 22% and a storage time of 100 ms were realised. These systems offer the possibility of realising heralded storage of single photons [157]. The use of single particles allows to perform quantum gates on stored qubits as in Refs. [158–160]; a first step towards quantum information processing and quantum error correction in these systems. For applications in quantum networks, entanglement between a trapped Yb ion and an emitted photon into the resonator mode with a fidelity of $\sim 90\%$ was reached in Ref. [161].
These systems, although very interesting to study, require highly complex experimental apparatuses. For long-distance quantum communication applications like entanglement distribution, the limited multimode capacity of single trapped particles poses a problem difficult to overcome.

Colour centres in diamond

In solid state systems, colour centres in diamond or silicon carbide which act as single emitters [162], have been shown to also be good candidates for quantum memories.

The most known one is the NV center, where a carbon atom has been substituted by a nitrogen atom next to a vacancy in the carbon lattice of bulk diamond. This leads to magnetically tunable fluorescence. These systems are widely used as highly sensitive quantum magnetic sensors and allow for access to the quantum properties of the nitrogen atom, any proximal carbon nuclear spin, and the associated free electron spin of the system. A ten-qubit memory register has been realised using these nuclei, showing a coherence time of 75 s for single-qubit states and of 10 s for two-qubit entanglement [163]. High fidelity storage of 98% for coherence times of 10 s has been achieved in Ref. [164]. Several techniques have been proposed to extend the reachable storage times [165–167]. Recently, a multi-node quantum network has been realised in such a system [168].
More recently, other similar systems, the tin-vacancy (SnV) [169] or the silicon-vacancy (SiV) [170] have become popular. They offer significant improvement in compatibility with photonic nanostructures as a consequence of their inversion symmetry (the electronic states of the SiV center have a vanishing permanent electric dipole moment, which makes them insensitive to Stark shifts), resulting in high detection efficiencies, [171, 172]. Among these systems, SnV shows sub-ms coherence times at temperatures above 1 K, while in SiV coherence times of 13 ms are achieved at 100 mK.
The read-out in theses systems has historically been performed using confocal microscopes, which hinder simple scalability. Therefore, developments in the use of optical cavities [172, 173], photonic chips, and nanostructures [174, 175] might help to aid this problem. As colour centres have been shown to act as single-photon sources [171], they offer great advantages in integrability of memory and source. A disadvantage of these systems is the low efficiency achieved in absorptive storage schemes, unless they are placed in cavities as in Ref. [172], which is why they might be better suited to act as read-out only memories in specific applications.

2.3.2 Ensembles

Warm atomic vapours

Warm atomic vapours are technically low-complexity systems, which allow for operation in a wide range of conditions, as they do not pose the need for cryogenic cooling or large magnetic fields. Thus, they are highly scalable systems. Commercial vapour cells or miniaturised wafer systems [176] are therefore very good candidates for, e.g., space applications. Due to their easily accessible low-lying spin states at infrared wavelengths, alkali atoms such as caesium or rubidium are the most commonly used candidates. Since their ground spin states do not fluoresce, they yield long coherence times. The storage

time in these types of systems is not limited by inherent coherence times, but by atomic diffusion from the interaction region, or by loss of coherence due to collisional processes such as spin-exchange collisions or wall collisions, among others [177]. In order to mitigate these effects, buffer gases are added to the atomic mixture, reducing the effect of some of these processes. The relevant parameter for efficient storage is the optical depth (OD), which is proportional to the atomic number density and can be easily tuned with temperature. Even at room temperature, these systems show reasonable optical depths. Drawbacks of these types of memory systems are their susceptibility to noise, such as fluorescence from the excited states, spontaneous Raman scattering (SRS) or four-wave mixing (FWM) [114, 178]. These memories typically make use of EIT or Raman storage (see Section 2.4) [179–181], although other techniques as AFC [182], FLAME/ORCA [183, 184] etc., are also commonly employed.

Recent and relevant experimental demonstrations in these systems include very long storage times of $150 - 430\,\mathrm{ms}$ for coherent pulses well above single-photon level by using spin-orientations degrees of freedom in Cs [185]. The achieved memory efficiencies in this experiment lie between $9\% - 14\%$. One of the highest memory efficiency achieved to date in such systems, reaching 82%, and a fidelity of 98% at single photon level, are reported in Ref. [186] using a Raman scheme in Rb. Before this, the gradient-echo (GEM) protocol (see Sec. 2.4.5) had kept the record for highest efficiencies in warm vapours, with efficiencies around 80% [187, 188]. A high bandwidth memory of $0.66\,\mathrm{GHz}$ in such a system was realised in Ref. [136], potentially allowing interfacing with single photons from semiconductor quantum dots. As for noise, characterised by the unconditional noise floor parameter μ_1 (see Sec. 2.2.2 for the definition), values below $\mu_1 = 0.04$ are achieved in Ref. [189], without the need of optical cavities as used in Ref. [190]. Recently, remarkable noise values of $\mu_1 \sim 10^{-4}$ were achieved in Ref. [191]. In the experiments above, always a trade-off with respect to additional memory parameters has to be made when reaching the mentioned values. Conversely, in this thesis, a simultaneous optimisation of end-to-end efficiency and signal-to-noise ratio at single photon level was performed [1].

Atomic vapours allow for spatial multiplexing, as we showed in Ref. [3]. Although already investigated in Ref. [192], the first true single photon storage experiment in a Λ-system to date, in which the single photon nature of the input photon was maintained upon retrieval, was performed in such a system in Ref. [191], where a spontaneous parametric down-conversion (SPDC) source was interfaced with an atomic vapour memory. Single photon storage in a ladder Ξ-system was achieved in Ref. [183]. If we, for a moment, consider CV encoding again, squeezed vacuum state storage in warm Rb vapour was realised already back in 2008 [193].

Cold atomic gases

By cooling atomic systems to cryogenic temperatures in the 100 μK regime or lower by using magneto-optical traps (MOTs) and dipole traps, reduction of the atomic motion and thus the coherence times of atomic gases can be achieved. This allows for the realisation quantum memories with long storage times. Bose-Einstein condensates (BECs) also have been proposed as storage systems [194, 195], but require even more laser cooling. The storage protocols used in these systems are the same as in warm atomic gases [114, 196]. Some notable experiments and results include a record efficiency of 87% via a GEM protocol [197] for an on-demand memory. Ref. [196] reaches a storage efficiency (not including retrieval) of 92% using an EIT scheme. Other significant results are a retrieval efficiency of 82% in a DLCZ-type memory in a cold Rb ensemble [198], and of 76% in the same kind of read-only memory again in cold Rb vapour, yet with a storage time of 220 ms [199]. Another similar experiment achieved an efficiency of 73% for 3.6 ms storage time in Ref. [200]. Using orbital angular momentum (OAM) degrees of freedom [201] and spatial multiplexing [202, 203], cold atoms have shown to allow multimode operation. Furthermore, two Rb memories have been entangled in the experiment in Ref. [204]. Moreover, storage of single photons from an SPDC source was shown in Ref. [205].
Much work has been put into on-chip operation [139, 206–208] and miniaturisation [209] of these types of systems, yielding astonishing scalability properties. Several missions have been working on sending these types of systems into space. Important examples are MAIUS [139], CAL [140], and the planned project BECCAL [141]. In this context, it has recently been shown that microgravity could enhance the performance of BEC memories dramatically [210].

Rare-earth ion-doped solids

REIDs grant optical access to long-lived nuclear and electronic spin states and show narrow homogeneous linewidths. Furthermore, they allow one to engineer their optical inhomogeneous broadening, giving rise to an inherent frequency multimode capacity. REIDs are compact systems with low complexity, and are very well suited for micro-integration. Thus, they are a great candidate for quantum information processing. Common materials used as donors are europium $^{151/153}Eu^{3+}$, or praseodymium $^{141}Pr^{3+}$ embedded in a yttrium-orthosilicate matrix Y_2SiO_5 [211–213]. Some of them are compatible with telecommunication wavelengths [214, 215]. These crystals have to be cooled to temperatures below 6 K.
At these cryogenic temperatures the effect of phonons in the host lattice is greatly

suppressed, such that the coherence of these systems is only limited by spin-spin interactions. Hyperfine coherence times on the order of milliseconds are common without external engineering. The achievable lifetimes of the excited states stem from the special electronic structure of the investigated transitions. Partially filled $4f$ electron shells are shielded by filled $5s^2$ and $5p^6$ shells [216]. Applying techniques from NMR spectroscopy or spinwave storage allows to extend these times to seconds [217] and even hours [218]. However, this requires very strong external magnetic fields of the order of $|\boldsymbol{B}| = 1 - 2\,\mathrm{T}$, and cryogenic temperatures below 4 K. Achieved noise levels for single-photon-level storage in these systems are at $\mu_1 = 0.069(2)$ [135] and $\mu_1 = 0.10(2)$ [127] for storage times of about 12 μs. Extension of storage times into the hour range has been achieved in Ref. [219], however using bright coherent pulses (i.e., it is not a quantum memory as such). A high efficiency value of 69% has been achieved in Ref. [220], again via the GEM protocol.

Because of the heterogeneous structure of the host material, the absorption lines are initially broadened inhomogeneously by hundreds of MHz or even GHz in AFC, CRIB or GEM protocols, then combined with spinwave storage to make the memories on-demand [220, 221]. Moreover, also EIT storage is used in these systems [222, 223]. In recent experiments, multimode operation using OAM [224] and entanglement between two REID memories [225] have been shown, using frequency down-conversion to match telecom frequencies [226, 227]. These techniques have also been used for interfacing with cold atomic gases [228].

Regarding space applications, miniaturisation and integration with optical waveguides might help reduce the need for large magnets [229–231]. Recently, there have been notable developments in compact cryocoolers, which can be of aid for such systems [232]. In a new proposal using ultra-long-lifetime (UUL) memories, it has been shown that a single satellite can be used for global quantum networking [233].

2.3.3 Delay lines and storage rings

In the introductory definition of quantum memories given in Ch. 1, Section 1.5, the necessity of a physical interaction of the storage system with the light was stated. However, loosening this definition of a memory slightly, it is not necessary to include interaction, or more specifically absorption of light within a medium, in order to store light. It is also possible to delay a light pulse or a single photon for a given amount of time, until it is needed for some application, e.g., synchronisation with another photon. This can

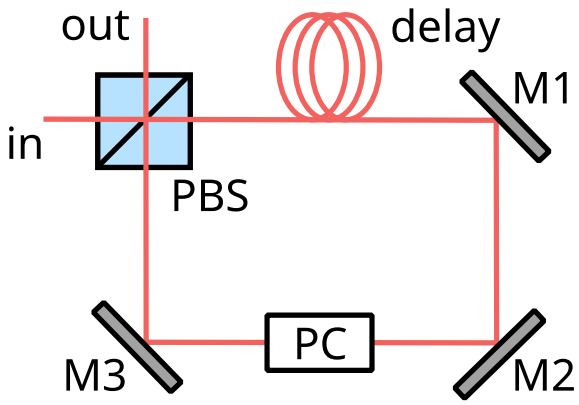

Figure 2.4: Storage loop in free space combined with an optical fibre delay. After a photon (or light pulse) enters the loop, the Pockels cell (PC) acts as a polarisation switch, first causing the photon to stay in the loop and, after a second switch, allowing the photon to exit the loop when needed. This extends the delay of the single round-trip time by an integer factor. M1-3: mirrors, PBS: polarising beam splitter.

be achieved using either optical fibres or storage loops. In this case, the retrieval is not exactly on-demand, but this is technically also the case in some other types of memory systems.

These types of memories are capable of very low optical losses. An ideal optical fibre loop has a loss of 50% in 100 μs [197], which can be seen as the a benchmark a 'real' quantum memory should surpass. However, in order to achieve long storage times, very long optical paths are required. For this reason, this type of platform is used more for local applications, such as synchronisation of single photon events. One of the first proposals of such a system as a memory was presented in Ref. [234] and there named a cyclical quantum memory (CQM). One envisioned application was the realisation of pseudo-on-demand single photon sources via synchronisation [235, 236]. Since then, several other experiments have been performed using such types of memory systems [100, 237, 238]. Even experiments involving interconnection and simultaneous operation between such a memory and an atomic ensemble-based memory have been performed in Ref. [239].

2.4 Light storage protocols

In this section, the most relevant storage protocols used in the different platforms described in the last section will be introduced. I will start with a short description of light storage in delay lines and storage rings for completeness, and then I will dive into light-matter-interaction-based protocols. There exist several ways of categorising these, either by atomic level structure used, by the specific range of a certain relevant parameter, or by the physical limit they work in best. Here, I decided to divide the protocols into optically controlled ones, being the ones that make use of a strong control pulse to mediate absorption, and protocols based on the engineering of the physical system in order to change some of its characteristics, i.e., its inhomogeneous broadening. The first ones can further be divided with respect to the level structure they are implemented on. Thus, among the optically controlled protocols we have EIT, Raman, and ATS working in Λ-systems, and FLAME/ORCA in ladder Ξ-systems. Engineered protocols include CRIB and AFC, as photon-echo type protocols. Moreover, also hybrid protocols exist. In fact, the engineered protocols presented here are actually hybrid. In other words, the 'pure' CRIB and AFC protocols were originally defined and implemented in two-level systems. As they are photon-echo techniques, their storage time is limited and an inherent result of the engineering of the specific system. In order to make these protocols truly on-demand, a third state needs to be added. The transfer to this state happens generally via a control π-pulse, which is what renders these protocols hybrid. This 'improved' version of the CRIB and AFC protocols is the one I present here.
Although this review aims to include also other types of platforms, since Chapter 4 will be dedicated to a warm atomic vapour memory, special importance will be given to this specific platform and its corresponding protocols.

In 2007, A. V. Gorshkov et al. published the first work on a universal theoretical approach to treat optimal photon storage in Λ-type atomic media [123]. Subsequent to this work, a series of four further papers appeared, giving a very detailed and general theoretical description of such systems in a cavity model [124], a free space model [125], including effects of inhomogeneous broadening [240], and lastly developing techniques for calculating optimal control pulses with a gradient ascent method [241]. These works have become the theoretical backbone for light storage in (Λ-type) atomic ensembles. Before introducing all the different protocols, I will here offer a short summary of the findings of these publications. A detailed theoretical description of storage based on these works is further presented in Ch. 3, Sec. 3.3.
In Ref. [123], a physical picture unifying many of the existing different approaches

to photon storage in Λ-type atomic media was introduced. Each approach can be optimised within this universal picture based on time reversal, and on the fixed branching ratio between the desired quantum state transfer and the existing losses. Moreover, in Refs. [241, 242], the authors advance (in theory and experiment, respectively) the optical control strategy that yields the maximal attainable efficiency in such systems. This efficiency is shown to depend solely on the optical depth of the medium, here denoted by d_{opt}. This (theoretical) optical depth is given as the product of the on-resonance absorption α of a given transition of the system, multiplied by the length L of the medium[1]. This fact results from the branching ratio between collectively enhanced emission into desired modes and spontaneous decay, only dependent on d_{opt}. Another essential fact arising from their investigations is that, when ignoring spinwave decay, the optimal storage process is the time reverse of the retrieval, leading to the conclusion that the attainable optimal efficiency is the same for all considered techniques. Again, it depends only on the optical depth and can be achieved by optimisation of the control pulses or the shape of the photon wave packet to be stored. The optimal strategy also yields the optimal possible spinwave in each case. The optimisation process in all of these techniques consists in finding the perfect balance between two possible sources of loss: the leakage of the input pulse through the ensemble and the scattering of input photons due to spontaneous emission. This does not include other possible sources of noise as these do not reduce the maximal attainable efficiency.

These works provide a further way of categorising the existing protocols, which is introduced here in order to gain a better understanding of the literature. In Λ-type systems, which will be the main focus of this review, the existing protocols can be divided into the ones corresponding to the adiabatic limit ($\Delta t_s d_{\text{opt}} \gamma_e \gg 1$, where Δt_s is the time length of the input pulse and $\gamma_e = \Gamma_e/2$ is half of the spontaneous decay rate of the excited state (defined in Eq. (3.36)), and can also include further broadening mechanisms[2]), among which we find EIT and Raman protocols, and the fast limit ($\Delta t_s d_{\text{opt}} \gamma_e \sim 1$) protocols corresponding to photon echo techniques [243], such as CRIB and AFC, and similar ones that make use of homogeneous broadening. The ATS protocol also corresponds to this limit. In the ladder Ξ-system realm, the FLAME and ORCA protocols would also be associated to the adiabatic limit. The main difference between these limits lies in the way the photonic information is transferred onto the atomic coherence. In the adiabatic limit this occurs via adiabatic elimination of the excited state (hence the name),

[1] See Ch. 3, Eq. (3.31) for a formal definition. Experimentalists, by convention, use a value of $2d_{\text{opt}}$ for the optical depth.
[2] See Ch. 3 Eq. (3.23).

meaning no polarisation P ($|g\rangle - |e\rangle$ coherence, see Ch. 3) is formed, while in the fast limit the transfer occurs via excitation to the state $|e\rangle$, which is de facto populated during the storage process. In both limits, the ideal performance is only reached in the limit of infinite d_{opt}. As a result of time reversal, an important finding is that the optimal efficiency can be achieved by sending the retrieval pulse in the backward direction. Since in general, experimentally it is simpler to implement forward retrieval, this case is also investigated, although here the storage and the retrieval processes have to be optimised independently, and a compromise has to be made. Thus, forward retrieval will yield lower total efficiencies compared to backward retrieval. After these general considerations, let us now dive into the specifics of each protocol. For comparison and to summarise the most important characteristics of each protocol, I have added Table 2.2 at the end of this chapter.

2.4.1 Delay of light

The 'storage' of light can be achieved by letting the photon propagate locally, either in free space or in an optical fibre. The delay time τ will then be given by $\tau = \frac{nL}{c}$, where n is the refractive index of the medium ($n = 1$ for free space or $n = 1.5$ for a standard optical fibre), L is the distance the photon travels, and c is the speed of light. Naturally, as the speed of light is large, significant delays will require long distances L.
This process will also involve some losses, which in free space are not so significant due to the (ideally) non-interacting nature of photons, but become relevant in optical fibres. The most prominent loss mechanisms in fibres are Rayleigh scattering in the visible frequency range [247] and the intrinsic absorption lines of silica, the fibre material, starting at the end of the near infrared [248]. These losses will depend on the wavelength of the transmitted light and reach their minimum for the so-called telecom C-band around 1550 nm. A measure for losses is the attenuation of the light intensity per distance L in units of decibels (dB), given by $aL = 10 \log_{10}\left(\frac{I_{\mathrm{in}}}{I_{\mathrm{out}}}\right)$, where a is the attenuation and I stands for the light intensity [94]. Common values for these losses are $a = 0.2\,\mathrm{dB/km}$ for the telecom C-band and $a = 0.35\,\mathrm{dB/km}$ for infrared wavelengths around 850 nm.

In order to extend the delay in a given system one can think of constructing some storage loop, again either in free space or using fibres. A sketch of this is given in Figure 2.4. Horizontally polarised light is initially transmitted at the beam splitter and enters the loop. A Pockels cell driven by a specific voltage is used to switch the polarisation of the light to vertical before it reaches the beam splitter again, thus trapping it in the loop. In order to exit the loop after an integer number of

round trips, another voltage pulse is applied to the Pockels cell, letting the light exit at the beam splitter port. Apart from the already mentioned losses in free space or fibre, it is important to consider some further losses of the beam splitter and the mirrors.

2.4.2 EIT

Electromagnetically induced transparency (EIT) is a phenomenon that occurs when an optically dense medium becomes transparent to resonant light due to the interaction of two lasers with a three-level system. While EIT can manifest in various three-level configurations (see Fig. 2.2), this discussion will focus on the Λ-system. The effect was first observed by Boller et al. in 1991 [249] in strontium, and can be well described in a static picture [250–252].

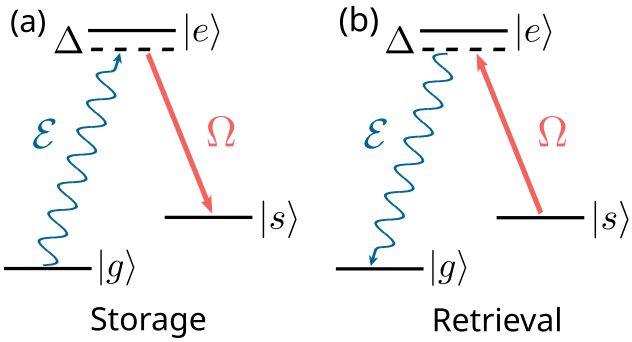

Figure 2.5: EIT storage (a) and retrieval (b) process. The signal field or single photon ($\mathcal{E}$, wiggly blue) and the control field (Ω, red) are on resonance or detuned by a small Δ. The control field alters the atomic response and creates a transparency window in the absorption spectrum. Meanwhile, the group velocity of the signal field is reduced. Adiabatically ramping off the control field brings the signal to a complete stop inside the medium. Here, one atom in the ensemble is transferred from $|g\rangle$ to $|s\rangle$. For retrieval, the control field is applied again. This reverses the process, transferring the excited atom back to the original ground state $|g\rangle$ and reemitting the signal photon.

In the Λ-system, a classical or quantum signal (probe) field $\mathcal{E}$, resonant with the $|g\rangle \rightarrow |e\rangle$ transition, interacts with the ensemble, while a stronger control field Ω, characterised by its Rabi frequency, is applied to the $|s\rangle \rightarrow |e\rangle$ transition, as shown in Figure 2.5. Depending on control field's strength relative to the decay rate γ_e of the excited state $|e\rangle$ (see Eq. (3.23)), two possible regimes can be defined. For moderate control powers

with $\Omega < \gamma_e$, the system response aligns with the EIT model. Conversely, for very strong control fields ($\Omega > \gamma_e$) the Autler-Townes regime is entered [253].
The control field's presence alters the atomic response, leading to the emergence of a transparency window due to an interference of the different paths the light can take to reach the excited state, namely either the path directly from $|g\rangle \rightarrow |e\rangle$, or the longer path $|g\rangle \rightarrow |e\rangle \rightarrow |s\rangle \rightarrow |e\rangle$. As the control field is much stronger than the signal field, the longer pathway is equally probable. This creates a quantum interference, dressing the eigenstates of the Hamiltonian and thus making the state $|e\rangle$ a dark state.

Mathematically, it is in the limit of the aforementioned Autler-Townes regime, where the behaviour is simpler to understand. The diagonalisation of the electric dipole interaction Hamiltonian

$$\mathcal{H} = \frac{\hbar\Omega}{2} |e\rangle \langle s| + \text{h.c.} \tag{2.10}$$

yields

$$\mathcal{H} = \frac{\hbar\Omega}{2} \left(|+\rangle \langle +| - |-\rangle \langle -|\right). \tag{2.11}$$

The corresponding dressed eigenstates are

$$|\pm\rangle = \frac{1}{\sqrt{2}} \left(|s\rangle \pm |e\rangle\right). \tag{2.12}$$

From this treatment, a double resonance appears (Autler-Townes splitting (ATS)), with energies shifted by $\pm\frac{\hbar\Omega}{2}$ from the original energy level (see Fig. 2.6 (c)).

In the EIT regime, the original absorption peak is not yet split into two, but shows precisely the characteristic transparency window. Nevertheless, the dressing of the original states is already applicable. Within the transparency window, the dispersion of the system changes so drastically at the point of minimal absorption (see Fig. 2.6(b)), such that the group velocity of a probe field is reduced significantly, giving rise to the phenomenon of 'slow light' [254, 255]. By looking at a steady-state calculation of the linear susceptibility $\chi^{(1)}$ of the probe field, as depicted in Figure 2.6, we can gain a better understanding of this behaviour. The imaginary part (blue) of $\chi^{(1)}$ is directly related to the absorption, while the real part of the susceptibility (green) is linked to the medium's refractive index as $n = \sqrt{1 + \text{Re}(\chi^{(1)})}$. Without a control field (Fig. 2.6(a)), the signal field would experience normal absorption (Lorentzian) and dispersion inside the medium. The presence of a

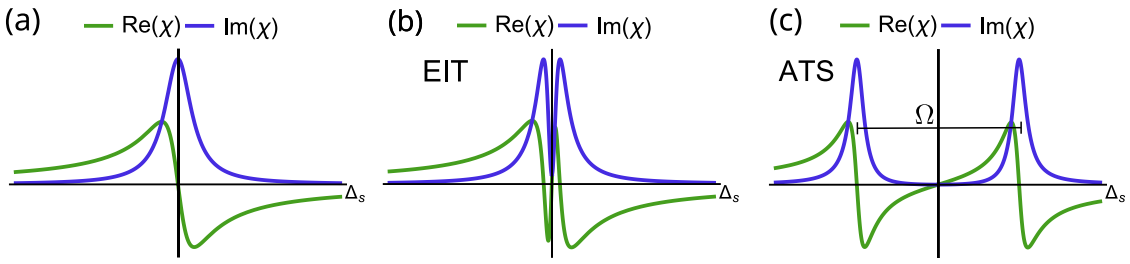

Figure 2.6: Real and imaginary parts of the linear susceptibility $\chi^{(1)} = \chi$, describing the dispersion and the absorption of the medium, respectively. (a) Normal absorption case, no control field. (b) EIT case, moderate Rabi frequency $\Omega < \gamma_e$. (c) ATS case, very strong Rabi frequency $\Omega > \gamma_e$, which determines the peak separation.

moderate control field ($\Omega < \gamma_e$) alters this behaviour, thus giving rise to EIT. This reveals the transparency window at the center of the absorption spectrum (Fig. 2.6(b)). In the case of a very strong control field ($\Omega > \gamma_e$), the regime changes from EIT to ATS, where two distinct absoption peaks separated by Ω appear (Fig. 2.6(c)). In the EIT case, it is the strong change in $\mathrm{Re}(\chi^{(1)})$ or strong dispersion within the transparency window, which leads to the aforementioned reduction of the group velocity of the signal beam, with $v_g \propto \left(\frac{\partial n}{\partial \omega}\right)^{-1}$ [256], that is proportional to the strength of the control field. As a result, there will be significant pulse compression inside the medium (see Figure 2.7). A more detailed theoretical derivation of the above mentioned effects will be given in Ch. 3, Sec. 3.2.4.

This effect led to the development of the EIT storage protocol, wherein light is brought to a complete halt within the medium, and thus stored and subsequently released on demand. Since its development by M. Lukin and M. Fleischhauer in the year 2000 [257, 258], many experimental demonstrations have been performed in a variety of systems including cold atomic vapours [196, 205, 259, 260], solid state systems [261, 262] and warm atomic gases [1, 179, 263–265]. It has evolved into one of the most established absorptive quantum memory protocols. To achieve quantum storage of the incoming signal pulse, that is, to bring the light to a complete stop, it is necessary to adiabatically close the transparency window. This requires adiabatically turning off the control field.

The working principle of such a memory is as follows: The signal pulse is spectrally tuned to the center of the transparency window and sent into the atomic ensemble. The presence of the control field changes the dispersion of the medium, causing the signal pulse to slow down and become spatially compressed until it entirely fits within

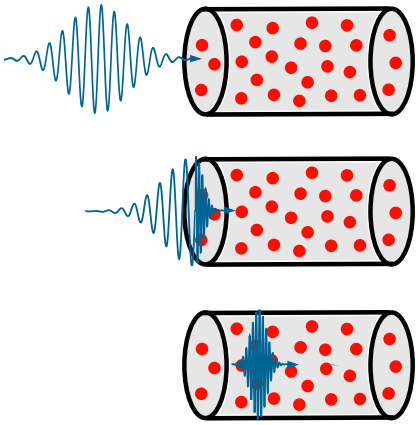

Figure 2.7: Pulse compression and slow light in EIT. Due to the slowing down of the group velocity v_g in the medium, the signal pulse is spatially compressed inside.

the atomic ensemble. At this point, the control field is ramped down adiabatically, narrowing the transparency window and increasing the steepness of the slope in the refractive index n, until it diverges as Ω vanishes. This process maps the quantum state of the signal onto the collective atomic excitation, known as the spinwave (see Eq. (2.1)). Turning the control field back on reverses the process and releases the light from the medium once again. A full quantum mechanic description of this process, including light-matter quasi particles known as dark-state polaritons [266], is needed in order to explain how this process occurs without absorption of the signal at any point, and is beyond the scope of this review. A more profound theoretical description is left for Chapter 3.

The EIT protocol offers many advantages. It is very well understood and the required control pulse energies to open a transparency window are easily attainable by commercial diode lasers. Some drawbacks include the collision-induced fluorescence noise resulting from on-resonant operation, as well as SRS and possibly FWM noise in detuned operation, which may become problematic for single-photon level operation [1, 246, 265, 267]. Furthermore, achieving high-bandwidth storage is not straightforward, as the spectral width of the transparency window, proportional to the strength of the control Rabi frequency Ω, determines the bandwidth of the memory. The full width at half maximum (FWHM) of the transparency window is given as [268]

$$\Delta\omega_{\mathrm{EIT}} = \frac{|\Omega|^2}{\gamma_e}\frac{1}{\sqrt{2d_{\mathrm{opt}}}}. \tag{2.13}$$

Note the factor two in the optical depth, since here the experimental optical depth is used, as explained below Eq. (3.31). In Ref. [269], a derivation of the initial conditions necessary for efficient EIT storage is performed. Assuming an ideal system without incoherent losses ($\gamma_s = 0$, where γ_s is the dephasing of the storage state $|s\rangle$), achieving 100% storage efficiency requires simultaneously fulfilling two conditions: To perfectly store a pulse of duration Δt_s in a medium of length L, the entire length L_s of the signal pulse must spatially fit inside the medium, i.e., $L_s = \Delta t_s v_g \leq L$. At the same time, the signal's spectrum must fit within the EIT window, such that $(\Delta t_s)^{-1} \leq \Delta\omega_{\mathrm{EIT}}$, in order to minimise losses due to spontaneous emission. Comparing these conditions to the relevant measure of comparison in static EIT, the group delay of the medium, given as $\tau_D = \sqrt{2d_{\mathrm{opt}}}/\Delta\omega_{\mathrm{EIT}}$, we can derive the following inequalities: $\frac{L}{L_s} \sim \frac{\tau_D}{\Delta t_s} \leq \sqrt{2d_{\mathrm{opt}}}$ [94]. This implies that components of the signal pulse that do not meet these conditions, such as long spectral or temporal tails of the pulses, will not be stored, especially as Ω is reduced, leading to lower storage efficiencies. For these two conditions to be met, very high optical depths are essential [123, 266].

In the high control power limit ($\Omega > \gamma_e$), as mentioned, the shift of energies due to a strong laser's Stark shift gives rise to the well known ATS [253, 270, 271]. Although there are similarities, this effect is not sufficient to explain the appearance of the EIT transparency window at low powers, which is a result of quantum interference. With increasing control power, the description goes from the EIT picture at low powers, to the ATS model at high powers, where the effect of interference is small compared to the splitting of the levels caused by the Stark shift [271]. In this ATS regime, another storage protocol has been proposed, which will be described in its dedicated section (Sec. 2.4.4).

2.4.3 Raman

Raman scattering is the name given to a weak inelastic scattering process of light by a material excitation in a vapour or a liquid. It serves as a valuable tool for gaining experimental insights into the electronic, vibrational, or rotational states of a system. This phenomenon was originally observed by C. V. Raman in 1928 [272], and has since become a commonplace technique in spectroscopy, quantum optics and related fields.
The scattering process is an inelastic two-photon process resulting from a second order dipole interaction between light and matter. In the Λ-system picture, a pump photon is absorbed, while simultaneously a red-detuned Stokes (S) photon is emitted. If the frequency of the emitted photon is blue detuned, that is, exceeds the one of the pump

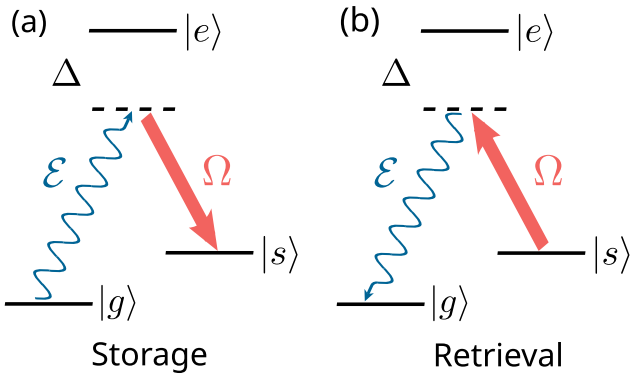

Figure 2.8: Raman storage (a) and retrieval (b) process. The signal field (wiggly blue) and the strong control field (red) are far off-resonant. The storage occurs via a stimulated two-photon Raman transition. Here, one atom in the ensemble is transferred from $|g\rangle$ to $|s\rangle$. For retrieval, the control field is applied again. This reverses the process, transferring the excited atom back to the original ground state $|g\rangle$ and reemitting the signal photon.

field, as it is in the reversed process, then the emitted photon is termed an anti-Stokes (AS) photon.

A similar interaction takes place in the Raman storage protocol, originally introduced in Ref. [273], and analysed and optimised in Ref. [274]. Specifically, for the storage process the Raman interaction is reversed. Here, the signal field $\mathcal{E}$ is detuned by Δ from the $|g\rangle \rightarrow |e\rangle$ transition, while the strong control field Ω is detuned by the same amount from its respective transition $|s\rangle \rightarrow |e\rangle$, such that they are in two-photon resonance. The simultaneous presence of the two fields drives the stimulated emission of a Stokes photon. Energy is conserved in this interaction, if the frequency difference between the control and the Stokes photon matches the frequency splitting between the states $|g\rangle$ and $|s\rangle$. The signal is thus mapped to the same long-lived atomic coherence of the two ground states $|g\rangle$ and $|s\rangle$, the spinwave. As it is not known which atom has undergone the transition, it is a collective process involving all atoms in the interaction region. This is depicted schematically in Figure 2.8.

The detuning Δ is chosen to be large compared to the excited state linewidth γ_e, and the bandwidth of the photon to be stored. Although the likelihood of a Raman process decreases with further detuning from resonance, the strength of the interaction can be amplified significantly with a strong control field and a large number of involved atoms, i.e., a high optical depth $2d_{\text{opt}}$.

A key difference between the Raman protocol and the EIT protocol described above, which is defined as a resonant process, is precisely the size of the detuning Δ. Both can

be seen as different limits of the same physical process, however, they exhibit distinct physical characteristics. While on resonance it is the quantum interference of different pathways that leads to the mapping, this is not the case in the Raman limit. Here, the atoms are never excited to the excited state $|e\rangle$ due to the large detuning (in EIT there is also no excitation to $|e\rangle$, but the reason for this is the quantum interference). The coupling can rather be described as an absorption of the signal into a virtual state created by the control field, from which the latter transfers the excitation onto the storage state $|s\rangle$. Moreover, in a Raman process there is no reduction of the group velocity of the signal field as a consequence of modified dispersion, as is the case for EIT.

Nevertheless, the Raman and EIT memories share many similarities in their underlying physics. In the dressed-state picture derived in the EIT case, the virtual state of the Raman process can be identified with the $|-\rangle$ state, which is a combination of $|e\rangle$ and $|s\rangle$. In EIT, the signal is tuned in between the dressed states, meaning the contribution of both states is equal. On the contrary, in the Raman case the signal is on resonance with one of the dressed states, consisting mostly of the $|s\rangle$ contribution, due to the large detuning Δ [18]. When the control field is turned off, in the EIT regime the light is stopped inside the medium, whereas in the Raman scenario, the virtual state into which the light is absorbed becomes dark when it is decoupled from the electromagnetic field.

An interesting feature of Raman storage, compared to EIT, is the inherent possibility of storing broadband pulses. These pulses are short in duration, and encompass a large range of frequencies. While in EIT the width of the transparency window poses a limit on the spectral bandwidth of the pulse to be stored, this is not the case in Raman storage, as it does not rely on a transparency effect. Here, the width of the control pulse determines the bandwidth of the virtual state, and therefore the possible bandwidth of the pulse to be stored. However, a necessary condition for efficient storage is that the excited state $|e\rangle$ never becomes populated, for which Δ must be much larger than the bandwidth of the signal photon.

The initial comprehensive theoretical description of Raman storage was provided in [274]. Since then, the technique was implemented and improved in Refs. [116, 178]. As mentioned, Raman memories offer the advantage of broadband storage, related to the storage of short pulses that enable high processing speeds, particularly in quantum network applications. Among its drawbacks, there is the necessity of achieving high powers in the control pulses to enhance the likelihood of the Raman interaction. The larger the detuning Δ, the larger the Rabi frequency of the control field Ω needs to be, in order to achieve efficient storage. Furthermore, while fluorescence noise contamination decreases with detuning, these memories are more susceptible to FWM and SRS noise due to the use of strong control powers [114, 178].

A well-known application of Raman-type memories is in DLCZ memories [82], originally proposed for quantum repeater networks. State-of-the-art experiments involving Raman storage include, e.g., Refs. [180, 181, 186, 190, 192].

2.4.4 ATS

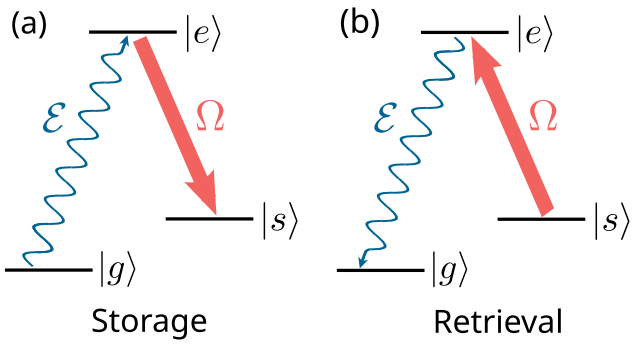

Figure 2.9: ATS storage (a) and retrieval (b) process. The signal field (wiggly blue) and the strong control field (red) are on resonance. The protocol is similar to EIT but uses a much stronger control field, leading to the appearance of an ATS doublet in the transition. It relies on 'fast' storage, i.e., the excitation from $|g\rangle$ to $|s\rangle$ occurs via the excitation of the atomic polarisation, e.g., excitation to the state $|e\rangle$.

In Ref. [244], yet another protocol for quantum storage was introduced. The following description is based on the discussion presented in that work. In this case, the presented protocol is a high-speed technique relying on dynamically controlled absorption of light via the 'Autler-Townes' splitting (ATS) effect [253]. The authors demonstrated this technique in a laser-cooled gas of rubidium atoms. They argue that the ATS memory is intrinsically suitable for efficient, broadband, and long-lived quantum storage and relaxes the requirements on optical depth, control-field coupling, technical complexity, and robustness to decoherence, when compared to other established techniques.
In a similar configuration to Λ-type EIT storage, as introduced above, but using a control field Rabi frequency ideally much larger than the coherence decay rate of the optical transition ($\Omega \gg \gamma_e = \Gamma_e/2$)[1], instead of an EIT window, the transition shows an ATS where the resulting two peaks are separated by a distance Ω (see Fig. 2.6 (c)). The acceptance bandwidth of the memory is determined by the control Rabi frequency as

[1] γ_e can include other contributions, see again Eq. (3.23).

$\Delta\omega_{\text{mem}} \approx \Omega/2\pi$.

The ATS scheme (depicted in Figure 2.9) is very similar to the EIT scheme, since it is an on-resonant interaction scheme, benefiting from large light-matter coupling. It also bears many resemblances to the far-off-resonant Raman protocol, in that it can have dynamically controlled absorption and bandwidth. The authors argue, despite some existing similarities between these protocols, that the physical processes underlying them are fundamentally different. In Raman and EIT, a necessary condition is the adiabatic elimination of the atomic polarisation, i.e., of the absorption to the excited level $|e\rangle$, while the ATS scheme requires 'fast' operation and thus exactly this excitation of the atomic polarisation. Mathematically, in Raman and EIT the adiabaticity condition $\Delta t_s d_{\text{opt}}\gamma_e \gg 1$ is met, while for ATS the condition is that $\Delta t_s d_{\text{opt}}\gamma_e \sim 1$ [123]. This fact makes the ATS protocol resemble photon-echo memory protocols, such as the ones introduced below, the difference being that the ATS memory only relies on the a.c. Stark splitting of an absorption line and does not make use of electric-, magnetic-field-controlled absorption mechanisms or on hole burning techniques, such as in CRIB/GEM or AFC protocols. Ref. [275] provides a very detailed study on the distinctions between the ATS and EIT storage protocols in different limits, and determines optimal memory conditions for both techniques. Notably, in the ATS regime, the conditions relating the bandwidth of the signal pulse to the width of the EIT window are no longer valid, as the ATS protocol does indeed relay on signal absorption and reemission. Compared to Raman and EIT protocols, ATS shows much lower noise levels, due to the lower required optical depths for efficient storage. In Ref. [195], the protocol was used to store single-photon-level pulses in a BEC.

2.4.5 CRIB

The controlled reversible inhomogeneous broadening (CRIB) protocol, sometimes referred to as gradient echo memory (GEM) protocol in certain cases with a specific (longitudinal) geometry, is a technique based on an artificial broadening of the atomic resonance of a system. Although originally proposed in Ref. [243] for Doppler broadened atomic gases, it has since then been developed and improved mainly in REID platforms [214, 220, 276–279]. Nevertheless, there are also realisations in cold atomic ensembles [280] and in warm vapours [281].

The fundamental principle of CRIB involves applying a spatially varying electric or magnetic field to an atomic or solid-state ensemble. This action results in a proportional shift of the resonance frequency of the $|g\rangle \rightarrow |e\rangle$ transition, varying for each atom based on

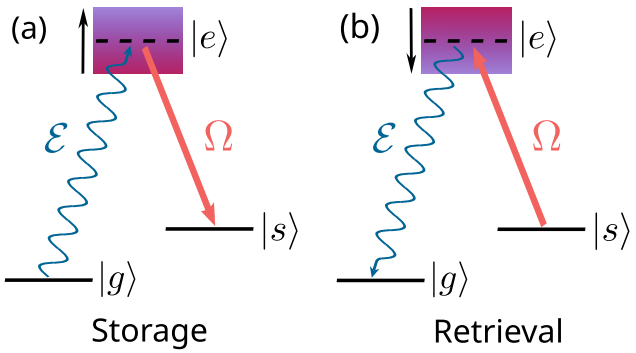

Figure 2.10: CRIB storage (a) and retrieval (b) process. The signal field (wiggly blue) is absorbed resonantly by the inhomogeneously broadened ensemble, exciting the atom to state $|e\rangle$. A control pulse (red) then transfers the excitation to a long-lived storage state $|s\rangle$. For retrieval, the control reexcites the atom back to $|e\rangle$. The polarity of the external field is then reversed, leading the optical dipoles to rephase and reemit the signal photon.

its position within the ensemble. Consequently, this creates inhomogeneous broadening of the atomic resonance. Thus, every individual atomic resonance remains narrow, but when combined, the ensemble exhibits a significantly broader absorption frequency spectrum. The approach hence allows to store photons with a bandwidth exceeding the natural linewidth of the atoms.

The storage process works as follows: A signal pulse resonant with the broadened $|g\rangle \rightarrow |e\rangle$ transition is initially absorbed by the ensemble. As the degree of broadening, and thus the width of the pulse to be stored, are governed by the applied external field, extremely short signal pulses can be used. This results in an absorption process much faster than the lifetime of the excited state $|e\rangle$, minimising losses due to spontaneous emission. After the absorption is finished, the external field is turned off, and the atoms regain their original absorption frequencies. The atomic dipoles then start to precess at different frequencies due to the inhomogeneous broadening, leading to an out-of-phase behaviour. Consequently, the information about the signal's arrival time is lost. Now, an optical control pulse, typically a π-pulse, is employed to transfer the excitation into a storage state $|s\rangle$, effectively 'freezing' the dipole precession.

Upon retrieval, another control pulse unfreezes the atomic motion and excites the atoms back to $|e\rangle$. To recover the signal pulse, the dephasing process needs to be reversed. A change in the polarity of the external field leads to precession of the atoms in the opposite direction, causing rephasing of the atomic spins and reemission of the signal when they all realign. This complete reversal of the storage process results in what is known as a

photon echo, mirroring the initial configuration. A schematic depiction of the storage and retrieval processes is shown in Figure 2.10.
In mathematical terms, between the absorption at $t = 0$ and the inversion of the external field polarity at $t = \tau$, the atoms with a detuning Δ relative to the carrier frequency of the light accumulate a phase $e^{-i\Delta\tau}$. When the polarity is inverted, the detuning for the atoms changes from $\Delta \rightarrow -\Delta$. After a time $t = 2\tau$, the accumulated phase factor of the atoms becomes $e^{i\Delta\tau}$. This results in rephasing of all atomic dipoles, determining the storage time t_{storage} of the memory. Consequently, CRIB memories are not precisely on-demand. The memory efficiency in CRIB is given as

$$\eta_{\text{CRIB}} = \left(1 - e^{-\bar{d}_{\text{opt}}}\right)^2 \text{sinc}^2\left(\gamma_{e,0}\, t_{\text{storage}}\right), \tag{2.14}$$

where $\bar{d}_{\text{opt}} = d_{\text{opt}} \frac{\gamma_{e,0}}{\gamma_e}$ [114, 122]. Here, $\gamma_{e,0}$ represents the width of initial narrow line, γ_e is the width of the broadened line, d_{opt} is the optical depth of the initial line, and t_{storage} stands for the storage time in the excited state. As the initial absorption depth is reduced by a factor $\frac{\gamma_{e,0}}{\gamma_e}$, increasing the broadening leads to a decrease in storage efficiency.
A primary advantage of CRIB lies in its inherent frequency multimode character, stemming from the broadening of the line. However, its main drawback is associated with the preparation of the storage medium. CRIB was developed and refined for REIDs, where the linewidth is already inhomogeneously broadened due to doping. This means, the medium often has to be narrowed down before controlled broadening can be achieved. This process results in the loss of many absorbers, reducing the optical depth of the system and thus posing challenges in achieving high memory efficiencies. The efficiency given in Eq. 2.14 is limited to a value of 54% because of reabsorption in the forward direction. However, many techniques and geometries (such as GEM, where the external field gradient is applied in propagation direction) have been proposed to mitigate these problems and achieve higher efficiencies, some of which held the record for the highest efficiencies achieved in memories for some time [187, 197, 280]. For more specific details I refer the reader to [128].

2.4.6 AFC

The Atomic Frequency Comb (AFC) protocol is closely linked to the CRIB protocol and was firstly introduced by Afzelius et al. in Ref. [282]. An AFC is an ensemble-based system, in which the excited state is spread into equally spaced absorption lines, again enabling the storage of bandwidths exceeding the atomic linewidth. This is achieved by engineering the ensemble to exhibit a periodic absorption pattern resembling a comb, with a series of periodic, narrow absorption peaks characterised by a width γ_0, a height

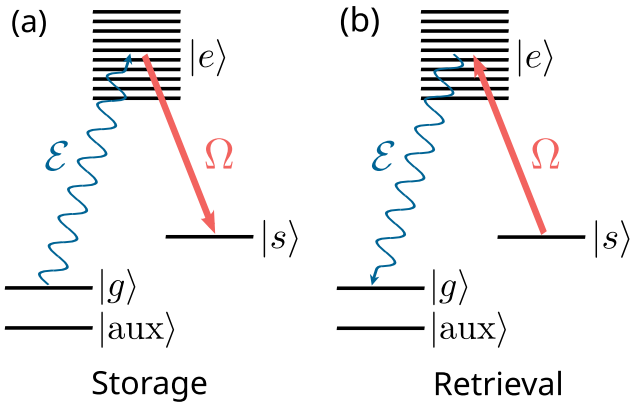

Figure 2.11: AFC storage (a) and retrieval (b) process. The broadband signal field (wiggly blue) is absorbed resonantly by the atomic frequency comb. A control pulse (red) then transfers the excitation to a long-lived storage state $|s\rangle$. For retrieval, the control reexcites the atom back to the frequency comb. Due to the periodic structure of the comb, the optical dipoles rephase after a time inversely proportional to the comb spacing δ_{AFC}, reemiting the signal photon. The $|\mathrm{aux}\rangle$ level is necessary to pump away the atoms in between the comb's teeth.

d, and separated by δ_{AFC}. This comb-like structure is created by optically pumping the ensemble with equal peak spacing.

The storage process in AFC closely resembles that of the CRIB protocol. However, it significantly enhances the memory's multimode capacity in comparison to CRIB [282, 283]. The main difference, and the special feature of the AFC protocol, becomes evident upon retrieval. In contrast to CRIB, where an external field is required to reverse the inhomogeneous broadening process, in the AFC case the revival or rephasing of the spins occurs automatically in a periodic manner as a result of the discrete structure of the excited state and the associated beat note of the corresponding frequencies. Figure 2.11 shows a schematic of the protocol.

The periodic rephasing occurs every $2\pi/\delta_{\mathrm{AFC}}$. Each rephasing event results in a photon-echo-type coherent retrieval. As in CRIB, the signal's broad bandwidth, and thus short duration, implies that the absorption process can be completed before the excited state has any time to decay. The single photon to be stored is absorbed by all atoms in the comb and the state of the light is transferred to a collective atomic excitation at the optical transition. Here again, for long-time storage the excitation can be transferred to an extra storage state $|s\rangle$ via an optical π-pulse.

The experimental preparation of such an atomic structure is challenging and was originally

proposed for REIDs [219, 221, 282], but has also been implemented in atomic vapours [182]. It involves selective optical pumping to excite unwanted atoms from the ground state into an auxiliary state $|\text{aux}\rangle$ with a very long lifetime, effectively "shelving" them for the memory protocol's duration. AFC's primary advantage lies in its remarkable increase in the memory's multimode capacity, surpassing even CRIB, and making it highly suitable for quantum repeater networks. However, its drawback lies in the complex preparation of the comb structure, which involves shelving many atoms away from the broad absorption spectrum.

A practical advantage of AFC over CRIB is that in the latter, all atoms except a single narrow resonance are pumped away, resulting in the discarding of numerous atoms compared to AFC, where N narrow resonances remain, corresponding to the number of comb teeth, which can be quite large. Consequently, fewer atoms are removed in AFC, and the optical depth of the system is larger, allowing for more absorption and improved efficiencies in an ensemble with the same doping concentration as in the less efficient CRIB protocol.

One might question whether an ensemble with a comb-like absorption structure is able to absorb all frequencies of the signal pulse. It could be expected that frequencies not overlapping with the comb teeth might be transmitted and lost. However, as is explained in the original AFC proposal, if the integral of the atomic density over the photon bandwidth is large enough, the photon will be totally absorbed by the AFC even though the spectral density of atoms is concentrated to the narrow peaks of the comb. This has to do with the Heisenberg energy-time uncertainty relation. For the time scale of the absorption, which is of the order of the input pulse duration $\tau = 1/\gamma_p$, the uncertainty of the optical transition will be of the order of $\gamma_p \gg \delta_{\text{AFC}}$, where γ_p is the spectral distribution of the input field. This will cause a spectral averaging of the sharp AFC comb structure into a smooth distribution. Therefore, when a sufficient number of atoms is involved, the collective absorption of the entire ensemble can store the full spectrum of the signal. An important condition for long-term storage, is that the control pulse used to transfer the excitation to the $|s\rangle$ state must be sufficiently strong and broadband to transmit all the involved frequencies of the signal.

In Ref. [282], a formula for the efficiency of the AFC is derived for the case where the two control fields are counter propagating. The formula applies to a series of Gaussian peaks:

$$\eta_{\text{AFC}} \approx \left(1 - \mathrm{e}^{-\bar{d}_{\text{opt}}}\right)^2 \mathrm{e}^{-\frac{7}{F^2}}, \tag{2.15}$$

where $\bar{d}_{\text{opt}} \approx \frac{d_{\text{opt}}}{F}$ is the effective optical depth and $F = \delta_{\text{AFC}}/\gamma_0$ is the finesse of the AFC.

2.4.7 FLAME/ORCA

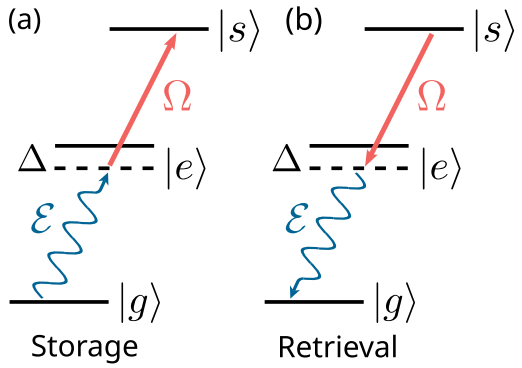

Figure 2.12: FLAME/ORCA storage (a) and retrieval (b) process. These protocols resemble EIT/Raman protocols, but operate in a ladder Ξ-system. Here, ORCA is a far-detuned FLAME. A signal photon (wiggly blue) is absorbed into $|e\rangle$ and adiabatically transferred to a storage state $|s\rangle$ by the control field (red). As the storage state $|s\rangle$ is a highly excited state, it does not have initial excitations, making the atomic noise sources in these protocols minimal. The storage time is limited by the decay time of $|s\rangle$.

The acronyms FLAME and ORCA stand for fast-ladder memory and off-resonant cascaded absorption protocols. These two closely related storage protocols were developed in the last decade by R. Finkelstein et al., and by K. T. Kaczmarek et al., respectively. They both are based on EIT/Raman type interactions, but in this case in ladder-type Ξ-systems. A general limitation of Λ-scheme-type protocols are noise processes resulting from unwanted coupling of the control field, or from unwanted population of the storage state, such as FWM and SRS, which limit the memory fidelity. As a result of these drawbacks, these new protocols were developed, that have the benefit of being inherently noise free. A general schematic representation of the working principle of both protocols is illustrated in Figure 2.12.
A drawback of FLAME/ORCA memories is their short storage time, which is limited by the lifetime of the excited state used as storage state. The main difference between ORCA and FLAME resides in the choice of the two-photon detuning Δ. ORCA can be described as a far-detuned FLAME (in the same manner that Raman can be seen as a far detuned EIT). There are also further technical differences between the protocols, which will be summarised below.

In his PhD thesis [120], K. T. Kaczmarek introduces the ORCA protocol by stating

that the release of the long storage time requirement opens the possibility of using non-spin states as storage states. One could, e.g., use highly excited Rydberg states which have lifetimes of tens of μs. However, if one desires a simple system working at room temperature, these types of schemes are problematic, as a result of the large wavelength mismatch on the order of nanometers between the two involved fields. This fact leads to a very strong Doppler broadening of the two-photon transition and thus to fast dephasing of the memory [183, 284]. In order to mitigate this effect, one could chose to use low-lying orbital states with a shorter, but still sufficient lifetime. The resulting transitions of the two fields thus become closer in wavelength, allowing for room-temperature operation. The ORCA protocol, described as a noise-free quantum memory protocol operating in a simple room-temperature platform, specifically in caesium, has an operational principle very similar to the Raman memory, in the sense that it uses two broadband optical fields, the signal and control, which are in two-photon resonance with the storage state, but are both far detuned of their respective transition. Unlike in Λ-type protocols, the bandwidth in ORCA is not in principle limited by the ground-state splitting of the atom, and the counter-propagating geometry of the fields reduces the Doppler-broadening and the motional-induced dephasing of the stored coherence. This then yields reasonable time-bandwidth products for specific applications [94, 138, 285]. A doubly excited electronic state with no thermal excitations at room-temperature is used as the selected storage state. This means, in principle, the protocol requires no preparation of the ensemble through optical pumping, allowing for higher operational speed of the memory. Moreover, the retrieved pulse suffers from no contamination through noise resulting from imperfect optical pumping, such as SRS. Also regarding noise, since the signal and control wavelengths are chosen to be off-resonant from the populated ground-state transitions, the control-induced fluorescence noise is eliminated. Stemming from the ladder structure, there is also no FWM noise, as no scattering process can populate the storage state. The only remaining source of loss is then technical and can be maximally reduced, yielding end-to-end efficiencies very close to the internal memory efficiencies, $\eta_{\mathrm{e2e}} \sim \eta_{\mathrm{mem}}$. In Ref. [183], for the first proof-of-principle experiment they report a $1/e$-lifetime of 5.4(1) ns and a memory efficiency of $\eta_{\mathrm{mem}} = 16.77(2)\%$ at the single photon level. They further show storage of real single photons from a type-II parametric down-conversion source.
The FLAME protocol [184, 245] is, as stated above, a version of the same protocol, but this time operating on resonance, or at much lower detunings ($\Delta = 0 - 1.15\,\mathrm{GHz}$). Due to the large energy difference of the ladder levels in caesium, which limits the lifetime of the memory to a few nanoseconds, the experiment in FLAME uses rubidium vapour and thus achieves larger storage times, while maintaining a large bandwidth and minimal noise levels. The first implementation (FLAME1, [184]) achieves a memory

lifetime of 86 ns and a end-to-end efficiency of $\eta_{\mathrm{e2e}} = 25\%$. An improved version of the experiment published recently (FLAME2, [245]), in which the experimental setup was upgraded by using stronger control pulses, wider beams, higher optical depth, an annular (ring-shaped) pumping beam, and a weak dressing field in order to counteract residual Doppler broadening, yielded an end-to-end memory efficiency of $\eta_{\mathrm{e2e}} = 35\%$ and a $1/e$-lifetime of 108 ns. The noise level in all of these types of memories is on the order of 10^{-5} photons per pulse. Recently, storage of telecom light in an ORCA memory was performed in Ref. [286]. In our group, a ladder-type memory on the Cs D_1 line compatible with single photons from InGaAs quantum dots has been developed [287].

	Ions/atoms in cavities	Colour Centres	Cold atomic vapours	Warm atomic vapours	REIDs	Delay lines
Temperature T	$\mathcal{O}(\mu\mathrm{K} - \mathrm{mK})$	$\mathcal{O}(100\,\mathrm{mK} - 8\,\mathrm{K})$	$\mathcal{O}(\mu\mathrm{K} - \mathrm{mK})$	$\mathcal{O}(300 - 370\,\mathrm{K})$	$\mathcal{O}(< 6\,\mathrm{K})$	all
Magnetic fields $\boldsymbol{B}$	$\mathcal{O}(100\,\mathrm{nT})$	$(\mathcal{O}(100\,\mathrm{mT}))^*$	$\mathcal{O}(\mu\mathrm{T} - 3\,\mathrm{mT})$	$(\mathcal{O}(100\,\mathrm{pT}))^*$	$\mathcal{O}(\mathrm{mT} - 30\,\mathrm{T})$	／
Vacuum	✓	✗	✓	✗	✗	✗
Technical simplicity	▲	▲	▲	■	▲	●

Table 2.1: Comparison of different light storage platforms with respect to experimental parameters such as operational temperatures and magnetic fields, and with respect to technical simplicity. *Magnetic fields are optional in colour centres and in warm vapours to lift the Zeeman degeneracy. ● , ■ , ▲ stand for simple, medium, and hard levels of technical implementation effort.

	Delay lines	EIT	Raman	ATS	CRIB (GEM)	AFC	FLAME/ ORCA
Platforms	free-space/ fibre loops	WA, CA, RE	WA, CA, RE	CA, (WA), (RE)	RE, WA, CA	RE, WA, (CA)	WA, CA
Detuning Δ	⁄	$\Delta \ll \omega_{sg}$, $\Delta \sim \gamma_e$	$\Delta \sim \omega_{sg}$, $\Delta \ll \gamma_e$	$\Delta \ll \omega_{sg}$, $\Delta \sim \gamma_e$	$\Delta \lesssim \gamma_e$	$\Delta \lesssim \gamma_{\text{comb}}$	$\Delta \lesssim \gamma_e$ (F.) $\Delta \gtrsim \gamma_e$ (O.)
Control field Ω_c	⁄	$\Omega_c \sim \gamma_e$	$\Omega_c \gg \gamma_e$	$\Omega_c \gg \gamma_e$	$\Omega_c \sim \Delta\omega_s$	$\Omega_c \sim \Delta\omega_s$	$\Omega_c \sim \gamma_e$ (F.) $\Omega_c \gg \gamma_e$ (O.)
External $\boldsymbol{E}/\boldsymbol{B}$ fields	⁄	(small $\boldsymbol{B}^*$)	(small $\boldsymbol{B}^*$)	(small $\boldsymbol{B}^*$)	large $\boldsymbol{E}/\boldsymbol{B}$ field gradients	⁄	⁄
Efficiency $\eta_{\text{mem}/e2e}$	$\eta_{e2e} = 98\%^\dagger$ [100]	$\eta_s = 92\%$ (CA) [196] $\eta_s = 76\%$ (RE) [223]	$\eta_{\text{mem}} = 82\%$ (WA) [186]	$\eta_{e2e} \sim 3\%$ (CA) [244]	$\eta_{\text{mem}} = 87\%$ (CA) [197] $\eta_{e2e} = 76\%$ (RE) [187]	$\eta_{\text{mem}} = 56\%$ (RE) [221]	$\eta_{e2e} = 35\%$ (WA, F.) [245]
(1/e) Storage times τ_{mem}	$\mathcal{O}(100\,\text{ns})$ [238]	$430\,\text{ms}^\ddagger$ (WA) [185]	$4\,\mu\text{s}$ (WA) [246]	$\sim 200\,\text{ns}$ (CA) [244]	$1\,\text{ms}$ (CA) [197]	$530\,\text{ms}$ (RE) [229]	$108\,\text{ns}$ (WA, F.) [245]
Bandwidth $\Delta\omega_{\text{mem}}$	all	$\Delta\omega_{\text{mem}} \leq \Delta\omega_{\text{EIT}}$	$\Delta\omega_{\text{mem}} \sim \Delta\omega_c$	$\Delta\omega_{\text{mem}} \sim \Delta\omega_c$	$\Delta\omega_{\text{mem}} \sim \gamma_{e,\text{CRIB}}$	$\Delta\omega_{\text{mem}} \sim \gamma_{e,\text{comb}}$	$\Delta\omega_{\text{mem}} \lesssim \Delta\bar{\omega}$ (F.) $\Delta\omega_{\text{mem}} \sim \Delta\omega_c$ (O.)
Noise μ_1	⁄	$2 \cdot 10^{-4}$ (WA) [191]	0.20 (WA) [181]	$5 \cdot 10^{-3}$ (CA) [195]	–	0.07 (RE) [135]	$3 \cdot 10^{-5}$ (WA, F.) [245]
Technical simplicity	●	■	■	■	▲	▲	■

Table 2.2: Comparison of different light protocols with respect to experimental parameters and exemplary state-of-the-art figures of merit (approximate values). Here (CA) stands for cold atomic gases, (WA) for warm atomic gases, (RE) for REIDs. In the second row, when in parenthesis it means it is theoretically possible to realise, but difficult. η_s stands for storage efficiency only, $\Delta\omega_s$ is the signal or input bandwidth, $\Delta\omega_c$ is the control pulse bandwidth, ω_{sg} is the ground-state hyperfine splitting $\Delta\bar{\omega}$ is the frequency distance to adjacent orbitals. Comments: *Small magnetic fields $\boldsymbol{B}$ can be used as guiding fields in the case of Zeeman-level storage. †Efficiency per loop cycle. ‡Experiment performed with macroscopic light pulses, well above single-photon-level. ⁄ not applicable, – no data found. ● , ■ , ▲ stand for simple, medium, and hard levels of technical implementation effort.

3 Theoretical Framework

"On the other hand I think I can safely say that nobody understands quantum mechanics."

Richard P. Feynman

This chapter will yield the theoretical background relevant for this thesis. First, a general introduction to caesium and its atomic structure will be given, as this is the atom which we use for our experiments. Next, the topic of light-matter interaction will be addressed, starting with the framework of the two-level atom. Here I will describe the relevant broadening mechanisms and the concepts of optical pumping and lifetime-limiting mechanisms. Then, the three-level atom and some effects arising in such a system will be introduced. Thereafter, I will present a summary of the theory behind light storage in a Λ-system and the corresponding control pulse optimisation, as developed by Gorshkov et al., in Refs. [123–125, 240, 241]. The following subsection will be devoted to the explanation of the relevant noise sources in warm vapour memories. The chapter will end with some general notes on spectral filtering.

3.1 Caesium atomic structure

Caesium, a silvery golden metal, is the rarest and most reactive of the naturally occurring alkali metals. In 1860, it was the first element to be discovered with a spectroscope by R. Bunsen and G. Kirchhoff, an instrument the two scientists had invented only a year before. It owes its name to the blue spectroscopic lines it produces, which were related to the Latin word 'caesius' meaning 'sky blue'. It reacts explosively with water already at very low temperatures, for which it is considered a hazardous material. It has only one stable isotope, ^{133}Cs, and has a melting temperature of 28.5 °C. With an atomic number of 55 and the chemical symbol Cs, it is used as a frequency standard, as the SI second is defined by the ground-state resonance frequency of exactly 9192631770 Hz. From its 55 electrons, only one is in the outermost shell, which makes Cs hydrogen-like

and therefore easier to describe physically. This, combined with the fact that there exist optical transitions in Cs (and other alkalis) with frequencies easily attainable by commercial diode lasers, makes these elements very attractive for quantum optical experiments.

The optical line of interest in this work is the Cs D_1 line at 894 nm, lying in the infrared, and therefore not visible with human eyes. The D_1 line stems from the fine structure of the Cs atom, which arises from the interaction between the orbital angular momentum $\boldsymbol{L}$ and the electron spin $\boldsymbol{S}$ of the valence electron. These two together form the total angular momentum $\boldsymbol{J} = \boldsymbol{L} + \boldsymbol{S}$. The nuclear spin of Cs is $I = \frac{7}{2}$. The interaction between the total angular momentum and the nuclear spin gives rise to the hyperfine structure. The resulting hyperfine angular momentum is

$$\boldsymbol{F} = \boldsymbol{J} + \boldsymbol{I}. \tag{3.1}$$

For the D_1 line, namely the transition between the ground state $6^2S_{1/2}$ and the excited state $6^2P_{1/2}$ we have $L = 0$, $S = 1/2$ for the ground state, and therefore $J = 1/2$, and $L = 1$, $S = 1/2$ and $J = 1/2$ for the excited state. These states then split into the hyperfine states labelled by the F quantum number with $|J - I| \leq F \leq |J + I|$, hence $F, F' = 3, 4$, giving rise to four possible transitions (see Table 3.1). The D_1 hyperfine structure is depicted in Fig. 3.1. The resulting ground-state splitting between the $F = 3$ and $F = 4$ states of the long-lived $6^2S_{1/2}$ state amounts to 9.193 GHz, the largest ground-state hyperfine splitting among alkali atoms. The excited state splitting between $F' = 3$ and $F' = 4$ amounts to 1.168 GHz.

Transition	Frequency ω	Wavelength λ
$\lvert 6^2S_{1/2}; F = 3\rangle \rightarrow \lvert 6^2P_{1/2}; F' = 3\rangle$	335.120563 THz	894.581 nm
$\lvert 6^2S_{1/2}; F = 3\rangle \rightarrow \lvert 6^2P_{1/2}; F' = 4\rangle$	335.121731 THz	894.578 nm
$\lvert 6^2S_{1/2}; F = 4\rangle \rightarrow \lvert 6^2P_{1/2}; F' = 3\rangle$	335.111370 THz	894.605 nm
$\lvert 6^2S_{1/2}; F = 4\rangle \rightarrow \lvert 6^2P_{1/2}; F' = 4\rangle$	335.112538 THz	894.602 nm

Table 3.1: Hyperfine optical transitions of the Cs D_1 line. Values are taken from Ref. [288].

Another closely related optical line used in many quantum memory experiments is the Cs D_2 line at 852 nm, that corresponds to the $6^2S_{1/2} \rightarrow 6^2P_{3/2}$ transition. In this case the excited state splits into four different lines $F' = 2, 3, 4, 5$ with separations between $150 - 250$ MHz.

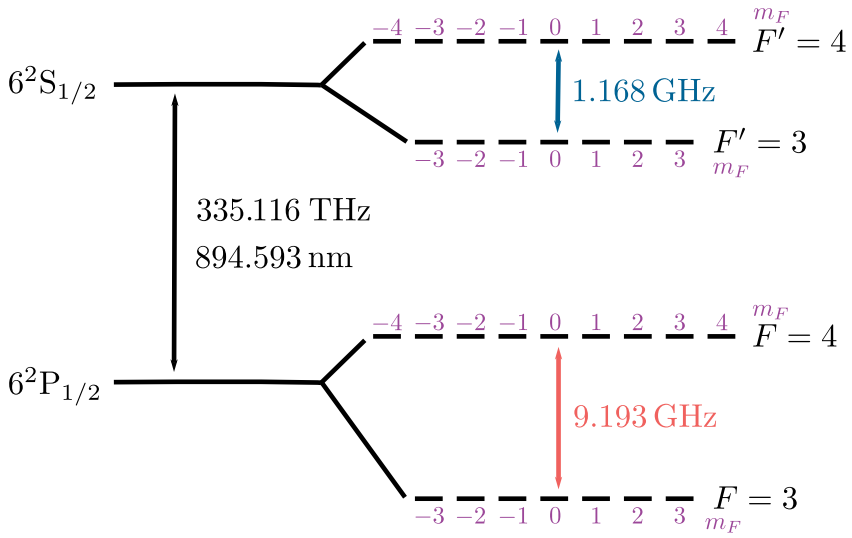

Figure 3.1: Hyperfine level scheme of the Cs D_1 line including the Zeeman sublevels. Data for the transition frequencies and wavelengths are from [288].

As for any angular momentum operator it holds

$$\hat{F}^2 |F\, m_F\rangle = F(F+1)\hbar |F\, m_F\rangle \tag{3.2}$$

$$\hat{F}_z |F\, m_F\rangle = m_F \hbar |F\, m_F\rangle\,, \tag{3.3}$$

where m_F is the magnetic quantum number and represents the projection of the F angular momentum along the z-axis in multiples of $\hbar$. It can take the values $-F \leq m_F \leq F$. Under normal conditions, without external magnetic fields, all the m_F levels have the same energy and are thus degenerate, and the population of the corresponding atomic hyperfine state is equally distributed among all of them. When an external magnetic field is applied, the hyperfine levels split into $m_F = 2F + 1$ magnetic sublevels, according to the Zeeman effect. This is the case when the splitting is small compared to the energy difference between the unperturbed hyperfine levels. This splitting amounts to the $\mathcal{O}$ (kHz-MHz) (radio frequency) range for the earth magnetic field. If the external field becomes very large, the system is said to be in the Paschen-Back regime, where the magnetic interaction disrupts the coupling between the angular momenta $\boldsymbol{J}$ and $\boldsymbol{I}$, and the hyperfine description no longer holds. Recently, this regime has been investigated for the realisation of quantum memories [289, 290].

For the possible optical transitions between the different hyperfine lines and their magnetic sublevels, it is important to note the relevant selection rules for dipole-allowed transitions

arising from the Wigner Eckert theorem [291]. The electric dipole operator only yields non-zero matrix elements between states of different parity. For a $|F\, m_F\rangle \rightarrow |F'\, m_{F'}\rangle$ transition with $\Delta F = F' - F$ and $\Delta m_F = m_{F'} - m_F$ it holds

$$\Delta F = 0, \pm 1 \tag{3.4}$$

$$\Delta m_F = 0, \pm 1 \tag{3.5}$$

$$\text{if } \Delta F = 0 \rightarrow \Delta m_F \neq 0. \tag{3.6}$$

The typical Doppler-free saturated absorption spectrum of the Cs D_1 line is depicted in Fig. 3.2. This technique allows to see the Lamb dips and thus to reliably determine the transition frequencies between different states.

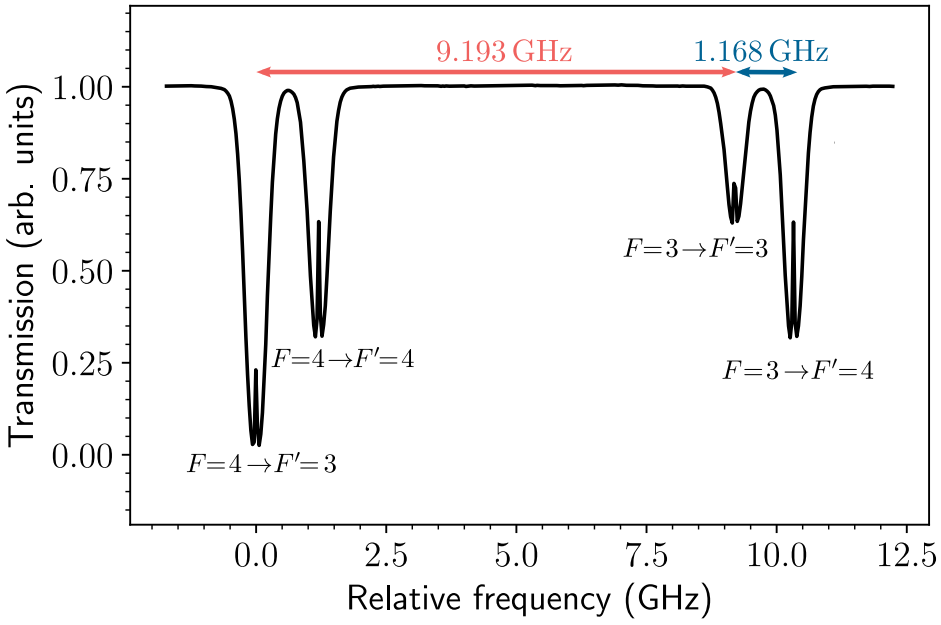

Figure 3.2: Doppler-free absorption spectroscopy of the Cs D_1 transition $6^2S_{1/2} \rightarrow 6^2P_{1/2}$. Data taken by David Becker, Bachelor student under my supervision [10] and values from Ref. [288].

A summary of the most relevant parameters related to the Cs D_1 line for the following chapters is given in Table 3.2. A very useful program to theoretically calculate and fit the behaviour of Cs vapour and other warm atomic systems and their absorption properties, among others, is ElecSus [292, 293].

Quantity	Abbreviation	Value
Atomic number	Z	55
Nucleons	$Z+N$	133
Atomic mass	m_{Cs}	$2.207 \cdot 10^{-25}\,\mathrm{kg}$
Nuclear spin	I	7/2
Vapour Pressure at 25°C	P_v	$1.49 \cdot 10^{-6}\,\mathrm{torr}$
Frequency	ω_0	$2\pi \cdot 335.116049\,\mathrm{THz}$
Wavelength	λ	$894.593\,\mathrm{nm}$
Nat. linewidth (FWHM)	Γ_{nat}	$2\pi \cdot 4.575\,\mathrm{MHz}$
Lifetime	τ	$34.791\,\mathrm{ns}$
Absorption osc. strength	f	0.3449
Transition dipole matrix element	$\mathcal{M}_{\mathrm{Cs,D1}} = \langle J=\frac{1}{2}\|\|er\|\|J'=\frac{1}{2}\rangle$	$2.7020 \cdot 10^{-29}\,\mathrm{C{\cdot}m}$

Table 3.2: Relevant physical and optical properties for Cs atoms and the $6^2\mathrm{S}_{1/2} \rightarrow 6^2\mathrm{P}_{1/2}$ D_1 transition [288].

3.2 Light-matter interaction

This section aims to present an overview of the theoretical description of light-matter interaction relevant for this work. First, some general concepts of the interaction will be reviewed, in which the atom is described with the simplest possible model, a two-level system. I assume the reader to be familiar with the quantum mechanical treatment of this system using a density-matrix formalism. Examples hereof are given in Refs. [110, 291]. Here, I will only shortly derive the absorption response and lineshape of an atom, and introduce important quantities such as the experimental optical depth $2d_{\mathrm{opt}}$ and the Rabi frequency Ω. Moreover, I will describe the relevant broadening mechanisms present in warm atomic systems. Thereafter, I will introduce the concept of optical pumping and describe lifetime-limiting mechanisms existent in such systems. Subsequently, the three-level system mainly used throughout the thesis, will be introduced. In such a model we can describe the effect of electromagnetically induced transparency (EIT) from a theoretical perspective, expanding on the overview given in Ch. 2. For now, a semiclassical model of light-matter interaction is sufficient to describe occurring phenomena, at least to first order. In such a treatment, the atom is treated quantum mechanically, while the light field is treated classically.

3.2.1 The two-level atom

We will work in the framework of the dipole approximation, where only the lowest-order term of the multipole light-atom interaction is considered. This approximation is justified as long as the wavelength of the field ($\lambda = 894\,\text{nm}$) is much larger than the size of the atom ($d_{\text{cov}} \approx 0.6\,\text{nm}$, where d_{cov} is the covalent diameter of a Cs atom [294]). Thus, we can ignore the spatial dependence of the electric field and assume it to be monochromatic, oscillating at a frequency ω. This field takes the form [291]

$$\boldsymbol{E}(t) = \hat{\boldsymbol{\epsilon}} E_0 \cos(\omega t), \tag{3.7}$$

where $\hat{\boldsymbol{\epsilon}}$ is the field unit polarisation vector and E_0 is the amplitude of the field. The field can be decomposed into a positive- and a negative rotating component as

$$\boldsymbol{E}(t) = \hat{\boldsymbol{\epsilon}} \frac{E_0}{2} (e^{-i\omega t} + e^{+i\omega t}) =: \boldsymbol{E}_{\boldsymbol{0}}^{(+)} e^{-i\omega t} + \boldsymbol{E}_{\boldsymbol{0}}^{(-)} e^{+i\omega t}. \tag{3.8}$$

Note that $\boldsymbol{E}_{\boldsymbol{0}}^{(\pm)}$ corresponds to $e^{\mp i\omega t}$.
The total Hamiltonian $\hat{H} = \hat{H}_{\text{A}} + \hat{H}_{\text{AF}}$ can be divided into the bare (free evolution) atomic Hamiltonian $\hat{H}_{\text{A}} = \hbar\omega_0 \left|e\right\rangle \left\langle e\right|$ (assuming zero ground state energy), and the atom-field interaction Hamiltonian

$$\hat{H}_{\text{AF}} = -\hat{\boldsymbol{d}} \cdot \boldsymbol{E} = -(-e\,\hat{\boldsymbol{r}}_e) \cdot \boldsymbol{E}, \tag{3.9}$$

where

$$\hat{\boldsymbol{d}} = \langle g|\hat{\boldsymbol{d}}|e\rangle \left(\hat{\sigma} + \hat{\sigma}^\dagger\right) \tag{3.10}$$

is the electric dipole operator, and $\hat{\boldsymbol{r}}_e$ is the position operator of the electron. Here, $\hat{\sigma} := \left|g\right\rangle \left\langle e\right|$ is the atomic lowering operator. The total Hamiltonian can then be written as

$$\hat{H} = \hat{H}_{\text{A}} + \hat{H}_{\text{AF}} = \hbar\omega_0 \hat{\sigma}^\dagger \hat{\sigma} - \langle g|\hat{\boldsymbol{d}}|e\rangle \cdot \boldsymbol{E} \left(\hat{\sigma} + \hat{\sigma}^\dagger\right), \tag{3.11}$$

with ω_0 being the transition frequency between states $\left|g\right\rangle$ and $\left|e\right\rangle$, and $\hat{\sigma}^\dagger\hat{\sigma} = \left|e\right\rangle \left\langle e\right|$ the excited state projection operator.

Rabi frequency

Inserting the specific time dependencies, separating the dipole operator and the electric field into positive and negative-rotating parts, and implementing the rotating-wave ap-

proximation (RWA), which ignores rapidly oscillating terms that average over time, one can derive

$$\begin{aligned}\hat{H}_{\mathrm{AF}} &= -\langle g|\hat{\boldsymbol{\epsilon}}\hat{\boldsymbol{d}}|e\rangle \left(E_0^{(-)}\hat{\sigma}e^{i\omega t} + E_0^{(+)}\hat{\sigma}^\dagger e^{-i\omega t}\right) \\ &= \frac{\hbar\Omega}{2}(\hat{\sigma}e^{i\omega t} + \hat{\sigma}^\dagger e^{-i\omega t}),\end{aligned} \tag{3.12}$$

where the electric field component $E_0^{(+)} = \frac{E_0}{2}$ is assumed to be real and the Rabi frequency Ω has been introduced as

$$\Omega := -\frac{2\,\langle g|\hat{\boldsymbol{\epsilon}}\hat{\boldsymbol{d}}|e\rangle\, E_0^{(+)}}{\hbar} = -\frac{\langle g|\hat{\boldsymbol{\epsilon}}\hat{\boldsymbol{d}}|e\rangle\; E_0}{\hbar}. \tag{3.13}$$

The phase of the dipole matrix element is normally chosen such that $\Omega > 0$. In the case where the light field is linearly polarised along the z-direction, we can write[1].

$$\Omega := -\frac{\langle g|\hat{d}_z|e\rangle\, E_0}{\hbar}. \tag{3.14}$$

For an estimation of the Rabi frequency from an experimental perspective, assuming a Gaussian beam with a beam waist w_0 ($1/e^2$ intensity radius), the peak intensity at the beam center as a function of the total beam power P is given as

$$I = \frac{2P}{\pi w_0^2}, \tag{3.15}$$

where the factor 2 is relevant since for the same optical power, the Gaussian mode has twice the peak intensity when compared to, e.g., a rectangular mode [295]. When written in terms of the electric field amplitude one has

$$I = \frac{E_0^2}{2\mu_0 c} \tag{3.16}$$

where $\mu_0 c = \sqrt{\mu_0/\epsilon_0} = z_0$ is the impedance of free space, and μ_0 and ϵ_0 are the permeability and the permittivity of free space, respectively. The Rabi frequency can thus be rewritten as

$$\Omega = -\frac{|\,\langle g|\hat{d}_z|e\rangle\,|\sqrt{2\mu_0 c I}}{\hbar} = \left[\frac{4\mu_0 c\,|\,\langle g|d_z|e\rangle\,|^2\,P}{\pi\hbar^2 w_0^2}\right]^{1/2}. \tag{3.17}$$

[1] This expression of the Rabi frequency is twice the value that will be used in the theoretical description of storage in a Λ-system in Sec. 3.2.4. The factor 2π common in angular frequency definitions is already included in the $\hbar$ in the denominator.

For the correct calculation of the dipole transition strength for, e.g., a hyperfine transition, one needs to consider the polarisation of the incident light and sum over all the contributing degenerate states, in the case of zero magnetic field. As an example, let us consider the transitions of the Cs D_1 line with π-polarised light. The reduction of the transition matrix element and its calculation via Clebsch-Gordan coefficients is extensively explained in Refs. [288, 291]. For the squared matrix element $|\langle g|d_z|e\rangle|^2$ one has[1]

$$|\langle g|\hat{d}_z|e\rangle|^2 = |d_{z,eg}|^2 = C^2_{FF'}\mathcal{M}^2_{\mathrm{Cs,D1}} = \frac{1}{2F+1}\, c^2_{FF'}\mathcal{M}^2_{\mathrm{Cs,D1}}, \tag{3.18}$$

where the transition dipole matrix element $\mathcal{M}_{\mathrm{Cs,D1}} = \langle J = \frac{1}{2}||er||J' = \frac{1}{2}\rangle$ can be taken from Table 3.2 and the transition strength factor $C^2_{FF'} = \frac{1}{2F+1}\, c^2_{FF'}$ is calculated by summing over all the involved $m_F \to m'_F$ Clebsch-Gordan coefficients and averaging over the number of possible transitions (factor $\frac{1}{2F+1}$). The values for $C^2_{FF'}$ for the Cs D_1 line are given in Table 3.3.

F	F'	
	3	4
3	$\frac{1}{12}$	$\frac{1}{4}$
4	$\frac{7}{36}$	$\frac{5}{36}$

Table 3.3: Transition strength factors $C^2_{FF'} = \frac{1}{2F+1}c^2_{FF'}$, where the $c^2_{FF'}$ are the summed up dipole matrix elements for π-transitions from [288].

From the treatment of resonance fluorescence in Refs. [288, 291], one obtains the relative transition strength factors $S_{FF'}$ for resonance fluorescence. There, assuming the case of an isotropic electric pump field, i.e., a field coupling to all three possible transitions $(\pi, \sigma^{\pm})$ coupling two F levels, the atom can be treated as a two-level atom and the resulting effective dipole moment is given as

$$|d_{\mathrm{iso,eff}}(F \to F')|^2 = \frac{1}{3} S_{FF'}\mathcal{M}^2_{\mathrm{Cs,D1}}. \tag{3.19}$$

Notably, $\frac{1}{3}S_{FF'} = C^2_{FF'}$, where the factor 1/3 accounts for the fact that generally any polarisation only couples to one out of three atomic transitions. The $S_{FF'}$ are given in Table 3.4.

[1] For symmetry reasons we have $|\langle g|\hat{\boldsymbol{d}}|e\rangle|^2 = |\langle e|\hat{\boldsymbol{d}}|g\rangle|^2 \to |\boldsymbol{d}_{eg}|^2 = |\boldsymbol{d}_{ge}|^2$.

$S_{FF'}$	Value
S_{33}	$\frac{1}{4}$
S_{34}	$\frac{3}{4}$
S_{43}	$\frac{7}{12}$
S_{44}	$\frac{5}{12}$

Table 3.4: Cs relative transition strength factors for resonance fluorescence $S_{FF'}$ for the D_1 line [288].

Susceptibility and atomic response

In order to characterise the response of an atomic system to an applied electric field from a macroscopic point of view, including its linear and nonlinear behaviour, we consider the polarisation of the material system $\boldsymbol{P}$, defined as the dipole moment per unit volume. Its dependence on the strength of the applied optical field $\boldsymbol{E}$ is given as a power series of the form [89, 110, 296]

$$\boldsymbol{P}(t) = \epsilon_0[\boldsymbol{P}_0 + \chi^{(1)}\boldsymbol{E}(t) + \chi^{(2)}\boldsymbol{E}^2(t) + \chi^{(3)}\boldsymbol{E}^3(t) + \dots], \tag{3.20}$$

where the $\chi^{(i)}$ are the the first, second, and third order susceptibilities of the medium, ϵ_0 is the permittivity of free space, and P_0 is any initial polarisation present in the material (if present).
In linear optics, the series is truncated after the first order and one has (assuming $\boldsymbol{P}_0 = 0$)

$$\boldsymbol{P}(t) = \epsilon_0\chi^{(1)}\boldsymbol{E}(t). \tag{3.21}$$

This is valid for an isotropic material, where due to symmetry considerations, the polarisation $\boldsymbol{P}$ of the medium must be parallel to the electric field $\boldsymbol{E}$, and the susceptibility can therefore assumed to be a scalar. In this case, the susceptibility for a transition $|g\rangle \rightarrow |e\rangle$ as a function of the frequency ω can be shown to take the form [110]

$$\chi^{(1)}_{eg}(\omega) \simeq \sum_n \frac{N f_{eg} e^2}{\epsilon_0 m}\left[\frac{1}{\omega^2_{eg} - \omega^2 - 2i\omega_{eg}\gamma_{eg}}\right]. \tag{3.22}$$

Here, n is a sum index over the total number of atoms N, ω_{eg} corresponds to the transition frequency from state $|g\rangle$ to state $|e\rangle$, and the decay rate γ_{eg} includes the natural decay rates $\Gamma_{e,g}$ and other possible homogeneous decay rates ($\gamma_{\mathrm{col,i}}$, etc.) stemming from different

types of collisions that will be described in more detail in the next section[1]. Generally, for homogeneous linewidths (see Sec. 3.2.2) it holds

$$\gamma_{eg,\mathrm{hom}} = \frac{1}{2}(\Gamma_e + \Gamma_g) + \gamma_{\mathrm{col,i}} + \ldots \tag{3.23}$$

The combination of homogeneous and inhomogeneus linewidths is a bit more complex and will be discussed in Sec. 3.2.2.
We have further introduced the oscillator strength of the $|g\rangle \rightarrow |e\rangle$ transition, defined as

$$f_{eg} = \frac{2m\omega_{eg}|\hat{\boldsymbol{d}}_{eg}|^2}{3\hbar e^2}, \tag{3.24}$$

which obeys the sum rule given by $\sum_n f_{eg} = 1$[2]. The factor 1/3 includes the summation over all magnetic sublevels, as on average, only one third of the $|g\rangle \rightarrow |e\rangle$ Zeeman transitions will have a dipole moment parallel to the polarisation vector of the incident field, and thus contribute effectively to the susceptibility.

From the linear susceptibility, the refractive index $n(\omega)$ and the absorption coefficient $\alpha(\omega)$ of the material can be calculated. The refractive index is related to the linear dielectric constant $\epsilon^{(1)}(\omega)$ and to the linear susceptibility $\chi^{(1)}(\omega)$ through

$$n(\omega) = \sqrt{\epsilon^{(1)}(\omega)} = \sqrt{1 + \chi^{(1)}(\omega)} \approx 1 + \frac{1}{2}\chi^{(1)}(\omega). \tag{3.25}$$

The last approximation is made assuming that the medium is sufficiently dilute because N is sufficiently small, such that $\chi^{(1)} \ll 1$.
Considering the propagation of a plane wave given as

$$E(z,t) = E_0 e^{i(kz-\omega t)} + \text{c.c.}, \tag{3.26}$$

through a material system, with a propagation constant $k = n(\omega)\omega/c$, the intensity of the light $I = n(\omega)c\epsilon_0 \langle E(z,t)^2 \rangle$ varies as a function of position z in the medium as

$$I(z) = I_0 e^{-\alpha(\omega)z}, \tag{3.27}$$

with the absorption coefficient α given as

$$\alpha(\omega) = 2n''\omega/c, \tag{3.28}$$

[1] For symmetry reasons we can state $\omega_{ij} = \omega_{ji}$, $\gamma_{ij} = \gamma_{ji}$, etc.
[2] Here we are assuming the case of a non-degenerate ground state ($J = 0$) and ($J = 1$) excited state. For a more detailed description assuming degeneracy I refer to Refs. [288, 291].

and $n(\omega) = n' + in''$, separated into real $n' = \mathrm{Re}(n)$ and imaginary parts $n'' = \mathrm{Im}(n)$ of the refractive index. The absorption coefficient can also be written as a function of the susceptibility as

$$\alpha(\omega) = \chi^{(1)''}\omega/c, \tag{3.29}$$

where $\chi^{(1)}(\omega) = \chi^{(1)'} + i\chi^{(1)''}$. Inserting Eq. (3.22) one finds (for narrow resonances with respect to the atomic transition frequency)

$$\alpha \approx \sum_n \frac{f_{eg} N e^2}{2m\epsilon_0 c\gamma_{eg}} \left[\frac{\gamma_{eg}^2}{(\omega_{eg}-\omega)^2 + \gamma_{eg}^2}\right]. \tag{3.30}$$

The absorption of the atom thus shows the typical Lorentzian lineshape. Moreover, one can define the experimental optical depth $2d_{\mathrm{opt}}$ as the product of the length of the ensemble $z = L$ and the on-resonance probe absorption α as [297]

$$2d_{\mathrm{opt}} = \alpha L = \frac{N\omega|\boldsymbol{d}_{eg}|^2 L}{\epsilon_0 \hbar c \gamma_{eg}}. \tag{3.31}$$

The factor 2 comes from the fact that the above definition of the optical depth is twice the value used in the theoretical description of light storage in Λ-systems (see Sec. 3.3). For the number of atoms N, as we are interested only in the atoms present in the interaction region, and from a quantised picture of the light-field interaction, the quantisation volume enters the equations in the denominator, we can replace the total atom number using the atomic number density as $N \to n = N/V$, which can be calculated from the ideal gas law (Eq. (3.47)) knowing the temperature T and vapour pressure P_v of the considered atomic vapour.

3.2.2 Broadening mechanisms

In an atomic transition, the emitted light is not perfectly monochromatic. The shape of the emission or absorption line is described by the spectral lineshape function $f_\omega(\omega)$ [298]. The peak of the function is at the center frequency given by $\hbar\omega = E_2 - E_1$, with E_i being the energies of the initial and final levels. The lineshape is normalised as $\int_{-\infty}^{\infty} d\omega\, f_\omega(\omega) = 1$. The width of the of the spectral line is given by its full width at half maximum (FWHM) γ or its $1/e^2$ width $\Delta\omega$, depending on convention. Atomic transitions are subject to several different broadening mechanisms, such as lifetime (natural) broadening, collision (pressure) broadening and Doppler broadening. These mechanisms can be divided into homogeneous ones, which affect all the atoms in an ensemble in the same manner, and

inhomogeneous ones, affecting the atoms differently, so that each atom contributes to a different part of the spectrum. The former two, lifetime and collisional broadening correspond to the homogeneous processes, which give rise to a Lorentzian lineshape, while Doppler broadening is an inhomogeneous mechanism and produces a Gaussian lineshape. When considering different mechanisms that lead to the total line broadening, the total lineshape is given by the convolution of the single lineshapes. From the linearity of the convolution one has that convolving two Lorentzians yields a third Lorentzian lineshape with a FWHM given by the sum of the single FWHM of its components, $\gamma_{\text{conv}} = \gamma_1 + \gamma_2$. Convolving two Gaussian profiles again leads to a Gaussian profile with a $1/e^2$ Doppler width given as $\Delta\omega_{\text{conv}} = \sqrt{\Delta\omega_1^2 + \Delta\omega_2^2}$. The relation between the FWHM and the $1/e^2$ width of a Gaussian spectral line is

$$\gamma_{\text{FWHM}} = 2\sqrt{2\,\ln(2)}\Delta\omega_{1/e^2}. \tag{3.32}$$

The convolution of a Lorentzian $L(\omega)$ and a Gaussian lineshape $G(\omega)$ yields a composite lineshape given by a Voigt profile as

$$V_\omega(\omega) = \int_{-\infty}^{\infty} d\nu L(\nu)\, G(\omega + \omega_0 - \nu). \tag{3.33}$$

For the convoluted width of a Voigt profile including homogeneous (Lorentzian) and inhomogeneous (Gaussian) widths, no analytical expression exists. There are a large number of studies [299] attempting to determine increasingly better approximations for the Voigt width. For an experimental estimation of the total linewidth of the system, I will here use a very simple approximation from Ref. [300] given as

$$\gamma_V \approx \sqrt{\gamma_L^2 + \gamma_G^2}, \tag{3.34}$$

from which we then have

$$\gamma_{eg,\text{tot}} \approx \sqrt{\gamma_{eg,\text{hom}}^2 + \gamma_{\text{Dopp}}^2}. \tag{3.35}$$

Figure 3.3 shows the three different lineshapes, Gaussian and Lorentzian with equal width, and the resulting convoluted Voigt profile. The Gaussian lineshape falls to zero faster than the Lorentzian, but the latter is narrower at the peak. The Voigt profile combines both characteristics and is thus broader at the peak than the Lorentzian and Gaussian profiles, but falls slower to zero compared to the Gaussian profile.

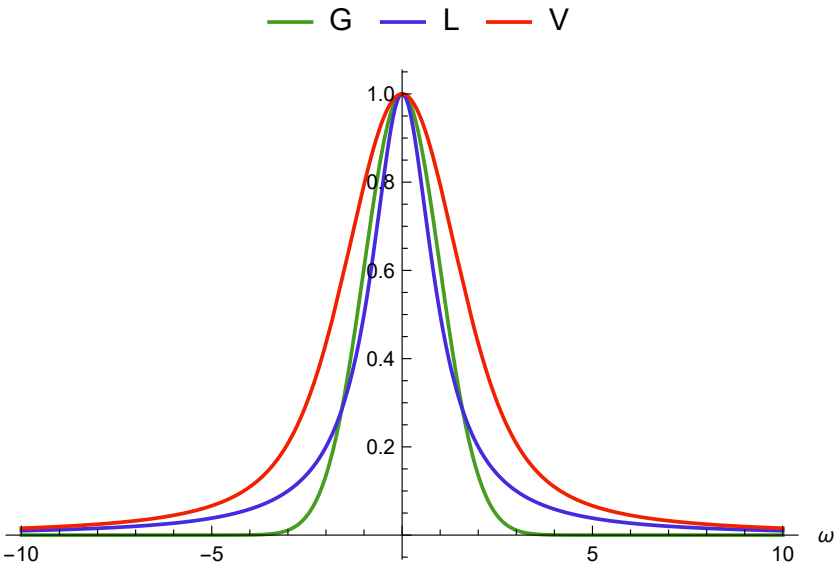

Figure 3.3: Normalised Gaussian (G, green), Lorentzian (L, blue), and Voigt (V, red) lineshapes. Here, the Gaussian width $\Delta\omega_G$ equals the Lorentzian width γ_L, and the Voigt profile results form the convolution of G and L.

Lifetime broadening

From the optical Bloch equations, describing the time evolution of the density operator (see Ref. [291]), we know that an atom in an excited state $|e\rangle$ will decay back into the ground state $|g\rangle$ by spontaneous emission. The rate at which this process occurs is given by the decay rate Γ_{eg} [298]

$$\Gamma_{eg} = \frac{e^2\omega_{eg}^3}{3\pi\epsilon_0\hbar c^3}\frac{1}{g_e}\sum_{m_g,m_e} |\langle e, m_e| r |g, m_g\rangle|^2, \tag{3.36}$$

where g_e is the degeneracy of state $|e\rangle$, which consists of a manifold of degenerate levels labelled by $m_{e,g}$. Its inverse determines the lifetime $\tau = 1/\Gamma_{eg}$ of the excited state. Because this lifetime is finite, this results in a broadening of the spectral line as a result of the time-energy uncertainty principle $\Delta E\Delta t \geq \hbar/2 \simeq \hbar$. With $\Delta t = \tau$, the broadening must satisfy

$$\Delta\omega = \frac{\Delta E}{\hbar} \gtrsim \frac{1}{\tau}. \tag{3.37}$$

The name natural broadening stems from the fact that it is intrinsic to the transition. The exact lineshape function can be derived by calculating the Fourier transform of an exponentially decaying light burst with time constant τ, and yields

$$f_\omega(\omega) = \frac{\Gamma}{2\pi} \frac{1}{(\omega - \omega_0)^2 + (\Gamma/2)^2}, \tag{3.38}$$

a Lorentzian with FWHM given by

$$\Gamma = \Gamma_{\text{nat}} = \frac{1}{\tau}. \tag{3.39}$$

This corresponds to the lineshape obtained for the absorption coeficient in Eq. (3.30).

Collisional broadening

In a vapour cell the contained atoms are constantly experiencing collisions with the cell walls and with other atoms. As a result, the light emission process of the atoms may be reduced and with it, the emission lifetime. When the mean time between collisions is shorter than the excited-state lifetime, this gives rise to an additional type of broadening. An estimate for the order of magnitude of the collision lifetime can be derived from the kinetic theory of gases and results in

$$\tau_{\text{col}} \sim \frac{1}{\sigma_{\text{col}} P} \left(\frac{\pi m k_B T}{8} \right)^{1/2}, \tag{3.40}$$

with σ_{col} being the collision cross-section, P the pressure, m the atomic mass, k_B the Boltzmann constant, and T the temperature of the gas. The dependence of the resulting FWHM $\gamma_{\text{col}} = 1/\tau_{\text{col}}$ on the pressure is the reason for the alternative name of pressure broadening. At standard temperature and pressure, typical collision lifetimes amount to $\tau_{\text{col}} \sim 10^{-10}$ s and are thus shorter than typical radiative lifetimes [11, 288]. More detailed information on collision types and rates will be given in Sec. 3.2.3.

Doppler broadening

The randomness of the atomic motion in a gas results in Doppler shifts in the observed frequencies, as atoms are moving towards or away from an observer. In the case an atom is moving towards (away) the reference frame of the observer with a velocity component v_z, the latter will measure a frequency Doppler shifted from the initial frequency ω_0 to

$$\omega = \omega_0 \left(1 \pm \frac{v_z}{c} \right), \tag{3.41}$$

where the the negative sign is for the case were the atoms are moving away. The Maxwell-Boltzmann distribution gives a measure for the number of atoms $N(v_z)dv_z$ with velocities between v_z and $v_z + dv_z$:

$$N(v_z) = N_0 \left(\frac{2k_BT}{\pi m}\right)^{1/2} \exp\left(-\frac{mv_z^2}{2k_BT}\right), \tag{3.42}$$

where N_0 is the total number of atoms. The Doppler lineshape thus results in a Gaussian lineshape

$$f_\omega(\omega) = \frac{c}{\omega_0}\sqrt{\frac{m}{2\pi k_BT}} \exp\left(-\frac{mc^2\left(\omega-\omega_0\right)^2}{2k_BT\omega_0^2}\right), \tag{3.43}$$

with FWHM given by

$$\gamma_{\text{Doppler}} = 2\omega_0\sqrt{\frac{(2\ln 2)\,k_BT}{mc^2}} = \frac{4\pi}{\lambda}\sqrt{\frac{(2\ln 2)\,k_BT}{m}}. \tag{3.44}$$

The magnitude of Doppler broadening at room temperature or in warm gases $\mathcal{O}(100-500\,\text{MHz})$ is generally much larger than the natural linewidth $\mathcal{O}(3-5\,\text{MHz})$, and is therefore generally the dominant broadening mechanism in these systems at low pressures $< 7.5-10\,\text{torr}$.

3.2.3 Optical pumping and lifetime-limiting mechanisms

Optical pumping

Optical pumping refers to one of the most important techniques used in atomic physics and quantum optics, that enables the preparation of atoms in specific states by utilising resonant light with different polarisations and frequencies [301, 302]. The resulting atomic polarisation can be quantified by detecting the intensity and polarisation of the emitted fluorescence light [116]. Standard pumping techniques involve orienting the spins of atoms by transferring photonic angular momentum to spin polarisation, aligning the spins along the direction of light propagation following atomic dipole interaction selection rules.
Specifically, the transfer of angular momentum from light to atoms follows dipole selection rules affecting the magnetic quantum number m_F (see Eq. (3.6)). For decay into possible ground states, all pathways conserving the angular momentum are possible. Specifically, π-polarised light, lacking angular momentum, allows only $\Delta m_F = 0$ transitions. Circularly polarised σ^+ light leads to $\Delta m_F = +1$ transitions, while σ^- light leads to $\Delta m_F = -1$ transitions [288]. Modelling optical pumping semiclassically using a rate equation model allows the calculation of pumping rates and efficiencies for specific transitions [177].

In the initial step, known as depopulation pumping, atoms are excited by a constant

resonant light field into an excited state $|e\rangle$. This is followed by decay into lower states through processes like spontaneous emission. This leads to the (re)population of either the initial state or another ground state, a dark state, which does not interact with the applied light field. If the atoms decay into this dark state they could theoretically remain there indefinitely, unless they are subject to external influences. The efficiency of the pumping process relies on factors such as pumping time and power, allowing for complete depopulation of a specific state with sufficient laser power and time. This process is applied in this work for the preparation of the atoms in a specific ground state before the memory interaction.

Despite the effectiveness of optical pumping, various dephasing processes, such as atomic collisions, interactions with vapour cell walls, drift of the atoms in and out of the interaction region of the laser, etc. [177] may lead to the repopulation of the initial state. In fact, almost perfect preparation of a specific hyperfine or Zeeman state is feasible, but the gradual deterioration of polarisation after a given relaxation time limits the lifetime or coherence time of the prepared state.

Lifetime-limiting mechanisms

As a result of optical pumping, memory interaction, or interaction with the environment, the population distribution between states, be it hyperfine states or Zeeman m_F states, is driven out of equilibrium. In the terminology of nuclear magnetic resonance (NMR), the lifetime of a population imbalance in the hyperfine states (diagonal elements of the density matrix, ρ_{ee} and ρ_{gg}) is called $T_1 = 1/\gamma_1$, the longitudinal relaxation time. As a reminder, the lifetime of a specific state denotes the time in which the population is reduced to $1/e \approx 37\%$ of the initially prepared population. This relaxation time T_1 is related to processes leading to energy loss in the system. Conversely, there are interactions with the environment where there is no net energy loss in the system, but which only cause the relative phases of the quantum states to become randomised or lost. This dephasing time, e.g., between different magnetic m_F sublevels, is known as the transversal relaxation time $T_2 = 1/\gamma_2$, and is related to the anti-diagonal elements of the density matrix (ρ_{eg} and ρ_{ge}). Here, one can differentiate between dephasing and decoherence mechanisms, where the former are considered to be reversible, while the latter are not. In this section we will have a closer look into the different relaxation, dephasing, and decoherence processes existent in warm atomic vapours, and into their calculation. The discussion mainly follows Ref. [177].

When dealing with warm atomic vapours, the aforementioned processes are caused

mainly by atomic motion and collisions between atoms, and are highly dependent on vapour pressure and temperature [303]. The main decoherence mechanism is considered to be the motion out of the interaction region with the laser. The associated broadening is referred to as transit time broadening. If only alkali atoms are present in the vapour cell, they will fly ballistically and collide with the cell walls, randomising their spin. Thus, unpumped atoms will enter the interaction region and pumped atoms will leave it, completely destroying the preparation. The mean velocity $\bar{v}$ of the atoms is $\sim 300\,\frac{\mathrm{m}}{\mathrm{s}}$[1], which in a large cell of a 2 cm diameter yields transit times across the whole cell of ca. 100 μs. The second main reason for spin decoherence or dephasing are various types of collisional processes. These can be divided into Cs-Cs collisions, collisions between Cs atoms and buffer gas atoms (if present) and Cs-wall collisions.

Different measures can be undertaken in order to reduce some of these effects. First, another atomic species is commonly added into the cell as a buffer gas. This turns the ballistic motion of the alkali atoms into a diffusive one, effectively causing the atoms to stay longer in the interaction region. As opposed to the case of ballistic motion, where for the transit time it holds $\Delta t_{\mathrm{transit}} \propto l$, the transit length l being, e.g., the laser beam size, in the diffusive case one has $\Delta t_{\mathrm{transit}} \propto l^2$, as in a random walk [304]. Typical buffer gases are N_2 and noble gases such as Ne, Ar or Xe. The addition of another atomic species naturally gives rise to interatomic collisions, which can also have a negative effect on polarisation and lead to further relaxation effects. However, this effect is generally much smaller than polarisation changes due to Cs-Cs collisions.

In order to model diffusion, from a two dimensional model (Fick's law) one can estimate the time it takes the atoms to diffuse out of the interaction region. The radial diffusion length Δr is given as [305]

$$\Delta r = \sqrt{4D\Delta t}, \tag{3.45}$$

where D is the diffusion constant and Δt is the transit or diffusion time. The motion can be considered to be diffusive, if the size of the interaction volume is much larger than the Cs mean free path ℓ, introduced below in Eq. (3.52). The diffusion constant D can be estimated mathematically as [177]

$$D = \frac{1}{3}\ell\bar{v}_{\mathrm{Cs,bg}} = \frac{1}{n_{\mathrm{bg}}\sigma_{\mathrm{total}}}\sqrt{\frac{8k_BT}{9\pi m_{\mathrm{Cs}}}}, \tag{3.46}$$

[1] e.g., $\bar{v} = 326\,\frac{\mathrm{m}}{\mathrm{s}}$ for Cs at $T = 60°\mathrm{C}$.

where n_{bg} is the buffer gas number density, which can be determined from temperature and pressure using the ideal gas law as

$$n_{\mathrm{bg}} = \frac{P}{k_B T}. \tag{3.47}$$

Moreover, σ_{total} is the total cross section for all collisional effects, which has been measured in several atomic physics experiments and can be found in the literature [306], and m_{Cs} is the Cs atomic mass. The value of the diffusion constant is however generally extracted from experiments. In the literature one can find a value D_0, which corresponds to the diffusion constant measured at the reference pressure $P_0 = 1\,\mathrm{atm}$, and a specific reference temperature T_0. Values of D_0 and the corresponding measurement temperature T_0 for various candidates of buffer gases are listed in Table 3.5. From this value one can calculate the diffusion constant D at given temperature and pressure values T, P. The dependence is given by the formula [307]

$$D = D_0 \frac{P_0}{P} \left(\frac{T}{T_0}\right)^{\kappa}, \tag{3.48}$$

where $\kappa = 3/2$ [308] and P can be calculated from the buffer gas pressure at filling time as $P = P_{\mathrm{fill}} T_0 / T_{\mathrm{fill}}$ [177, 288]. If a combination of buffer gases is used, the total diffusion constant is given as $1/D_{\mathrm{tot}} = \sum_i 1/D_i$, where the D_i are the diffusion constants corresponding to each buffer gas species.

As a further measure to reduce spin decoherence or dephasing, anti-relaxation coatings made of materials that prevent the change of spin in collisions, can be added to the cell walls from the inside. Common coatings are paraffin or long hydrocarbon-chain-based materials [314]. These coatings are however very hard to apply and not many people possess the needed expertise, making these complicated to obtain commercially [177]. In this work, the addition of a buffer gas is assumed to be enough to reduce the effect of spin randomisation due to wall collisions, but for future work both measures applied together, as is commonly done in the literature, see Refs. [185, 186], will likely lead to better results.

Now let us turn to the description of the relevant collisional processes. The resulting total rate for all collisional mechanisms is the sum of the rates of the contributing mechanisms

$$\gamma_{1,2} = \gamma_{\mathrm{Cs}1,2} + \gamma_{\mathrm{bg}1,2} + \gamma_{\mathrm{wall}}, \tag{3.49}$$

where γ_{Cs} is the Cs-Cs total collision rate, γ_{bg} is the relaxation rate due to Cs-buffer-gas

Species	D_0 ($\frac{\text{cm}^2}{\text{s}}$)	T_0 (°C)	Ref.
He	0.370	26	[309]
	0.315	15	[308]
	0.204	0	[310]
Ne	0.200	20	[311]
	0.240	26	[309]
	0.185	15	[308]
	0.350	40	[180]
	0.153	0	[310]
Ar	0.190	26	[309]
	0.120	15	[308]
	0.134	0	[310]
Kr	0.138	30	[312]
Xe*	0.048	0	[313]
N_2	0.106	15	[308]
	0.240	40	[180]
	0.073	0	[310]

Table 3.5: Diffusion constants D_0 of Cs for different buffer gases and the corresponding measurement temperature T_0. *Value for Xe is calculated theoretically.

collisions, and γ_{wall} corresponds to the relaxation rate due to collisions with the cell walls [300]. Here, the subscripts $1, 2$ refer to the T_1, T_2 relaxation types [177, 315, 316]. The rate γ_{wall} is assumed to be the same for both longitudinal and transverse relaxation. In two-level systems it holds that $T_2 \leq 2T_1$, but the bound is slightly lower in multilevel systems [177, 315].

In general, the calculation of the collision rate between a Cs atom and a second species S_2 (subscript 2 stands for second species, either another Cs atom or a buffer gas atom) is given as [177]

$$\gamma_{\text{col}} = n_{S_2}(T)\sigma\bar{v}_{\text{Cs},S_2}, \tag{3.50}$$

where $n_{S_2}(T)$ is the atomic number density of species S_2 at a temperature T of the vapour, and σ is the collisional cross-section for the given interaction, which is determined

Species	σ_{tot} (cm^2)
Cs	$2.24 \cdot 10^{-13}$
He	$2.81 \cdot 10^{-14}$
Ne	$3.32 \cdot 10^{-14}$
Ar	$7.15 \cdot 10^{-14}$
Kr	$1.10 \cdot 10^{-13}$
Xe	$1.35 \cdot 10^{-13}$
N_2	$8.86 \cdot 10^{-14}$

Table 3.6: Total collision cross sections σ_{tot} for Cs with different atomic (molecular) species generally used as buffer gases. The total cross sections are calculated from the data in [306]. In that work, several values for σ_{tot} determined with varying experimental conditions are given. The value given here is calculated as the mean of all the noted values, as an approximation.

experimentally and can be found in the literature. As an example, the total collision cross sections σ_{tot} for Cs with different noble gases and other species are given in Table 3.6. $\bar{v}_{\text{Cs,S}_2}$ denotes the mean relative velocity of the Cs and S_2 atoms and is given as

$$\bar{v}_{\text{Cs,S}_2} = \sqrt{\frac{8k_BT}{\pi\mu}} \quad \text{with} \quad \mu = \frac{m_{\text{Cs}}m_{\text{S}_2}}{m_{\text{Cs}} + m_{\text{S}_2}}. \tag{3.51}$$

Here μ is the reduced mass of the atomic pair. The temperature dependence does not only appear in the mean velocity. γ_{col} and σ can also be temperature and/or pressure-dependent. For a detailed model of such effects, I refer the reader to Ref. [177]. The mean free path between collisions is given as

$$\ell = \frac{1}{n_{\text{S}_2}\sigma\sqrt{m_{\text{Cs}}/\mu}}. \tag{3.52}$$

Let us now review the most important collision types and their effects, starting with Cs-Cs collisions, and then turning to Cs-buffer-gas collisions. Among the Cs-Cs collisions, the spin-exchange (SE) mechanism tends to be the most relevant one. As mentioned above, it is highly dependent on temperature. As the name indicates, in such a collision the partners exchange their spin under conservation of the total angular momentum, i.e., the total m_F value, but not necessarily the F value [317]. Although the underlying mechanisms of SE are not completely understood, one can determine the rates using Eq. (3.50) with

the corresponding cross section σ_{SE} and the Cs number density at a given temperature $n_{\mathrm{Cs}}(T)$. The latter is taken from Ref. [318] where a phenomenological formula is given:

$$n_{\mathrm{Cs}}(T) = n_0 \frac{T_0}{T} e^{b(1-T_0/T)}, \tag{3.53}$$

where $n_0 = 10^{10}\,1/\mathrm{cm}^3$, $T_0 = 283.12\,\mathrm{K}$, and $b = 32.523$ are experimental parameters. The resulting number density is approximated with a $\pm 5\%$ accuracy. Methods to reduce or minimise SE include optically pumping the atoms to the stretched states ($|F = 4, m_F = \pm 4\rangle$ in Cs), as these are somewhat protected from SE relaxation due to m_F conservation [177]. However, as some population will always remain in other m_F states, SE cannot be completely eliminated in this way. There are special techniques in magnetometry which can be of aid, such as SERF (spin exchange relaxation free), where strong magnetic fields and high atomic densities are used [319]. SE can also be an advantage when trying to polarise gases which are not easily polarised, such as noble gases. This technique is known as SEOP (spin exchange optical pumping) and is also widely employed in magnetometry [319].

Another relevant effect among Cs-Cs collisions is given by dipole-dipole interactions leading to broadening of the optical lines. For the Cs D_1 line this broadening, also called self-broadening, is given as

$$\gamma_{\text{Cs-Cs,dip}} = \beta_{\mathrm{Cs}} n_{\mathrm{Cs}}. \tag{3.54}$$

Values for β_{Cs} can be found, e.g., in Ref. [320].
Further types of mechanisms exist in Cs-Cs collisions, notably spin-destruction effects, in which m_F is randomised and not conserved. As the rate of this mechanism is much lower than the SE rate by several orders of magnitude, we will not consider it further.

When turning to Cs-buffer-gas collisions the relevant interactions are the hyperfine shift interaction, resulting from electronic and nuclear wavefunction overlap, and the spin-rotation interaction, where the Cs spin couples to the angular momentum of the colliding pair. The latter is the most relevant mechanism leading to hyperfine spin relaxation caused by the buffer gas. These types of interactions are the ones leading to pressure broadening, as introduced in Sec. 3.2.2. In Ref. [321], experimental values for the pressure broadening rate per pressure $\alpha_p(T_0)$ of different noble gases and relevant molecules for the Cs D lines are measured at specific temperatures. From this value, the rate at the actual cell temperature and pressure can be calculated as

$$\gamma_{\mathrm{bg}}(T) = \alpha_p(T_0) P_{\mathrm{bg}} \left(\frac{T_0}{T}\right)^{1/2}, \tag{3.55}$$

where $P_{\mathrm{bg}} =$ is the buffer gas pressure. This gives another method for calculating pressure broadening rates independently of Eq. (3.50).

Finally, it is important to mention radiation trapping and quenching, relevant effects occurring in vapour cells, which help to determine the best choice of buffer gas atoms. Radiation trapping refers to the effect that occurs in ensembles with a high optical depth, where excited atoms, e.g., due to optical pumping, emit a photon with an unfavourable frequency (e.g., the signal frequency), which is reabsorbed by another atom before it manages to fly out of the vapour cell. This unwanted effect lowers the pumping efficiency. A solution for this problem stems from quenching, an effect where the excited Cs atoms are able to decay back to the ground state by exciting internal molecular states of the quenching gas in collisions, thus hindering optical decay. Quenching collisions are thus inelastic and lead to energy loss. They are therefore related to T_1 relaxation. The used quenching gases should ideally also be good buffer gases. Most generally N_2, with a quenching cross section $\sigma_{Q,N_2} = 7.70 \cdot 10^{-15}\,\mathrm{cm}^2$ [322], is used as a quenching gas, as it presents internal vibrational states near to the alkali optical transitions. The quenching rate γ_Q is given by Eq. (3.50), with the corresponding number density of quenching atoms n_Q, the quenching cross-section σ_Q, and the mean relative velocity between a Cs atom and the quenching gas $\bar{v}_{\mathrm{rel}}$ (see Eq. (3.51)) [177]. The probability for a Cs atom to decay from an optically excited state emitting a photon is then given as

$$Q = \frac{1}{1 + \gamma_Q/\Gamma_{\mathrm{nat}}}. \tag{3.56}$$

The quenching cross sections of Cs with noble gases are negligible, compared to σ_{Q,N_2}. However, some of these gases lead to larger diffusion times of the Cs atoms out of the interaction region, compared to N_2, which makes the use of a combination of N_2 and a noble gas as buffer gases a good choice.

3.2.4 The three-level atom

The physics of atomic systems becomes much more interesting by adding a third level to the model of the atoms. The presence of two optical fields in such system gives rise to many interesting linear and non-linear effects [89, 296, 323]. We will here constrain the discussion to electromagnetically induced transparency (EIT), as it is the memory

protocol used in this work. The relevant noise processes in our memory, such as FWM and SRS, are also effects arising due to the interaction of one or two laser fields in three-level atoms. These will be discussed later on in Sec. 3.4.

Electromagnetically induced transparency

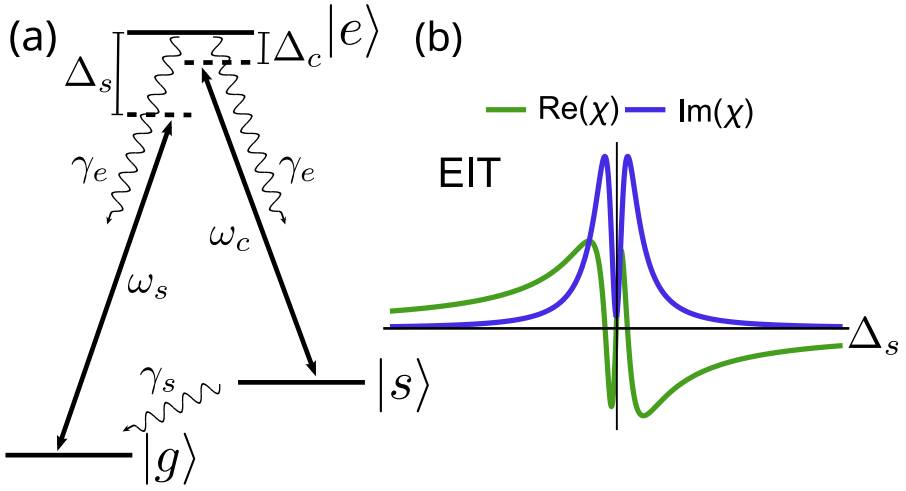

Figure 3.4: (a) Three level Λ-system for EIT description. (b) Real and imaginary parts of the linear susceptibility $\chi^{(1)}$ in the EIT case calculated using Eq. (3.66) by setting the prefactor $\frac{n|\boldsymbol{d}_{eg}|^2}{\epsilon_0\hbar} = 1$. Used parameters are $\Omega_c = 500\,\text{MHz}$, $\gamma_e = 500\,\text{MHz}$, $\gamma_s = 100\,\text{kHz}$, and $\Delta_c = 0$.

As was already introduced in Sec. 2.4.2, EIT is a nonlinear effect by which a normally absorbing medium is rendered transparent for a weaker signal field by the presence of another much stronger control laser field. The signal field, which can be quantum or classical in nature, is slowed down extremely in this process, and can even be brought to a halt inside the medium, thus allowing its storage for a given amount of time. We will begin the description with a static picture, which is enough to explain the effect of slow light in atomic vapours. For the storage of light pulses, a dynamic EIT picture is necessary. Here we will only shortly mention the framework of dark-state polaritons. The full theoretical description of light storage in a three-level Λ-system, valid not only for EIT but also for related protocols, will be treated in more detail in a separate section (Sec. 3.3).

There are several ways to describe the EIT process mathematically. We will first motivate the effect from a simplified dark-state picture resulting from the Stark shift that a strong

control field causes in a three-level system. Due to two-photon resonance, this control field mediates the absorption of a weaker signal field.
We consider the case of a Λ-system with two long-lived ground states $|g\rangle$ and $|s\rangle$, sharing a common excited state $|e\rangle$, and two laser fields, a weak signal field with frequency ω_s coupling the states $|g\rangle$ and $|e\rangle$, and a strong classical control field with frequency ω_c coupling $|s\rangle$ and $|e\rangle$, as depicted in Fig. 3.4 (a). Due to the presence of the control field, a transparency window appears in the absorption profile of the signal field (Fig. 3.4 (b)). The transparency window arises as a result of an interference between the probability amplitudes for two different absorption pathways simultaneously excited by the two resonant light fields. As the control field is much stronger than the signal field, the longer pathway is equally probable. This creates a quantum interference, making the state $|e\rangle$ a dark state.

Recalling the framework of the dipole approximation, the atom-field interaction Hamiltonian $\hat{H}_{\mathrm{AF}} = \hat{\boldsymbol{d}} \cdot \boldsymbol{E}$ is generally expressed in terms of the Rabi frequency of the system, given as $\Omega = \langle g|\hat{d}_z|e\rangle\, E_0/\hbar$, with E_0 representing the amplitude of the electric field $\boldsymbol{E}$, and $\langle g|\hat{d}_z|e\rangle$ the electronic transition dipole matrix element. Using the RWA, the interaction Hamiltonian of a three-level atom interacting with a signal field with Rabi frequency Ω_s and a strong control field with Rabi frequency Ω_c reads [270, 323]

$$\hat{H}_{\mathrm{AF}} = -\frac{\hbar}{2}\begin{bmatrix} 0 & 0 & \Omega_s \\ 0 & -2(\Delta_s - \Delta_c) & \Omega_c \\ \Omega_s & \Omega_c & -2\Delta_s \end{bmatrix}, \tag{3.57}$$

where $\Delta_s = \omega_s - \omega_{eg}$, $\Delta_c = \omega_c - \omega_{es}$ are the detunings of the laser fields from the respective atomic transitions, as depicted in Fig. 3.4 (a). The detunings are chosen such that a red detuning from resonance is negative, while a blue detuning is positive.

The solution of the stationary Schrödinger equation yields the eigenstates of the system, which can be expressed in terms of two so-called mixing angles θ and ϕ, dependent on the Rabi frequencies and the single-photon (Δ_s) and two-photon ($\delta = \Delta_s - \Delta_c$) detunings. For the case of two-photon resonance ($\delta = 0$), these mixing angles are given as

$$\tan\theta = \frac{\Omega_s}{\Omega_c} \tag{3.58}$$

$$\tan 2\phi = \frac{\sqrt{\Omega_s^2 + \Omega_c^2}}{\Delta_s}. \tag{3.59}$$

The corresponding eigenstates then take the form

$$|+\rangle = \sin\theta \sin\phi \,|g\rangle + \cos\phi \,|e\rangle + \cos\theta \sin\phi \,|s\rangle \tag{3.60}$$

$$|\,0\,\rangle = \cos\theta \,|g\rangle - \sin\theta \,|s\rangle \tag{3.61}$$

$$|-\rangle = \sin\theta \cos\phi \,|g\rangle - \sin\phi \,|e\rangle + \cos\theta \cos\phi \,|s\rangle \,. \tag{3.62}$$

The calculation of the eigenvalues leads to a zero energy for the $|\,0\,\rangle$ state, while the energies of the $|\pm\rangle$ states are shifted by a value

$$\hbar\omega^{\pm} = \frac{\hbar}{2}\left(\Delta_s \pm \sqrt{\Delta_s^2 + \Omega_s^2 + \Omega_c^2}\right). \tag{3.63}$$

By looking at Eqs. (3.60) - (3.62), we see that while the $|\pm\rangle$ states contain contributions from all the bare atomic states, there is no contribution of state $|e\rangle$ in $|\,0\,\rangle$. This means that if the atom is pumped or decays into $|\,0\,\rangle$, it cannot be excited by any means. $|\,0\,\rangle$ is thus a so-called dark state of the system, where the population remains trapped. This is also known as coherent population trapping (CPT) [324].
Given the case of a weak signal field, $\Omega_s \ll \Omega_c$, one obtains $\sin\theta \to 0$ and $\cos\theta \to 1$, yielding $|\,0\,\rangle \to |g\rangle$, the ground state of the system, from which excitation does not take place any more.
In the limit $\Delta_s = 0$, when the fields are on resonance, one obtains $\tan\phi \to 1$, i.e., $(\phi = \pi/2)$, and the dressed EIT states become

$$|+\rangle = \frac{1}{\sqrt{2}}(|s\rangle + |e\rangle), \tag{3.64}$$

$$|-\rangle = \frac{1}{\sqrt{2}}(|s\rangle - |e\rangle). \tag{3.65}$$

Thus, the excited state splits into two states with equal contribution from $|s\rangle$ and $|e\rangle$. Although the original absorption peak is not yet split into two peaks, as it occurs in the Autler-Townes limit (see Ch. 2), it shows precisely the characteristic transparency window of EIT.

From a more detailed derivation in a density matrix framework, one obtains for the linear susceptibility in a three level system [110]

$$\chi^{(1)} = \frac{n|\boldsymbol{d}_{eg}|^2}{\epsilon_0\hbar} \frac{(\Delta_s - \Delta_c) + i\gamma_s}{|\Omega_c|^2 - (\Delta_s + i\gamma_e)\left[(\Delta_s - \Delta_c) + i\gamma_s\right]}, \tag{3.66}$$

where we have replaced N with n, $\gamma_{eg} \to \gamma_e = \frac{1}{2}\Gamma_e + \gamma_{\text{col}}$[1], assumed $\Gamma_g = 0$, and introduced the dephasing $\gamma_s = \gamma_{s,\text{col}}$ from state $|s\rangle$ to state $|g\rangle$. This means all possible decay channels,

[1] and possibly convoluted with γ_{Dopp}.

radiative or collisional, and possible dephasing mechanisms are included into the total decay rate of the excited state into state $|g\rangle$. As for the decay rate γ_s, it only includes dephasing, since radiative decay is forbidden by selection rules of the dipole operator. Generally, in dilute media, it holds that $\gamma_e \gg \gamma_s$. For EIT to be observable in warm atomic systems, it further must hold that the control field satisfies $|\Omega_c|^2 \gg \gamma_e\gamma_s$. Even in the presence of Doppler broadening, a coherent effect like EIT will still be observable, given the former condition. This fact results from the copropagating nature of both light fields, which ensures that the differential Doppler shift is small compared to the control Rabi frequency $\gamma_{\text{Dopp}} \ll \Omega_c$.
In the resonant limit with $\Delta_s = \Delta_c = 0$ the above expression simplifies to

$$\chi^{(1)} = \frac{n|\boldsymbol{d}_{eg}|^2}{\epsilon_0\hbar}\frac{i\gamma_s}{|\Omega_c|^2 + \gamma_e\gamma_s}, \tag{3.67}$$

which is purely imaginary, resulting in vanishing absorption.
Dividing Eq. (3.66) into its real $\chi^{(1)'}$ and imaginary $\chi^{(1)''}$ components we obtain

$$\chi^{(1)'} = \frac{n|\boldsymbol{d}_{eg}|^2}{\epsilon_0\hbar}\frac{\delta\left[|\Omega_c|^2 + \delta(\gamma_e\gamma_s - \Delta_s)\right] - \gamma_s\left[\gamma_e\delta - \gamma_s\Delta_s\right]}{\left[|\Omega_c|^2 - \Delta_s\delta + \gamma_e\gamma_s\right]^2 + \left[\gamma_e\delta + \gamma_s\Delta_s\right]^2} \tag{3.68}$$

$$\chi^{(1)''} = \frac{n|\boldsymbol{d}_{eg}|^2}{\epsilon_0\hbar}\frac{\delta\left[\gamma_e\delta - \gamma_s\Delta_s\right] + \gamma_s\left[|\Omega_c|^2 + \delta(\gamma_e\gamma_s - \Delta_s)\right]}{\left[|\Omega_c|^2 - \Delta_s\delta + \gamma_e\gamma_s\right]^2 + \left[\gamma_e\delta + \gamma_s\Delta_s\right]^2}. \tag{3.69}$$

The real and imaginary parts of the susceptibility $\chi^{(1)}$ are depicted in Fig. 3.4 (b). $\text{Im}(\chi^{(1)}) = \chi^{(1)''}$ shows the characteristic transparency window. The refractive index can again be written as $n = n' + in'' = \sqrt{1+\chi^{(1)}}$. The linear dispersion of the refractive index $dn/d\omega_s$ is positive and is related to a reduction of the group velocity in the medium according to [323]

$$v_g = \frac{d\omega_s}{dk_s} = \frac{c}{n' + \omega_s\frac{dn'}{d\omega}\Big|_{\omega_s}}. \tag{3.70}$$

In the resonant case one has $n' = \sqrt{1+\chi^{(1)'}} = 1$ and the group velocity results in

$$v_g = \frac{c}{1+n_g(z)} \text{ with } n_g = \frac{2d_{\text{opt}}}{L}\frac{\gamma_e c}{|\Omega_c|^2}, \tag{3.71}$$

where n_g is the group refractive index, d_{opt} is the the optical depth of the medium (see Eq. (3.31)), L its length, and c the vacuum speed of light. The amplitude of the transmitted light through the medium, with $T = \frac{I(z)}{I_0}$ (see Eq. 3.27) can be expressed as

[270, 323]

$$T(\omega_s, z) = \exp\left(\frac{-ik_s\chi^{(1)}z}{2}\right), \tag{3.72}$$

k_s being the propagation vector of the light. From an expansion of $\chi^{(1)''}$ around the point of maximum transmission ($\Delta_s = 1 - (\gamma_s/\gamma_e)\Delta_c$) [268], we obtain [266]

$$T(\omega_s, L) \approx \exp\left(-\frac{(\omega - \omega_s)^2}{\Delta\omega_{\mathrm{EIT}}^2}\right), \tag{3.73}$$

a Gaussian with a $(1/e^2)$ width given by

$$\Delta\omega_{\mathrm{EIT}} = \frac{\Omega_c^2}{\gamma_e}\frac{1}{\sqrt{2d_{\mathrm{opt}}}}. \tag{3.74}$$

If the bandwidth of the signal pulse lies within the transparency window, the pulse will be delayed with only little absorption while propagating through the medium. The group delay is given as [269]

$$\tau_D = \frac{L}{v_g} = 2d_{\mathrm{opt}}\frac{\gamma_e}{|\Omega_c|^2}. \tag{3.75}$$

This means the intensity of the control field determines the group velocity of the signal field by dictating the spectral width of the transparency window. A stronger control field results in less group delay. Thus, by adiabatically ramping down the control field one can control the dynamics of the signal pulse with minimal losses. When the control field vanishes, the signal group velocity will vanish too, effectively stopping the pulse inside the medium and storing it. The complete description of this effect has to be performed in a dynamic picture for which there exist several frameworks. We will choose the one by Gorshkov et al. [123–125, 240, 241], described in detail in Sec. 3.3. Another possible framework are so-called dark-state polaritons, as introduced by M. Fleischhauer and M.D. Lukin [266, 325]. For these models, a semiclasical treatment of light-matter interaction is no longer sufficient, as we are generally dealing with the storage of single photons, or few-photon pulses. Therefore, a quantised model of, at least, the signal field becomes necessary. Slow-light propagation is now described by quasi-particles called dark-state polaritons $\Psi(z,t)$. These are a combination of photonic modes $\mathcal{E}(z,t)$ and ensemble spin coherence or spinwave modes $S(z,t)$, and are written as [269]

$$\Psi(z,t) = \cos(\vartheta)\mathcal{E}(z,t) - \sin(\vartheta)S(z,t), \tag{3.76}$$

with the mixing angle ϑ given as

$$\cos(\vartheta) = \frac{\Omega_c}{\sqrt{\Omega_c^2 + g^2 N}} = \sqrt{\frac{v_g}{c}}. \tag{3.77}$$

Here, g is the atom-field coupling constant, also known as one-photon Rabi frequency, obtained in the quantisation of the electromagnetic field (e.g., Jaynes–Cummings model [291]), and equals

$$g = |\boldsymbol{d}_{eg}| \sqrt{\frac{\omega_s}{2\epsilon_0 \hbar V}} = \sqrt{\frac{d_{\mathrm{opt}} \gamma_e c}{NLV}}, \tag{3.78}$$

where V denotes the quantisation volume[1]. Within this description, the stored light pulse can be simply described as a dark-state polariton completely turned into an ensemble spin coherence with $\cos(\vartheta) = 0$ by adiabatically turning off the control field ($\Omega_c = 0$) once the pulse is inside the EIT medium. The pulse is then stored for a time fundamentally limited by the spin coherence time of the medium ($T_2 = 1/\gamma_s$). The spinwave can be converted back into a slowly propagating photonic mode and then released from the medium by switching the control field on again ($\Omega_c \neq 0, \rightarrow \cos(\vartheta) \neq 0$).

3.3 Description of light storage in a Λ-system

After having presented the concept of static EIT in the previous section, which gives rise to the phenomenon of slow light, this section will introduce the underlying theoretical model for light storage in a three-level Λ-system used throughout this thesis. This model is valid to describe the full dynamical picture leading to EIT storage, but it further yields a theory that encompasses all protocols used in Λ-systems, adiabatic or fast, as explained in Ch. 2, Sec. 2.4. The derivation presented here closely follows Refs. [124, 125, 326].

We consider an ensemble of length L and cross-section A containing $N = \int_0^L dz\, n'(z)$ Λ-type three-level atoms interacting with a classical field and a copropagating quantum field. Here, $n'(z)$ is the number of atoms per unit length. Within the interaction volume, the concentration of atoms in the transverse direction of the ensemble is assumed to be uniform. The three-level Λ-system coupled by the corresponding fields is presented in Figure 3.5.
Only quantum electromagnetic field modes with a single transverse profile are assumed to be excited. Furthermore, the quantum and classical fields are assumed to be narrowband

[1] Here we see the quantisation volume V entering the equations. Thus, as stated above, the substitution $N \rightarrow n$ is valid for the calculations of susceptibility, absorption, and optical depth, as now the volume will cancel out.

and centred at $\omega_s = \omega_{eg} - \Delta_s$ and $\omega_c = \omega_{es} - \Delta_c$, with ω_{eg} and ω_{es} being the respective atomic transition frequencies. For simplicity, we assume $\Delta_s = \Delta_c = \Delta$. The quantum field is described by a slowly varying operator $\hat{\mathcal{E}}(z,t)$ and the classical field is represented by the Rabi frequency envelope $\Omega(z,t) = \Omega(t - z/c)$.
For the analysis, the reabsorption of spontaneously emitted photons is neglected, as we are only interested in the storage of single- or few-photon pulses. Therefore, there will be at most a few spontaneously emitted photons. The probability for an emission onto the mode $\hat{\mathcal{E}}$ is given by the corresponding far field solid angle $\sim \lambda^2/A \sim d_{\text{opt}}/N$, where A is the cross section area of the quantum field and the atomic medium, $\lambda = 2\pi c/\omega_s$ is the wavelength of the quantum field, and $d_{\text{opt}} \sim \lambda^2 N/A$ corresponds to the resonant optical depth of the ensemble. Although in an optically thick medium these emitted photons could be reabsorbed and reemitted, this probability is very small in most experiments.
For the following treatment, a one-dimensional approximation is used. This yields a good approximation in the case that the control beam is much wider than the signal field (single mode of the quantum field). As a result, the transverse profile of the control beam can be considered constant.

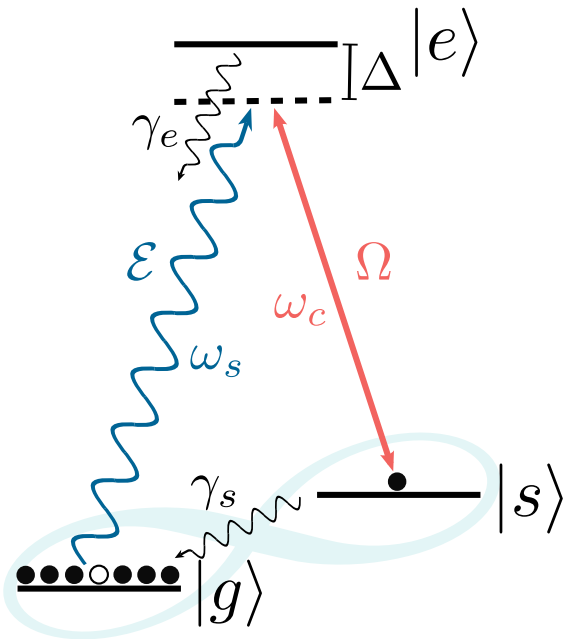

Figure 3.5: Three-level Λ-system for light storage of a quantised signal field $\mathcal{E}$ mediated by a strong control field Ω. After the storage, the ground states $|g\rangle$ and $|s\rangle$ form a spatially distributed long-lived coherence (light blue), the spinwave.

Before diving into the specific model, a discussion about the relevant figure of merit used

to characterise the performance of the memory is given from a mathematical point of view. This yields more detail to the definition given in Chapter 2.
Assuming the incoming mode consists of a single incoming photon in a known spatiotemporal mode denoted as $\mathcal{E}_{\text{in}}(t)$ (or, in the case of calculating the retrieval efficiency alone, a single excitation in a known atomic spinwave mode), the efficiency η of all the mappings considered (be it storage alone, retrieval alone, or storage followed by retrieval) is defined as the probability to find the excitation in the appropriate (photonic or atomic) output mode after the interaction.
For all considered interactions, the full evolution results in a passive beam-splitter-like transformation of the type

$$\hat{b}_j = \sum_k U_{jk} \hat{a}_k, \tag{3.79}$$

where $\hat{b}_j$ and $\hat{a}_k$ denote the annihilation operators for all the output and input modes, respectively (including all photonic, spinwave, and Langevin noise operators), with commutation relations $[\hat{a}_j, \hat{a}_k^\dagger] = [\hat{b}_j, \hat{b}_k^\dagger] = \delta_{jk}$. The matrix U has to be unitary in order to preserve the commutation relations. The mapping from a certain input mode $\hat{a}_0$ to an output mode $\hat{b}_0$ with efficiency η is therefore described by $\hat{b}_0 = \sqrt{\eta}\hat{a}_0 + \sqrt{1-\eta}\hat{c}$, where $\hat{c}$ satisfies $[\hat{c}, \hat{c}^\dagger] = 1$ and represents some linear combination of all other input modes orthogonal to $\hat{a}_0$. If all input modes other than $\hat{a}_0$ are in the vacuum state, then η completely characterises the mapping, as will be shown later in more detail.
If, for instance, the mode to be stored is in an entangled state with some other system $(|0\rangle_{\hat{a}_0}|x\rangle + |1\rangle_{\hat{a}_0}|y\rangle)/2$, where $|0\rangle_{\hat{a}_0}$ and $|1\rangle_{\hat{a}_0}$ are the zero- and one-photon Fock states of the input mode, and $|x\rangle$ and $|y\rangle$ are two orthonormal states of the other system, the fidelity of the entangled state after the mapping is easily found to be $F = (1+\eta)/2$. In the description of the model it will be shown why in most experimental situations it is reasonable to assume that the incoming noise included in $\hat{c}$ is vacuum noise, e.g., noise related to the zero-point fluctuations of the electromagnetic field.

The starting point for the derivation of the Maxwell-Bloch equations of motion is the electric field, whose quantum field vector operator is given by

$$\hat{\boldsymbol{E}}_s(z) = \boldsymbol{\epsilon}_s \left(\frac{\hbar\omega_s}{4\pi c\epsilon_0 A}\right)^{1/2} \int d\omega \hat{a}_\omega e^{i\omega z/c} + \text{h.c.}, \tag{3.80}$$

where h.c. stands for the hermitian conjugate. The continuum of annihilation operators $\hat{a}_\omega$, one for each field mode of different frequency ω, satisfy the commutation relations

$$[\hat{a}_\omega, \hat{a}^\dagger_{\omega'}] = \delta(\omega - \omega'). \tag{3.81}$$

The field modes corresponding to $\hat{a}_\omega$ for different ω have, by assumption, the same transverse profile and are nonempty around $\omega = \omega_s$. Since, as will be shown, the final equations will only depend on the optical depth d_{opt} of the ensemble and not on the specific cross section A, the precise definition of A, if it covers the whole ensemble or only the interaction region with the beams, and the number of atoms N are irrelevant.
The copropagating classical control field vector is given as

$$\boldsymbol{E}_c(z,t) = \boldsymbol{\epsilon}_c\, \mathcal{E}_c(t - z/c)\, \cos[\omega_c(t - z/c)], \tag{3.82}$$

a plane wave with polarisation unit vector $\boldsymbol{\epsilon}_c$ and carrier frequency ω_c modulated by an envelope $\mathcal{E}_c(t - z/c)$, assumed to be propagating with group velocity equal to the speed of light c. This results from the fact that almost all the atoms are assumed to be in $|g\rangle$, and thus do not alter the propagation of the strong classical field coupled to the $|s\rangle \to |e\rangle$ transition.
In the dipole and rotating wave approximations (RWA), the Hamiltonian of the system is given as

$$\hat{H} = \hat{H}_{\text{A}} + \hat{H}_{\text{AF}}, \tag{3.83}$$

where

$$\hat{H}_{\text{A}} = \int d\omega\, \hbar\omega\, \hat{a}^\dagger_\omega \hat{a}_\omega + \sum_{i=1}^{N} (\hbar\omega_{es} \hat{\sigma}^i_{ss} + \hbar\omega_{eg} \hat{\sigma}^i_{ee}), \tag{3.84}$$

$$\begin{aligned} \hat{H}_{\text{AF}} = & -\hbar \sum_{i=1}^{N} \Bigg(\Omega(t - z_i/c)\, \hat{\sigma}^i_{es} e^{-i\omega_c(t - z_i/c)} \\ & + g \sqrt{\frac{L}{2\pi c}} \int d\omega\, \hat{a}_\omega e^{i\omega z_i/c}\, \hat{\sigma}^i_{eg} + \text{h.c.} \Bigg). \end{aligned} \tag{3.85}$$

Here, $\hat{\sigma}^i_{\mu\nu} = |\mu\rangle_{i\,i}\langle\nu|$ represents the internal state operator of the ith atom between states $|\mu\rangle$ and $|\nu\rangle$, z_i is the position of the ith atom, $\hat{\boldsymbol{d}}$ is the dipole moment vector operator, $\Omega(t - z/c) = \langle e|\boldsymbol{\epsilon}_c \hat{\boldsymbol{d}}|s\rangle\, \mathcal{E}_c(t - z/c)/(2\hbar)$ is the Rabi frequency of the classical control field, and $g = \langle e|\boldsymbol{\epsilon}_s \hat{\boldsymbol{d}}|g\rangle \sqrt{\frac{\omega_s}{2\hbar\epsilon_0 AL}}$ (assumed to be real for simplicity) is the coupling constant between the atoms and the quantised field mode. The quantisation length of the quantisation volume has here been chosen to be identical to the ensemble length, which does not affect the obtained results. The Rabi frequency here is defined as half of the traditional (experimental) definition, such that here a π-pulse takes time $\pi/(2\Omega)$.

Although the length of the ensemble does not affect the results, the position dependence along it is of relevance. The ensemble is thus divided into slices along the length $0 \leq z \leq L$ and slowly varying operators are introduced

$$\hat{\sigma}_{\mu\mu}(z,t) = \frac{1}{N_z}\sum_{i=1}^{N_z}\hat{\sigma}^i_{\mu\mu}(t), \tag{3.86}$$

$$\hat{\sigma}_{es}(z,t) = \frac{1}{N_z}\sum_{i=1}^{N_z}\hat{\sigma}^i_{es}(t)e^{-i\omega_c(t-z_i/c)}, \tag{3.87}$$

$$\hat{\sigma}_{eg}(z,t) = \frac{1}{N_z}\sum_{i=1}^{N_z}\hat{\sigma}^i_{eg}(t)e^{-i\omega_s(t-z_i/c)}, \tag{3.88}$$

$$\hat{\sigma}_{sg}(z,t) = \frac{1}{N_z}\sum_{i=1}^{N_z}\hat{\sigma}^i_{sg}(t)e^{-i(\omega_s-\omega_c)(t-z_i/c)}, \tag{3.89}$$

$$\hat{\mathcal{E}}(z,t) = \sqrt{\frac{L}{2\pi c}}\,e^{i\omega_s(t-z/c)}\int d\omega \hat{a}_\omega(t)e^{i\omega z/c}, \tag{3.90}$$

where the sums go over all N_z atoms in a slice of the ensemble positioned at z, thick enough to contain $N_z \gg 1$, but thin enough that the resulting collective fields can be considered continuous. The normalisation of $\hat{\mathcal{E}}$ is chosen so that it is dimensionless. For these slow-varying operators, the effective Hamiltonian results in

$$\begin{aligned}\hat{\tilde{H}} = &\int d\omega \hbar\omega\, \hat{a}^\dagger_\omega \hat{a}_\omega - \hbar\omega_s \frac{1}{L}\int_0^L dz \mathcal{E}^\dagger(z,t)\mathcal{E}(z,t) + \int_0^L dz \hbar n'(z) \\ &\times \{\Delta\hat{\sigma}_{ee}(z,t) - [\Omega(t-z/c)\hat{\sigma}_{es}(z,t) + g\,\hat{\mathcal{E}}(z,t)\,\hat{\sigma}_{eg}(z,t) + \text{h.c.}]\},\end{aligned} \tag{3.91}$$

and the same-time commutation relations are

$$\begin{aligned}[\hat{\sigma}_{\mu\nu}(z,t), \hat{\sigma}_{\alpha\beta}(z',t)] = &\frac{1}{n'(z)}[\delta_{\nu\alpha}\hat{\sigma}_{\mu\beta}(z,t) - \delta_{\mu\beta}\hat{\sigma}_{\alpha\nu}(z,t)] \\ &\times \delta(z-z'),\end{aligned} \tag{3.92}$$

$$[\hat{\mathcal{E}}(z,t), \hat{\mathcal{E}}^\dagger(z',t)] = L\,\delta(z-z'). \tag{3.93}$$

Defining the (dimensionless) polarisation operator $\hat{P}(z,t) = \sqrt{N}\hat{\sigma}_{eg}(z,t)$ and the (dimensionless) spinwave operator $\hat{S}(z,t) = \sqrt{N}\hat{\sigma}_{sg}(z,t)$, in the dipole and RWA approximations, to first order in $\hat{\mathcal{E}}$, and assuming that almost all atoms are in the ground state $|g\rangle$ at all times, and thus $\hat{\sigma}_{gg} \approx 1$ (due to normalisation) and $\hat{\sigma}_{ee} \approx \hat{\sigma}_{ss} \approx \hat{\sigma}_{es} \approx 0$, the Heisenberg equations of motion are given as

$$(\partial_t + c\partial_z)\hat{\mathcal{E}} = ig\sqrt{N}\hat{P}n'(z)L/N, \tag{3.94}$$

$$\partial_t \hat{P} = -(\gamma_e + i\Delta)\hat{P} + ig\sqrt{N}\hat{\mathcal{E}} + i\Omega\hat{S} + \sqrt{2\gamma_e}\hat{F}_P, \tag{3.95}$$

$$\partial_t \hat{S} = -\gamma_s\hat{S} + i\Omega^*\hat{P} + \sqrt{2\gamma_s}\hat{F}_S, \tag{3.96}$$

where the spinwave decay rate γ_s, the polarisation decay rate γ_e, which may include extra dephasing in addition to radiative decay resulting from, e.g., collisions with buffer gas atoms in warm vapour cells, and the corresponding Langevin noise operators $\hat{F}_P(z,t)$ and $\hat{F}_S(z,t)$ are introduced. Ω^* is the complex conjugate of the Rabi frequency (which is however generally assumed to be real). In turn, the spinwave decay rate γ_s may result from, e.g., diffusion of the atoms out of the interaction region of the quantised light mode, among other effects such as collisions leading to dephasing, etc. (see Sec. 3.2.3). As a result of collective enhancement [325], the atom-field coupling constant g (assumed real for simplicity) is increased by a factor of $\sqrt{N}$ up to $g\sqrt{N}$. In the case that there might be a population redistribution between the states $|g\rangle$ and $|s\rangle$, it has to be ensured that the corresponding resulting noise is vacuum, as is needed for the following analysis. If diffusing atoms are entering the interaction region, they will be assumed to be already pumped into the level $|g\rangle$, which experimentally is the case if the (pump) and control beam diameters are much larger than the diameter of the quantised light mode.

Turning to the Langevin noise operator, from the generalised Einstein relations [296, 327] one obtains

$$\begin{aligned}\langle \hat{F}_{\mu\nu}(t), \hat{F}^\dagger_{\alpha\beta}(t')\rangle = \langle & D(\hat{\sigma}_{\mu\nu}\hat{\sigma}_{\alpha\beta}) - D(\hat{\sigma}_{\mu\nu})\hat{\sigma}_{\alpha\beta} \\ & - \hat{\sigma}_{\mu\nu}D(\hat{\sigma}_{\alpha\beta})\rangle\, \delta(t-t'),\end{aligned} \tag{3.97}$$

where $D(\hat{\sigma}_{\mu\nu})$ stands for the deterministic part, i.e., the part of Eqs. (3.94) - (3.96) excluding noise. Again, making use of the approximation that almost all atoms are in the ground state, one finds that the only non-vanishing noise correlations between $\hat{F}_P$, $\hat{F}_S$, $\hat{F}^\dagger_P$, and $\hat{F}^\dagger_S$ are [327]

$$\langle \hat{F}_P(z,t), \hat{F}^\dagger_P(z',t')\rangle = \frac{N}{n'(z)}\,\delta(z-z')\delta(t-t'), \tag{3.98}$$

$$\langle \hat{F}_S(z,t), \hat{F}^\dagger_S(z',t')\rangle = \frac{N}{n'(z)}\,\delta(z-z')\delta(t-t'). \tag{3.99}$$

The normally ordered noise correlations $\hat{F}_P$ and $\hat{F}_S$ vanish under reasonable experimental conditions [124]. This translates to the fact that the incoming noise is vacuum noise, and thus the efficiency is the only number required to completely characterise the mapping. This fact results from the absence of decay from state $|g\rangle$ into states $|e\rangle$ and $|s\rangle$. Decay into $|e\rangle$ does not happen because the energy of the optical transition $\mathcal{O}(10^4\,\mathrm{K})$ is much greater than the temperature at which experiments are typically done. However, the energy of the $|s\rangle \to |g\rangle$ transition may be smaller than the temperature in some experiments. Since this transition is typically not dipole allowed, the decay rate of $|g\rangle$ into $|s\rangle$ can be neglected as well. As mentioned before, for the case where atoms are diffusing in and out of the interaction region, i.e., the quantised light mode, in order to keep the decay rate of $|g\rangle$ zero, all incoming atoms are assumed to be fully pumped into $|g\rangle$ (see Sec. 3.2.3).
The field and atomic operators are now expanded in terms of modes. Initially, no atomic excitations are present (all atoms are supposed to be in the ground state $|g\rangle$). Under this assumption, the commutation relations (3.92) imply

$$[\hat{S}(z,t), \hat{S}^\dagger(z',t)] = \frac{N}{n'(z)}\,\delta(z-z'), \tag{3.100}$$

$$[\hat{P}(z,t), \hat{P}^\dagger(z',t)] = \frac{N}{n'(z)}\,\delta(z-z'). \tag{3.101}$$

From Eq. (3.100), $\hat{S}(z,t)$ can be expanded in terms of any basis set of spatial modes $\{g_\alpha(z)\}$ that satisfy the orthonormality relation $\int_0^L dz\, g_\alpha^*(z) g_\beta(z) = \delta_{\alpha\beta}$ and the completeness relation $\sum_\alpha g_\alpha^*(z) g_\alpha(z') = \delta(z-z')$ as

$$\hat{S}(z,t) = \sqrt{\frac{N}{n'(z)}} \sum_\alpha g_\alpha(z)\hat{c}_\alpha(t), \tag{3.102}$$

where the annihilation operators $\{\hat{c}_\alpha\}$ for the spinwave modes satisfy

$$[\hat{c}_\alpha(t), \hat{c}_\beta^\dagger(t)] = \delta_{\alpha\beta}. \tag{3.103}$$

The commutation relations applying to the freely propagating input field $\hat{\mathcal{E}}_{\mathrm{in}}(t) = \hat{\mathcal{E}}(0,t)$ and the output field $\hat{\mathcal{E}}_{\mathrm{out}}(t) = \hat{\mathcal{E}}(L,t)$ are

$$[\hat{\mathcal{E}}_{\mathrm{in}}(t), \hat{\mathcal{E}}_{\mathrm{in}}^\dagger(t')] = \frac{L}{c}\,\delta(t-t'), \tag{3.104}$$

$$[\hat{\mathcal{E}}_{\mathrm{out}}(t), \hat{\mathcal{E}}_{\mathrm{out}}^\dagger(t')] = \frac{L}{c}\,\delta(t-t'). \tag{3.105}$$

From the above, one can expand the input and output fields in terms of a basis set of field envelope modes $\{h_\alpha(t)\}$ defined in the interval $t \in [0, \infty)$, satisfying the orthonormality relation $\int_0^\infty dt\, h_\alpha^*(t) h_\beta(t) = \delta_{\alpha\beta}$ and the completeness relation $\sum_\alpha h_\alpha^*(t) h_\alpha(t') = \delta(t - t')$ as

$$\hat{\mathcal{E}}_{\text{in}}(t) = \sqrt{\frac{L}{c}} \sum_\alpha h_\alpha(t) \hat{a}_\alpha, \tag{3.106}$$

$$\hat{\mathcal{E}}_{\text{out}}(t) = \sqrt{\frac{L}{c}} \sum_\alpha h_\alpha(t) \hat{b}_\alpha, \tag{3.107}$$

where the annihilation operators $\{\hat{a}_\alpha\}$ and $\{\hat{b}_\alpha\}$ satisfy the usual bosonic commutation relations

$$[\hat{a}_\alpha, \hat{a}_\beta^\dagger] = [\hat{b}_\alpha, \hat{b}_\beta^\dagger] = \delta_{\alpha\beta}. \tag{3.108}$$

Initially, as stated, no $\hat{P}$ or $\hat{S}$ excitations are present in the atomic system, as all atoms are pumped into the ground state. The only present input excitation is thus assumed to be the quantum field mode with annihilation operator $\hat{a}_0$ corresponding to an envelope shape $h_0(t)$ nonzero on $[0, T]$. Thus, photon storage and retrieval refers to the mapping of this incoming mode $h_0(T)$ onto some mode $\hat{S}$, and the retrieval of it at a later time $T_r > T$ onto an outgoing field mode. Only the parts proportional to $\hat{a}_0$ will then contribute to the efficiency. This reduces the equations and the problem to complex number equations. The storage efficiency η_s is given as the ratio of the number of stored excitations to the number of incoming photons

$$\eta_s = \frac{\displaystyle\int_0^L dz \frac{n'(z)}{N} \langle \hat{S}^\dagger(z, T) \hat{S}(z, T) \rangle}{\displaystyle\frac{c}{L} \int_0^L dt \langle \hat{\mathcal{E}}^\dagger(0, t) \hat{\mathcal{E}}(0, t) \rangle}, \tag{3.109}$$

where one can ignore the noise operators $\hat{F}_P$ and $\hat{F}_S$ in Eqs. (3.94) - (3.96) and treat the operators as complex numbers describing the shapes of quantum modes. Transformation into a comoving frame with $t' = t - z/c$, introducing a dimensionless time $\tilde{t} = \gamma_e t'$, a dimensionless rescaled spatial coordinate $\tilde{z} = \int_0^z dz'\, n'(z')/N$, and absorbing a factor $\sqrt{c/(L\gamma_e)}$ into the definition of $\mathcal{E}$, reduces Eqs. (3.94) - (3.96) to

$$\partial_{\tilde{z}}\mathcal{E} = i\sqrt{d_{\text{opt}}}P, \tag{3.110}$$

$$\partial_{\tilde{t}}P = -(1+i\tilde{\Delta})P + i\sqrt{d_{\text{opt}}}\mathcal{E} + i\tilde{\Omega}(\tilde{t})S, \tag{3.111}$$

$$\partial_{\tilde{t}}S = i\tilde{\Omega}^*(\tilde{t})P, \tag{3.112}$$

where the optical depth is given by $d_{\text{opt}} = g^2NL/(\gamma_e c)$ and $\tilde{\Delta} = \Delta/\gamma_e$ and $\tilde{\Omega} = \Omega/\gamma_e$. The optical depth d_{opt} is independent of the beam sizes and depends only on the density and length of the ensemble for a given transition. This fact results from inserting the definition of g into d_{opt} and defining the atomic number density $n(z) = n'(z)/A$, assuming a uniform field in the direction transverse to the propagation direction. The expression for the optical depth then becomes

$$d_{\text{opt}} = |\langle e|\boldsymbol{\epsilon}_s\hat{\boldsymbol{d}}|g\rangle|^2\,\omega_s \int dz \frac{n(z)}{2\hbar\epsilon_0\gamma_e c}, \tag{3.113}$$

which is indeed independent of the beam size and, for a given transition, depends only on the density and length of the ensemble.
The definition of d_{opt} is related to the intensity attenuation of a resonant probe in a three-level system without control field, yielding an attenuation of $e^{-2d_{\text{opt}}}$. For the derivation of the above equations (3.110) - (3.112), the decay of the spinwave γ_s is neglected. Non-vanishing, but slow decay γ_s will introduce an exponential decay without making the solution harder [124].

The boundary conditions for storage are given by $\mathcal{E}(\tilde{z}=0,\tilde{t}) = \mathcal{E}_{\text{in}}(\tilde{t})$, $P(\tilde{z},\tilde{t}=0) = 0$, and $S(\tilde{z},\tilde{t}=0) = 0$, where $\mathcal{E}_{\text{in}}(\tilde{t})$ is nonzero for $\tilde{t}\in[0,\tilde{T}]$ (with $\tilde{T} = T\gamma_e$), and is normalised to $\int_0^{\tilde{T}} d\tilde{t}|\mathcal{E}_{\text{in}}(\tilde{t})|^2 = 1$. The spinwave mode onto which the excitation is stored is given by $S(\tilde{z},\tilde{T})$. The storage efficiency thus reduces to

$$\eta_s = \int_0^1 d\tilde{z}|S(\tilde{z},\tilde{T})|^2. \tag{3.114}$$

Losses during the storage process result from the decay γ_e and imperfect storage resulting in 'leakage' $\mathcal{E}(\tilde{z}=1,\tilde{t})$. At the time of retrieval $\tilde{T}_r > \tilde{T}$ (with $\tilde{T}_r = T_r\gamma_e$), the stored mode is to be mapped onto an outgoing mode, either in the forward or in the backward direction, i.e., with the control pulse coming from the right. In this thesis we mainly focus on forward retrieval. The corresponding boundary conditions are $S(\tilde{z},\tilde{T}_r) = S(\tilde{z},\tilde{T})$, $\mathcal{E}(\tilde{z}=0,\tilde{t}) = 0$, and $P(\tilde{z}=0,\tilde{T}_r) = 0$. If the spinwave is renormalised before retrieval, the retrieval efficiency is given by

$$\eta_r = \int_{\tilde{T}_r}^{\infty} d\tilde{t} |\mathcal{E}(1,\tilde{t})|^2. \tag{3.115}$$

If no normalisation is performed, then the above equation describes the total retrieval efficiency $\eta_{\text{tot}} = \eta_s \eta_r$.

In Ref. [125], an analytically calculated upper limit for the total efficiency in the case of storage followed by backward retrieval is given as

$$\eta_{\text{tot}}^{\text{bw}} \approx 1 - \frac{5.8}{d_{\text{opt}}}, \tag{3.116}$$

which is said to be valid as $d_{\text{opt}} \to \infty$. $\eta_{\text{tot}}^{\text{bw}}$ is higher than the achievable $\eta_{\text{tot}}^{\text{fw}}$ of storage followed by forward retrieval. This stems from the fact that for optimal backward retrieval, storage and retrieval are each separately optimal. Moreover, in forward retrieval it is more problematic to minimise propagation and the associated losses, since the whole excitation has to propagate through the entire medium before being read out. This is generally not the case for backward retrieval, as, at least for EIT conditions, the spinwave tends to build up rather at the beginning of the cell (see Ch. 4, Fig. 4.30 (a3)). This equation yields a theoretical maximal limit for the experimentally achievable efficiency of an EIT-like memory, given the optical depth of the system.

3.3.1 Control pulse optimisation

The main results of the analytical treatment presented in Ref. [123] and extended in the subsequent series of works [124, 125, 240, 241], is that there is a certain degree of equivalence between several different photon storage protocols, and that, provided there exists a sufficient degree of control over the shape of the incoming photon wave packet and over the used classical control pulse, all considered types of protocols yield the same achievable efficiency, which is only dependent of the optical depth d_{opt} of the system. In Refs. [124, 125], general results of efficiency optimisation are presented in certain physical limits, such as the adiabatic and the fast limits, where exact analytical solutions exist. However, it is necessary to have methods for solving the above presented problem in previously inaccessible regimes. These methods fall into the category of optimal control problems, for which powerful numerical optimisation methods are available. In Ref. [241], exactly these methods are applied to the problem of photon storage in atomic media. This subsection follows the discussion presented there. In many experiments, the attainable optical depths are low ($d_{\text{opt}} \sim 10$) as a result of experimental imperfections

comprising competing effects such as FWM, inhomogeneous broadening of the lines, or spatially varying light shifts, among others [241, 328]. Therefore, the obtained efficiencies are not very high ($\ll 50\%$) and thus, optimisation of the storage and retrieval processes becomes relevant. This optimisation can be performed in many different ways. The chosen method in the theoretical analysis is a numerical iterative method with respect to a set of control parameters, which are updated to yield a higher photon storage efficiency at each iteration. The concrete technique used is a simple gradient ascent method. The optimisation is performed with respect to the storage control field, although retrieval optimisation or input-signal-field optimisation are also possible, and are treated as well in the mentioned references.

The case of resonant photon storage in a homogeneously broadened atomic ensemble with negligible spinwave decay γ_s is chosen as a starting point. In a free-space case (as opposed to the cavity models also discussed in [124, 241]), there is access to different spinwave modes, thus turning the retrieval efficiency dependent on how storage is performed. Therefore, storage optimisation alone will not necessarily be sufficient, as will be discussed below.
Starting from the equations of motion (3.110) - (3.112) and assuming the incoming signal and control fields are real, one obtains

$$\partial_{\tilde{z}}\mathcal{E}(\tilde{z},\tilde{t}) = i\sqrt{d_{\mathrm{opt}}}P(\tilde{z},\tilde{t}), \tag{3.117}$$

$$\partial_{\tilde{t}}P(\tilde{z},\tilde{t}) = -(1+i\tilde{\Delta})P(\tilde{z},\tilde{t}) + i\sqrt{d_{\mathrm{opt}}}\mathcal{E}(\tilde{z},\tilde{t}) + i\tilde{\Omega}(\tilde{t})S(\tilde{z},\tilde{t}), \tag{3.118}$$

$$\partial_{\tilde{t}}S(\tilde{z},\tilde{t}) = i\tilde{\Omega}(\tilde{t})P(\tilde{z},\tilde{t}), \tag{3.119}$$

with initial boundary conditions

$$\mathcal{E}(0,\tilde{t}) = \mathcal{E}_{\mathrm{in}}(\tilde{t}), \tag{3.120}$$

$$P(\tilde{z},0) = 0, \tag{3.121}$$

$$S(\tilde{z},0) = 0. \tag{3.122}$$

Again, the equations are written in dimensionless variables, time and Rabi frequency are rescaled by γ_e, as $\tilde{\Omega} = \Omega/\gamma_e$ and $\tilde{t} = \gamma_e t$, and the position is rescaled by the length of the ensemble $\tilde{z} = z/L$. Furthermore, the input mode $\mathcal{E}_{\mathrm{in}}(\tilde{t})$ satisfies the normalisation constraint $\int_0^{\tilde{T}} d\tilde{t}\,|\mathcal{E}_{\mathrm{in}}(\tilde{t})|^2 = 1$.
The goal is to maximise the storage efficiency η_s in Eq. (3.114) with respect to $\tilde{\Omega}(\tilde{t})$.

Since this optimisation is constrained by the equations of motion (3.117) - (3.119), Lagrange multipliers $\bar{\mathcal{E}}(\tilde{z},\tilde{t})$, $\bar{P}(\tilde{z},\tilde{t})$, and $\bar{S}(\tilde{z},\tilde{t})$ are introduced to ensure that these equations are fulfilled. Thus, the problem converts into an unconstrained maximisation of

$$\begin{aligned} J = & \int_0^1 d\tilde{z}\, S(\tilde{z},\tilde{T})S^*(\tilde{z},\tilde{T}) \\ & + \int_0^T d\tilde{t} \int_0^1 d\tilde{z}\, \{\bar{\mathcal{E}}^*[-\partial_{\tilde{z}}\mathcal{E} + i\sqrt{d_{\text{opt}}}P] + \text{c.c}\} \\ & + \int_0^T d\tilde{t} \int_0^1 d\tilde{z}\, \{\bar{P}^*[-(\partial_{\tilde{t}} + 1 + i\tilde{\Delta})P + i\tilde{\Omega}(\tilde{t})S + i\sqrt{d_{\text{opt}}}\mathcal{E}] + \text{c.c.}\} \\ & + \int_0^T d\tilde{t} \int_0^1 d\tilde{z}\, \{\bar{S}^*[-\partial_{\tilde{t}}S + i\tilde{\Omega}(\tilde{t})P] + \text{c.c}\}, \end{aligned} \tag{3.123}$$

where the time and space dependence has been dropped for conciseness.
Finding the optimum requires that J is stationary with respect to any variation in $\mathcal{E}$, P, S and Ω. This requires the Lagrange multipliers to satisfy the equations of motion. These adjoint equations for the Lagrange multipliers are then given as

$$\partial_{\tilde{z}}\bar{\mathcal{E}}(\tilde{z},\tilde{t}) = i\sqrt{d_{\text{opt}}}\bar{P}(\tilde{z},\tilde{t}), \tag{3.124}$$

$$\partial_{\tilde{t}}\bar{P}(\tilde{z},\tilde{t}) = (1 + i\tilde{\Delta})\bar{P}(\tilde{z},\tilde{t}) + i\sqrt{d_{\text{opt}}}\bar{\mathcal{E}}(\tilde{z},\tilde{t}) + i\tilde{\Omega}(\tilde{t})\bar{S}(\tilde{z},\tilde{t}), \tag{3.125}$$

$$\partial_{\tilde{t}}\bar{S}(\tilde{z},\tilde{t}) = i\tilde{\Omega}(\tilde{t})\bar{P}(\tilde{z},\tilde{t}), \tag{3.126}$$

with initial boundary conditions

$$\bar{\mathcal{E}}(1,\tilde{t}) = 0, \tag{3.127}$$

$$\bar{P}(\tilde{z},\tilde{T}) = 0, \tag{3.128}$$

$$\bar{S}(\tilde{z},\tilde{T}) = S(\tilde{z},\tilde{T}). \tag{3.129}$$

These equations describe the process of backward retrieval and provide a mathematical connection between time reversal and optimality. In order to move up along the gradient, the control field should be optimised as

$$\tilde{\Omega}(\tilde{t}) \to \tilde{\Omega}(\tilde{t}) - \frac{1}{\lambda}\int_0^1 d\tilde{z}\, \text{Im}[\bar{S}^*(\tilde{z},\tilde{t})P(\tilde{z},\tilde{t}) - \bar{P}(\tilde{z},\tilde{t})S^*(\tilde{z},\tilde{t})]. \tag{3.130}$$

It is discussed in Ref. [125], that in the case of forward retrieval, which is the one we focus on in this thesis, the control field that maximises the storage efficiency does not generally

maximise the total efficiency of storage followed by retrieval. Thus, in order to maximise the total efficiency of storage followed by retrieval with respect to the storage control field, the following approach has to be taken.

We suppose the control pulse consists of a storage control pulse at time $\tilde{t} \in [0, T]$ and a retrieval control pulse at time $\tilde{t} \in [T_r, T_f]$, where T_r stands for the retrieval time and T_f stands for the final time. The optimisation is performed with respect to the storage control pulse given the retrieval pulse and the incoming input mode. It is noted in Ref. [241] that for sufficiently strong retrieval control pulses, the total efficiency is independent of the retrieval control pulse. Therefore, the optimisation with respect to the retrieval pulse can generally be ignored. For the different times $0 < T \leq T_r < T_f$ holds, and the time interval $[T, T_r]$ corresponds to the storage time in the memory which starts when the storage process is finished and ends when the retrieval process begins.

Suppose storage is described by Eqs. (3.117) - (3.122) on $\tilde{t} \in [0, T]$. Then, forward retrieval (which follows after the storage time interval $[T, T_r]$) is described by the same equations (3.117) - (3.119) but on the time interval $\tilde{t} \in [T_r, T_f]$ with initial and boundary conditions

$$\mathcal{E}(0, \tilde{t}) = 0, \tag{3.131}$$

$$P(\tilde{z}, \tilde{T}_r) = 0, \tag{3.132}$$

$$S(\tilde{z}, \tilde{T}_r) = S(\tilde{z}, \tilde{T}), \tag{3.133}$$

with $\tilde{T}_r = \gamma_e T_r$ and $\tilde{T}_f = \gamma_e T_f$. For Eq. (3.132) it is assumed that the polarisation has sufficient time to decay before the retrieval process begins, and Eq. (3.133) assumes that the spinwave decay is negligible during storage time.

The goal is to maximise the total efficiency of storage followed by forward retrieval,

$$\eta_{\text{tot}} = \int_{\tilde{T}_r}^{\tilde{T}_f} d\tilde{t} |\mathcal{E}(1, \tilde{t})|^2, \tag{3.134}$$

with respect to the storage control field. Constructing J and taking the corresponding variations, as before, one obtains the initial and boundary conditions for the Lagrange multipliers

$$\bar{\mathcal{E}}(1, \tilde{t}) = \mathcal{E}(1, \tilde{t}) \quad \text{for} \quad \tilde{t} \in [\tilde{T}_r, \tilde{T}_f], \tag{3.135}$$

$$\bar{P}(\tilde{z}, \tilde{T}_f) = 0, \tag{3.136}$$

$$\bar{S}(\tilde{z}, \tilde{T}_f) = 0, \tag{3.137}$$

and

$$\bar{\mathcal{E}}(1,\tilde{t}) = 0 \quad \text{for} \quad \tilde{t} \in [0,\tilde{T}], \tag{3.138}$$

$$\bar{P}(\tilde{z},\tilde{T}) = 0, \tag{3.139}$$

$$\bar{S}(\tilde{z},\tilde{T}) = \bar{S}(\tilde{z},\tilde{T}_r). \tag{3.140}$$

When taking the variational derivative of J with respect to $\tilde{\Omega}(\tilde{t})$, one finds that the update corresponds exactly to the update for the storage optimisation alone, and can be performed using Eq. (3.130). The extension of the former problem to include backward instead of forward retrieval, complex Ω and $\mathcal{E}_{\text{in}}$, nonzero γ_s, and inhomogeneous broadening (see Ref. [240]) is, in Gorshkov's words, trivial[1].

3.4 Noise in atomic vapour memories

In quantum storage the preservation of the fidelity of the stored state by the memory device is fundamental. Thus, any spurious noise photons which are added to the retrieved signal in the storage and retrieval processes pose a significant problem.

There exist various different noise sources in warm vapour memories, which will be described in detail in this section. The first type of noise that will be considered is what we call technical noise. In Raman and EIT Λ-memories it is of high importance to be able to filter out the strong control field from the readout signal. For this, three different filtering procedures can be employed, namely polarisation, spatial, and spectral filtering. As a rough estimation, if we take the Cs D_1 line and use the $|F=3\rangle \rightarrow |F'=3\rangle$ transition with a frequency of $\omega_s = 2\pi \cdot 335.120563\,\text{THz}$ as the signal transition and the $|F=4\rangle \rightarrow |F'=3\rangle$ transition with a frequency of $\omega_c = 2\pi \cdot 335.111370\,\text{THz}$ as the control transition, a signal photon has an approximate energy of $E = \hbar\omega_s = 2.221 \cdot 10^{-19}\,\text{J·s}$ [288]. Assuming a signal pulse width of $\Delta t_s = 50\,\text{ns}$ FWHM, the resulting power of a signal photon amounts to $4.44 \cdot 10^{-12}\,\text{W} \sim 10\,\text{pW}$. Typical control pulse powers for these experiments lie between $P_{\text{C}} \in [10\,\text{mW} - 100\,\text{mW}]$. Thus, between 9 and 10 orders of magnitude control-field suppression (or higher) are necessary to filter out a single photon from the strong control field.

In Λ-type memories, signal and control fields are typically orthogonally polarised, such that polarising beam splitters (PBS) or more elaborate polarising optics such as Wollaston

[1] As a reminder to the reader, when a scientist says something is trivial, it almost always turns out to be exactly the opposite.

or calcite prisms can be used in order to separate the beams. Attenuations of $70 - 80\,\mathrm{dB}$ can be achieved in this manner.
A second option is to make use of spatial filtering, meaning introducing a small angle θ between the signal and control beams. This works very well in ladder schemes, where signal and control are counterpropagating. However, this turns out to be problematic in warm vapour memories using a Λ-scheme, as it causes perturbations on the phase of the spinwave, leading to fluctuations and decoherence, and thus reducing the storage time of the memory [119]. The lifetime of this dephasing process can be estimated from the time it takes the atoms in the vapour to cross $\frac{1}{2\pi}$ of the wavelength λ of the spinwave (see Eq. (2.1)). This yields a lifetime of $\tau_D \sim (\lambda/2\pi v_z)$, where $v_z = \sqrt{k_B T/m}$ is the average thermal speed of the atoms in z-direction. The spinwave wavelength $\lambda = (2\pi/\Delta k)$ is related to the wavevector mismatch between signal and control given by $|\Delta\vec{k}| = |\vec{k}_C - \vec{k}_S| \simeq k_C \sin(\theta)$. For small angles of the order of 1°, the resulting dephasing times lie in the order of μs. Therefore, this becomes a dominant decoherence mechanism in such memories. This is not the case in cold atomic vapours, where the average atomic velocities are much smaller. Furthermore, in EIT memories there is also an angular dependence of the width (and depth) of the EIT window [329], which could also lead to worse performance of the memory, with respect to, e.g., efficiency.
Finally, spectral filtering is normally done by stacking several Fabry-Pérot etalons one after the other and making use of the frequency difference between signal and control light ($\sim 9.2\,\mathrm{GHz}$ in Cs) in order to filter out the noise. Typical suppressions of $20 - 30\,\mathrm{dB}$ per etalon can be achieved in this manner.
Another possible source of technical noise is given by broadband amplified spontaneous emission (ASE), resulting from the amplification of the control pulses using either tapered amplifiers (TAs) or semiconductor optical amplifiers (SOAs). Most frequency bands of this type of noise are filtered out as explained before, unless they have the same frequency as the signal field, which may become a problem.

However, much more interesting, and hence problematic than technical noise, are noise photons resulting from atomic processes induced by the control field. Some of these photons produced in linear and non-linear optical processes lie at the control frequency and can be filtered out spectrally as before, but some of them share the same frequency as the signal and are thus harder to distinguish from the readout signal photons. The three possible noise sources of this type are fluorescence noise, sometimes also called collisional fluorescence, spontaneous Raman scattering (SRS), and four-wave mixing (FWM). They will each be discussed in more detail below. The discussion follows Refs. [114, 178].

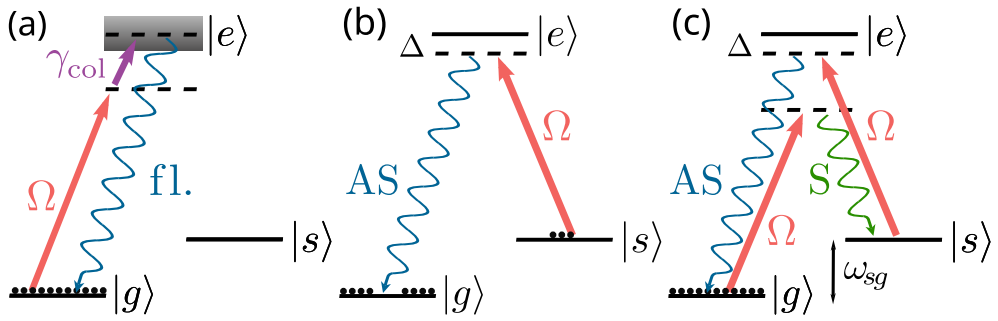

Figure 3.6: Noise mechanisms in atomic vapour memories. (a) Fluorescence noise, (b) Spontaneous Raman scattering (SRS). (c) Four-wave mixing (FWM).

3.4.1 Fluorescence noise

In resonant and near-resonant schemes, the control pulse may excite atoms from $|g\rangle$ up to the excited state $|e\rangle$ ($F' = 3$), and possibly also to the $F' = 4$ excited state, either directly or obtaining the remaining energy ($\propto \gamma_{\mathrm{col}}$) from collisions of the Cs atoms with buffer gas atoms such as N_2. The atoms will then spontaneously decay from the excited state while emitting a photon. As we are dealing with warm vapours, the lineshape is Doppler- and pressure broadened, and has a total width of $\gamma_{e,\mathrm{tot}} \approx 400\,\mathrm{MHz}$. This means, that the emitted photon can be shifted in frequency due to velocity changes or collisions, and thus equal the signal frequency. This is shown in Fig. 3.6 (a). In order to eliminate fluorescence noise, larger detunings Δ of both the signal and control fields are necessary. However, large detunings reduce the control field coupling and thus require stronger control field powers to maintain memory performance. This in turn can lead to the magnification of further noise sources discussed in the following. Conversely, in cold atomic vapours, already small detunings will be enough to mitigate fluorescence noise. The theoretical modelling of such processes has already been introduced in the discussion about lifetime-limiting mechanisms (Sec. 3.2.3), and is generally added phenomenologically to the equations of motion via the decay rates.

3.4.2 Spontaneous Raman scattering

In the Λ-scheme, generally both states $|g\rangle$ and $|s\rangle$ belong to the hyperfine ground-state manifold. The ground-state splitting in the alkalis is of the order of $\omega_{sg} \lesssim 10\,\mathrm{GHz}$. The thermal population ratio of the two states at a given temperature T is proportional to the Boltzmann factor, given as $e^{-\hbar\omega_{sg}/k_B T}$. Therefore, at room temperature where $\hbar\omega_{sg} \ll k_B T$, if no preparation of the sample (optical pumping) is performed beforehand,

the atomic population will be distributed practically equally between both ground states, taking into account their Zeeman degeneracy. In order to change this fact, small Boltzmann factors are desirable, which can be attained either by using atoms with a large ground-state hyperfine splitting ω_{sg}, or by drastically reducing the temperature, as is done in (ultra)-cold atomic samples. If the storage state $|s\rangle$ is not fully empty at the time of storage, the control pulse can spontaneously excite an atom via Raman scattering, creating an anti-Stokes (AS) noise photon at the signal frequency in our configuration (where $|s\rangle$ lies higher in energy compared to $|g\rangle$), as is depicted in Fig. 3.6 (b). This photon will have the same polarisation and temporal shape as the signal photons and will thus be indistinguishable from them. In order to mitigate this process, optimal preparation of the sample via optical pumping is essential. Either the control laser or an extra pumping laser (counterpropagating to signal and control) is used before the storage process in order to pump the atoms out of state $|s\rangle$ into $|e\rangle$, from where they can spontaneously decay into the ground states. If the pump laser illuminates the sample long enough, the state $|s\rangle$ will be almost fully depleted, depending on the attainable pumping efficiency [177]. The dependence of SRS on control pulse energy is linear. However, the behaviour of SRS as a function of detuning is more complex and will be analysed in detail in Chapter 4. From a theoretical analysis, the Raman coupling strength can be derived [178]. Integrating the squared Rabi frequency in time, one obtains an expression for the pulse energy of a beam with area πw_0^2, where w_0 is again the $1/e^2$ beam waist, and Δt_c is the FWHM pulse duration, given as (in units of $\hbar$)

$$W = \int_{-\infty}^{\infty} |\Omega_c(\tau)|^2 d\tau \approx |\Omega_c|^2 \cdot \Delta t_c. \tag{3.141}$$

With this, we can now define the Raman coupling constant (here for the AS case) as

$$C_{\mathrm{AS}} = \sqrt{\frac{W d_{\mathrm{opt}} \gamma_e}{\Delta_{\mathrm{AS}}^2 + \gamma_e^2}}. \tag{3.142}$$

The inclusion of the spontaneous Raman process into the equations of motion is not explicitly necessary, as it has the same form as the retrieval process [178].

3.4.3 Four-wave mixing

Four-wave mixing (FWM) consists of a double Raman scattering process induced (twice) by the control field. It is a third-order nonlinear process ($\propto \chi^{(3)}$) and scales quadratically with control pulse energy. In more detail, a photon from the control pulse can off-resonantly excite an atom in $|g\rangle$ via a virtual state into $|s\rangle$, while emitting a Stokes (S) photon. A

second photon from the control pulse (either used for storage or retrieval) will then scatter from the atom in $|s\rangle$, producing an AS photon. In the chosen Λ-configuration used here, and if the memory is operated red-detuned from the excited state $|e\rangle$, the first part of the FWM process happens at a detuning $\Delta_{\mathrm{S}} = \Delta + \omega_{sg}$ (see Fig. 3.6 (c)). If $\Delta \lesssim \omega_{sg}$, then the SRS contribution is stronger than the FWM contribution and the latter is suppressed. Conversely, if $\Delta \gg \omega_{sg}$, as is the case in far-detuned Raman memories (see Ch. 2), the FWM process has a large coupling strength and can become a very detrimental noise source. In this case, more elaborate tricks have to be used in order to reduce this type of noise, such as exploiting the magnetic Zeeman levels for tailoring the Λ-system, so that FWM will be forbidden by selection rules [185, 330, 331]; or putting the memory inside an optical cavity [190, 332]. In order to minimise FWM it is theoretically beneficial to have a large ground-state splitting and to operate as close to resonance as possible without increasing fluorescence noise. In order to determine the rate of SRS noise to FWM noise we can calculate the ratio between the coupling strengths as

$$R_{\mathrm{SRS/FWM}} = \frac{C_{\mathrm{AS}}}{C_{\mathrm{S}}} = \frac{\sqrt{\frac{W d_{\mathrm{opt}} \gamma_e}{\Delta_{\mathrm{AS}}^2 + \gamma_e^2}}}{\sqrt{\frac{W d_{\mathrm{opt}} \gamma_e}{\Delta_{\mathrm{S}}^2 + \gamma_e^2}}} = \sqrt{\frac{(\Delta + \omega_{sg})^2 + \gamma_e^2}{\Delta^2 + \gamma_e^2}}. \tag{3.143}$$

FWM is theoretically modelled by adding another term to the equations of motion, representing the S optical mode, since the AS channel is already included (as explained above). The shape of the equations can be motivated from symmetry conditions. This is derived in great detail in Ref. [178], where we refer the interested reader.

We have stated before that FWM is only a problem in far off-resonant Raman memories, but this is not the whole story. As we have noted in the theoretical description of atomic Λ-memories (Sec. 3.3), efficient storage in atomic vapours requires high optical depths. It has been shown that at high OD's the FWM process can dominate over EIT, even on resonance [94, 333, 334], thus leading to what is known as FWM gain, which means that the FWM noise starts to increase exponentially with the optical depth. This effect is detrimental for quantum memories as it drastically reduces the fidelity of the retrieved photons [335]. In Ref. [179] it is shown that if $2d_{\mathrm{opt}} > 25$, experimental efficiencies start to decrease compared to theoretical values, and FWM is determined to be a possible reason for this effect. In Ref. [336], a combined EIT-FWM model is developed, with the help of which the authors show that FWM starts to become a problem at high optical depths, and thus explain their former observations of efficiency saturation and decrease in this regime. Moreover, in Ref. [335] a general limit to the optical depth from which FWM begins to be become detrimental (noise grows exponentially) is given as $2d_{\mathrm{opt}} > \frac{2\Delta|\Omega'|}{\gamma_e|\Omega|}$, where Ω' is the Rabi frequency of the control coupling to the $|g\rangle \rightarrow |e\rangle$ transition.

3.5 Spectral filtering

The spectral filtering of the different noise sources presented in Sec. 3.4 and of the remaining control noise is achieved by using a series of etalons or Fabry-Pérot cavities. This allows to isolate the single-photon-level signal from the large background, when it differs in frequency. The working principle of such a filter is that an incoming light beam is reflected back and forth between the surfaces and only constructively interfering beams can exit the cavity. This is schematically shown in Fig. 3.7.

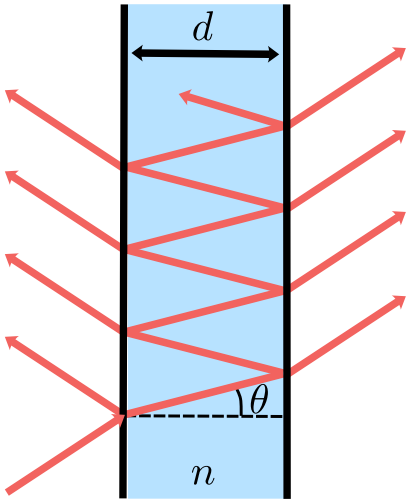

Figure 3.7: Working principle of an etalon (Fabry-Pérot interferometer) with a thickness d, refractive index n and reflectivity of the plane-parallel surfaces R. The incoming beam is reflected several times at the surface and the resulting beams constructively interfere.

The transmission of the etalon as a function of the frequency dependent phase shift δ, attained by the light beam in each round trip, is [337]

$$\mathcal{T} = \left(\frac{T}{1-R}\right)^2 \frac{1}{1+\frac{4R}{(1-R)^2}\sin^2(\delta/2)}, \tag{3.144}$$

where T, R are the transmission and reflection of the mirror surfaces, respectively. The phase shift can be determined as [338]

$$\delta = \frac{4\pi n d}{\lambda}\cos(\theta), \tag{3.145}$$

where λ is the wavelength of the incident light and θ is the angle of the light beam inside the resonator. The quality of an etalon is given by its finesse $\mathcal{F}$, defined as

$$\mathcal{F} = \frac{\pi\sqrt{R}}{(1-R)}. \tag{3.146}$$

This definition holds in the ideal case, where disturbing factors such as surface defects leading to cavity losses, or incorrect mode-matching may be neglected. The mode-matching quality depends on the correct alignment of beam and cavity and can be experimentally optimised.

The spacing in optical frequency (or wavelength) between two successive transmitted maxima of the etalon, the free spectral range, is given as

$$\mathrm{FSR} = \frac{c}{2nd}. \tag{3.147}$$

The finesse and the FSR are related through the (FWHM) linewidth of the transmitted maxima Δf as

$$\Delta f = \frac{\mathrm{FSR}}{\mathcal{F}}. \tag{3.148}$$

Eq. (3.148) implies that for broadband noise reduction, such as the ASE mentioned above, one obtains a reduction by a factor $\mathcal{F}$, as only a fraction Δf of the spectral range is transmitted through the etalon.

Transmission frequency tuning of the cavity is achieved via temperature tuning. Temperature changes affect both the cavity length or thickness d, and the refractive index n. The frequency shift is given by [337]

$$\frac{df}{dT} \approx -\left[\beta + \frac{1}{n}\frac{\partial n}{\partial T}\right] f, \tag{3.149}$$

where β is the thermal expansion coefficient of the material, and $\frac{\partial n}{\partial T}$ can be obtained from the Sellmeyer equations. This change of the refractive index with temperature is often neglected, as it can be assumed to be generally small when compared to the thermal expansion. In materials such as SiO_2 (and for limited temperature tuning ranges as the ones we are interested in), the resonance frequency shift with temperature can therefore be assumed to behave linearly (see Ch. 4).

4 The Hyperfine Λ-Memory

> "I was taught that the way of progress
> is neither swift nor easy."
>
> Marie Skłodowska-Curie

This chapter is mainly based on Ref. [1]:
L. Esguerra, L. Meßner, E. Robertson, N. V. Ewald, M. Gündoğan, and J. Wolters, Optimization and readout-noise analysis of a warm-vapor electromagnetically-induced-transparency memory on the Cs D_1 line. *Phys. Rev. A*, 107, 042607, 2023.

It describes the first implementation of the hyperfine memory experiment, which was the basis for many more experiments to come in the lab. When I started the PhD in September 2019, the lab consisted only of a small breadboard in a corner of an old storage room in the cellar, full of old equipment (see Fig. 4.1), which has developed into an 'almost' modern IKEA-lab, as I like to call it, due to its DIY nature. We started building the setup around January 2020, just after getting the first two optical tables, some months before the corona pandemic hit. Here 'we' refers to Leon Meßner, Janik Wolters, and yours truly. Although probably not reflected in the text, the construction of the setup was a slow process full of trials and many, many errors. After 3 months of locked labs due to the pandemic, we were able to return and continue building. In September 2020, Elizabeth (Lizzy) Robertson joined the team and also helped further developing the experiments, especially in the automation process, by writing a lot of the code that now runs the experiment. The setup has changed and been improved many times over the last four years, and I will try to comment on these improvements in every subsection.
As stated in Chapter 2, many implementations of quantum memories on different platforms exploit the advantages of the latter with respect to certain figures of merit, in which the given platform excels. At the time of conducting the first measuring campaign in June 2021, and writing the paper in the subsequent months, there had been, to the best of our knowledge, no realisation of a room temperature quantum memory in the literature that had focussed on optimising several figures of merit simultaneously. We therefore set this as the goal of that first measuring campaign, and focussed on optimising

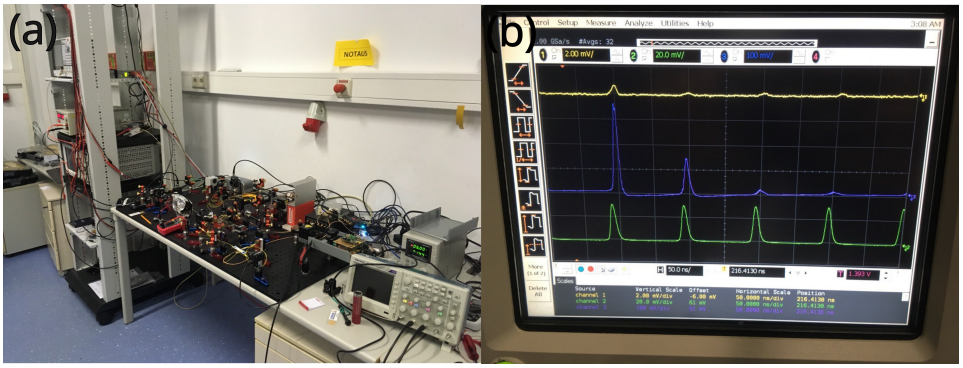

Figure 4.1: (a) Photo of the setup from December 2019, before we had optical tables. With this little 'student laboratory' we achieved our first storage of macroscopic coherent pulses (purple trace, second peak shows retrieval of a stored pulse in the memory) on December 2nd 2019, as shown in (b).

the end-to-end efficiency η_{e2e} and the signal-to-noise ratio (SNR) of the memory, as these are key parameters especially for applications in quantum communication.
In the midst of the review process of the manuscript, we decided to remeasure some data again, specifically for the noise analysis section of the manuscript. This led to a second round of measurements of the memory experiment, which focussed not on the measurements of efficiency and SNR as before, but on the noise behaviour of the system. These measurements were carried out from July to November 2022. At this point, some parts of the experimental setup had been modified and improved. The modifications to each part will be noted in each section.

4.1 Experimental scheme and implementation

The scheme to realise a warm atomic quantum memory based on EIT was inspired on the experiment conducted in Basel by Janik Wolters et al. [136]. This experiment was conducted using rubidium. Alkali metal atoms, like Rb, are ideal systems to implement these types of memories, due to their hydrogen-like structure with one optically addressable electron in the outermost shell. This allows for a simpler theoretical description and thus easier prediction of their experimental behaviour. For our experiments, we decided to change the atomic species to another alkali atom, caesium. This choice was motivated by various factors. First, Cs is the heaviest stable alkali atom and has only one stable isotope. In a thermal environment it is therefore the slowest, resulting in less Doppler broadening of the transitions. Since atomic diffusion out of the interaction region with the

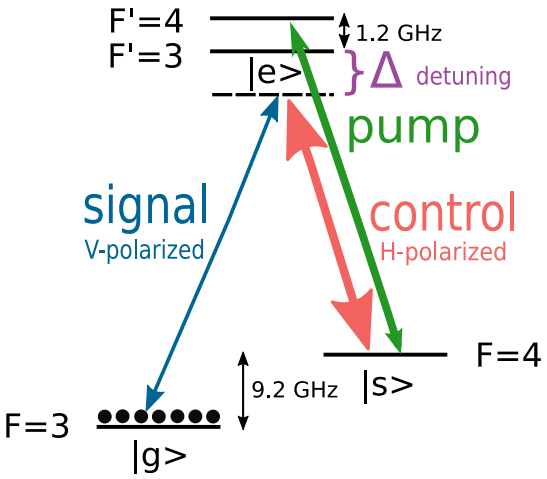

Figure 4.2: Three-level Λ-system with signal (control) laser frequency red-detuned by Δ from the respective hyperfine transitions of the Cs D_1 line. A pump laser initially prepares the atoms in the $F = 3$ ground state ($|g\rangle$). Both ground states $|g\rangle$ and $|s\rangle$ are naturally long-lived.

light is one of the primary decoherence mechanisms in warm vapour memories (see Ch. 3 and Ref. [177]), this fact becomes highly relevant. Second, Cs offers a higher possible storage bandwidth, due to a larger ground-state hyperfine splitting, as compared to, e.g., rubidium or lithium. Comparatively, Cs also shows a larger excited-state hyperfine splitting, which reduces the influence of the additional, parasitic excited state $F' = 4$. Third, it has a longer D_1 wavelength, which results in less absorption in optical fibres compared to, i.e., the Rb D_1 line. A further benefit of Cs is its high vapour pressure, which allows to achieve high atomic number densities, and therefore high optical depths at moderate temperatures.

Let us turn, as a reminder, to the atomic structure of Cs. The D_1 line at 894 nm is the collection of hyperfine transitions into which the fine structure transition $6^2S_{1/2} \rightarrow 6^2P_{1/2}$ is split. The levels split into two ground states with $F = 3$ and $F = 4$, split by 9.193 GHz, and two excited hyperfine states with $F' = 3$ and $F' = 4$, split by 1.168 GHz, respectively. This is depicted in Fig. 4.2. The transition between the two ground states is dipole forbidden and therefore long-lived. Thus, the higher-lying ground state ($F = 4$) can be used as the storage state $|s\rangle$ in a Λ-system, while the lower state acts as the ground state $|g\rangle$ of the memory. To our knowledge, this was the first realisation of a warm single-photon-level memory in caesium on this transition, although there exist realisations using cold atoms, e.g., Ref. [205].

The Λ-system used for EIT in this scheme, represented in Fig. 4.2, results from coupling

the memory ground state $|g\rangle$ and the common excited state $|e\rangle$, in this case the lower excited state $F' = 3$, by the signal laser, which corresponds to the light that is going to be stored in the memory. The control laser, which will mediate the storage process, couples the storage state $|s\rangle$ and the same excited state $|e\rangle$. In order to minimise the influence of the remaining excited state with $F' = 4$, both signal and control lasers are here red-detuned by a varying detuning Δ from resonance of their respective transitions. Furthermore, as in Λ-EIT both lasers are co-propagating, they must be orthogonally polarised, in order to be able to filter the strong control laser out of the transmitted signal path.
A pump laser is tuned to the $F = 4 \rightarrow F' = 4$ transition for state preparation in the $|g\rangle$ state. This laser will pump the majority of the atoms out of the storage state $|s\rangle$. The chosen transition yields a higher pumping efficiency when compared to the $F = 4 \rightarrow F' = 3$ transition, due to a larger coupling. However, for $F = 4 \rightarrow F' = 4$, the $m_F = 0 \rightarrow m'_F = 0$ transition will not couple to the pump laser. This fact will be described in more detail below.

The hyperfine levels are degenerate in absence of external magnetic fields, which will be the assumption for the hyperfine memory scheme. For completeness, it is nevertheless important to note that each of the hyperfine levels splits into $2F + 1$ magnetic Zeeman sublevels in the presence of such a field. Due to optical selection rules, even though the states are degenerate in absence of an external magnetic field $\boldsymbol{B}$, there are some forbidden transitions in the manifold, which do not contribute to the calculated matrix elements (see Eq. 3.18 in Chapter 3.). An example of this would be the $m_F = 0 \rightarrow m'_F = 0$ element of the $F = 3 \rightarrow F' = 3$ transition, which is not allowed as $\Delta F = 0$ and $\Delta m_F = 0$ holds simultaneously, as is the case for the pump laser. These selection rules determine the optimal choice of the signal and control transitions to be the $F = 3 \rightarrow F' = 3$ and $F = 4 \rightarrow F' = 3$, respectively, as other Λ-systems would lead to residual parasitic absorption due to incomplete coupling of the control field, and therefore to incomplete EIT. Since the control laser is much stronger than the signal laser, the former will define the quantisation axis. Therefore, the linearly-polarised control field couples to π-transitions and the linear polarisation of the weaker signal laser can be assumed to drive a sum of $\sigma^+ + \sigma^-$ transitions.

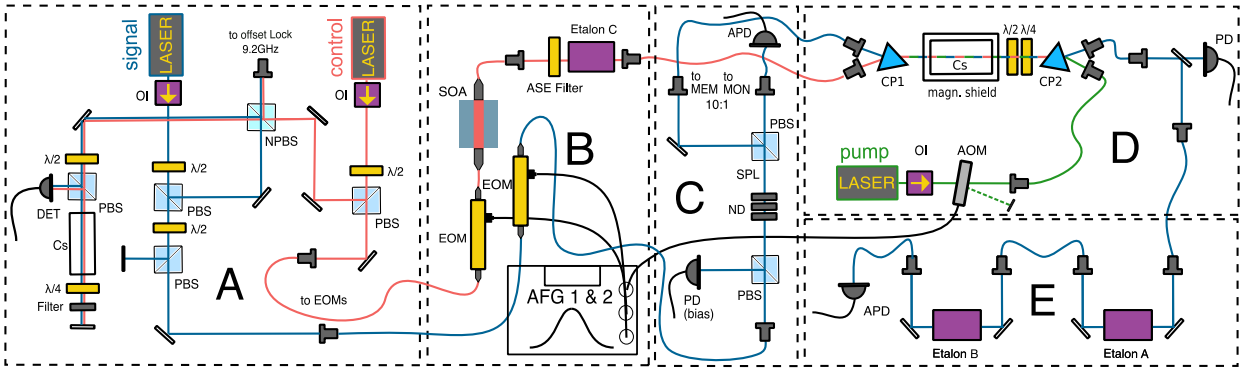

Figure 4.3: Sketch of the whole experimental setup consisting of A: laser systems, spectroscopy, and offset lock; B: pulse generation and amplification, and filtering of the control pulses; C: attenuation to single-photon level and monitoring stage; D: memory part with pump laser setup and polarisation filtering; and E: spectral filtering and detection stage. $\lambda/2$, $\lambda/4$: waveplates; AFG: arbitrary function generator; AOM: acousto-optical modulator; APD: avalanche photodiode; ASE: amplified spontaneous emission; CP: calcite prism; Cs: Caesium-filled vapour cell; EOM: electro-optic modulator; MEM: memory; MON: monitor; ND: neutral density attenuation filters; NPBS: non-polarising beam splitter; OI: optical (Faraday) isolator; PBS: polarising beam splitter; PD: photodiode; SOA: semiconductor optical amplifier; SPL: single-photon level. Several waveplates and mirrors have been omitted for clarity. Fibre collimators and mirrors are not labelled for simplicity. Straight lines represent free-space propagation, while curved lines represent optical fibres. All fibres are single mode and polarisation maintaining (PM).

4.2 Experimental setup

The complete, recursively built, experimental setup is depicted in Figure 4.3. It can be divided into multiple functional segments that are then combined in order to perform the memory experiments described in this chapter. The different segments will be shortly described here and in more detail in the following subsections. These are A: the laser system, consisting of the signal and control lasers, the spectroscopy used to find the necessary transitions, and the offset lock implemented to keep the frequency difference between the lasers at the correct value, corresponding to the hyperfine splitting of the ground state hyperfine levels. This is essential for the storage protocol to work in a stable manner. Part B contains the pulse generation via EOMs for both lasers, controlled by an arbitrary function generator (AFG). This part further contains the amplification of the control pulses via a semiconductor optical amplifier (SOA), and the filtering of the amplified spontaneous emission (ASE) by means of an etalon. Part C consists of the signal attenuation and the calibration to single-photon-level (SPL) via the monitor signal on the

APD, and further the EOM bias level calibration on the photodiode. Part D consists of the actual memory cell, the pump laser and its pulsing via an AOM, and the first part of the filtering, by means of polarisation. Finally, part E contains the spectral filtering system and the detection. A photo of the experiment from June 2021 can be seen in Fig. 4.4.

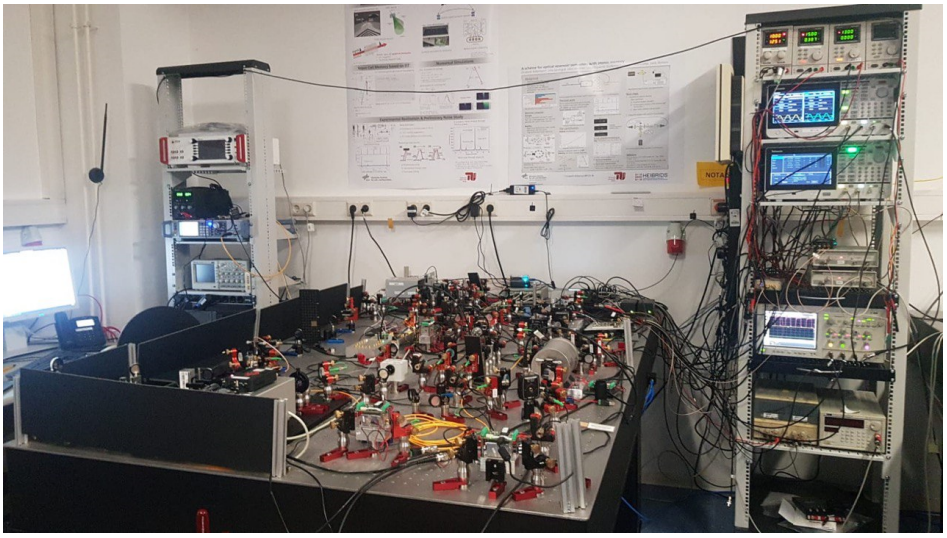

Figure 4.4: Photo of the full setup from June 2021, at the time of the first iteration of the experiment. It fills the complete optical table as it is not optimised with regards to compactness. The control electronics are divided among the the two racks on the side. Further improvements have been iteratively added over the years.

4.2.1 Laser systems and offset lock

Lasers

All of the lasers used in this first generation memory experiment were self-assembled from components, mostly by Leon Meßner, at the time a master student, now PhD student in the group. They consist of Sacher Lasertechnik 895 nm ECDL 14 pin butterfly lasers, Koheron DRV200-A-200 diode drivers, Meerstetter TEC-1091 temperature controllers (TEC), Qioptiq FI-930-5SC optical isolators, custom printed circuit boards (PCB) and machined parts. The frequency of these self-assembled lasers can be controlled via RF modulation. For detailed information about the design of these laser sources I refer to Leon's Master's Thesis [12]. Both lasers are connected to Red Pitaya (RP) STEMLab 125-14 field programmable gate arrays (FPGAs), which act as function generators for the modulation of the laser frequency, as oscilloscopes, in order to look at the spectroscopy,

and are also used to stabilise the lasers. These have maximal optical output powers in the range of $50 - 80\,\mathrm{mW}$, and can be tuned in a mode-hop-free frequency range of about $4 - 8\,\mathrm{GHz}$. They are driven with voltages of $V \sim 2.5 - 3.5\,\mathrm{V}$, depending on the specific laser, and their scanning behaviour (via current modulation with the RP) corresponds to $\sim 2.5\,\frac{\mathrm{MHz}}{V}$. In order to tune the lasers and set them at the correct frequency, Doppler-free spectroscopy is performed on both of them (via frequency modulation of the laser's with the RP) on a single spectroscopy cell (see Fig. 4.3 A). The probe beam is detected by a Thorlabs DET36A2 Si photodiode connected to the RP's oscilloscope. This allows to find the Cs D_1 hyperfine transitions and set the correct laser frequencies with a certainty proportional to the width of the Lamb dips of the corresponding transitions. For more detail on Doppler-free spectroscopy, and how the correct current and temperature settings for each laser are determined experimentally, I refer again to [12]. The drift of the lasers amounts to $\approx 1 - 3\,\mathrm{MHz}$ in one minute, when not locked. This was estimated from letting the lasers run free and monitoring the frequency drift for several hours. It is naturally not the most exact measurement, as this drift depends on several factors, such as the lab temperature, and the wavemeter stability, but it constitutes a fair estimation. The pump laser is frequency-locked to the intended transition (discussed below in Sec. 4.2.2) via Doppler-free spectroscopy, using active frequency stabilisation with a proportional-integral-derivative (PID) controller with the Linien software [339] on a RP. In the first implementation we did not have a stable wavemeter in the lab and could therefore not monitor the laser frequencies accurately. This changed for the second iteration, where we had acquired a High Finesse WS-7 wavemeter with an absolute accuracy of $\pm 60\,\mathrm{MHz}$ and a stability of $\approx 10\,\mathrm{MHz}$.

Offset lock

For the EIT window to be as large as possible, the two-photon detuning should vanish as $\delta = \Delta_s - \Delta_c = 0$. This ensures efficient storage of the signal pulse inside this EIT window, given the pulse has an appropriate spectral width. As the laser frequencies will drift due to thermal fluctuations in the lab, and locking each laser to its transition frequency was problematic, since we wanted to be able to change the detuning in a simple manner and have stable detuned operation, we decided to implement an offset lock that would maintain the frequency difference between the signal and control lasers constant, and regulate for any changes.

The scheme used for this offset lock was inspired by Ref. [340] and makes use of the frequency-dependent phase shift generated by a signal that propagates through a delay

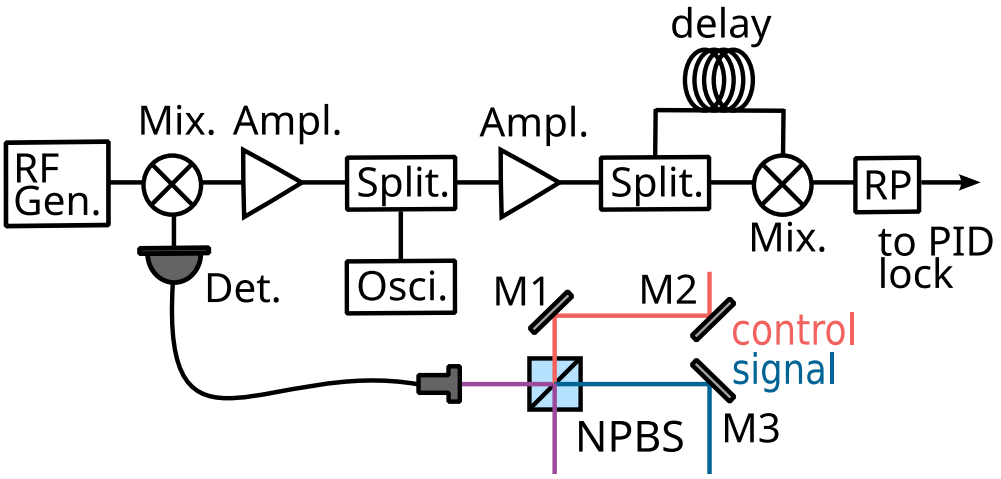

Figure 4.5: Schematic of the offset-lock setup. Ampl.: amplifier; delay: coaxial cable; Det: fast photodetector; M1-3: mirrors, Mix.: mixer; NPBS: non-polarising beam splitter; Osci.: oscilloscope; RF Gen.: radio frequency generator; Split.: splitter; RP: red pitaya.

line consisting of coaxial cable. This allows to control frequency differences in the radio frequency range, specifically the $\sim 9.2\,\mathrm{GHz}$ difference, corresponding to the ground state energy splitting of Cs, intended in this experiment.

For the generation of the error signal for stabilisation, small fractions $\mathcal{O}(1\,\mathrm{mW})$ of the output of both lasers are superimposed on a non-polarising beam splitter (NPBS), such that they show the same polarisation, and coupled into a single mode fibre, connected to a fast photodetector (EOT InGaAS ET-350FEXT) with a large enough bandwidth to detect frequencies in the order of 10 GHz. As the beam sizes of both lasers are not equal at the position of the coupler, and we need both beams to couple in with an acceptable efficiency, the mode matching is not ideal, and only $\mathcal{O}(100\,\mu\mathrm{W})$ of each laser reaches the photodetector. The measured signal is then mixed with a radio frequency of $f_{\mathrm{FG}} = 8.836\,\mathrm{GHz}$ at $-3\,\mathrm{dBm}$ generated by an RF generator (Rohde und Schwarz SMA100B HF). Subsequently, the difference signal of 357 MHz is amplified by 35 dB and sent through a splitter to divide the signal into a part going to an oscilloscope that measures the power spectrum of the beat note (via fast Fourier transform (FFT) in Math mode), and a second part which is then amplified again by 35 dB. This signal is split further into one part going through a 2 m coaxial cable delay line, and later mixed again with the remaining part of the signal. This beat note is then detected with a RP, where the zero crossings of the signal provide the error signal for locking on the difference frequency. This configuration yields a lock stable to $< 1\,\mathrm{MHz}$. A schematic of the locking setup is depicted in Fig. 4.5. All the RF components are from Mini-Circuits. The frequency resolution is determined

by the slope of the error signal at the locking point. A longer cable can enhance this resolution but it reduces the achievable frequency locking range. The locking is performed again on the Linien software [339]. For the frequency $f_{\mathrm{OL}} = 357\,\mathrm{MHz}$, on which the lock should be executed it holds

$$f_{\mathrm{OL}} = \frac{\omega_{sg}}{2\pi} - \Delta f_{\mathrm{S}} - f_{\mathrm{FG}}, \tag{4.1}$$

where $\frac{\omega_{sg}}{2\pi} = 9193\,\mathrm{MHz}$ is the hyperfine ground-state splitting, Δf_{S} (if present) is a small deviation from the exact hyperfine splitting caused by the AC-Stark shift induced by the control laser, and $f_{\mathrm{FG}} = 8836\,\mathrm{MHz}$ is the generated RF frequency for the mixing. This last value was changed slightly during the experiment to optimise the storage trace and thus Δf_{S} varied accordingly.
On later runs of the experiment the offset lock was modified due to stability reasons and the second amplification was removed, while the delay cable was changed to a 5 m one. As will be explained later, the pulsing device for the control laser was changed from an electro-optic modulator (EOM) to an acousto-optic modulator (AOM). The calculation of the locking frequency then changed to

$$f_{\mathrm{OL}} = \frac{\omega_{sg}}{2\pi} - \Delta f_{\mathrm{S}} - f_{\mathrm{FG}} + \Delta f_{\mathrm{AOM}}, \tag{4.2}$$

where $f_{\mathrm{OL}} = 1155\,\mathrm{MHz}$ is the new locking point, $f_{\mathrm{FG}} = 8256\,\mathrm{MHz}$ is the generated RF frequency at $-1.1\,\mathrm{dBm}$, and $\Delta f_{\mathrm{AOM}} = 196\,\mathrm{MHz}$ is the frequency shift generated by the pulsing of the control laser with the AOM. The experimentally determined AC Stark shift is now $\Delta f_{\mathrm{S}} = 22\,\mathrm{MHz}$. The resulting power spectrum is depicted in Fig. 4.6. This signal is obtained using the FFT function of the oscilloscope (Tektronix DPO5104B with a bandwidth of 2 GHz) using a Hanning type window and a resolution bandwidth of $\Delta f = 36.0\,\mathrm{kHz}$. This implies an integration window length of $T = \frac{1}{\Delta f} \approx 30\,\mu\mathrm{s}$. Thus, the oscilloscope bandwidth is large enough, and the resolution bandwidth small enough to resolve the beat signal.

From the spectrum in Fig. 4.6, we can estimate the relative stability of the signal and control lasers. Since they both possess the same type of diode from Sacher Lasertechnik and the same driving electronics, we can assume they will have a similar linewidth, which can be estimated from the relative value. Linearising the power spectrum, we obtain the spectrum shown in Fig. 4.7. Since the linearised data shows a curious oscillatory behaviour, it is not really possible to fit it properly. Therefore, we estimate its width by plotting a Gaussian function with a similar width. The choice of a Gaussian is related to the assumption that the noise processes present here are probably thermal

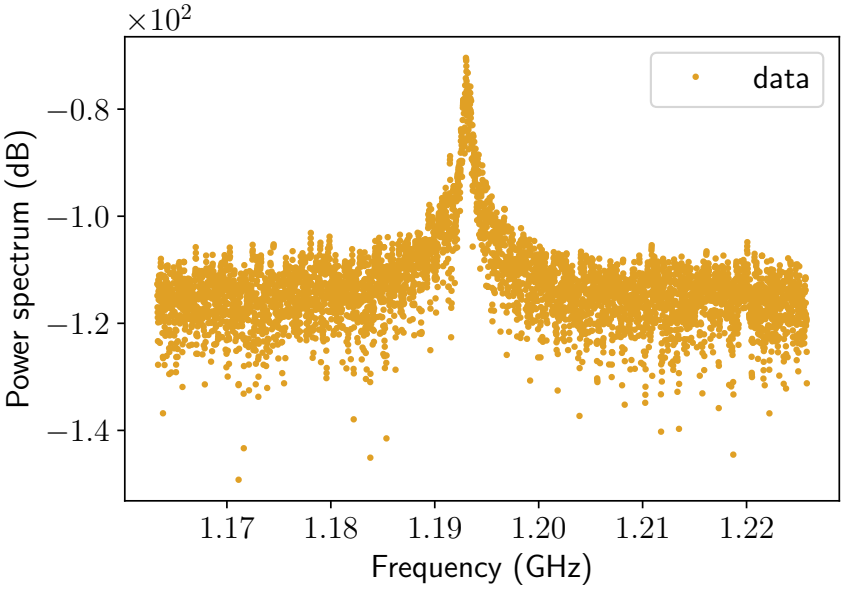

Figure 4.6: Power spectrum (dB) of the offset-lock signal measured on the oscilloscope. Although the signal is relatively noisy, it suffices to lock on the error signal.

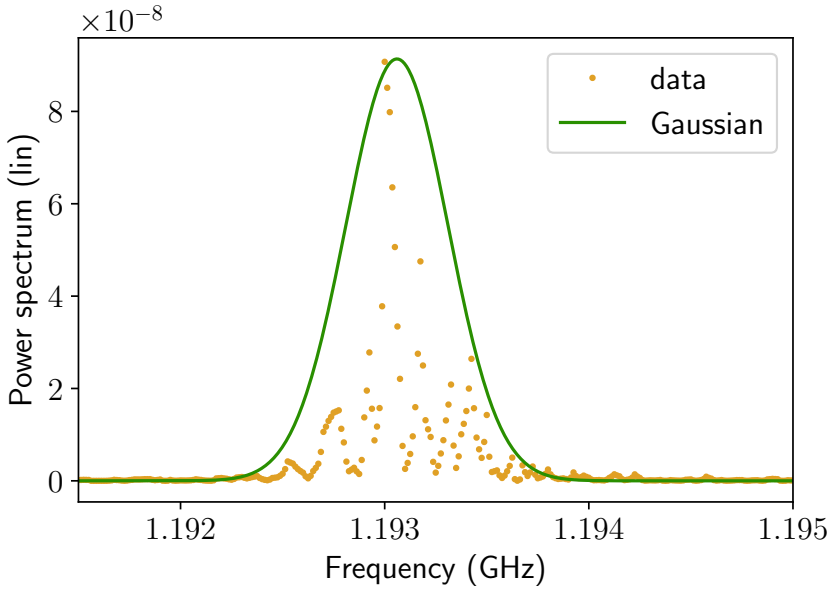

Figure 4.7: Linearised power spectrum of the offset-lock signal and estimated Gaussian function with FWHM $\approx$ 600 kHz (no fit) superimposed to approximate the width of the signal. A smaller width does not suffice to include the peak points and all the oscillations at the base.

or of similar type, which can be well described by a Gaussian distribution. From this function, we can determine a relative frequency linewidth of $\approx 600\,\mathrm{kHz}$. With the assumption of both lasers behaving similarly, we obtain an approximate linewidth of $\Delta f = \frac{600\,\mathrm{kHz}}{\sqrt{2}} \approx 420\,\mathrm{kHz}$. Therefore, the resulting laser linewidth amounts to $\sim 420\,\mathrm{kHz}$ in $30\,\mu\mathrm{s}$, a timescale comparable to the length of our experimental sequences (see Sec. 4.2.3). The manufacturer (Sacher Lasertechnik) states linewidths of $< 100\,\mathrm{kHz}$ in 1 ms in the general data sheet for this type of butterfly diodes. From the obtained linewidth, an estimate of the coherence length of the laser L_c can be obtained as $L_c = \frac{c}{\pi \Delta f} \approx 190\,\mathrm{m}$.

4.2.2 Optical pumping

Efficient and noise-free memory operation requires the atoms to be prepared in the correct ground state $|g\rangle$ before the memory interaction begins. As we are dealing with warm systems close to thermal equilibrium, both ground states will be equally populated, as can be seen from the calculated Boltzmann factor $e^{-\hbar\omega_{sg}/k_B T} \approx e^{-0.7/T} \approx 1$ at $T \sim 330\,\mathrm{K}$. Consequently, the system needs to be prepared via optical pumping. We do this by applying a linearly polarised laser field, that couples to the π transitions of the $F = 4 \rightarrow F' = 4$ manifold. The choice of this specific transition was determined by comparison of the resulting strength factors for the possible pumping transitions:

$$F = 4 \rightarrow F' = 3 \propto C_{43}^2 \cdot S_{33} = \frac{7}{36} \cdot \frac{1}{4} = \frac{7}{144} \tag{4.3}$$

$$F = 4 \rightarrow F' = 4 \propto C_{44}^2 \cdot S_{34} = \frac{5}{36} \cdot \frac{3}{4} = \frac{15}{144}. \tag{4.4}$$

The total factor is the product of the strength factors $C_{FF'}^2$ of the pumping transitions, and the strength factors for resonance fluorescence $S_{FF'}$ of the respective excited state to the $|g\rangle$ ($F = 3$) ground state (see Ch. 3, Tables 3.3 and 3.4). Therefore, a pump laser on the aforementioned transition, turned on and off using an AOM (see Sec. 4.2.3), is used for state preparation. Its beam diameter is $540(5)\,\mu\mathrm{m}$ FWHM at its focus at the center of the memory cell, with a peak power of $P_{\mathrm{pump}} = 12.3\,\mathrm{mW}$. For an estimation of the lower bound for the total pumping time required to transfer all the population from the storage state $|s\rangle$ to the ground state $|g\rangle$, the following assumptions are made, following the treatment of Ref. [116]. Approximating the pumping volume from an area of $A = \pi r_{1/e^2}$, where r_{1/e^2} is the $1/e^2$ beam radius, and a cell length of $L = 7.5\,\mathrm{cm}$, we obtain a pumping volume of $V \approx 0.05\,\mathrm{cm}^3$. The calculated Cs atomic density at $T = 60°\mathrm{C}$ is $n_{\mathrm{Cs}} \approx 10^{12}\,\frac{1}{\mathrm{cm}^3}$. This gives a total number of atoms of $N = 5 \cdot 10^{10}$ in the

pump interaction volume at this temperature. Assuming that in every pump cycle 50% of the atoms are pumped out, and after M pumping cycles only one atom is left in the $|s\rangle$ state, yields $M = 35$[1]. The lifetime of the Cs D_1 line is $\tau \approx 35\,\mathrm{ns}$. This means the lower bound for the total pumping time is on the order of $t_{\mathrm{pump}} = M\tau = 1.2\,\mu\mathrm{s}$. This estimation ignores all the atomic mechanisms decreasing pumping efficiency that were described in Ch. 3. Thus, we chose a total pumping time of $t_{\mathrm{pump,tot}} = 10\,\mu\mathrm{s}$.
The topic of optical pumping is rather complex in itself and fills review articles and books [301, 302]. The theoretical calculation of required pump rates can be done using a semiclassical model, as in Ref. [177]. We instead opted for a more phenomenological determination of relevant pumping parameters. Three Bachelor theses have been written about the topic in the group, by Jinglan Wu, Florian Günther, and David Becker, the first and last under my supervision. Currently a fourth student, Paul Gölz, is working on the Zeeman level pumping setup for the QToRX memory (see Ch. 5, Sec. 5.5).

For a determination of the pumping efficiency, we performed two different measurements. As a first approximation, we pumped for $t_{\mathrm{pump,tot}} = 10\,\mu\mathrm{s}$ and let the system evolve freely for $\sim 1.5\,\mathrm{ms}$, while probing on the signal ($F = 3 \rightarrow F' = 3$) transition with a weak laser. Here it is important to note that the signal must be very weak, in order not to excite the atoms back again. Because the laser transmission is given by the exponential of the optical depth, which is proportional to the atomic number density as $T = e^{-2d_{\mathrm{opt}}} \propto e^{-n}$, we can estimate the pumping efficiency from the ratio of the logarithms of the maximal transmission and the minimal transmission. At this configuration we obtain a pumping efficiency estimate of

$$\eta_{\mathrm{pump}} \approx \frac{2d_{\mathrm{opt},F=3\rightarrow F'=3}}{2d_{\mathrm{opt},F=4\rightarrow F'=4}} = \frac{3.65}{4.43} \approx 82\%. \tag{4.5}$$

From this experiment[2], we can determine an experimental value for the optical depth of the signal transition ($F = 3 \rightarrow F' = 3$) of $2d_{\mathrm{opt}} = 3.65$, which can yield a point of comparison with values calculated theoretically later on (see Table 4.3). However, a systematic and more exact experimental determination of the OD should be performed in order to obtain a more accurate value. As mentioned shortly in Sec. 4.1, there will be some residual parasitic transmission of the pump laser, since the $m_F = 0 \rightarrow m'_F = 0$ transition is forbidden because of dipole selection rules. Considering that the hyperfine

[1] From $1 \stackrel{!}{=} \left(\frac{1}{2}\right)^M \cdot N$.

[2] As this is to be taken as an approximation, I did not calculate corresponding experimental uncertainties. The second measurement of the pumping efficiency, this time at SPL, was taken as the more accurate one, for which experimental (fit) errors were determined.

states ($F = 4$ and $F' = 4$) each have 9 magnetic sublevels, a rough estimation yields that $\frac{1}{9}$ of the atoms will not be addressed by the pump laser. This translates to a reduction of the pumping efficiency of $\sim 11\%$, meaning that the maximally achievable pumping efficiency amounts to $\sim 89\%$. In this case, the above calculated estimate of the pumping efficiency can be considered satisfactory, but still leaves room for improvement. From this measurement, we further obtained an estimate of a $1/e$ lifetime of the hyperfine state $|g\rangle$ after pumping of $\tau_{\mathrm{T}} = 240\,\mu$s (T as it is determined from the transmission, see Fig. 4.8). This estimation is however not very accurate, as it stems from the transmission curve and not from a measurement of the decay of the optical depth, which is proportional to the atomic population in a specific state. Moreover, this measurement was performed with the cell heaters on, which was problematic, as will be explained later in Sec. 4.2.4.
Since we wanted to better understand the lifetime-limiting mechanisms in our memory, we decided to pursue more detailed investigations on this topic with the help of motivated Bachelor students. First investigations on the pumping lifetime of the hyperfine transitions by Jinglan Wu resulted in lifetimes on the order of $\bar{\tau}_{\mathrm{OD}} = 1\,$ms (this time determined from the optical depth decay curves) [9]. Building on this work, David Becker then determined a maximal D_1 pumping lifetime $\bar{\tau}_{\mathrm{OD}} = 0.8\,$ms of the $F = 4 \rightarrow F' = 4$ transition at $T \approx 60°$C (see Fig. A.3 (b) in the Appendix and Ref. [10]). His investigations also show that spurious absorption resulting form forbidden transitions due to selection rules (as discussed earlier) are visible in the obtained absorption spectra while pumping (Fig. A.2). The lifetimes obtained in this last work exhibit a higher degree of reliability.

Table 4.1 shows the determined average lifetimes $\bar{\tau}_{\mathrm{OD}}$ of the $|g\rangle$ state after hyperfine pumping at two different cell temperatures $T = 21.5(5)°$C and $T = 56(6)°$C for different probe powers P_{probe} on the $F = 4 \rightarrow F' = 3$ transition. These measurements, performed by David are explained in more detail in Appendix A.1. We can see that the dependence of the lifetimes on probing power is not very large for $T = 21.5(5)°$C, but clearly visible at the higher temperature $T = 56(6)°$C. This hints to the fact that the probe laser power was probably not low enough and introduced a competing process of re-exciting the atoms back again. This explains why the data of the OD rises (as the ones presented in the Appendix in Fig. A.3), were better fitted by a sum of exponential functions when compared to a fit using only one exponential, as David discusses in detail in his thesis [10]. This means, we should take the achieved lifetime values with care and still, more detailed investigations should be performed in this direction, as will be done in further experiments I will describe later on.

The second, more exact, determination of the pumping efficiency was conducted later on, at the single photon level. As was explained in Ch. 3, SRS noise is proportional to

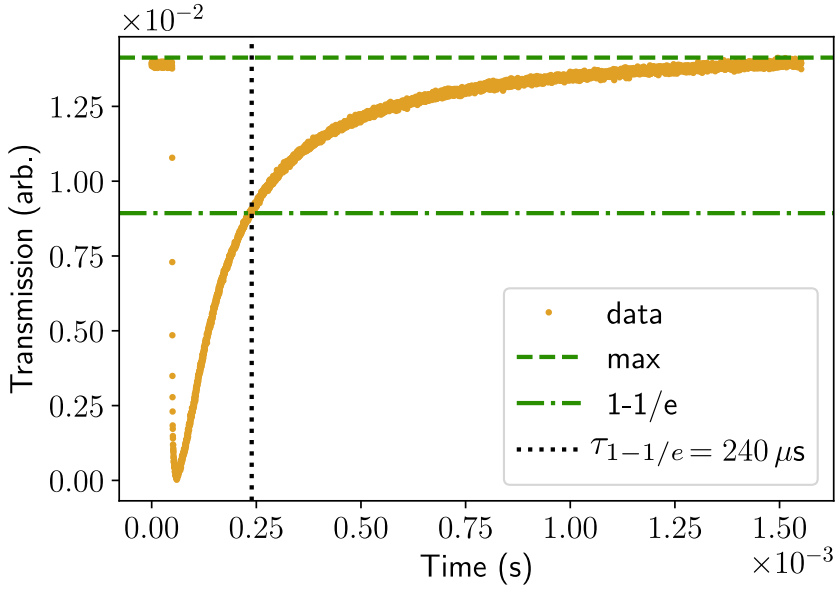

Figure 4.8: Measurement of the probe transmission of the signal ($F = 3 \rightarrow F' = 3$) (yellow dots) after pumping for $t_{\mathrm{pump,tot}} = 10\,\mu$s and letting the system evolve freely for ~ 1.5 ms. The horizontal lines are the maximum transmission (green dashed) and the $(1 - 1/e)$-value (green dash-dotted). The vertical black dotted line corresponds to the determined pumping lifetime $\tau_{\mathrm{T}} = \tau_{\text{1-1/e}}$ of the state $|g\rangle$.

P_{probe}	$\bar{\tau}_{\mathrm{OD}}$ (ms)	
	$T = 21.5(5)$°C	$T = 56(6)$°C
7.9 μW	2.90(9)	0.80(1)
1.1 μW	2.97(6)	0.30(1)
335 nW	2.73(8)	0.57(1)

Table 4.1: Comparison of average pumping lifetimes $\bar{\tau}_{\mathrm{OD}}$ for hyperfine one-colour pumping (D_1) for different probing powers P_{probe} on the $F = 4 \rightarrow F' = 3$ transition, at different cell temperatures T.

the number of atoms remaining in the $|s\rangle$ state after state preparation, and thus during memory operation. Without pumping, we could always see a non-vanishing constant noise floor in SPL histograms. Therefore, if we let the atoms in the cell evolve freely for a long time $\mathcal{O}(1\,\mathrm{ms})$, and then turn on the pump laser, a SPL measurement of the exponential decay of fluorescence (from the aforementioned noise floor) at the signal frequency, while the pumping pulse is on, will yield a better measure for the population difference of state $|s\rangle$ before and after pumping. This measurement is shown in Figure 4.9. The data, which

scatters quite significantly, is fitted with a decaying exponential function of the form $y = a \cdot e^{t/t_{\text{pump}}} + c$. The fit values, from which the pumping efficiency is determined as $\eta_{\text{pump}} = 1 - \frac{c}{a}$, are given in Table 4.2.

	$P_{\text{pump}} = 12.3\,\text{mW}$	$P_{\text{pump}} = 14.5\,\text{mW}$
a	51(1)	148(2)
t_{pump}	1.90(6) μs	1.41(2) μs
c	17.0(2)	10.5(2)
η_{pump}	67(1)%	92.9(2)%

Table 4.2: Single-photon level pumping-measurement fit results and calculated pumping efficiencies for the two measured pumping powers in the SPL measurement.

From this measurement, for a pumping time of $t_{\text{pump,tot}} = 15\,\mu\text{s}$, we could estimate a more exact value for the pumping efficiency of $\eta_{\text{pump}} = 1 - \frac{n_{|s\rangle,\text{pump}}}{n_{|s\rangle,0}} = 67(1)\%$ at the above mentioned pump power of $P_{\text{pump}} = 12.3\,\text{mW}$. This is significantly lower than the 82% assumed before. Approximately the same value was already achieved at $t_{\text{pump,tot}} = 10\,\mu\text{s}$. This was the maximally achievable power at the time of the experiment. Later on, we conducted the same pump efficiency measurement for a (then already achievable) pump power of $P_{\text{pump}} = 14.5\,\text{mW}$ (Fig. 4.10), and in this case obtained a pumping efficiency of 92.9(2)%, showing that the available pump power has a large effect on the attainable pumping efficiency. This large difference of pumping efficiencies for laser powers differing by only 15% seems rather surprising. The measurements were however performed one after the other, so no alignment difference should have occurred. From these two measurements, a more precise determination of the required time t_{pump} in order to empty the storage state $|s\rangle$ is obtained. These can be compared with our first estimation of the lower bound for the required pumping time of $t_{\text{pump,tot}} = M\tau = 1.2\,\mu\text{s}$. The obtained t_{pump} values of Table 4.2 agree relatively well with this estimation.

We observed in various measurements that optical pumping is less efficient while the cell heater (see Sec. 4.2.3) is turned on, resulting from spurious magnetic fields. Also, the higher the temperature, the worse optical pumping becomes, since all the competing atomic processes like collisions, etc., become more probable as more atoms are in the interaction region. In addition, the optical depth is higher, leading to increased radiation trapping in the radial direction.

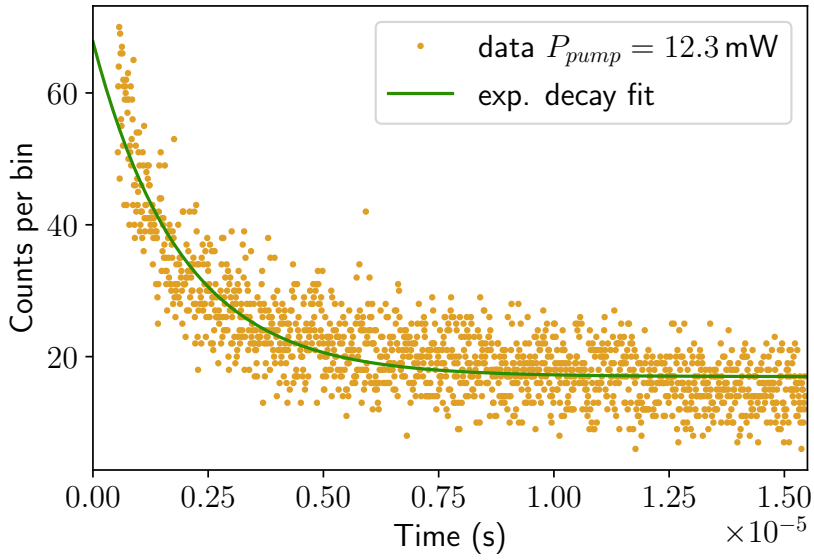

Figure 4.9: Measurement of exponential decay of fluorescence at the signal frequency ($F = 3 \rightarrow F' = 3$) while the pumping pulse is on for $t_{\mathrm{pump,tot}} = 15\,\mu\mathrm{s}$ (yellow dots), and corresponding exponential decay fit (green) for a cw pump laser power of $P_{\mathrm{pump}} = 12.3\,\mathrm{mW}$. The fit yields a pumping efficiency of 67(1)%.

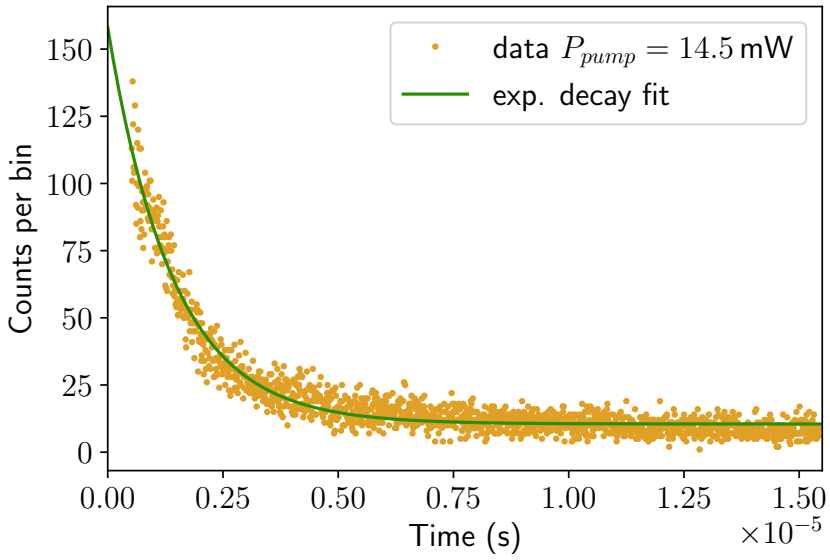

Figure 4.10: Measurement of exponential decay of fluorescence at the signal frequency ($F = 3 \rightarrow F' = 3$) while the pumping pulse is on for $t_{\mathrm{pump,tot}} = 15\,\mu\mathrm{s}$ (yellow dots), and corresponding exponential decay fit (green) for a cw pump laser power of $P_{\mathrm{pump}} = 14.5\,\mathrm{mW}$. The fit yields a pumping efficiency of 92.9(2)%.

4.2.3 Pulse generation and amplification

Electro-Optic Modulator

For the pulse generation of the first measuring campaign, electro-optic modulators (EOMs) were used in the signal and control arms. Among these devices there are phase modulators and amplitude modulators. Common commercial devices are built as fibre connected, integrated optical waveguides fabricated on a substrate. Compared to bulk construction, integrated devices yield high frequencies and large operational bandwidths [341]. Furthermore, they reduce the need for high operational voltages. The most common material used for fabrication is Lithium niobate $LiNbO_3$. The modulation of the phase is based on a second order non-linear effect, known as the Pockels effect or linear electrooptic effect, which describes the change of the refractive index of a material when an external electric field is applied. The change is proportional to the strength of the field E, and is generally anisotropic. In polar materials, this effect also depends highly on the polarisation of the light, which is required to be linear. The change of the refractive index n_z is given by

$$\Delta n_z = -\frac{1}{2} n_z^3 r_{zz} E^3, \tag{4.6}$$

where $r_{zz} = 33\,\mathrm{pm/V}$ is the electrooptic coefficient of $LiNbO_3$.
In the fabrication of these integrated devices, electrodes of a given length L are placed along the waveguide. Applying a voltage to these electrodes then changes the refractive index of the waveguide, which gives rise to a phase shift of the guided light. If this type of phase modulator is built in a Mach-Zehnder configuration one obtains an amplitude modulator [94, 341]. A voltage applied to the electrodes, here in a 'push-pull' configuration [342] leads to a phase difference along the arms, which results in a change of the output power of the light due to interference. This means the transmission of the EOM can be tuned between a minimal and a maximal power $P_{\mathrm{min/max}}$. The voltage needed to induce a phase shift of π is known as the half-wave voltage V_π and amounts to $1 - 3\,\mathrm{V}$ in our integrated devices at 894 nm.
The output power of the device as a function of the applied control voltage is given by its periodic cosine transfer function

$$P_{\mathrm{opt}}(V) = P_{\mathrm{min}} + (P_{\mathrm{max}} - P_{\mathrm{min}}) \left(\frac{1}{2} \cos\left(\frac{\pi(V - V_0)}{V_\pi} \right) + \frac{1}{2} \right). \tag{4.7}$$

Here, V_0 is the bias voltage of the EOM, which normally differs from the ideal $V_0 = 0$ and has to be controlled by special electronics.
Using this effect it is naturally possible to modulate the amplitude of the output light by applying an RF signal to the modulator on top of the bias voltage. The optical output

will then follow the electrical input and translate it into amplitude information, which depends on the amplitude and shape of the former.
The maximal power $P_{\max}$ is determined by the injection power, which cannot exceed the device's damage threshold, and the insertion loss, while $P_{\min}$ is a function of the device's extinction ratio and the input power.
In our experiments we make use of the Jenoptik AM905 model, for which the manufacturer states an extinction ratio of $36 - 38\,\mathrm{dB}$, an insertion loss of $4.7\,\mathrm{dB}$, a (cw) damage threshold of $100\,\mathrm{mW}$, and a typical half-wave voltage of $\sim 2.5\,\mathrm{V}$. However, experimental values are typically worse and we measure, e.g., insertion losses of $\sim 9\,\mathrm{dB}$, including fibre coupling loss. As for the extinction ratio, it should be noted that the manufacturer's value is given for the case of cw operation. In pulsed operation, this ratio tends to be less. The main reason for this is that the devices are designed for narrowband operation, and are highly wavelength/frequency dependent. An increase in the spectral width of the light, as is inevitable in pulsed operation, lowers the extinction due to the interference-based operational principle. In pulsed operation we see an extinction ratio of $\sim 20\,\mathrm{dB}$. Pulse generation works by keeping the EOM at the point of minimum transmission at $V_0 \pm V_\pi$ and then sending electrical pulses with an amplitude of V_π. This will produce optical pulses with a similar shape at an amplitude $P_{\max}$. The small shape distortion between the electrical pulses and the resulting optical pulses due to the cosine function is negligible. If driven with smaller peak voltages, the response of the EOM is kept in the linear regime and the optical pulse shapes behave well (no distorted peaks or similar). Moreover, this reduces the probability of permanently damaging the device [343], or at least increases its lifetime.
The main technical complication associated to working with EOMs is the drift of the bias voltage in timescales of seconds or minutes. This drift results from different physical processes in the substrate, such as charge accumulation, photorefractive effects, etc. [94]. It is mostly a problem for some time right after the devices are turned on. They seem to need a time for stabilisation where the bias drifts are larger and after some hours this behaviour reduces drastically. Permanent damage to the devices can be reduced if they are not constantly driven, but the driving voltage is turned off when not needed. When driven, operation at low powers also reduces these effects.
In our setup, the electrical control of the EOMs is connected via a bias tee to a Tektronix AFG31152 arbitrary function generator (AFG) (see Fig. 4.3 B) used to program the needed pulse sequences (see Sec. 4.2.3). The DC bias voltage sets $V_0 \pm V_\pi$, such that the transmission of the EOM without pulses is minimal. The DC drift is controlled via a RP, by looking at the baseline on a photodiode and setting it to zero manually when it drifts (see Fig. 4.3 C). For operations with low duty cycles,

i.e., when the width of the pulses is much lower than the repetition rate, EOMs can also be actively stabilised. We never went so far as to implement a real EOM active stabilisation, but in later rounds of the experiment we improved the manual bias finding by a python script (written by Christian Liedl and courtesy of Daniel Lechner, both from HU Berlin) that automatically looked for the minimum of the EOM response function and set the bias at this point (without active stabilisation). This program was problematic when measuring at SPL, since the finding of the minimum involved performing first a coarse scan and then a narrow scan around said minimum, which resulted in some jumps of the bias which could become problematic for the single photon counting avalanche photodiode (APD). Therefore, at SPL we decided to keep the manual bias reduction by looking at the baseline of the pulses and minimising it when it drifted.

Acousto-Optic Modulator

In the first implementation of the experiment, the pump laser switching was accomplished using an acousto-optic modulator (AOM). The same is true for the pulsing of the control laser in a later version of the experimental setup. An AOM is a device used to control the transmitted power, frequency, phase, and direction of a laser beam by means of an electrical driving signal [116, 344]. Its working principle follows the acousto-optic effect, as can be inferred from its name. The application of an oscillating mechanical sound wave on a crystal or glass material will generate a travelling strain wave and thus momentarily alter the material's microscopic structure. As a result of the photo-elastic effect, again the refractive index of the material will be affected. Not only will this induce an intensity modulation, but it can be used to shift the frequency and direction of the light. These devices are thus also referred to as acousto-optic deflectors (AOD) or Bragg deflectors/cells, as will be explained below.

An AOM or AOD is built of a transparent material, in our case tellurium dioxide, TeO_2, which acts as a propagation medium for the incoming light. The material's acoustic mode velocity amounts to 4200 m/s. A piezoelectric transducer is attached to the crystal and is fed with a strong oscillating RF signal. This gives rise to a vibrating sound wave with an acoustic frequency f_s of the order of some 100 MHz, a wavelength $\Lambda = 10 - 100\,\mu$m, and an acoustic power of $1 - 10$ W. This intense sound wave generates a travelling strain wave in the material, which creates a travelling refractive index grating. Light travelling through the device is then diffracted through Bragg diffraction.

Most AOMs, specially the ones used in our experiments, operate in the Bragg regime, where the substantial part of the diffraction efficiency goes into the ± 1 order, while the

transmission onto higher orders becomes negligible. When the Bragg condition is fulfilled, the diffraction angle θ_B of light of wavelength λ is given as

$$\sin\theta_B \approx \theta_B = \frac{m\lambda}{2\Lambda}, \tag{4.8}$$

for $m = 0, \pm 1$.
The optical frequency of the diffracted beam is increased or decreased by the acoustic frequency f_s depending on the order, due to a Doppler shift resulting from scattering from a moving plane. The transmitted $m = 0$ beam sees no change in frequency.
Furthermore, the acoustic power determines the diffracted optical power. This process might be sensitive to polarisation, depending on the device's design and material. The diffraction efficiency is defined as the ratio of the diffracted power to the incident optical power and can be tuned by selecting the correct driving frequency and power, and by optimal alignment. Moreover, the switching time of the device is determined by the transit time of the sound wave across the beam waist of the incident beam. Thus, AOMs expect a certain beam size for ideal operation.
In the optical setups used in this thesis, the model MT200-B100A0,5-800 AOM from AA Opto-Electronic is used. They are driven close to their center frequency of 196 MHz. The required input beam diameter is $200 - 300\,\mu$m, and their rise/fall time lies between $32 - 48$ ns. Therefore, AOMs should only be used to generate longer pulses. Moreover, the diffraction efficiency is specified at 85% at 800 nm. For information about the RF electronic components used to drive the AOMs, I again refer to Ref. [12]. In general, the diffracted beam is used, as it can be switched on and off. For the pump switching, the AOMs are driven with a sine wave of constant frequency and switched off after the required pumping time. In the case of the control pulse shaping, adding some modulation to the RF signal allows to modulate or pulse the output intensity. Accordingly, the sine wave is mixed with a programmable pulse shape. This was done in later rounds of the experiment to generate the control pulses and yielded a much better extinction ratio for the control laser compared to the one achieved by the EOMs, which allowed to reduce early unwanted readout of the signal (see Sec. 4.3).

Control amplification and filtering

Due to the power loss as a result of using an EOM for pulse shaping (due to their injection loss), the control pulses were amplified by a SUPERLUM SOA-352-870 semiconductor optical amplifier (SOA), in order to reach the necessary powers for efficient storage. The SOAs broadband amplified spontaneous emission (ASE) is suppressed by a combination of

a narrow-band dielectric filter of 1 nm FWHM (Alluxa), and a self-assembled Fabry-Pérot etalon (Name: Carl, $d = 0.50(2)$ mm length, Bernhard Halle GmbH) with a free spectral range of FSR $= 205.5$ GHz and a finesse of $\mathcal{F} \sim 47$ (see Fig. 4.3 B). This results in a control laser peak power of $P_{\mathrm{C,max}} = 12.9(1)$ mW before entering the memory cell.
In the second iteration of the experiment, the pulsing device for the control was, as mentioned above, changed from an EOM to an AOM. As a result, it was not necessary to amplify the control pulses with the SOA any more, as the AOM does not suffer from large injection losses like an EOM. This also removed the need for the ASE filtering with the first etalon. The optical powers were adjusted such that the same control power was achieved before entering the memory cell.

Experimental pulse sequences

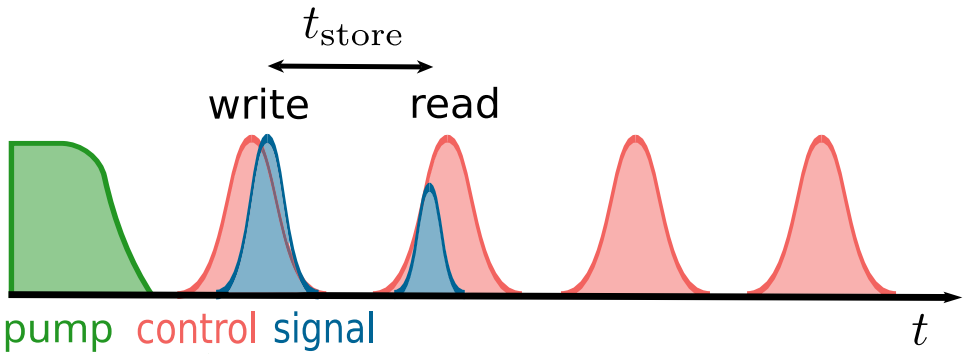

Figure 4.11: Experimental pulse sequence (not to scale). Shortly after the pumping is finished, the signal pulse enters the memory, delayed by a small amount with respect to the first control pulse, and is written into the memory by it. The second control pulse reads out the stored signal on demand. The third and fourth control pulses serve to test for extra read out and to determine the magnitude of the noise. The storage time t_{storage} is defined from the peak of the first signal pulse (left blue), to the peak of the retrieved pulse (right blue).

The first iteration of the experiments was conducted with Gaussian signal and control pulses of varying full width at half maximum (FWHM) generated by the Tektronix AFG. The latter is programmed in its Advanced Mode with a sampling rate of 2 GSa/s. Gaussian pulse shapes are chosen, as they have been shown to behave well in other memory experiments, as can be found in the literature [179, 241, 242]. This fact was analysed later in detail by Lizzy Robertson in the Genetic Algorithm optimisation experiment (see Sec. 4.4.3). The FWHM of the signal pulses here ranges from $5 - 50$ ns,

while for the control pulse it ranges from $8.75 - 87.5\,\mathrm{ns}$. The ratio between the width of the signal and the control pulses $\Delta t_C/\Delta t_S = 1.75$ remains equal throughout the experiment. This value was determined after an optimisation measurement, performed during the preparation of the memory experiment.
Since the (later on) chosen optimal FWHM width of the control pulses of $\Delta t_\mathrm{C} = 44\,\mathrm{ns}$ is long enough, the rise/fall or switching time of the AOM ($32\,\mathrm{ns} \leq T_r \leq 48\,\mathrm{ns}$) did not pose a problem as it would have for much shorter pulse widths. On the contrary, the pulsing of the signal remained being realised by an EOM.
A single run of the storage-retrieval experiment begins by switching on the pump laser for $10\,\mu\mathrm{s}$ to prepare the state $|g\rangle$. The falling edge of the pump pulse serves as the trigger for the rest of the experiment. The signals to trigger the AFG and the measurement devices were originally generated by a T564 digital delay generator from Highland Technologies, which set the clock of the experiment. After pumping, the control and signal pulses enter the memory. Here, the signal pulse is delayed for several ns with respect to the control pulse, such that its maximum lies at the beginning of the falling edge of the control pulse, as depicted in Fig. 4.11. This fact ensures that the signal pulse enters the memory at the time the EIT window starts to close adiabatically, such that maximal pulse compression and storage is achieved. This variable delay can be adjusted to optimise the readout efficiency and varies slightly with experimental parameters. To retrieve the signal photon from the memory, a second identical control pulse is sent into the cell after $t = 200\,\mathrm{ns}$. Two further control pulses separated by the same time difference serve as comparative measure for the noise suppression. If the first retrieval was not efficient enough, the second retrieval pulse will in some cases yield a second readout. The storage and retrieval experiment is repeated at a rate $f_\mathrm{rep} = 1/(11\mu\mathrm{s})$.
In later iterations of the experiment, after changing the control EOM for the AOM, it was necessary to drive both AOMs with an AFG and to automatise the programming of the pulses. Therefore, the Tektronix AFG was exchanged for a Zürich Instruments 4-channel HDAWG Arbitrary Waveform Generator with a bandwidth of 750 MHz and a sampling rate of 2.4 GSa/s. This device then set the clock for the experiments, again starting with the falling edge of the pump pulse.

Single photon level calibration

For single-photon-level measurements, the signal pulse intensity is attenuated with a combination of optical AR-coated neutral density (ND) filters from Thorlabs. To calibrate the photon number, a monitoring line is set up before the signal enters the memory

cell. Here, 10% of the signal pulse (N_{mon}) is split from the signal, coupled into a fibre, and monitored on the avalanche photodiode (APD, see Sec. 4.2.5). The splitting ratio $\sigma = 10:1$ of memory to monitor is measured with two power meters (Thorlabs PM160). Their measurement uncertainty lies at ±3%. This is depicted in Fig. 4.3 C.
The idea behind this calibration stems from the photon statistics of coherent pulses. A coherent light source shows Poissonian statistics. This means, the probability of detecting ν photons in a pulse containing, on average, $\mu = 1$ photons is given as

$$p_{\mu=1}(\nu) = \frac{e^{-\mu}\mu^{\nu}}{\nu!} = \frac{1}{e\,\nu!} \quad \text{for } \nu \geq 0. \tag{4.9}$$

Thus, the probability of detecting exactly one photon is $p_{\mu=1}(1) \approx 37\%$, while the probability of detecting none or more photons is then $p_{\mu=1}(\nu \neq 1) \approx 66\%$. Conversely, if the pulse contains, on average, $\mu = 0.1$ photons, this probability changes to

$$p_{\mu=0.1}(\nu) = \frac{e^{-0.1} \cdot 0.1^{\nu}}{\nu!} \quad \text{for } \nu \geq 0, \tag{4.10}$$

resulting in a probability of detecting a photon being $p_{\mu=0.1}(1) \approx 9\%$ and of detecting zero photons $p_{\mu=0.1}(0) \approx 90\%$, while the higher order probabilities are negligible. Therefore, monitoring at the signal arm with 10% of the total intensity ensures a higher accuracy by lowering the probability of detector saturation resulting from a too low vacuum component. This will yield a much lower probability of sending more than one photon into the memory, and thus a lower experimental error.
The desired number of counts we want to measure on the monitor APD are determined from the sequence length $t_{\mathrm{seq}} = 11\,\mu$s, knowing we have one signal pulse per sequence and thus per trigger. This amounts to ∼ 91000 counts/s. 10% of these go into the monitor arm. Including the APD efficiency of $\eta_{\mathrm{APD}} \approx 33\%$, this yields about 3000 counts. From this value, the dark-count rate of the detector needs to be subtracted. However, if the EOM bias is well minimised, we see the dark count rate tends to 0. Therefore, if the monitor arm is maintained at a count rate of ∼ 3000 cts, we can ensure a SPL signal with an average photon number of $|\alpha|^2 = \mu = 1.0(1)$.

4.2.4 Memory cell and system preparation

The orthogonally polarised signal and control beams are outcoupled from their respective polarisation-maintaining (PM) fibres, overlapped using a calcite prism, and sent through the Cs memory cell (see Fig. 4.3 D). The fibre collimators used throughout the experiment are all different versions of the Fibre Collimator series 60FC-SF from Schäfter+Kirchhoff.

The choice of the collimator depends on the (intended or actual) beam waist size at different points of the experiment. We put special care into making signal and control beams co-propagate in parallel through the cylindrical vapour cell. The control and signal beam diameters are 109(5) μm and 93(5) μm FWHM at their focus at the center of the memory cell, and their Rayleigh length (as for all beams) extends beyond the cell's end. With a dipole moment of $\mathcal{M}_{\mathrm{Cs,D1}} = 2.7 \cdot 10^{-29}$ C·m (Table 3.2, [288]) for the Cs D_1 transition, and the aforementioned peak power of $P_{\mathrm{C,max}} = 12.9(1)$ mW, this yields a peak control Rabi frequency of $\Omega_{\mathrm{C}} \approx 2\pi \cdot 540$ MHz (see Eq. (3.14)). The peak control field intensity amounts to $I_{\mathrm{C}} \approx 100 \frac{\mathrm{W}}{\mathrm{cm}^2}$ (see Eq. (3.16)).
In order to estimate the wavelength of the spinwave, we estimate the residual angle between signal and control to be $\beta \approx 330\,\mu$rad. This results from the fact that the control couples worse than the signal into the coupler that goes from the memory to the detection. Specifically, this coupling efficiency for the control is $\sim 65\%$, while for the signal it achieves an efficiency of $\sim 88\%$. Therefore, assuming the beams are displaced by approximately the size of the fibre input (5 μm), and using the coupler's focal length of $f = 15$ mm, we can calculate this angle. This is surely an upper bound on the beam displacement, but serves as an approximation. This results in an approximate wavelength of the spinwave of $\lambda_{\mathrm{sw}} = 2\pi/|\vec{k}_{\mathrm{S}} - \vec{k}_{\mathrm{C}}| \approx 3$ mm[1].

The Cs cell is 7.5 cm long and has a 2 cm diameter. It was manufactured by Precision Glassblowing and is made out of quartz. It contains ^{133}Cs and 5 Torr of N_2 buffer gas, which is added in order to reduce the atomic motion of the Cs atoms as a result of collisions with the buffer gas atoms. This transforms the Cs motion from a ballistic one to a diffusive one as explained in Ch. 3, Sec. 3.2.3. The cell windows are coated with double-sided anti-reflection (AR) coating at the Cs D_1-line transition frequency. However, it is not coated with paraffin anti-relaxation coating to reduce spin-destruction mechanisms in possible wall collisions of the atoms, as the buffer gas is assumed to reduce these unwanted effects by a sufficient amount, at least on the timescales of the experiment. The vapour cell is enclosed inside a cylindrical two-layer μ-metal magnetic shielding fabricated by Sekels. This nominally reduces the spurious (earth) magnetic field in its interior by a factor of 2000 and is important to reduce relaxation mechanisms involving the different Zeeman sublevels, such as spin exchange collisions. Measurements from our project partners at PTB confirmed a field reduction factor of 1000, if the shield is well degaussed.
The cell is heated using two Thorlabs HT10K flexible polyimide foil heaters with a 10 kΩ thermistor, controlled by a Meerstetter TEC 1091 temperature controller, and is

[1] The value given in Ref. [1] was overestimated by a factor 2 in the calculation.

kept at a temperature of $T_{\text{cell}} = 60\,°\text{C}$. This temperature corresponds to the temperature of the heating pads (determined from the measured resistance) and not necessarily of the whole cell, but was nevertheless used as the approximate reference temperature. Temperature fluctuations inside the cell are ignored. We assume that the cell will be in thermal equilibrium after some time. The aforementioned temperature was determined to be a good compromise between a large enough optical depth, not too large Doppler broadening (proportional to $\sqrt{T}$), and acceptable pumping behaviour, as explained in Sec. 4.2.2. The Doppler-broadening-reduced OD of the signal transition ($F = 3 \rightarrow F' = 3$) is calculated via Eq. (3.31) to be $2d_{\text{opt}} = 13$. This value can be compared with the experimentally estimated value from preliminary pumping efficiency measurements (see Sec. 4.2.2) of $2d_{\text{opt}} = 3.65$. The values differ by a factor of 3. As mentioned earlier, more accurate measurements of the OD at the experimental configurations should definitely be performed. Therefore, I here take the theoretically calculated value for further measurements and calculations.
The heating pads were placed inside the shielding in this first simple heater design. Since the heating pads have to be driven with a current, this creates residual magnetic fields inside the shield, which reduce the possible storage time of the memory. To eliminate this effect caused by the heating, the latter was switched off during measurements.
As a result of these effects, and with the goal to extend the achievable storage times in later runs of the experiment, a new heating system made out of oxygen-free-high-conductivity (OFHC) copper was designed, where the heating was implemented from outside the magnetic shielding. A version of this new system was used in the memory built for rack integration by Alex Erl in the QuMSeC project [11] (see Ch. 5), and is described there in more detail.

Vapour cell parameters

In Chapter 3, the atomic processes occurring in warm atomic vapour cells were described in length. Here, we want to give specific values calculated for the above mentioned vapour cell at the memory operation temperature of $T_{\text{mem}} = 60\,°\text{C} \approx 330\,\text{K}$.
For the diffusion, we estimated the diffusion constant D at the mentioned temperature with Eq. (3.48) from the D_0 values given in the literature (see Table 3.5). For the pressure value we assumed the N_2 buffer gas pressure $P_{\text{bg}} = 5\,\text{torr}$. From the diffusion constant we calculate the diffusion length Δr using Eq. (3.45) for a diffusion time of $t = 1\,\mu\text{s}$. This time, i.e., the time it takes the atoms to diffuse out of the interaction region, is experimentally determined to be similar to the achievable storage time with the present

setup (see Sec. 4.3.3).
We also give a value for the mean free path ℓ between Cs and buffer gas collision, estimated from Eq. 3.52. From the Cs vapour pressure and the ideal gas law, we calculate the Cs density n_{Cs} at T_{mem}. Comparatively, we also calculate $n_{\mathrm{Cs,ph}}(T_{\mathrm{mem}})$ from the phenomenological Eq. (3.53). As the second value has an accuracy of $\pm 5\%$ [318], it is sensible to keep this one.

Regarding the collisional broadening rates, we calculate first the Cs-Cs collisional rates, which can be divided into an optical self-broadening rate $\gamma_{\text{Cs-Cs,dip}}$ resulting from dipole-dipole interaction (Eq. 3.54), and the spin exchange (SE) rate γ_{SE}, calculated using Eq. (3.50) with the spin exchange cross-section $\sigma_{\mathrm{SE}} = 2.1 \cdot 10^{-4} \frac{1}{\mathrm{cm}^2}$ from Ref. [302].
Secondly, we calculate the relaxation rates resulting from Cs-buffer-gas collisions, which result from the hyperfine shift interaction and the spin rotation interaction [177, 302]. In this case, we calculate the total rate γ_{bg} in two different manners, in order to compare the results. The first calculation is obtained via Eq. (3.50), with the total collisional cross section $\sigma_{\mathrm{tot}} = 8.86 \cdot 10^{-14}\mathrm{cm}^2$ given in Table 3.6[1]. The second calculation is done using the value for the pressure broadening rate per pressure $\alpha_p(T_0) = 16.36 \frac{\mathrm{MHz}}{\mathrm{torr}}$, given in Ref. [321] with Eq. (3.55) and using a buffer gas pressure of $P_{\mathrm{bg}} = 5\,\mathrm{torr}$.
The total collision rate, corresponding to T_2 relaxation mechanisms, is given as $\gamma^{\mathrm{col}} = \gamma_{\mathrm{Cs}} + \gamma_{\mathrm{bg}} + \gamma_{\mathrm{wall}}$, as from Eq. (3.49). Its main contribution comes from Cs-buffer-gas collisions, while the remaining broadening rates are comparatively negligible, as can be taken from the calculated values in Table 4.3. Here we ignore the contribution due to wall collisions γ_{wall}, since from the results for the diffusion process, we assume that the atoms do not reach the walls in the timescales of memory operation ($\mathcal{O}(\mu\mathrm{s})$). The time between collisions of different species can be calculated as the inverse of the respective collisional rates.
At the memory operation temperature T_{mem}, we further calculate the Doppler broadening $\gamma_{\mathrm{Doppler}}$ using Eq. (3.44). Adding all homogeneous contributions following Eq. (3.23) and calculating the approximate convoluted linewidth from Eq. 3.35, we can also estimate the total dephasing rate of the excited state γ_e. Furthermore, we calculate the probability Q that an atom decays radiatively (i.e., by emitting a photon) from an excited state as a result of quenching, using Eq. (3.56).
Additionally, we estimate the width of the EIT window $\Delta\omega_{\mathrm{EIT}}$ at memory operation with Eq. (3.74).
Last but not least, in Sec. 3.3 of Ch. 3, an analytically calculated maximal limit for the total efficiency in the case of storage followed by backward retrieval is given as a function

[1] Note the extra factor $\frac{1}{10}$ that has to be added phenomenologically, as in Ref. [177].

Magnitude	Value	Eq.
Control Rabi frequency	$\Omega_C \approx 2\pi \cdot 540\,\mathrm{MHz}$	(3.17)
Optical depth	$2d_{\mathrm{opt}} = 13$	(3.31)
Cs number density	$n_{\mathrm{Cs}} = 9.2 \cdot 10^{11}\,\frac{1}{\mathrm{cm}^3}$	(3.47)
	$n_{\mathrm{Cs,ph}} = 1.1 \cdot 10^{12}\,\frac{1}{\mathrm{cm}^3}$	(3.53)
Diffusion constant	$D = 25\,\frac{\mathrm{cm}^2}{s}$	(3.48)
Diffusion length	$\Delta r(\Delta t = 1\,\mu\mathrm{s}) = 100\,\mu\mathrm{m}$	(3.45)
Mean free path*	$\ell \approx 300\,\mathrm{nm}$	(3.52)
Broadening & collision rates	$\gamma_{\mathrm{Cs\text{-}Cs,dip}} = 2\pi \cdot 500\,\mathrm{kHz}$	(3.54)
	$\gamma_{\mathrm{SE}} = 2\pi \cdot 0.6\,\mathrm{kHz}$	(3.50)
	$\gamma_{\mathrm{bg},1} = 2\pi \cdot 90\,\mathrm{MHz}$	(3.50)
	$\gamma_{\mathrm{bg},2} = 2\pi \cdot 80\,\mathrm{MHz}$	(3.55)
Doppler broadening	$\gamma_{\mathrm{Doppler}} = 380\,\mathrm{MHz}$	(3.44)
Total dephasing rate of $\lvert e\rangle$	$\gamma_e = 2\pi \cdot 390\,\mathrm{MHz}$	(3.35)
Radiative decay prob.	$Q = 0.06$	(3.56)
Width of EIT window	$\Delta\omega_{\mathrm{EIT}} = 230\,\mathrm{MHz}$	(3.74)
Max. total efficiency**	$\eta_{\mathrm{tot}}^{\mathrm{bw}} \approx 55\%$	(3.116)

Table 4.3: Calculated parameters for the memory cell at the operation temperature $T_{\mathrm{mem}} = 60\,°\mathrm{C}$. The equations used for the calculation can be found in Ch. 3. *Mean free path between Cs and N_2 collisions. Used values for the collision cross sections are $\sigma_{\mathrm{SE}} = 2.1 \cdot 10^{-4}\frac{1}{\mathrm{cm}^2}$ [302] and $\bar{\sigma}_{\mathrm{tot}} = \frac{1}{10} \cdot 8.86 \cdot 10^{-14}\mathrm{cm}^2$ [306]. The factor $\frac{1}{10}$ has to be added phenomenologically for $\gamma_{\mathrm{bg},1}$ and $\gamma_{\mathrm{bg},2}$ to agree (see Ref. [177]). The time between collisions of different species can be calculated as the inverse of the respective collisional rates. Further used values are $\alpha_p(T_0) = 16.36\,\frac{\mathrm{MHz}}{\mathrm{torr}}$, given in Ref. [321], $\beta_{\mathrm{Cs}} = 5.7\,\frac{\mathrm{Hz}}{\mathrm{cm}^3}$ [320], and $P_{\mathrm{bg}} = 5\,\mathrm{torr}$. Max. total efficiency** of storage followed by backward retrieval (analytic) from Ref. [125] calculated using $2d_{\mathrm{opt}}$ instead of d_{opt}.

of the optical depth of the system in Eq. (3.116). As this formula is obviously only valid for $d_{\mathrm{opt}} > 5.8$[2] and in theory in the limit $d \to \infty$, we will use the value $2d_{\mathrm{opt}} = 13$, calculated for the experimental optical depth. This yields a rough estimate of the regime of efficiencies we can expect from our memory. The resulting values are summarised in Table 4.3.

[2]Since for lower optical depths it yields negative memory efficiencies.

4.2.5 Filtering system and detection

Filtering

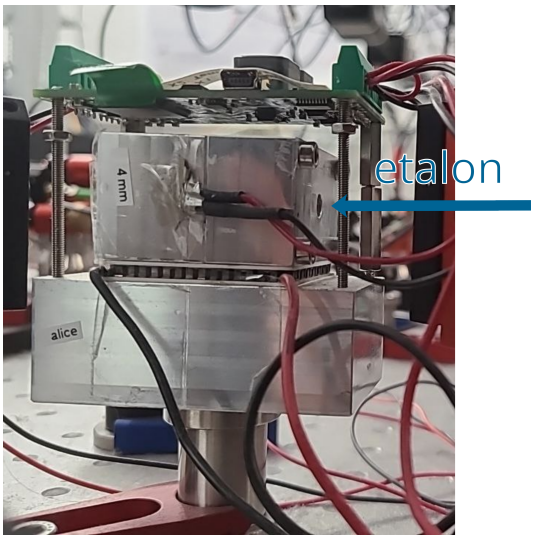

Figure 4.12: Photo of the designed etalon mount.

In Chapter 3, a comprehensive description of the main noise sources in a Λ-type EIT (Raman) memory was presented. As a reminder, the largest source of noise tends to be technical noise, which needs to be filtered out before one can tackle the remaining noise types arising from the atoms themselves, these being fluorescence, SRS, and FWM. From the estimation performed there, we came to the conclusion that between 9 and 10 orders of magnitude control-field suppression are necessary to filter out a single photon from the strong control field. For achieving a good SNR, an even higher suppression of > 11 orders of magnitude is desirable. This is achieved via a combination of spatial, polarisation, and spectral filtering.

Our spatial filtering, since we try to reduce the angle between signal and control to a minimum ($\beta \approx 330\,\mu$rad, see above), and make them copropagate in parallel in order to increase the achievable lifetime of the spinwave and prevent fast dephasing [119], consists only of the different mode matching at the coupler going to the detection. This coupler (Schäfter+Kirchhoff (SuK) A15-02) is intended to couple the signal beam as efficiently as possible, and will therefore ideally be less optimised for the larger mode of the control.

The polarisation filtering is achieved by the combination of a $\frac{\lambda}{2}$- and a $\frac{\lambda}{4}$-waveplate, and the second calcite prism. This separates vertical and horizontal polarisations, and allows us to increase the control field suppression on the signal-to-detection arm by up to 7 orders of magnitude. For this to work well it must be ensured that the beams to not impinge on

the cell walls at exactly 90°, but at a minimal angle, in order to reduce unwanted reflections.

The following spectral filtering is accomplished by two Fabry-Pérot etalons housed on a self-designed mount (Names: Alice and Bob), with an FSR = 25.6 GHz and a finesse of $\mathcal{F} = 47$, as estimated from transmission measurements. These are solid etalons made out of quartz glass (SiO_2) from Bernhard Halle GmbH. This material shows a high trasmittance at infrared frequencies. The two etalons have a length of $d = 4.00(2)$ mm. The refractive index of the material is $n \approx 1.5$ and the reflectivity of the dielectric-coated plan-parallel surfaces is $R = 95(2)\%$ at $\lambda = 894$ nm, as stated by the manufacturer. The stated FSR was determined in experiments. The finesse is an approximate value, since we did not carry out a thorough filter characterisation and relied on results from colleagues who had etalons from the same batch. There will always be some variation between the etalons, but we assumed it to be negligible. The etalon mounts were originally designed for this work and have been improved over the years for better performance [11]. They consist of custom-made (at the DLR workshop) aluminium holders that contain the etalon in the center. The latter is held in its place with a rubber retaining ring. In later designs this was changed for an aluminium retaining ring, in order to increase the stability. A Peltier element is glued to the holder below the etalon using thermal adhesive. Below, further aluminium parts serve as a heat sink. In order to measure and control the temperature, a PT100 standard thermistor is glued on the holder as close as possible to the etalon. It is connected to a TEC-1091 (Meerstetter Engineering). This allows to tune and control the temperature with an accuracy of ~ 10 mK, in order to vary the maximal transmission frequency. Fig. 4.12 shows a picture of the mount of etalon Alice. To optimise the transmission through the etalons, a pilot-beam configuration is used. Such a beam will have an almost constant beam diameter over its working distance, that is, the distance between the two identical couplers used for out and in-coupling. This ensures that the beam waist is positioned exactly at the center of the etalon and the spatial mode is minimally divergent. Because these are plane-parallel, no transverse mode matching is required. The signal coming from the memory exits the coupler (SuK A.6.2S-02) which is mounted on a tip/tilt adjustable mount and is reflected on a mirror before entering the first etalon (Alice). Since the etalons have plane-parallel surfaces, this allows to have enough degrees of freedom for the transmission optimisation (see Fig. 4.3 E). For the second etalon (Bob), a pair of SuK M5.10 couplers are used, and the configuration is analogous, adapted to the different focal length of the couplers. The adjustment of the etalons was achieved through firstly centring the beam at the etalon and matching the back-reflected beam with the incoming one, and then scanning the laser to find the fundamental mode and optimising it (increasing its height) via beam walking.

Only then, the temperature can be scanned to find the maximal transmission frequency, with the laser not scanning any more. Subsequent fine tuning via beam walking can lead to some small extra percentage in transmission. The maximal (and repeatedly achievable) transmission through the etalons after careful adjustment was 93% for Alice, and 85% for Bob, not including the fibre coupling efficiencies. Including the latter, the total transmission (end-to-end) through each etalon system was 82% for Alice, and 78% for Bob. This is always measured in cw at powers of some mW and will not be exactly the same at SPL. It is important to note that etalons show a lower performance at too high laser powers due to a high thermal load [94].
Each of these etalons further attenuates the control laser by 3 orders of magnitude within the signal beam path. In total, this amounts to a control laser suppression by 13 orders of magnitude. Meanwhile, the signal light is only attenuated by a factor of 2.5, measured from before the vapour cell. This allows us to achieve a good SNL at single photon level, as will be shown below.
As the two etalons were connected via a single mode fibre, if the mode matching was too good, an 'etaloning' effect between the end surface of Alice and the first surface of Bob was visible. If the transmission maxima of both etalons were minimally shifted with respect to one another, this caused large oscillations of the transmitted signal, which resulted in large variations of the measured efficiency. This effect can be seen in Fig. A.6. Therefore, the optimisation of each etalon had to be conducted independently and care had to be taken to minimise these oscillations by very slightly diminishing the alignment of the fibre coupling of Alice into Bob. This resulted in a more stable signal without significantly deteriorating the transmission.
The second etalon (Bob) was not only used for filtering but also for spectral noise measurements (see Sec. 4.3.2). For this, it was necessary to scan the transmission frequency over twice its spectral width using the TEC. This implied a temperature scan over $\sim 20\,°\mathrm{C}$. The shift of the maximum transmission frequency as a function of temperature was determined to be practically linear (meaning the second term in Eq. (3.149) is negligible) with a thermal expansion coefficient for the Cs D_1 line for Alice of $\beta_{\mathrm{Alice}} = 2.163\,\frac{\mathrm{GHz}}{°\mathrm{C}}$. This was assumed to be the same for Bob, since they originate from the same substrate. It is important to note that the etalons tended to drift after some time, on the order of hours to days, due to thermal fluctuations in the lab, and it was mostly required to readjust them slightly before each measurement. After having changed the temperature, some minutes were necessary for them to stabilise in temperature and maximal transmission. A thorough characterisation of the behaviour of similar etalons (of the same batch), in that case with a length of $d = 4.00(2)\,\mathrm{mm}$, was performed by Alex Erl in his Masters thesis [11], in the context of the portable rack-mounted memory-system

demonstrator developed in the QuMSeC project (see Ch.5, Sec. 5.7).

Detection

From the spectral filtering, a single mode PM fibre connects to the detection. On the first iteration of the experiment, the signal photons were detected by a single-photon-counting avalanche photodiode (APD) (Laser Components COUNT-50C-FC), with a nominal detection efficiency of $\eta_{\mathrm{APD}} = 33(5)\%$ at 894 nm, and a dark-count rate of 50 cts/s. The dead time of this APD lies between $42 - 48$ ns. To minimise stray photons entering the APD, it was covered with Thorlabs BK5 blackout fabric. The measurements were, to the delight of my colleagues, always carried out with the room lights off. The APD is connected to a time-to-digital converter, the Time Tagger 20, from Swabian Instruments. This allows to analyse the measured signal using time-correlated (or time-stamped) single photon counting, i.e., to obtain histograms of the incoming photons for varying integration times. These histograms are taken for a total integration time t_{int} of 60 s using a bin size of 1 ns.
For the second iteration of the experiment during the review process, we had acquired a Opus One superconducting nanowire single-photon detector (SNSPD) from Quantum Opus. This detector offers a much higher detection efficiency of $\eta_{\mathrm{QO}} \approx 97\%$ and an almost vanishing dark-count rate of 1 cts/s at 895 nm. The dead time of this device is ~ 25 ps, and thus negligible for our experiments.
The total setup efficiency measured from before entering the memory until detection amounts to $\eta_{\mathrm{setup}} = 40\%$, measured in cw.

As a summary, a schematic view of the first implementation of the experimental setup is depicted in Fig. 4.13. For the second iteration, as mentioned, the control EOM was replaced by an AOM, the SOA was removed, and the APD was exchanged for a SNSPD.

4.3 Results

I will now present the results obtained for the hyperfine Λ-memory, mainly in the measurements for the publication and review of Ref. [1], and some further measurements carried out in the preparation for these measuring campaigns. This will include some measurements on the achievable storage time of the memory system.
Figure 4.14 shows a typical measured photon arrival time histogram, as used for all further analysis. Shown are measured data for storage and retrieval of a coherent state containing

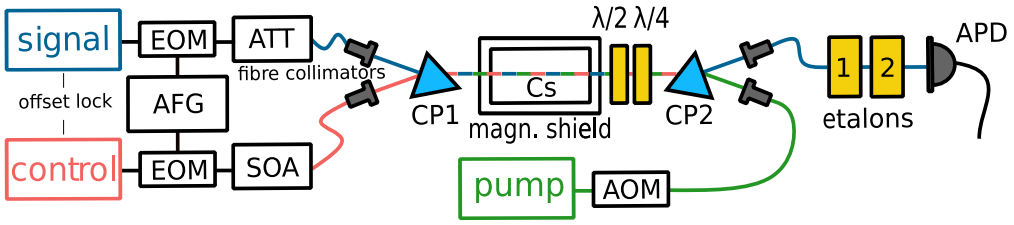

Figure 4.13: Schematic memory experiment setup. AFG: arbitrary function generator; AOM: acousto-optic modulator; APD: single-photon counting avalanche photodiode; ATT: attenuator; CP1, CP2: calcite prisms; Cs: vapor cell inside magnetic shielding; EOM: electro-optic modulator; $\lambda/2$, $\lambda/4$: wave plates; SOA: semiconductor optical amplifier.

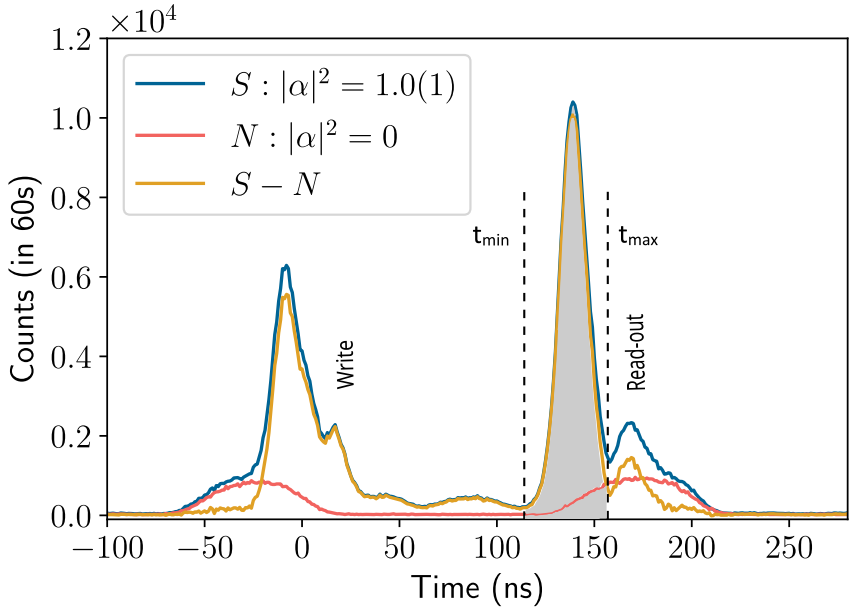

Figure 4.14: Exemplary arrival time histogram of detected photons in a memory experiment integrated for 60 s for an incoming coherent state with a Gaussian envelope containing $|\alpha|^2 = 1.0(1)$ photons on average (blue), for blocked input signal ($|\alpha|^2 = 0$) (red), as well as the resulting noise-corrected signal (yellow). The shaded area shows the detection window of width $t_{\max} - t_{\min}$ used for further analysis of the end-to-end efficiency η_{e2e} of the memory setup and the signal-to-noise ratio SNR. The storage time is $t_{\mathrm{storage}} = 140(1)$ ns, as measured from the maximum of the input signal to the global maximum of the retrieval pulse.

$$|\alpha|^2 = \frac{N_{\mathrm{mon}}\,\sigma}{f_{\mathrm{rep}}\,t_{\mathrm{int}}\,\eta_{\mathrm{APD}}} = 1.0(1) \tag{4.11}$$

photons on average, a noise measurement resulting from storage of a vacuum state with $|\alpha|^2 = 0$, arising from a blocked input and thus corresponding to the memory noise (residual control and further noise contributions), and the noise-corrected signal. The uncertainty of $|\alpha|^2$ arises from the error in the splitting ratio σ of signal to monitor, measured with two power meters (Thorlabs PM160), the uncertainty of the APD efficiency $\eta_{\mathrm{APD}} = 0.33(5)$, and the statistical error in the monitored photon number N_{mon}. The peak at $t = 0\,\mathrm{ns}$ corresponds to the part of the signal pulse that is not stored and thus transmitted through the memory (leakage). The peak at $t = 140\,\mathrm{ns}$ corresponds to the signal readout from the memory. As shown in Fig. 4.14, the temporal profile of the retrieved signal peak is distorted by the memory and shows two distinct maxima. The exact reason for this distortion is not completely clear, but depends on the timing between signal and control pulses, among other effects. The leakage also shows a similar distortion. We define the storage time t_{storage} as the difference between the first (and highest) of these maxima, and the peak of the incoming signal at $t = 0\,\mathrm{ns}$. The used storage times were chosen to be short in order to focus on the η_{e2e} and SNR, but can be extended into the μs range with the present setup (see Sec. 4.3.3).

In the second iteration of the experiment, performed during the review process, the pulse generation of the control pulse using an EOM, and the subsequent amplification with the SOA had been exchanged for pulse generation via an AOM and no further pulse amplification (as the same maximal powers $P_{\mathrm{C}} \approx 13\,\mathrm{mW}$ could be reached without amplification, since no strong attenuation of the control power is caused by the AOM compared to the EOM). The main reason for this exchange was the above mentioned problematic extinction of the control pulse power to zero when no pulse was present. This caused a small premature readout from the memory, detrimental for the achievable memory efficiency, as can be seen between the leakage and the retrieval pulse in Fig. 4.14. Comparatively, Fig. 4.15 shows the improved power extinction to zero when no pulse is present, achieved by using an AOM for pulsing the control, instead of an EOM. Here, the storage time is chosen to be $t_{\mathrm{storage}} \sim 340\,\mathrm{ns}$. In this case, the retrieved signal still shows some distortion after the memory, but for the leakage the distortion has disappeared, a fact that is still not very clear.

4.3.1 Efficiency and SNR optimisation

Now we will turn to the discussion of the results of the simultaneous optimisation of the end-to-end efficiency and the signal-to-noise ratio of the memory, with respect to three

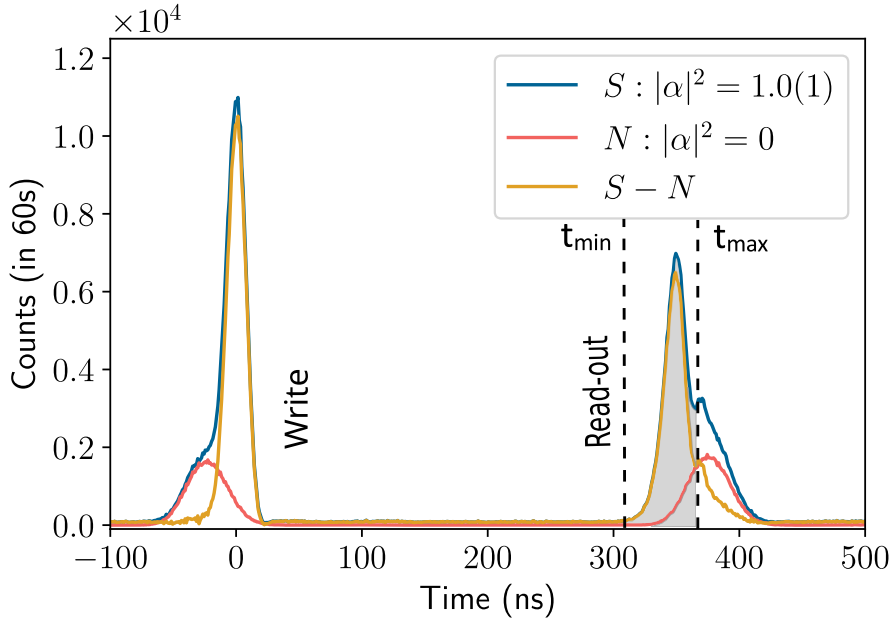

Figure 4.15: Arrival time histogram from the second iteration of the experiment, where the pulse generation device for the control pulse was switched from an EOM to an AOM. The chosen storage time in this case is $\sim 340\,\mathrm{ns}$. Note the improved extinction ratio of the AOM allows to better turn off the control pulse, and thus leads to no unintended early readout.

relevant parameters: the signal pulse width Δt_S, the control pulse energy E_C, and the detuning Δ.

Given the temporal envelope of the retrieved signal, the η_e2e of the memory setup, including the filtering system, and the SNR at single-photon level are given as

$$\eta_\mathrm{e2e} = \frac{N_\mathrm{signal} - N_\mathrm{noise}}{|\alpha|^2\,\eta_\mathrm{APD}\,f_\mathrm{rep}\,t_\mathrm{int}}, \tag{4.12}$$

$$\mathrm{SNR}_\alpha = \frac{N_\mathrm{signal,\alpha} - N_\mathrm{noise}}{N_\mathrm{noise}}, \tag{4.13}$$

where $N_\mathrm{signal,\alpha}(N_\mathrm{noise})$ correspond to the number of signal (noise) counts integrated over the detection window. Due to the long integration time, the statistical error is small and the uncertainty in η_e2e is dominated by the systematic error in the power measurement and the calibration of SPL. For the SNR, as it is measured at SPL, the error bars are proportional to the uncertainty of $|\alpha|^2$. The η_e2e increases with the length of the retrieval time integration window t_max, while the SNR decreases, as can be taken

from the Fig. 4.16. Hence, a compromising value of $t_{\max} = 155\,\text{ns}$ was chosen. The lower integration limit is always taken at the minimum before each retrieval peak (present in the measurements conducted with a EOM, see Fig. 4.14).
For all measurements performed in the following, we took $\Delta t_S = 25\,\text{ns}$, $\Delta = 2300(100)\,\text{MHz}$, and $E_C = 560(50)\,\text{pJ}$ as baseline parameters, and varied only the respective parameter in each optimisation.

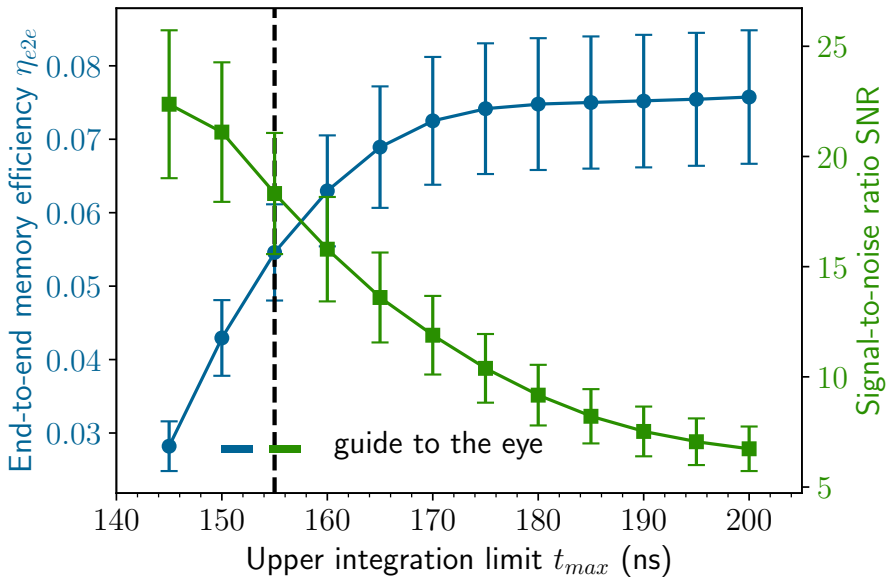

Figure 4.16: Exemplary end-to-end efficiency (η_{e2e}, blue circles) and signal-to-noise ratio (SNR, green squares) of the memory as a function of the maximal bound of the detection window of width $t_{\max} - t_{\min}$. We use $t_{\max} = 155\,\text{ns}$ (black dashed line), being a good compromise between η_{e2e} and SNR, and keep this value for the rest of the analysis.

Figure 4.17 shows the dependence of η_{e2e} and SNR on the signal pulse width Δt_S. Here, the control pulse width was also increased, while keeping the ratio between it and the signal pulse width constant at $\Delta t_C/\Delta t_S = 1.75$, as explained in Sec. 4.2.3. Δt_S is related to the bandwidth $\Delta\omega_S$ (FWHM) of the pulses that are stored in the memory as $\Delta t_S\,\Delta\omega_S = 2\ln(2)/\pi$, for Fourier-transform-limited Gaussian pulses. Here, both η_{e2e} and the SNR show a saturation behaviour.
The efficiency as a function of signal pulse width in Fig. 4.17 is modelled by the following formula

$$\eta_{\mathrm{e2e}}(\Delta t_{\mathrm{S}}) = \frac{\eta_{0,t_{\mathrm{S}}}}{\sqrt{1+(\frac{4\ln(2)}{\Delta t_{\mathrm{S}}\,\Delta\omega_{\mathrm{mem}}})^2}}, \tag{4.14}$$

where $\eta_{0,t_{\mathrm{S}}}$ is the maximal achievable efficiency and $\Delta\omega_{\mathrm{mem}}$ is the bandwidth of the memory. This model arises from the Maxwell-Bloch equations and describes how efficiently a pulse of given width Δt_{S} is converted into an atomic spinwave, when limited by the available control Rabi frequency Ω_{C}, which determines the spectral width of the EIT window, and therefore the memory bandwidth [196]. It is in good agreement with the measured data and yields $\eta_{0,t_{\mathrm{S}}} = 0.128(7)$ and $\Delta\omega_{\mathrm{mem}} = 220(30)\,\mathrm{MHz}$. The resulting width of the EIT window agrees extremely well with the theoretical value of $\Delta\omega_{\mathrm{EIT}} = 230\,\mathrm{MHz}$ calculated in Table 4.3 and thus validates our findings. This implies that signal pulses with a bandwidth smaller than the EIT window will be stored efficiently in the memory. Once the pulse tails of the Gaussian pulses do not fit into the window any more ($\Delta\omega_{\mathrm{S}} \gtrsim 2\pi \cdot 20\,\mathrm{MHz}$), the efficiency will start decreasing. From the behaviour of η_{e2e} we can further deduce that our memory works well for temporally long pulses even above 50 ns, with a relatively constant end-to-end efficiency of $\eta_{\mathrm{e2e}} \sim 13$ (corrected for zero storage time). The efficiency will only begin to decrease again once the spatial length of the pulse does not fit inside the memory cell any more.

Figure 4.18 shows the dependence of η_{e2e} and SNR on the energy in the control pulses E_{C}. In this case, η_{e2e} again shows a saturation behaviour, the SNR reaches a maximum at $E_{\mathrm{C}} \sim 230\,\mathrm{pJ}$, and then decreases again. Therefore, there exists a trade-off between reaching the maximally possible efficiency, and adding more noise to the retrieval signal. The maximum value of the SNR results from the fact that a high enough control Rabi frequency Ω_{C} is needed in order to achieve a complete mapping and thus efficient storage, but some of the noise sources are proportional (linearly and quadratically) to the control pulse energy. This will be discussed in more detail in the following section.
In this case, the model for the efficiency is given as

$$\eta_{\mathrm{e2e}}(E_{\mathrm{C}}) = \eta_{0,\mathrm{C}}\, e^{-a/E_{\mathrm{C}}}, \tag{4.15}$$

motivated by the dependence on the control pulse energy of the former model in Eq. (4.14), where the control Rabi frequency enters in the size of the EIT window. For the fit parameters we find $\eta_{0,\mathrm{C}} = 0.107(7)$ and $a = 1.56(9) \cdot 10^2\,\mathrm{pJ}$. Due to non-ideal etalon adjustments, the maximal efficiency $\eta_{0,\mathrm{C}}$ in this experiment is slightly reduced compared to $\eta_{0,t_{\mathrm{S}}}$.

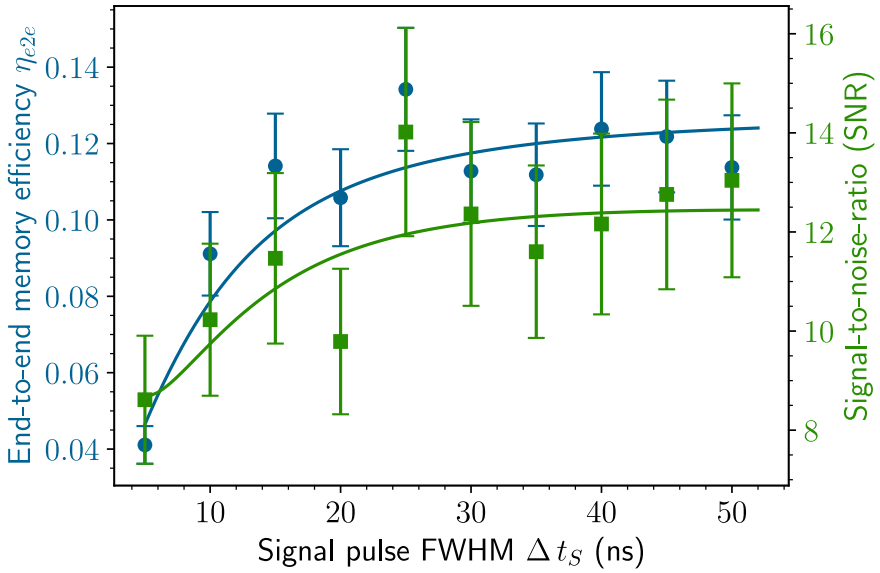

Figure 4.17: End-to-end efficiency (η_{e2e}, blue circles) and signal-to-noise ratio (SNR, green squares) of the memory as a function of signal pulse width Δt_{S}. The values of the control pulse energy and the detuning selected for the measurements are $E_{\mathrm{C}} = 560(50)\,\mathrm{pJ}$ and $\Delta = 2300(100)\,\mathrm{MHz}$ red detuning from the atomic resonance.

Figure 4.19 depicts the dependence of η_{e2e} and SNR on the laser's detuning Δ. Here, same as before, η_{e2e} shows a saturation behaviour, and the SNR reaches a maximum at $\Delta \approx 800\,\mathrm{MHz}$, and then decreases again. Thus, we observe the same trade-off between reaching the maximal efficiency, and adding more noise to the retrieved signal. We note that the large scatter in the SNR visible in Fig. 4.19 was due to imperfect measurement in the early stage of the experiment. With more accurate noise measurements achieved later on, taken while monitoring the laser frequency using a wavemeter (WavelengthMeter WS/7-60), such a large scatter was not visible any more (see Sec. 4.3.2). The maximum SNR value at $\Delta \approx 800\,\mathrm{MHz}$, was then not present any more. The lack of means to monitor the laser frequency in the first implementation of the experiment also leads to the large experimental error in the detuning values of $\pm 100\,\mathrm{MHz}$, not shown in the figures for clarity.

The dependence on the detuning Δ shown in Fig. 4.19 is modelled by

$$\eta_{\mathrm{e2e}}(\Delta) = \eta_{0,\Delta}\, e^{-\alpha(\Delta)}, \tag{4.16}$$

where $\alpha(\Delta)$ is a Lorentzian, reflecting that the memory efficiency is limited, among other issues, by collision-broadened absorption from the atomic ensemble. We obtain

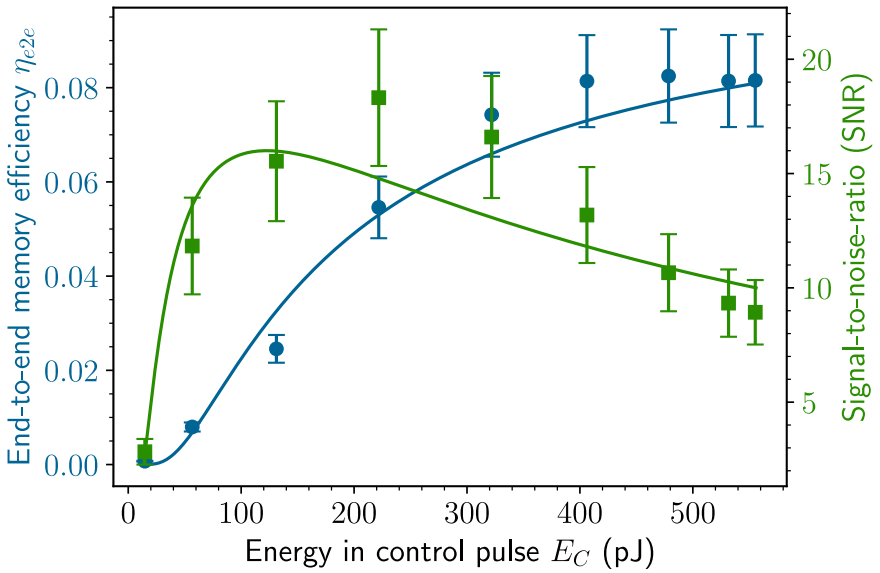

Figure 4.18: End-to-end efficiency (η_{e2e}, blue circles) and signal-to-noise ratio (SNR, green squares) of the memory as a function of the control pulse energy E_{C}. The values of the signal pulse width and the detuning selected for the measurements are $\Delta t_{\mathrm{S}} = 25\,\mathrm{ns}$ and $\Delta = 2300(100)\,\mathrm{MHz}$ red detuning from the atomic resonance.

$\eta_{0,\Delta} = 0.098(1)$, again lower than $\eta_{0,t_{\mathrm{S}}}$ due to non-ideal etalon adjustments. More investigations on this regard were planned by comparing the achieved figures of merit using different cells containing different buffer gas species in corresponding pressures, for which several new cells were ordered. Storage in these different cells has to date not been investigated, but could lead to a better understanding of the detuning dependence of the relevant figures of merit and to the choice of the ideal cell parameters for efficient storage. This issue will be discussed in more detail in Ch. 5.

These models are not to be taken as a result from a microscopic theory, but more as a heuristic description of the underlying physical mechanisms. A full theoretical model is outlined in Refs. [123–125, 240, 241, 326]. Simulations based on a simple version of this model were performed and will be described in Sec. 4.5.
The models for the SNR are determined as the ratio between the efficiency and the noise models, the latter of which are described in the next section. The large discrepancy between the data for the SNR and the model in Fig. 4.19 will be discussed in detail there.

From this combined analysis we thus achieve storage and retrieval with maximal

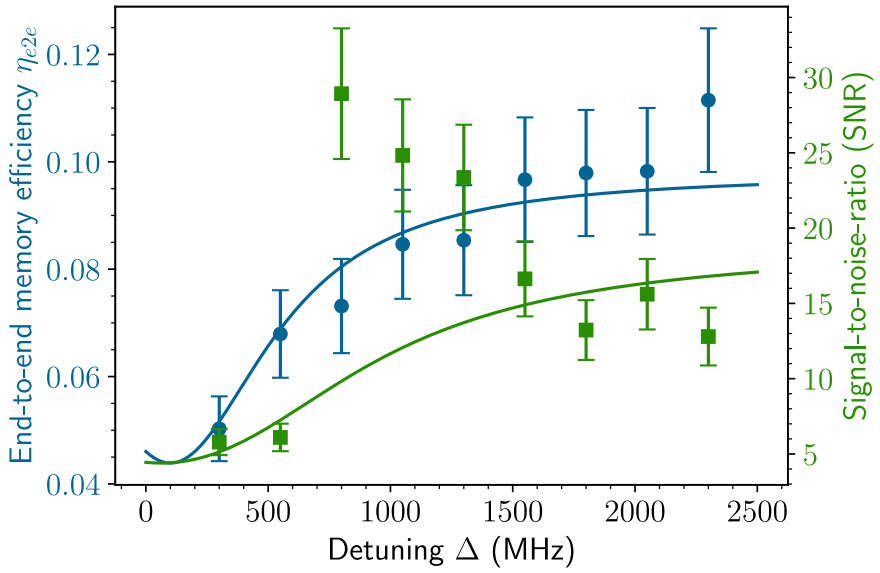

Figure 4.19: End-to-end efficiency (η_{e2e}, blue circles) and signal-to-noise ratio (SNR, green squares) of the memory as a function of the laser's red detuning from resonance Δ. The values of the signal pulse width and the control pulse energy are $\Delta t_{\mathrm{S}} = 25\,\mathrm{ns}$ and $E_{\mathrm{C}} = 560(50)\,\mathrm{pJ}$.

end-to-end efficiencies of $\eta_{e2e} = 13(2)\%$, which correspond to internal memory efficiencies of $\eta_{\mathrm{mem}} = 33(1)\%$ for coherent pulses containing one photon on average. The analytically calculated maximal limit for the total efficiency in the case of storage followed by backward retrieval is $\eta_{\mathrm{mem}} \approx 55\%$ (calculated from Eq. (3.116), see Table 4.3). This value is calculated assuming a Doppler-corrected optical depth of $2d_{\mathrm{opt}} = 13$. Comparing our achieved efficiency with this theoretical limit, we are still a factor ~ 1.7 below. This means there is still room for improvement, specifically by control pulse optimisation. This result led us to develop a control pulse optimisation experiment using a genetic algorithm, which was carried on by Lizzy later on (see Sec. 4.4.3 and Ref. [4]).

4.3.2 Noise analysis

To understand the limiting noise sources, a thorough experimental noise analysis was conducted. When the temporal, spatial, and spectral leakage of the control light is sufficiently suppressed, the three most relevant noise sources in warm vapour quantum memories are fluorescence, SRS, and FWM, as described in detail in Ch. 3 and Refs. [114, 178].

As a starting point for the noise analysis, it is essential to determine what kind of

noise we are dealing with, and obtain an estimation of its magnitude after spatial and polarisation filtering. For this, a spectral analysis is very helpful. We can thus compare how much noise passes the etalons when they are on resonance with the control field, compared to how high the noise counts of atomic origin are. We know that SRS, FWM and fluorescence noise will have approximately the same frequency as the signal pulse, and that SRS and FWM will vary their frequency when the laser's detuning is changed, while the frequency of fluorescence noise is intrinsic to the atoms.

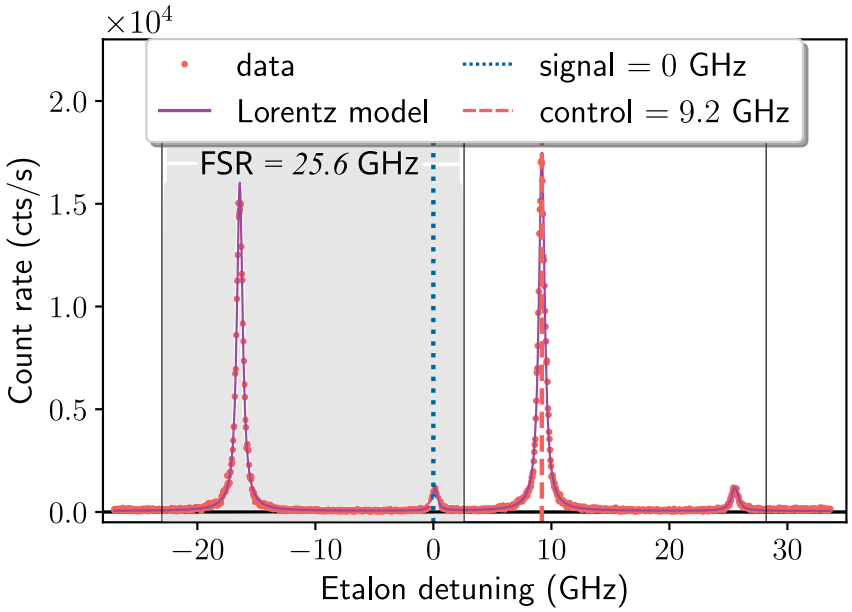

Figure 4.20: Noise detected on the APD, while scanning one of the etalons (Bob) used for spectral filtering over two free spectral ranges (FSR) (shaded area corresponds to one FSR= 25.6 GHz), while keeping the other etalon (Alice) on resonance with the signal frequency. Large peaks at −16.4 GHz and 9.2 GHz detuning correspond to leaked control laser light, and small peaks close to the signal frequency (at ∼ 0 GHz and at 25.6 GHz detuning) originate from atomic noise (fluorescence, SRS and FWM). Vertical coloured lines indicate the signal (blue dotted) and control (red dashed) frequencies and vertical black solid lines indicate the limits of one FSR.

Figure 4.20 shows the frequency dependence of the measured noise count rate, obtained by scanning the second etalon (Bob) of the filtering system over two FSR, each of 25.6 GHz, by temperature tuning, while keeping the first etalon (Alice) on resonance with the signal frequency. Thus, we see twice the same measurement depicted in the Figure. This measurement is taken with blocked signal laser. Two large peaks at

−16.4 GHz and 9.2 GHz detuning appear, corresponding to leaked control laser light. This frequencies result from setting the signal frequency to be at zero detuning for this figure. The transmitted control laser power is negligible when the etalon is in resonance with the signal, i.e., during storage experiments. Additionally, two smaller peaks close to the signal frequency appear approximately at 0 and 25.6 GHz detuning. This indicates that the only relevant noise sources during memory operation are of atomic origin.

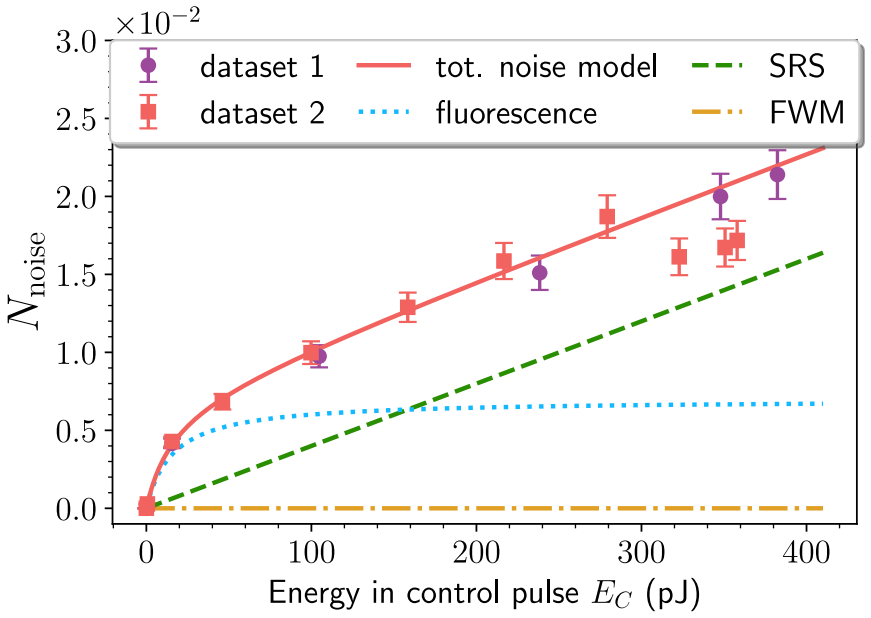

Figure 4.21: Exemplary measurement of total noise counts (the two different datasets were taken on different days) per retrieval attempt as a function of the energy in the control pulse E_C for $\Delta = 334$ MHz (red detuning), and corresponding fits of the different noise components: fluorescence, spontaneous Raman scattering (SRS), and four-wave mixing (FWM).

In order to attain a better understanding of these, we measured the number of noise photons N_{noise} counted on the APD by varying the laser's detuning Δ, while monitoring the control laser frequency with the wave meter. Here, $\Delta = 0(60)$ MHz corresponds to the control transition. At each detuning, we determined the noise count dependence on E_C, yielding a two-dimensional analysis. Figure 4.21 depicts the noise counts as a function of the control pulse energy E_C at $\Delta = 334$ MHz (red detuning). Two data sets were taken, as the first one showed some strange behaviour at high control pulse energies ($E_C > 300$ pJ), probably due to non-ideal etalon adjustments or other experimental imperfections. The data can be modelled by a second-order polynomial plus a saturating component as

$$N_{\text{noise}} = bE_{\text{C}}^2 + cE_{\text{C}} + \frac{d\,E_{\text{C}}}{(e + E_{\text{C}})}, \tag{4.17}$$

where the quadratic and linear contributions account for FWM and SRS, respectively, and the saturating part corresponds to fluorescence noise. For the shown detuning value we find $b = 0(10^{-8})\,(\text{pJ})^{-2}$, $c = 4(2) \cdot 10^{-5}\,(\text{pJ})^{-1}$, $d = 7(2) \cdot 10^{-3}\,(\text{pJ})^{-1}$, and $e = 16(16)\,\text{pJ}$, indicating that both fluorescence and SRS noise have a significant contribution, while FWM vanishes.

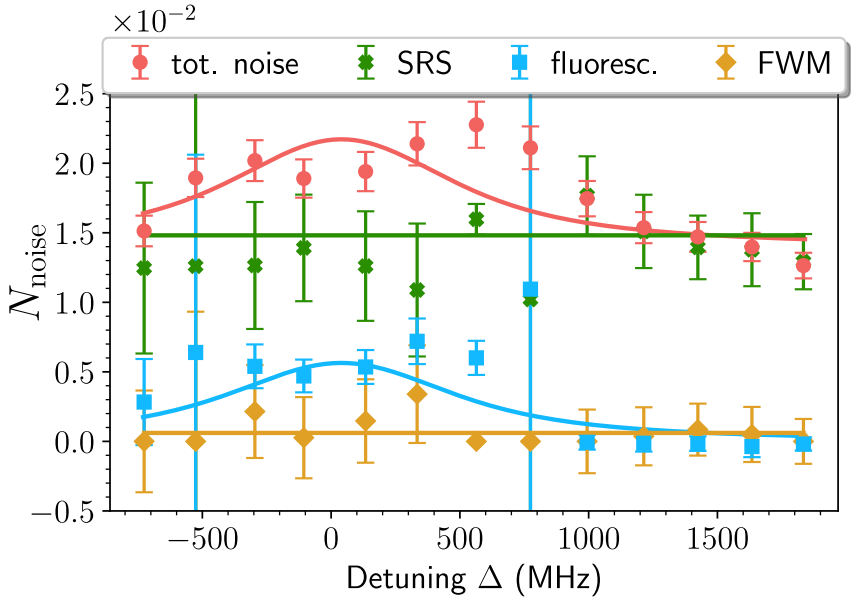

Figure 4.22: Systematic study of the measured total noise counts and the corresponding fitted noise components at retrieval as a function of the control laser detuning Δ. Negative values of Δ correspond to blue detuning from resonance (differs from convention, as we generally red-detuned the lasers and set this direction as positive). The noise is mainly dominated by SRS and florescence, while FWM is negligible in this setting.

Figure 4.22 depicts the behaviour of the noise for varying detuning Δ at maximal $E_C \approx 375(8)\,\text{pJ}$. This value is the average maximal pulse energy, which varies slightly for each detuning as it is set by hand by turning a waveplate and letting the intended maximal control power into the cell, while measuring it with a Thorlabs power meter. The error bars of the total noise are of statistical origin. From fitting the different noise components as a function of the control field energy at each detuning value (as in Fig. 4.21), the corresponding components fluorescence, SRS, and FWM are determined at

each point. Here, the error bars arise from the fit error of the E_C dependence. The error bars at $\Delta = -526$ and 774 MHz are comparatively large, since the fit hardly converged and FWM was manually excluded for these data points. From the analysis we assume that FWM is negligible in the experiment, SRS yields mainly a constant contribution to the noise, and the detuning dependence of the total noise arises mainly from fluorescence. In the theoretical description of the noise sources from Chapter 3 it was derived that if $\Delta \lesssim \omega_{sg}$, then the SRS contribution is stronger than the FWM contribution and the latter is suppressed. This is the case in the present realisation, since $\left(\frac{\Delta}{\omega_{sg}}\right)_{\max} \approx 0.2$, and confirms this fact. For the ratio between SRS and FWM derived in Eq. (3.143) we obtain $R_{\mathrm{SRS/FWM,th}} \approx \{18, 15, 5\}$ for $\Delta = \{0, -0.33, -1.5\}$ GHz, using $\omega_{sg} = 9.2$ GHz and $\gamma_e = 0.5$ GHz. The experimentally obtained value calculated from the average (constant fits) of SRS and FWM amounts to $R_{\mathrm{SRS/FWM,exp}} \approx 24$, for all measured detunings. Because this is a very rough estimation, I have not determined experimental uncertainties. This calculation is merely to motivate the reason for the vanishing FWM contribution. The experimental and theoretical values differ by some amount, but they all seem to reflect the fact that FWM is suppressed in the experiment.

The fluorescence was modeled as a Voigt distribution with a Gaussian component of 380 MHz width at FWHM due to Doppler broadening, and a Lorentzian component of 920 MHz at FWHM, arising from power broadening by the control light and pressure broadening due to collisions with the buffer gas, with the only free parameter being the height of the Lorentzian. The combined width is extremely large and does not really arise from theory. However, this simple model conveys the general trend and is valid for the here investigated small detunings on the order of the broadened atomic transition. For increasing detunings, a decay of SRS is expected, but even for the largest here-measured detuning values it is not pronounced enough to cause significant deviations from the model. The negligible FWM contribution is particularly interesting, as this type of noise is commonly understood to be the main drawback of vapour cell quantum memories, and efforts are made for its active mitigation [181, 190]. As we operate with low-bandwidth pulses, moderate control powers, at the D_1 line, and in a sensible (red) detuning range, we manage to practically suppress this type of noise. At detunings close to zero, a local minimum appears in the noise data. We presume this minimum to be caused by re-absorption of the light due to residual spatial mismatch of the beams along the whole length of the vapour cell. A more detailed model considering this reabsorption, the decay of SRS at large detunings, and the slight fluctuations of the noise data has too many free parameters to fit the number of existing data points. More investigation would be required to fully understand this fact, and should be pursued in further experiments and

theoretical calculations. The resulting total noise model

$$N_{\text{noise}}(\Delta) = N_{\text{SRS}} + N_{\text{fl}} V(\Delta) + N_{\text{FWM}} \tag{4.18}$$

is then a sum of the constant SRS contribution and the Voigt distribution resulting from fluorescence. For completeness, we also add the FWM contribution to the model. The resulting parameters are $N_{\text{SRS}} = 14(1) \cdot 10^{-3}$, $N_{\text{fl}} = 7(2) \cdot 10^{-3}$, and $N_{\text{FWM}} = 0(1) \cdot 10^{-3}$. It is thus essential to reduce the former two for future optimisation.

Combining the models for η_{e2e} with the noise model yields the SNR models shown in Figs. 4.17-4.19. These are in reasonable agreement with the measured data, and confirm the applicability of the former models. The discrepancy between the SNR model and the data observable in Fig. 4.19 results from the fact that the SNR data corresponds to the first implementation of the experiment, while the noise model used stems from the second iteration. As in the second iteration of the experiment we did not focus on optimising the achievable efficiency and SNR due to time reasons, but only measured the noise in detail, we decided to keep the previous data and use the new, more accurate noise model. This model shows a saturation of the SNR for large (red) detunings, similar to the behaviour of the efficiency, which seemed reasonable to us.
Summarising, we achieve a SNR = 14(2), corresponding to a noise level of $\mu_1 = 0.07(2)$ signal photons. This noise is dominated by constant spontaneous Raman scattering, with contributions from fluorescence. Four-wave mixing noise is negligible, allowing for further minimisation of the total noise level.

4.3.3 Storage time measurements

As mentioned in the previous sections, achieving long storage times was not the focus of the first implementation of our experiment, as we wanted to concentrate on the η_{e2e} and SNR optimisation. However, as we have discussed in detail in Ch. 2, long enough storage times of the order of milliseconds are primordial for applications of quantum memories in, e.g., long-distance quantum communication. It was important during the preparation of the experiments to determine the achievable storage time with the present setup, and to understand its limiting mechanisms, in order to be able to mitigate them for further implementations. Furthermore, the determination of the $1/e$ storage time τ_{mem} is important to rescale the measured efficiencies to the value at zero storage time, where they are defined by convention, assuming an exponential decay of the efficiencies $\propto e^{-t_{\text{storage}}/\tau_{\text{mem}}}$. For this, we performed storage measurements using macroscopic coherent

pulses, i.e., not at the SPL, and varying the time between the storage- and the retrieval control pulses (first two red pulses in Fig. 4.11) in a range $t_{\mathrm{storage}} \in [100 - 3000]$ ns. We then determined the memory and the end-to-end efficiency of the setup by integration of the area of the retrieval pulse. We did not perform this measurement at SPL for historical reasons. This was one of the first measurements we conducted on the memory. Because, as already discussed, for the publication of Ref. [1] we had decided to focus on optimising the η_{e2e} and the SNR, we did not pursue a repeated determination of the maximally achievable storage time. This is planned for further experiments (see, e.g., Ch. 5, Sec. 5.5). Since this measurement was done using macroscopic pulses, we normalised the result with the integrated pulse value of a far-detuned ($\Delta = 2\,\mathrm{GHz}$ red detuned) signal pulse, which does not get absorbed by the memory. This is necessary, since now the incoming pulse does not contain only one photon on average (at SPL the normalisation is by a factor of $|\alpha|^2 = 1$). It is important to consider that since the reference signal is measured far detuned, its power level will not be the same one of a resonant pulse stemming from a different laser current, and the data needs to be corrected for this fact. Figure 4.23 shows the memory efficiency (in the figure normalised to 1) and its decay as a function of time. As in Sec. 4.3 we had defined the storage time t_{storage} as the difference between the first (and highest) maxima of the retrieval pulse, and the peak of the incoming signal at $t = 0\,\mathrm{ns}$, but experimentally we can only vary the time between storage and retrieval control pulses, the storage times determined here will be somewhat longer (time axis of Fig. 4.23).

The data is modelled with an exponential decay function of the form

$$\eta_{\mathrm{mem}} = \eta_{\mathrm{mem},0}\, e^{-t_{\mathrm{storage}}/\tau_{\mathrm{mem}}} + c, \tag{4.19}$$

where $\eta_{\mathrm{mem},0}$ is the memory efficiency at time 0, τ_{mem} is the $1/e$ storage time or coherence time of the memory, and c is an extra parameter to aid the fit, which should tend to zero. The choice of an exponential decay is valid for systems with no angle-dependent spinwave dephasing [94]. As our signal and control beams are practically collinear, this type of decay is a good choice [94, 269] since the processes leading to atomic loss are diffusion out of the interaction region before read-out (no ballistic motion due to N_2 buffer gas), spin scrambling by collisions, or premature read-out by a scattered photon. Moreover, the exponential decay yields a good fit of the data. For the efficiencies we find $\eta_{\mathrm{mem},0} = 44(1)\%$, $\tau_{\mathrm{mem}} = 890(50)\,\mathrm{ns}$ and $c = 1(1)\%$. The obtained memory efficiency, which translates to an end-to-end efficiency of $\eta_{e2e,0} = 18(1)\%$ (using a setup efficiency value of $\eta_{\mathrm{setup}} = 40\%$), is higher than the optimal value of $\eta_{e2e,\mathrm{SPL}} = 13(2)\%$, obtained

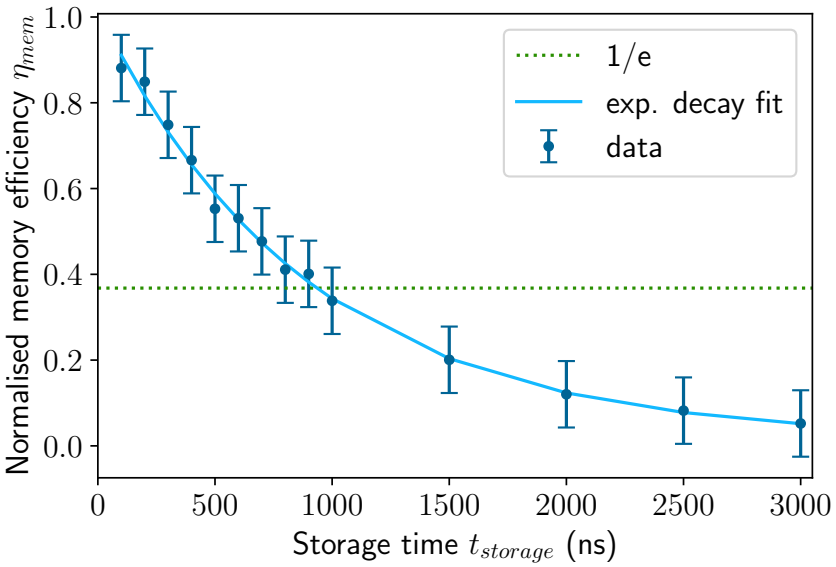

Figure 4.23: Decay of the normalised memory efficiency η_{mem} over storage time t_{storage} measured with macroscopic coherent pulses and corresponding exponential decay fit. The resulting coherence $(1/e)$ time of the memory is $\tau_{\text{mem}} = 890(50)$ ns.

in Sec. 4.3.1. Possible reasons could be an underestimation of the needed detuning for the reference measurement ($\Delta = -2\,\text{GHz}$), leading to residual absorption of the signal, or an underestimation of the input pulse energy. Nevertheless, the temporal behaviour of the memory can be well inferred from this measurement, even if not performed at SPL. Thus, the present setup can reach maximal storage times of approximately 1 μs. However, accurate measurements at SPL should still be performed in order to validate this correspondence. It again serves as an estimation and a starting point for further optimisations of the setup, in this case regarding the storage time.

The main reason for the spinwave decay in this memory configuration is the diffusion of the atoms out of the interaction region. In Table 4.3 we estimated the diffusion length in a time of $t = 1\,\mu$s to be $\Delta r = 100\,\mu$m. This is comparable to the FWHM beam diameter of the signal pulse of $93(5)\,\mu$m (see Sec. 4.2.4). This means, after this time, the atoms will most probably have left the interaction region and will thus not be addressed by the lasers anymore, leading to a loss of the spin-coherence. For applications, the extension of these storage times into the millisecond range will be vital and should be possible to achieve. We recall here that the only fundamental limitation on the storage time is given by the lifetime of the storage-state $|s\rangle$ due to non-radiative decay γ_s stemming as mentioned, from diffusion or from collisions (see Ch. 3, Sec. 3.2.3). Extension of the storage time can be achieved by increasing the beam diameters drastically, and by changing the Λ-system

configuration to one exploiting the magnetic Zeeman sublevels of the hyperfine ground states [185], as will be explained in detail in the next section 4.4.1.

4.4 Improvements and further developments

4.4.1 Zeeman pumping

As was shown in Sec. 4.3.2, our memory still suffers from noise sources, especially fluorescence and SRS. In future experiments, we are planning to extend the used beam sizes to reach storage times in the order of milliseconds. This might pose the need for stronger control pulses with possibly higher Rabi frequencies, which is bound to increase SRS noise, linear in control pulse energy, but surely also the FWM noise, quadratic in control pulse energy. Therefore, further noise reduction schemes will become necessary. A possible solution, which simultaneously leads to longer storage times (at least in theory), comes from exploiting the Zeeman substructure of the caesium hyperfine states and preparing the atoms in the so-called stretched states $|F = 4, m_F = \pm 4\rangle$ with $\sigma^{\pm}$ polarised light [345]. If perfect state preparation is achieved, this will allow to suppress residual SRS and FWM by selection rules [185, 330, 331]. Further benefits of using the stretched states include the reduction of SE collisions [177]. Considering the case of preparation in the $|F = 4, m_F = +4\rangle$ state with σ^+ polarised pump light (see Fig. 4.24 (a)), a possible $\Lambda-$memory scheme is shown in Fig. 4.24 (b).

For a complete state preparation, the use of a two-color pumping scheme is necessary. We chose a combination of two σ^+-polarised lasers, a D_1 pump laser on the $|F = 4\rangle \rightarrow |F' = 4\rangle$ transition, and a D_2 repump laser on the unresolved $|F = 3\rangle \rightarrow |F' = (2, 3, 4, 5)\rangle$ transition. The repump laser is necessary, in order to empty the lower hyperfine state $|F = 3\rangle$. If both pump lasers have enough power and shine long enough on the transition, almost complete state preparation in the $|F = 4, m_F = 4\rangle$ state should be achievable. Under this assumption, the role of the signal and control lasers used in the hyperfine memory (with respect to which hyperfine transition they are on) needs to be exchanged. The now σ^--polarised signal laser (blue arrow) is tuned to the $|F = 4, m_F = 4\rangle \rightarrow |F' = 3, m'_F = 3\rangle$ transition, while the now σ^+-polarised control (red arrow) is tuned to the $|F = 3, m_F = 2\rangle \rightarrow |F' = 3, m'_F = 3\rangle$ transition, analogous to the scheme used in Rb in Refs. [94, 191]. The signal and control lasers can both be detuned by a common two-photon detuning Δ. For a sensible choice of the detuning, a comparison of the relative strength factors of the intended and competing transitions for both lasers can be made [94]. Comparing the strength factors [288] for σ^- signal of

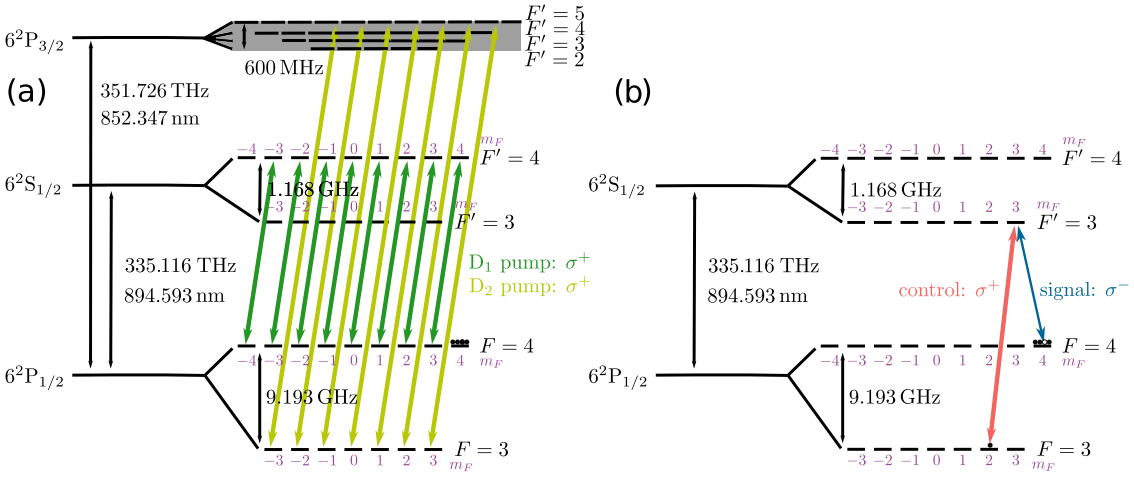

Figure 4.24: Zeeman memory preparation and scheme. (a) State preparation for the Zeeman memory in order to pump the atoms to the stretched state $|F = 4, m_F = +4\rangle$ via a D_1 pump laser (dark green) on the $|F = 4\rangle \rightarrow |F' = 4\rangle$ transition, and a D_2 repump laser (light green) on the unresolved (grey area) $|F = 3\rangle \rightarrow |F' = (2, 3, 4, 5)\rangle$ transition, both σ^+-polarised, such that they can only excite transitions with $\Delta m_F = +1$. (b) Zeeman memory scheme on the D_1 line after the atoms have been prepared in the stretched state. The σ^--polarised signal (blue arrow) is on the $|F = 4, m_F = 4\rangle \rightarrow |F' = 3, m'_F = 3\rangle$ transition, while the σ^+ polarised control (red arrow) is on the $|F = 3, m_F = 2\rangle \rightarrow |F' = 3, m'_F = 3\rangle$ transition. Due to selection rules, the control laser cannot couple to the outermost Zeeman (stretched) state $|F = 4, m_F = 4\rangle$, and thus SRS and FWM noise processes are forbidden in this scheme. Possible detuning Δ of both lasers from the excited state has been ignored here for simplicity.

$|F = 4, m_F = 4\rangle \rightarrow |F' = 3, m'_F = 3\rangle$ and $|F = 4, m_F = 4\rangle \rightarrow |F' = 4, m'_F = 3\rangle$, one has a ratio of $\frac{7}{12} : \frac{1}{12} = 7 : 1$, while for σ^+ control of $|F = 3, m_F = 2\rangle \rightarrow |F' = 3, m'_F = 3\rangle$ and $|F = 3, m_F = 2\rangle \rightarrow |F' = 4, m'_F = 3\rangle$, the ratio amounts to $\frac{1}{16} : \frac{7}{16} = 1 : 7$. This means, using a red detuning, as done before in the hyperfine memory, will favour signal absorption but will lead to weaker control coupling on the competing transitions, and thus seems again a good choice regarding noise. Using this scheme inhibits SRS and FWM noise inherently [346] (again, under the assumption of ideal state preparation), since the σ^+ control cannot couple to the $|F = 4, m_F = 4\rangle$ state due to selection rules, as there is no state with $|F' = 3, 4, m_F = 5\rangle$.

In order to implement this scheme in the next iteration of our memory, we wanted to better understand the procedure of Zeeman level pumping to the stretched states. Moreover, we sought to investigate the attainable lifetimes and the corresponding life-limiting mechanisms. Therefore, in David Becker's BA thesis [10], he set about to shed

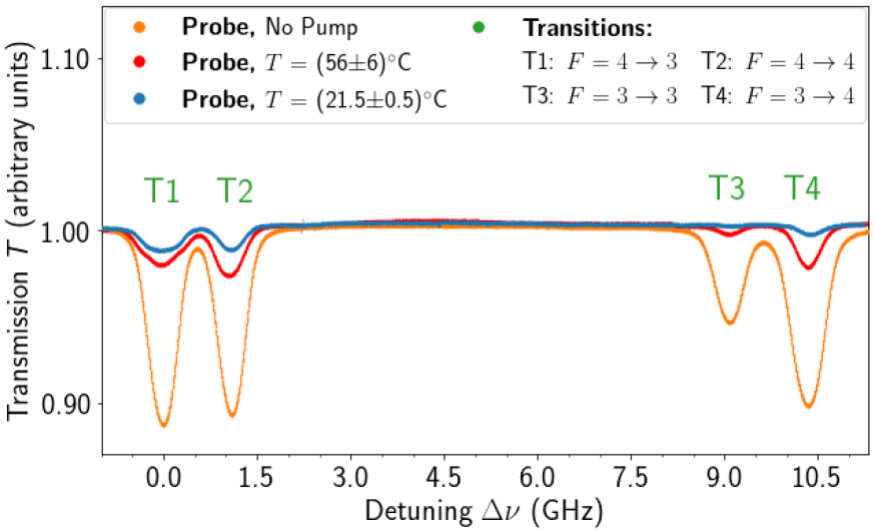

Figure 4.25: Normalised Cs D_1 line transmission spectrum measured at $T = 21.5(5)$°C (blue) and $T = 56(6)$°C (red) after two-color (D_1 & D_2) $\sigma^{\pm}$-polarised Zeeman pumping, and reference spectrum at $T = 21.5(5)$°C without pumping (yellow). The maximal pump power is $P_{\text{pump}} = 6.8(3)$ mW.

(pumping) light on exactly these issues. Using the setup shown in Fig. A.1, David firstly observed the effect of the two-color $\sigma^{\pm}$-polarised pumping on the absorption spectrum of the D_1 line, as shown in Fig. 4.25.

Later he used the two-color pump scheme in a sequence of 12 ms pumping, and a subsequent waiting time of 6 ms to let the system relax. From fitting the decay of the transmission of the signal laser on different transitions, and the optical depth (OD) exponential saturation curves determined from the data (see Fig. A.4 for the obtained figures), he was able to determine the $1/e$ lifetimes[1] of the stretched state (or outermost Zeeman state) $|F = 4, m_F = \pm 4\rangle$ for different temperatures of the cell and various probing powers. He thus obtained a maximal Zeeman pumping lifetime by probing on the $|F = 4\rangle \to |F' = 3\rangle$ transition of $\bar{\tau}_{\text{OD}} = 1.71(4)$ ms (see Fig. A.4 (a)) at room temperature ($T = 21.5$°C), and of $\bar{\tau}_{\text{OD}} = 0.39(1)$ ms (see Fig. A.4 (b)) at a temperature $T = 56(6)$°C, for the maximal used probe power of $P_{\text{probe}} = 7.9\,\mu$W. The maximally attainable pumping power (of both lasers) was limited to $P_{\text{pump}} = 6.8(3)$ mW. Table 4.4 shows the determined average lifetimes $\bar{\tau}_{\text{OD}}$ of the $|g\rangle$ state after two-colour D_1+D_2 Zeeman pumping with circularly polarised pumping lasers at two different cell temperatures $T = 21.5(5)$°C and $T = 56(6)$°C for different probe powers P_{probe} on the $F = 4 \to F' = 3$ transition. Here, we again see a

[1] Sometimes I also refer to these lifetimes as (Zeeman) pumping lifetimes, not to be confused with the required time of pumping t_{pump}.

dependence on the probing power, as discussed in Sec. 4.2.2.

P_{probe}	$\bar{\tau}_{\text{OD}}$ (ms)	
	$T = 21.5(5)$°C	$T = 56(6)$°C
7.9 μW	1.71(4)	0.39(1)
1.1 μW	1.72(3)	0.20(1)
335 nW	1.53(4)	0.26(1)

Table 4.4: Comparison of average pumping lifetimes $\bar{\tau}_{\text{OD}}$ for Zeeman two-colour (D_1+ D_2) pumping for different probing powers P_{probe} on the $F = 4 \rightarrow F' = 3$ transition, at different cell temperatures T.

In Fig. 4.25, at both measured temperatures, there is still some remnant absorption observable from the $F = 3$ states. Since only atoms outside of the stretched state $|F = 4, m_F = +4\rangle$ are allowed to absorb the σ^+-polarised probe beam, this indicates imperfect state preparation. Thus, the used pump power is probably not high enough. Other limiting factors may be atomic relaxation processes or the known problem of diffusion out of the interaction region. Another limiting factor of the lifetimes, which were initially expected to be longer (see Fig. A.5 and Table A.1 in the Appendix), presumably are stray magnetic fields resulting from insufficient shielding or from the heating pads used to heat the vapour cell (see Sec. 4.2.3). Even though here again, the heater was turned off for measurements, this still could be a remaining problem. In the literature, small magnetic guiding fields ($\boldsymbol{B} \,||\, z$ on the order of 100 pT) or gradients for Zeeman state preparation have been employed [185], and seem to help obtaining larger storage times. This seems sensible, especially for the memory scheme presented above, as in the case of no magnetic field, the strong control laser sets the quantisation axis, whereas a guiding field would take this role otherwise. Since the control field is turned on and off for storage, and in the Zeeman pumping scheme circularly polarised, the quantisation axis would no longer be the z-axis during the experiment, as it is assumed to be in the hyperfine memory case. The presence of spurious transverse magnetic fields can thus tilt the spins during the storage process and map these transverse spins onto the output signal, as a result from the Faraday effect [347] or even the Hanle effect [348]. To phrase it in Steck's words [288]: "[...]if there are any 'remixing' effects such as collisions or magnetic fields not aligned with the axis of quantisation, the system may come to equilibrium in some other configuration". In summary, these investigations definitely left many open questions regarding the role of magnetic fields in warm atomic memories. More investigation into the effects of magnetic guiding fields in memories is definitely necessary, and will be

pursued in future experiments (see Ch. 5).

4.4.2 Multimode quantum memory

This section is based on Ref. [3]:
L. Meßner, E. Robertson, **L. Esguerra**, K. Lüdge, and J. Wolters, Multiplexed random-access optical memory in warm cesium vapor. *Opt. Express*, 31, 10150-10158 2023.

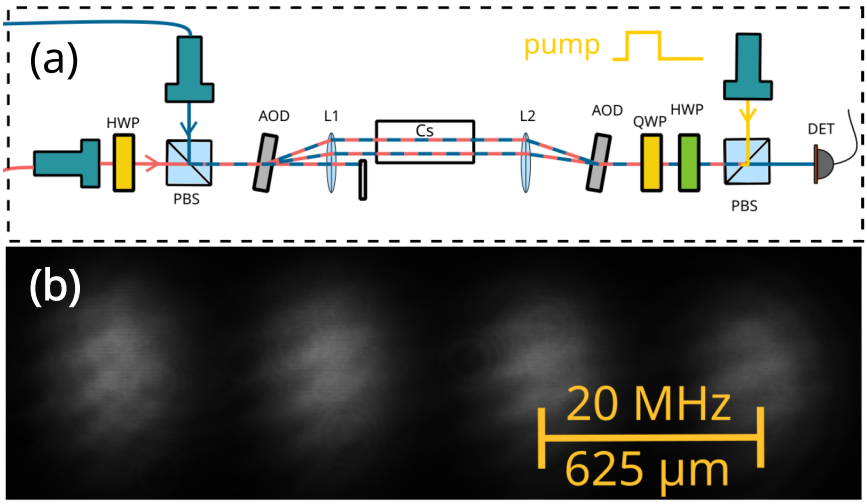

Figure 4.26: Multimode memory setup and photo of multiple cells. (a) Section of the multi-rail storage setup. AODs are used in order to deflect the laser beam into different rails that act as different memory cells. AOD: accousto-optic deflector; Cs: Caesium vapour cell; Det: Si photodiode; HWP, QWP; half-wave and quarter-wave plates; L1, L2: lenses; PBS: polarising beam splitter. (b) Photo of the four memory rails separated by 626 μm and 20 MHz. (Slightly modified) figures taken from [3].

In Refs. [130, 131], parameters for high enough key rates for sensible information transfer in space-borne quantum-repeater schemes are determined. From these investigations, a value of $m = 1000$ required memory modes for realistic near-term implementations is obtained. Multimode operation has been investigated in several quantum memory systems, including time-bin [349], orbital angular momentum (OAM) [350], and spatial multiplexing [202, 203, 351, 352]. From these approaches, Ref. [352] is probably one of the most suited ones to achieve the required value of $m = 1000$ random accessible memory modes. However, this experiment is conducted using cold atoms, and as we have discussed

in Ch. 2, the technological overhead of such experiments is significantly higher than our simpler warm vapour systems. Therefore, inspection into the realisability of multimode storage in our memory systems is a fundamental step towards real implementations. For the above mentioned publication, mainly Leon, but also Lizzy and I worked towards the realisation of this goal.

The used setup for this experiment is the same memory setup as the one described in the sections above, with some changes and extra parts, which will only be shortly mentioned here. Firstly, the memory section is updated in order to realise the different rails. These are obtained by using an AOD (or AOM) to diffract the incoming laser beam into the needed rails, which are then recombined using a second AOM, as is depicted in Fig. 4.26 (a). The resulting four rails, separated by 20 MHz in driving frequency and spatially by 625 μm, are shown in Fig. 4.26 (b). Secondly, in order to obtain a high enough control power, as the beam sizes are larger in this experiment than in the original memory experiment, a self-built (by Leon) tapered amplifier (TA) is added to the setup. The resulting usable coupled control laser power in cw amounts to 200 mW. For more details about the setup, I refer to Leon's Master's thesis [12]. The resulting spot size ($1/e^2$) of the signal beams is 230 μm.

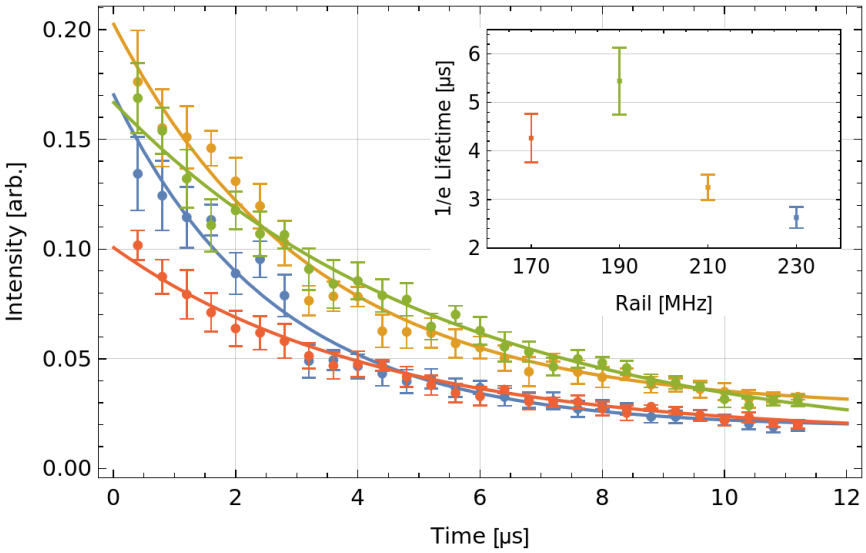

Figure 4.27: Measured retrieval amplitudes of different rails of the multimode memory as a function of storage time in the range $t_{\text{storage}} \in [0.4 - 11.4\mu\text{s}]$ and corresponding exponential fits. The inset shows the determined $1/e$ storage time for each rail. Figure adapted from [3].

Using this setup and the same memory scheme described in Sec. 4.1, different experiments

were conducted, after determining the optimal operating conditions in terms of analysing the interaction between memory rails and minimising the cross-talk. The $1/e$ storage time of each rail was determined by conducting several memory experiments on each rail and extending the time between storage and retrieval control pulses each time, as described in Sec. 4.3.3. The obtained retrieval amplitudes as a function of storage time are depicted in Fig. 4.27, together with their exponential fits. The inset shows the determined $1/e$ storage times for each rail. The achieved mean $1/e$ storage lifetime of this memory is $\tau_{\text{mem}} = 3.2\,\mu\text{s}$, with an internal memory efficiency of 36 % using macroscopic coherent pulses. Subsequently, random-access memory operation is investigated in the setup. For this, a memory sequence containing different operations (read or write) on different rails is created. The random-access memory must abide to three defined features: 1) reading or writing on a rail should not affect the neighbouring rails (interaction-free); 2) rails where nothing has been stored or written into should not return anything upon retrieval (empty state); and 3) a read pulse should completely read out the rail and leave no excitations, such that a subsequent read pulse yields no output (full retrieval). With the chosen rail separation of 20 MHz, random access storage and retrieval that fulfils the aforementioned criteria was observed. For more information on the experiment, I refer to Ref. [3].

4.4.3 Genetic algorithm optimisation

This section is based on Ref. [4], currently in review:
E. Robertson, **L. Esguerra**, L. Meßner, G. Gallego, and J. Wolters, Machine learning optimal control pulses in an optical quantum memory experiment. *arXiv*.2401.05077, 2024.

As discussed in the theoretical analysis of Λ-type atomic quantum memories in Chapter 3, optimisation of such memories using a gradient ascent method was theoretically derived by Gorshkov and colleagues in Ref. [241]. Initial theoretical simulations based on this theory are described in Sec. 4.5. Experiments using control pulses determined in such a way are implemented in Refs. [179, 186, 353], showing a good performance. However, this model does not account for much of the physics occurring in warm atomic vapour experiments, such as the presence of a (inhomogeneously broadened) fourth level that notably changes the dynamics of the system [326], competing effects like FWM, or the slight differences in Rabi frequencies coupling to the different m_F states. As the aforementioned optimisation is performed theoretically, many other effects arising from the devices used in the experiment, such as specific transfer functions of optical modulators or experimental delays between signal and control cannot be easily included in such a model.

For this reason, in this work it was decided to carry out an in-experiment optimisation of the control pulses using a genetic algorithm. The latter was chosen due to the fact that in the experiment one does not have access to the spinwave gradients needed for the theoretical optimisation, and genetic algorithms are widely acknowledged as noise-robust, gradient-free optimisation algorithms, well suited to be used in an experimental setting.

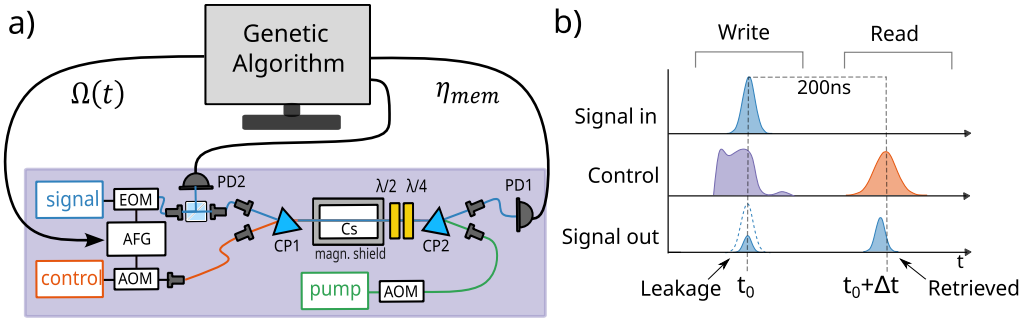

Figure 4.28: Schematics of the genetic algorithm experiment. (a) Overview of the online genetic algorithm setup. Possible solutions generated by the algorithm are evaluated by performing a memory experiment and determining the efficiency. AFG: arbitrary function generator; AOM: accousto-optic modulator; CP1, CP2: calcite prisms; Cs: caesium vapour cell; EOM: electro-optic modulator; $\lambda/2$, $\lambda/4$: half- and quarter waveplates; PD: photodiode. (b) Experimental pulse sequence. (Slightly modified) figures taken from [4].

This experiment and the coding of the genetic algorithm was performed by Lizzy Robertson. The setup used for this experiment is the updated version of the memory setup we had built together, already introduced in the beginning of this chapter (see Sec. 4.2.2). As a reminder, the most important change is the generation of the control pulses using an AOM instead of an EOM, and the loss of the originally needed amplification using the SOA. A schematic reduced version is shown in Figure 4.28 (a). Fig. 4.28 (b) shows a typical memory experiment sequence. Only the write control pulse is optimised in this experiment, while the read control pulse is always a Gaussian with 40 ns FWHM.

Using the genetic algorithm, optimal control pulses with a temporal form encoded either using Gaussian pulses, with the amplitude a, pulse width (FWHM) f, and the delay with respect to the signal pulse d as free parameters; or free-form pulses of 16 parameters, are learned. An overview of the genetic algorithm and the gene representations of these two types of pulses are depicted in Figure 4.29.

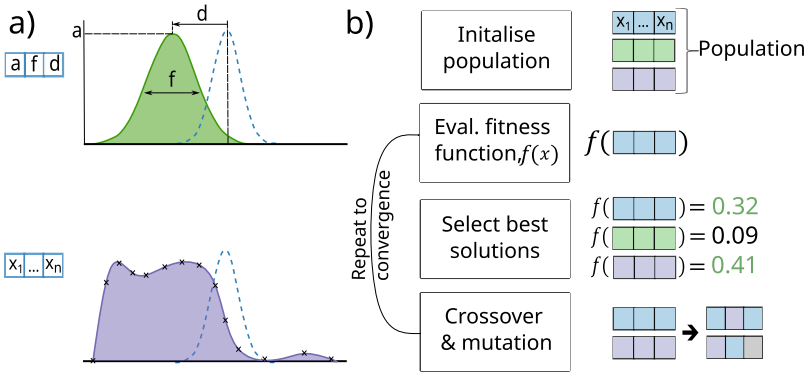

Figure 4.29: (a) Gene representation of the Gaussian pulse using the amplitude a, (FWHM) f and the delay d (above); and of the free-form pulse with 16 evenly distributed points (below). The Gaussian signal pulse is represented in dashed blue. (b) Overview of the genetic algorithm. Figure taken from Ref. [4].

The main results of the experiment are that the attained efficiencies using Gaussian control pulses are very similar to the ones where free-form control pulses are employed. The improvement factor of using the latter amounts to 3(7)%. This confirms the theory demonstrated in Ref. [354] for shorter pulse widths, which is here shown to be extendible to longer pulse widths. A further important finding is that the relevant temporal regions of the control pulse with respect to the efficiency are those temporally overlapping with the signal pulse [355]. Moreover, as we have learned in Sec. 4.2.3, much of the noise present in these warm memories is proportional to the control pulse energies. Therefore, if these can be reduced without remarkably lowering the attainable memory efficiencies, we could achieve good memory performance with even lower noise levels. Thus, in this work optimal control pulses were learned under the added constraint of minimising the control pulse energy. For specific signal pulse widths, a 30% reduction of the energy of the learned pulses with a minimal trade-off in efficiency of 4(6)% is shown. However, these last results should be taken with care and require further investigation. For more details on the experiment, the genetic algorithm, and the obtained results, I refer the reader to Ref. [4].

4.5 Theoretical simulations

At the beginning of the PhD, in order to gain better understanding of the behaviour of warm vapour atomic memories and to be able to determine good operation points for our future experiment, I set out to numerically simulate a warm Λ-type atomic memory, following the theoretical work of Gorshkov and colleagues [123–125, 240, 241], presented

in Chapter 3 Sec. 3.3.1. This work represents a tool to optimise the performance of a quantum memory in realistic experimental regimes. Since Gorshkov's work was, to be honest, not exactly light reading material, I followed the description by Rakher et al. presented in Ref. [326], which I found to be more approachable. In this work, Gorshkov's treatment for a three-level Λ-system is extended to include a second excited state, and the scenario of storage of photons emitted by a quantum-dot in an ultracold ^{87}Rb ensemble is simulated. When the pandemic hit in March 2020, this simulation work became my main project, while we had no access to the lab. The starting point was to simulate a three-level system in one spatial dimension without inhomogeneous broadening (see Ref. [240]). Initially, the plan was to include Rakher's extension and further ones, such as the mentioned broadening, the effect of the Zeeman sublevels, the spatial geometry of the signal and control fields, but unfortunately (or not), when we got back our lab access, other projects took precedence and thus, these improvements remain open for now. Therefore, there is still room for improvement, hopefully for the next PhD student in the group. Exactly this has been done by Roberto Mottola in Basel during his PhD [95].

The equations of motion Rakher uses are similar to Eqs. (3.117)-(3.119) in Ch. 3, but with some modifications. They are given as

$$\partial_{\tilde{z}}\mathcal{E} = i\tilde{\mu}_{eg}\sqrt{d_{\text{opt}}\gamma_e}\,P, \tag{4.20}$$

$$\partial_{\tilde{t}}P = (i\delta_g - \gamma_e)P + i\tilde{\mu}_{eg}\sqrt{d_{\text{opt}}\gamma_e}\,\mathcal{E} + i\tilde{\mu}_{es}\,\Omega(\tilde{t})S, \tag{4.21}$$

$$\partial_{\tilde{t}}S = i(\delta_g - \delta_s)S + i\tilde{\mu}_{es}\,\Omega^*(\tilde{t})P, \tag{4.22}$$

where all fields are functions of the coordinates $\tilde{z} \in [0, L]$, and $\tilde{t} = t - z/c$, in a co-moving reference frame. The spatial coordinates are later renormalised to 1, so that $\tilde{z} \in [0, 1]$. The equations include the relative dipole moments $\tilde{\mu}_{\alpha\beta}$, defined as the dipole moments relative to that of the two-level, cycling transition $\tilde{\mu}_{\text{cyc}}$, where a measurement of the optical depth would take place [326]. This is done for (apparent) easier comparison between different implementations of the Λ-system. δ_g and δ_s are the respective single-photon-detunings (in the rest of the thesis called Δ_s and Δ_c). Furthermore, the variables are not scaled by the decay of the excited state γ_e as in Gorshkov's theory. The initial conditions are the same ones given in Eqs. (3.120)-(3.122).

In order to solve the first-order, coupled partial differential equations (PDEs) (4.20)-(4.20), the space and time coordinates are discretised. The discretisation of time coordinate was

conducted using a time-bin of 1 ns. The rest of the variables were then transformed into equivalent units. The space coordinates were thus transformed into the time light takes to travel through them (in vacuum). Therefore, the cell length of $L = 7.5\,\mathrm{cm}$ corresponds to 0.25 ns. Frequency units are thus given in $\mathrm{GHz} = \frac{1}{1\,\mathrm{ns}}$, and then scaled by the decay of the excited state γ_e, prior to the calculation. This scaling allowed to describe the parameter ranges relevant to our EIT regime, with input signal and control pulse lengths in the order of $25 - 80\,\mathrm{ns}$, keeping the computational time short. The equations are solved with the simplest approach of using the Euler method. This method generally suffices for the three level system in the stationary case (i.e., without inhomogeneous broadening), although, as will be discussed later, this already caused some instabilities of the code in certain parameter ranges. The equations are solved through an iterative process, stepping forward in time starting from $\tilde{t} = 0$. Spatial derivatives are computed simultaneously for all $\tilde{z}$ points, followed by incremental computation of the time derivatives. The input signal pulse $\mathcal{E}_{\mathrm{in}}$, assumed to very weak in the theoretical formulation (such that only linear terms are kept), is programmed to be a Gaussian, with an amplitude normalised to one ($\int_0^{\tilde{T}} d\tilde{t}\,|\mathcal{E}_{\mathrm{in}}|^2 = 1$), in order to calculate the efficiencies as given in Refs. [241, 326]. The initial control pulse is also assumed to be Gaussian, and its amplitude is scaled with respect to γ_e for the calculation.

The simulation is performed in Python. Since the equations, at least in time, have to be solved iteratively, complete parallelisation is not possible and for loops cannot be fully avoided. These are rather slow in Python (even with NumPy), a reason why in the early stages of the project the optimisation already took long enough to make testing complicated and especially annoying. This motivated us to seek help from a theory group, who could use their knowledge to come to our aid. This collaboration came about in one of the first retreats of the graduate school of Berlin Optical Sciences and Quantum Technologies (BOS.QT) in 2020. Here we (Janik and I) met Prof. Christiane Koch from the FU, whose group focusses on theoretical quantum dynamics and control. Originally, the plan was to adapt our problem, such that it could be solved using their Fortran 95 library QDYN [356]. I started working on this together with Alexander Blech with some supervision by Daniel Reich. After some time (more than we would like to accept), we realised that the problem was more complex than we initially thought, and came back to the idea of optimising my existing code in order to make it more efficient. Alex was a great help in this, and we ended up accelerating the PDE solver using Numba [357], an open source JIT compiler that translates Python and NumPy code into fast machine code. This rendered the simulation about a 100 times faster.

The simulation is done in two parts: First, the storage process is simulated by solving Eqs. (4.20)-(4.20), with boundary conditions given in Eqs. (3.120)-(3.122). This yields the storage efficiency η_s given by Eq. (3.114). Second, the retrieval process is simulated. As I was interested in a scenario similar to our experiment, I implemented the case of forward retrieval, where the retrieval control pulse enters the memory from the same side as in the storage process. This means, as mentioned in Ch. 3, that the equations of motion are the same as for storage, but with boundary conditions given by Eqs. (3.131)-(3.133). In the simulations, the time interval $\tilde{t} \in [\tilde{T}_r, \tilde{T}_f]$ is the same one as for storage, i.e., $[0, T] = [\tilde{T}_r, \tilde{T}_f]$, since these are two independent calculations. This yields the retrieval efficiency η_r, which in the case that the spinwave is not renormalised before retrieval is given as

$$\eta_r = \frac{\int_{\tilde{T}_r}^{\tilde{T}_f} d\tilde{t} |\mathcal{E}_{\text{out}}(\tilde{t})|^2}{\int_0^1 d\tilde{z} |S(\tilde{z}, \tilde{T})|^2}, \tag{4.23}$$

where $\mathcal{E}_{\text{out}}(\tilde{t}) = \mathcal{E}(1, \tilde{t})$ is the signal field at the end of the cell ($\tilde{z} = L$). The total efficiency $\eta_{\text{tot}} = \eta_s \eta_r$, which corresponds to what we experimentalists call the internal memory efficiency η_{mem}, is then given as in Eq. (3.134), or in the above notation as

$$\eta_{\text{tot}} = \int_{\tilde{T}_r}^{\tilde{T}_f} d\tilde{t} |\mathcal{E}_{\text{out}}(\tilde{t})|^2. \tag{4.24}$$

The choice of the necessary length of the time coordinate for an efficient simulation was a bit tricky, as choosing very long integration times $\tilde{T}$ led to some oscillations in the optimal control pulses at times much longer than the signal width, which were deemed as unphysical. As a compromise, an integration length of $\tilde{T} = 250\,\text{ns}$ was chosen. The number of grid points was chosen to be $\tilde{z}_{\text{steps}} = 251$ for the spatial grid, and $\tilde{t}_{\text{steps}} = 15001$ for the time grid. These stability issues show that elaborating of the algorithm from a simple Euler method to, e.g., a second or even fourth-order Runge-Kutta method will surely become necessary when implementing the aforementioned improvements. As an example to show the results delivered by the simulation, I calculated the optimal control field and the resulting $\mathcal{E}, P, S$ fields for storage and retrieval (in the code and in Fig. 4.30 referred to as $\mathcal{E}_r, P_r, S_r$) for a configuration similar to our experiment, presented in the sections above. The parameters used for the simulation are given in Table 4.5. The used value for the optical depth d_{opt} corresponds to 1/2 of the calculated OD of the signal transition, not scaled with respect to Doppler broadening, but only considering natural and power broadening. This choice is due to the fact that since the simulation does not (yet) account

for inhomogeneous broadening, the resulting efficiencies assuming the Doppler-scaled OD given in Table 4.3 were very low. Thus, I decided to account for the Doppler broadening by including it in the dephasing rate of the excited state $|e\rangle$ (γ_e), but not in the OD. As the resulting efficiencies were closer to what we observed experimentally, this was deemed to be a sensible choice. As I consider the D_1 line in Cs, scaling the relative dipole moments $\tilde{\mu}_{\alpha\beta}$ with respect to the D_2 cycling transition did not seem sensible. Therefore, I assumed the $\tilde{\mu}_{\alpha\beta}$ to be related to the transition strength factors $S_{FF'}$ from Table 3.4. As the simulation calculates field strengths and not intensities, one needs to take the square root of these. For simplicity, and relating to the calculated d_{opt} being that of the signal transition, I assumed $\tilde{\mu}_{eg} = 1$ and rescaled $\tilde{\mu}_{es}$ as $\tilde{\mu}_{es} = \sqrt{\frac{7}{3}}\tilde{\mu}_{eg}$. As a reminder, the theoretical values for γ_e and Ω are half of the calculated experimental values, following convention [125, 326]. Also, the control field is assumed to be real. The resulting squared field amplitudes are depicted in Fig. 4.30, where the left column shows the storage fields, and the right column shows the retrieval fields.

Magnitude	Value
Cell length	$L = 7.5\,\text{cm} \mathrel{\hat{=}} 0.25\,\text{ns}$
Integration time	$\tilde{T} = 250\,\text{ns}$
Grid size	$\tilde{z}_{\text{steps}} = 251$ $\tilde{t}_{\text{steps}} = 15001$
Th. optical depth	$d_{\text{opt}} = 30.5$
Relative dipole moments	$\mu_{eg} = 1$ $\mu_{es} = \sqrt{\frac{7}{3}}$
Control Rabi frequency	$\Omega = \pi \cdot 0.54\,\text{GHz}$
Detuning	$\delta_g = \delta_s = \Delta = 2\pi \cdot 1.5\,\text{GHz}$
Decay rate of $\|e\rangle$	$\gamma_e = \pi \cdot 0.39\,\text{GHz}$
Gaussian pulse widths (FWHM)	$\Delta t_s = 25\,\text{ns}$ $\Delta t_c = 50\,\text{ns}$
Optimal efficiencies	$\eta_s = 56.1\%$ $\eta_r = 60.6\%$ $\eta_{\text{tot}} = 34.0\%$

Table 4.5: Simulation parameters and resulting optimal efficiencies for the given configuration.

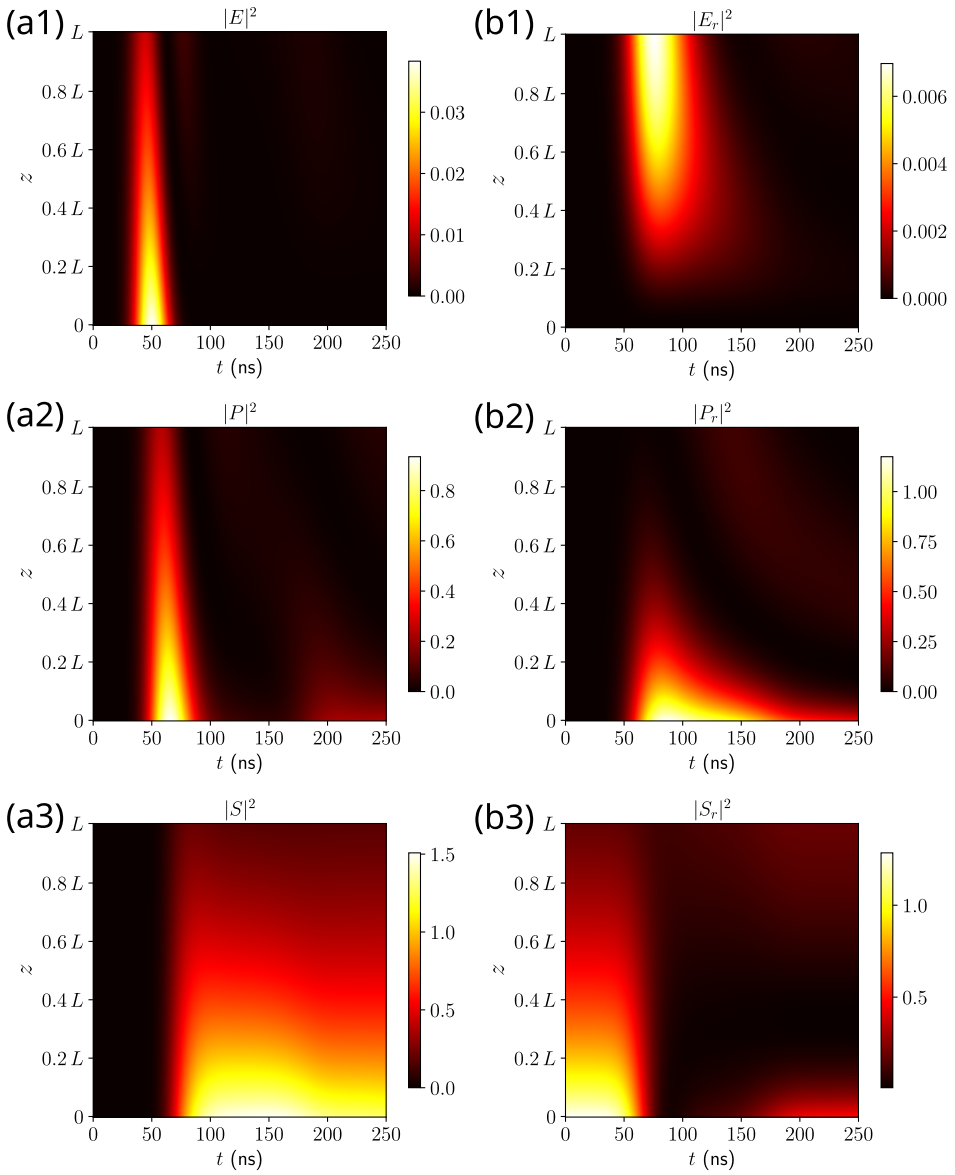

Figure 4.30: Simulation results. (a1)-(a3) Squared field amplitudes $\mathcal{E}^2$, P^2, and S^2 for the optimal storage process. The storage efficiency is $\eta_\mathrm{s} = 56.1\%$. (b1)-(b3) Squared field amplitudes $\mathcal{E}_r^2$, P_r^2, and S_r^2 for the optimal retrieval process. The retrieval efficiency is $\eta_\mathrm{r} = 60.6\%$. The resulting total efficiency for this configuration then amounts to $\eta_\mathrm{tot} = 34.0\%$.

The results of the control field optimisation, i.e., the solutions for each iteration, as well as the initial signal field $\mathcal{E}_\mathrm{in}$ (not to scale) are shown in Figure 4.31. The signal field's amplitude (not to scale) is normalised to one and only enlarged in the figure for comparing its timing with respect to the control field. The simulation yields the optimal

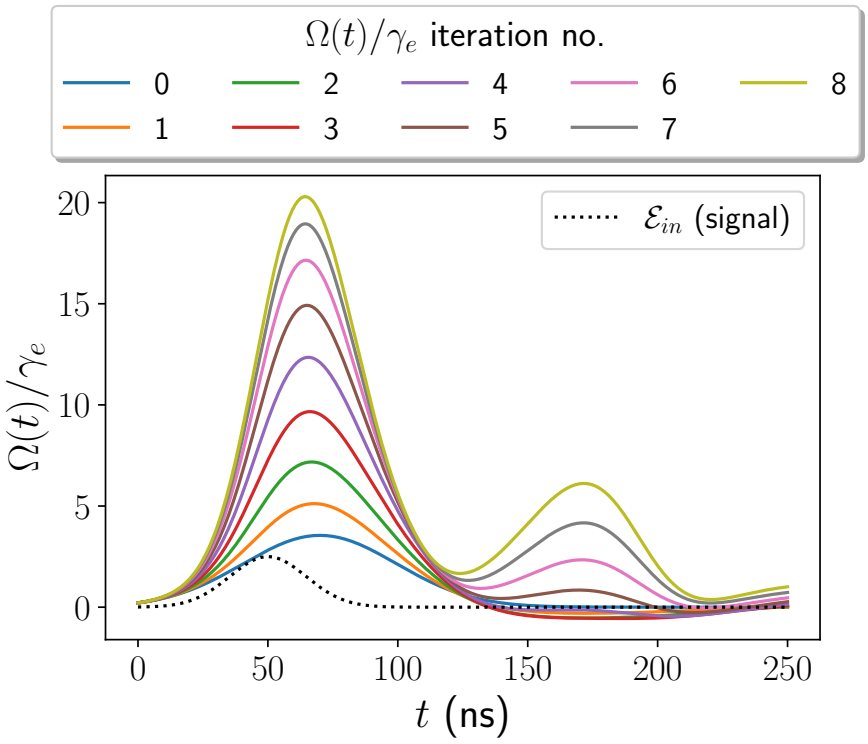

Figure 4.31: Control field optimisation results (simulation). For the given configuration, the optimal control field is found after 8 iterations of the gradient ascent algorithm. The Gaussian input field $\mathcal{E}_{\text{in}}$ (not to scale) is also plotted as a reference.

control pulse for the given configuration in 8 iterations. The resulting control pulses show a Gaussian-like behaviour around the time interval where the signal pulse is large ($\tilde{t} \in [0 - 100]$ ns), then fall slightly below zero, here probably only due to numerical effects, and then show some extra peak at times $\tilde{t} \approx [110 - 220]$ ns. This behaviour seems curious, as turning on the control field after having stored the signal should lead to early readout, here similar to leakage. These are probably artefacts of the stability issues of the simulation and where thus not considered further. However, more investigation is required regarding this fact. The significant part of the optimal pulses is taken to be its Gaussian-like part. The resulting efficiencies calculated for the optimal pulse are also given in Table 4.5. The agreement with our measured internal memory efficiency of $\eta_{\text{mem}} = 33(1)\%$ (see Sec. 4.3.1) has to be taken with care. The simulated optimal efficiency is attained by using a very strong control field, approximately $10\times$ higher than our experimental control pulses. Notably, the optical depth used for the simulation was larger than the Doppler-broadening-reduced OD determined from theory (as mentioned

earlier). Lower values of the optical depth, corresponding to our measured experimental values, resulted in very low efficiencies in the simulation. This behaviour was confirmed in conversations with Roberto Mottola regarding the simulations shown in his thesis [95]. As the description by M. Rakher is developed for cold atoms, there might be assumptions about the optical depth I did not take into account. These issues rise several questions, such as if we need to increase the control Rabi frequency even more in our experiments to increase the obtained efficiencies (optimisation), if better results will be obtained by increasing the OD, or if both cases are even comparable.
Interestingly, the optimal control pulse seems to be centred later in time compared to the signal, as opposed to the optimal scenario we observed experimentally. I tried out many configurations placing the signal pulse on the falling edge of the control pulse, such that the control pulse would adiabatically go to zero when the signal entered the memory, thus transferring it better into the spinwave, as EIT-memory theory predicts. However, the simulation always determined the optimal control pulse to be later and the signal pulse to arrive closer to the rising edge of the control. Gorshkov's theory states that this adiabatic ramping down is not necessarily required for optimal storage, however this fact seemed counter-intuitive to me.
Notably, the simulation lacks many effects highly relevant for memory operation. The spinwave decay between storage and retrieval is assumed to be negligible, which does not correspond to reality. As discussed above, the main source of decoherence in our memory (deterioration of the spinwave) is the diffusion of atoms out of the interaction region, a fact which is completely ignored in this description, as well as are other spin-dephasing effects described in Ch. 3, Sec. 3.2.3. Nevertheless, since this can be modelled using a simple exponential decay (see Sec. 4.3.3), (at least) this effect can be accounted for easily. More complicated issues, such as noise, are not accounted for at all in this description. Therefore, the simulation which, if stable, should approach efficiencies close to one for $d_{\mathrm{opt}} \to \infty$ will, e.g., yield the best efficiencies on resonance, where from experience we know that remaining absorption due to imperfect EIT tends to reduce the attainable efficiencies, and where readout fluorescence noise is maximal. Also, all the improvements and further effects mentioned before (inhomogeneous (Doppler) broadening, the presence of the second parasitic excited state ($F' = 4$), etc.) are not yet included in the simulation. Finally, all the technical noise sources and experimental issues leading to reduced efficiencies are basically impossible to account for in this simulation. For this reason, we later on in time decided to go about the optimisation of the memory by using an in-experiment approach via the Genetic Algorithm, as was done by Lizzy in her experiment (see Sec. 4.4.3 and Ref. [4]). This theoretical simulation, at least at the level of complexity it includes now, can thus be seen as a means to understand the behaviour

of the involved fields, rather than to obtain exact results.

4.6 Discussion and intermediate conclusions

In summary, in this section I have presented the warm, hyperfine EIT memory on the Cs D_1 line, with which we have realised single-photon-level storage of coherent pulses containing one photon on average. We have achieved an end-to-end efficiency of $\eta_{\mathrm{e2e}} = 13(2)\%$, which translates to an internal memory efficiency of $\eta_{\mathrm{mem}} = 33(1)\%$. Simulations based on the theory by Gorshkov et al. [123–125, 240, 241] and Rakher et al. [326] were carried out, yielding maximal memory efficiencies comparable with our experimental results. However, these results are obtained after a control pulse optimisation and at a higher value of the optical depth than the one calculated for our system, and thus it is not clear how comparable they are. Nonetheless, the simulation helps to qualitatively understand the storage process better. The theoretical limit for the memory efficiency calculated using a (Doppler scaled) optical depth of $2d_{\mathrm{opt}} = 13$ was determined to be $\eta_{\mathrm{mem}} \approx 55\%$ (calculated from Eq. (3.116), see Table 4.3). Therefore, the efficiencies of the experiment can still be improved. The same calculation using the optical depth considering only power broadening, that is, not Doppler scaled, yields a limit of $\eta_{\mathrm{mem}} \approx 81\%$. The obtained experimental efficiency values show we are on a good path towards achieving the needed key figures of merit for practical implementations on QRs [130, 131], and that these efficiencies can be improved in our experiment by control pulse optimisation. The simultaneously obtained SNR is 14(2), which can be converted to a noise level corresponding to $\mu_1 = 0.07(2)$ signal photons. As the limiting noise sources, SRS and fluorescence are identified. The present memory is not yet fully optimised for long storage times and reaches a $1/e$ storage time of $\tau_{\mathrm{mem}} = 890(50)\,\mathrm{ns}$ ($\tau_{\mathrm{mem}} = 3.2\,\mu\mathrm{s}$ in the multimode memory), but the geometry with parallel signal and control beams in principle allows for storage times not limited by motional dephasing, at least in the ms regime. With the achieved bandwidth of $\Delta\omega_{\mathrm{mem}} = 220(30)\,\mathrm{MHz}$, this yields a time-bandwidth product of $\mathrm{TBP} = \Delta\omega_{\mathrm{mem}} \cdot \tau_{\mathrm{mem}} = 200(30)$. This is comparable to the value achieved, e.g., in Ref. [191] of $\mathrm{TBP} = 250(20)$. With these characteristics, our device can already find a use in, e.g., the enhancement of the generation rate of multiphoton states for applications in optical computation or sensing [138].
The used control powers in this experiment were comparatively low. However, much higher powers on the order of hundreds of mW will be needed in future experiments, where larger beam sizes are planned, in order to further extend the storage times. The pumping efficiencies for the experiment were certainly not high enough. There are several

possible reasons, such as the forbidden $|F = 4, m_F = 0\rangle \rightarrow |F' = 4, m'_F = 0\rangle$ transition, which does not couple to the pump laser, and the insufficient pump power and beam size. Furthermore, residual radiation trapping and other competing collisional processes leading to dephasing, even if not very large, still have a non-negligible effect. This is probably the reason for the experimentally observed fact that higher temperatures, and thus a higher optical depth, do not lead to monotonically improved efficiencies, but that there seems to be an optimal temperature (in our case the chosen $T = 60°\mathrm{C}$), above which the attained efficiencies start to decrease, contrary to Gorshkov's theory. An open issue for investigation in this regard is the usage of (radially) thinner cells with different buffer-gas species and pressures. The smaller diameter will aid in the reduction of radiation trapping in the radial direction, and the different buffer gas concentrations could possibly reduce the effect of collisions leading to spinwave dephasing. These investigations could also lead to improved pumping characteristics and longer spinwave lifetimes.

From Gorshkov's theory [123–125, 240, 241], we further know that EIT and Raman memories correspond to different limits of adiabatic storage. EIT operates closer to resonance and is based on a quantum interference, while Raman memories operate far detuned ($\Delta > \gamma_e$) and allow for broadband storage. However, it is difficult to discern how exactly memories work in intermediate regimes. Our memory shows good performance for longer pulses in the time domain, and thus narrower in the spectral domain, but the ideal operating point with respect to detuning lies at about $\Delta = 1.5\,\mathrm{GHz}$, which is more than three times larger than the total excited state linewidth, including all broadening mechanisms (homogeneous and inhomogeneous), of $\gamma_e = 390\,\mathrm{MHz}$. Therefore, our memory is exactly in such an intermediate regime. The question arises if determining, e.g., the width of the EIT window in this regime (using Eq. (3.74)), is still sensible, if storage is still based on an interference, or not. We know that the EIT window changes its shape with large detunings [11, 358], such that the same input pulse will not fit spectrally as well in a detuned EIT window as in a resonant one. However, here we see that the EIT model yields good results when compared to our experimental data. Specifically, the model for the efficiency as a function of the signal pulse width of Eq. (4.14), and the size of the EIT window it predicts, agree very well with the theoretical value (see Table 4.3), as we have mentioned above. Regarding the changing shape of the EIT window at large detunings, specifically outside of the absorption peak where the transmission is maximal, if one closely looks at the spectrum, the detuned 'EIT window' could be interpreted as induced absorption. One could argue that the regime resembles electromagnetically induced absorption (EIA), a regime where light storage has also been investigated [359–361]. In this regime, the signal pulse experiences negative group velocities. Due to time reasons,

I did not have a chance to further investigate this matter, but it might be something worth looking into. All these issues have provided us with hot topics of discussion with colleagues over the years, to which I have still not found totally satisfying answers. Maybe the discussion goes to much into the philosophical realm, since the EIT model does yield sensible results. But as we have learned, philosophical discussions can lead to interesting (and maybe even practical) results. Thus, I comment this here as an invitation to further look into these questions with more theoretical and experimental investigations.

Regarding noise, for SRS minimisation, the pumping efficiency should be increased using higher pump laser powers and larger beams. Further noise reduction is planned by exploiting the Zeeman substructure of the caesium hyperfine states and preparing the atoms in the $m_F = +4$ sublevel with σ^+ polarised light, thus ideally suppressing residual SRS by selection rules, and further reducing possible FWM noise contributions [185, 330, 331]. In this configuration, larger SNRs should also be attainable. First investigations in this direction have been performed (see Sec. 4.4.1). The resulting coherence times of pumping into Zeeman states are not as long as expected, pointing to spurious magnetic fields. A new and improved heating system which does not lead to magnetic fields inside the shielding has been developed and already tested in other experiments (see Chapter 5). Furthermore, future experiments are planned with an improved four-layer magnetic shield from Twinleaf, including coils for generating magnetic (guiding) fields and gradients. These improvements will help to extend the attainable storage times and to better understand the effects of magnetic fields for our storage protocols. With these improvements, storage times of a few milliseconds might be within reach. They can thus be extended to reach the benchmark $\tau_{\mathrm{mem}} = 1 - 100\,\mathrm{ms}$ for practical applications in QRs, by considerably increasing the beam diameters, ideally up to the cell diameter, hence inhibiting atomic diffusion out of the optical interaction volume.

Moreover, we have investigated spatially multimode operation in Ref. [3], paving the way to near-term implementations as the ones discussed in Refs. [130, 131]. Furthermore, by use of machine-learned optimal control pulses as the ones obtained in Ref. [4] (see Sec. 4.4.3), we will simultaneously boost the memory efficiency even further. With this, higher end-to-end efficiencies and simultaneously even higher signal-to-noise ratios, as well as ms-long storage times should be within reach, bringing us closer to laying the foundations for memory-assisted, satellite-suited QRs for long-distance quantum communication.

5 Applications and Developments

"The most effective way to do it is to do it."

Amelia Earhart

This chapter is meant as a thorough portrayal of the most discussed applications of quantum memories, ranging from ones realisable in forthcoming experiments or in the near future, to long-term ideas, more in the realm of the speculative. The overview is intended to give a flavour and an outlook of what will and may lie ahead in the field. I will first review the area of satellite-based long-distance quantum communication and repeater networks, and then continue with a (for now) more ground-based application, optical machine learning. Then, I will discuss synchronisation of photon generation in quantum light sources, an essential issue for both, ground and space scenarios. Thereafter, I will describe the more speculative ideas proposed in the white paper we wrote for NASA in collaboration with the DLR in Ulm, the Forschungszentrum Jülich, and the Universität Hannover [2], concerning space-based tests of fundamental physics. Later on, stepping more into current and near-future projects, the next realisation of a memory experiment currently under construction, the QToRX alkali-noble-gas memory and my contributions to that project will be presented. Lastly, I will discuss the realisation of the portable memory-system demonstrator built for the QuMSeC project. For explanations of these acronyms, I refer the reader to the respective sections.

5.1 Long-distance satellite-based quantum communication

Photonic losses remain to this day the longstanding bottleneck of long-distance quantum communication. Absorption losses scale exponentially with node distance, independent of fibre or free-space transmission. Due to the no-cloning theorem (see Ch. 1, Sec. 1.1.1), it is not possible to simply amplify the information by creating many copies, as is commonly done in classical communication. This issue limits applications beyond a few hundreds of km, e.g., $\sim 300\,\mathrm{km}$ in fibre [364]. As discussed in Ch. 1, quantum repeaters (QR)

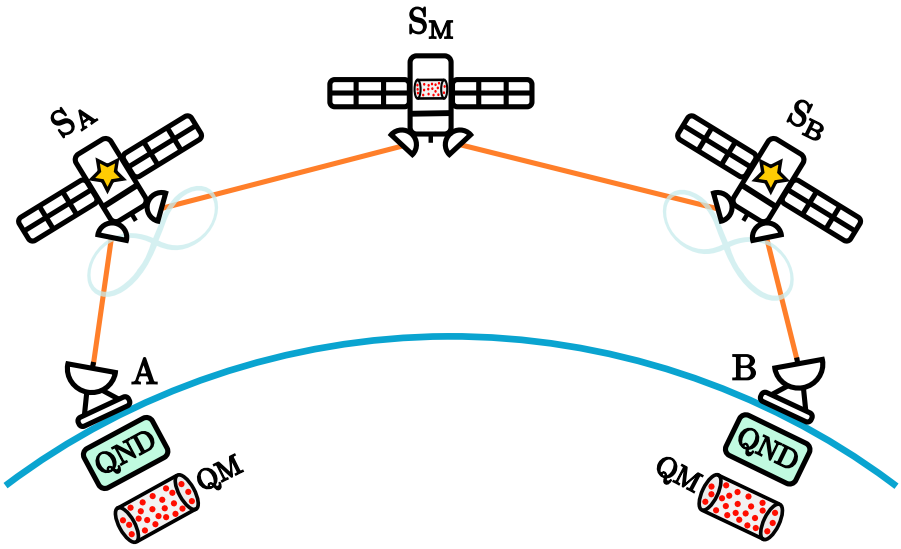

Figure 5.1: Schematic of a satellite-based quantum repeater architecture as considered in Refs. [130, 131]. The external satellites S_A and S_B contain onboard photon-pair sources (stars) that emit entangled photon pairs. They each send one photon to the central satellite S_M containing quantum memories (and also QND detection devices), and the other to the respective ground station A or B. After a quantum non-demolition measurement (QND) [362, 363] heralds the arrival of the photons they are loaded to quantum memories (QM) at each ground station and on the central satellite. A BSM at the central satellite will then lead to entanglement of the photons at ground stations A and B. This procedure can be cascaded further using several of such links.

and space-based communication were introduced to alleviate precisely this problem. The advantage of satellite-based free-space QKD (SatQKD) over ground-based fibre architectures is that transmission losses in vacuum are governed by diffraction and show an inverse square scaling, as opposed to the exponential scaling mentioned above.

Worldwide, research initiatives and missions in the field of SatQKD have emerged over the last years or are currently in preparation [365–369], and are supported by several studies [370–372]. These missions are generally based on the BB84 [34] and BBM92 [62] protocols. Among these, the remarkable Quantum Experiments at Space Scale (QUESS) project and its Micius satellite are highly famous, having accomplished major milestones, such as ground-to-satellite teleportation [373], decoy state BB84 QKD from satellite to ground [374], long-distance, entanglement-based QKD employing the BBM92 protocol [375], and remarkable beyond-line-of-sight trusted-node QKD connecting Vienna and Beijing [376]. Typical achieved key rates from satellite to ground in these implementations are in the kbit/s regime [374, 376] and in the bit/s range for [375].

However, with the goal of a global and 'user-friendly' quantum communication network in mind, beyond line-of-sight untrusted-node operation via QRs is undoubtedly necessary, since not everyone has the means to put up a trusted satellite in orbit. For untrusted operation with sensible key-rates, onboard quantum memories are an essential requirement. Up until recently, there had been no theoretical works analysing the performance of both ground- and satellite-based memory-assisted quantum communication in a global scale. In Refs. [130, 377], the use of memory-equipped satellites for quantum communication focussing on global-range repeaters and memory-assisted measurement-device-independent MA-MDI-QKD [378, 379] is analysed, providing one of the first investigations towards the goal of a global untrusted quantum repeater network. These works show that the QMs allow an increase in the achievable key rates as a result of synchronisation of otherwise probabilistic Bell-state measurements, which are the foundation of MDI-QKD protocols. Specifically, a single repeater station with an onboard QM reduces the scaling of the key rate from η_{ch} to $\sqrt{\eta_{\text{ch}}}$, where η_{ch} represents the channel transmission [131]. Moreover, placing intermediate links in space as opposed to on ground also reduces the necessity of simultaneous good weather conditions in more than two ground stations. A decisive finding of Ref. [130] is the enhancement of entanglement distribution rates over three orders of magnitude by using satellites equipped with quantum memories, compared to existing protocols where the memories are placed in ground-based stations [380]. This yields key rates in the order of 100 Hz-1 kHz for intermediate distances up to ~ 500 km. For ground-station distances of 10.000 km, required storage times for intercontinental and global (half of the earth's circumference) quantum communication are determined to be in the range of some tens to hundreds of milliseconds. In addition to global scale quantum networking, the authors analyse shorter range, line-of-sight satellite settings for MA-QKD and determine necessary memory characteristics for near-term feasible implementations, producing sensible key rates above 10 Hz. These represent already more than an order of magnitude improvement with respect to the no-memory case, e.g., a secret key rate of 0.12 bits/s achieved by the Micius team [375]. Exemplary resulting figures of merit of Ref. [130] are memory efficiencies of $\eta_{\text{mem}} = 80\%$, a number of memory pairs or spatial modes of $m = 100$, $N = 1000$ temporal modes, storage times of 100 ms, and detector efficiencies of $\eta_{\text{det}} = 70\%$ for LEO satellites at a height of $h = 400$ km and a ground-station distance of 1000 km. Simulations are conducted to determine sensible parameter ranges for various of these figures of merit.

Furthermore, in Ref. [131], the authors perform calculations based on a large-scale event-based Monte Carlo simulation of repeater networks, that can faithfully represent

multimode memories, realistic protocols, and the corresponding losses and imperfections of the employed memories. They determine achievable QKD rates in different satellite and ground station geometries for feasible experimental parameters. For a configuration consisting of three satellites, where the two outer ones carry entangled photon-pair sources and only the central one carries a QM, they determine attainable key rates in the kHz range. The two considered sources of loss are the elevation-angle-dependent atmospheric loss $\eta_{\text{atm}}(\theta)$, and the distance-dependent diffraction loss η_{dif}. They analyse the key rates depending on the positioning of the two outer satellites and show that a trade-off exists between these two sources of loss. Moreover, they show that reaching intercontinental distances over 10.000 km with currently available or near-future parameters is feasible. With their simulation they are able to model situations with more than two repeater links. However, the overhead of using multiple satellites is still considerable. In Ref. [381], the numerical simulation mentioned above is developed further, in order to include further realistic effects and protocols like time-dependent memory noise, entanglement purification, etc. With this method they further analyse, compare, and combine different repeater strategies to determine the corresponding benefits and drawbacks.
A slightly different approach is taken in Ref. [233], in order to reduce the extensive hardware overhead necessary for global scale QR networks to some extent. The authors propose a single satellite equipped with a photon-pair source and two quantum memories, one with ultra-long-lifetime (ULL) (> 1 h) and another shorter-lived one (tens of ms). This satellite effectively acts as a time-delayed version of a single QR node, physically transporting stored qubits from above one ground station to the next. Entanglement distribution is thus performed in the overpass time of a typical Leo satellite (~ 4 min).
In summary, immense technical, scientific, and economic resources are being invested into SatQKD and the development of a global quantum communication network. Theoretical investigations show that these ideas are feasible to some extent, but require extreme technical overhead. Still, the technology readiness level of the relevant components, especially of quantum memories and single-photon sources needs to improve considerably. Nonetheless, the field remains highly exciting and interesting, and draws a lot of attention. However, it is not the only interesting application for quantum memories, as will be discussed in the next sections.

5.2 Optical machine learning

Due to its numerous great qualities in terms of speed, inherent parallelisation, enhanced information-carrying and multiplexing capabilities, as well as low power consumption,

light is an attractive candidate for information processing [382–384]. These characteristics have, of course, been harnessed widely in telecommunications in the past decades, but not so much in the realm of computing. Especially regarding different types of neuromorphic-inspired machine learning methods, which are famously computationally- and resource intensive, the use of optics could alleviate these demands and foster more sustainable data-based prediction methods [385]. However, these methods all require a nonlinearity of some sort, something that tends to be rather elusive or difficult to implement in optics, due to, i.e., the very small nonlinear (second and third-order) susceptibility of conventional materials. This lack of simply attainable nonlinearity poses a limit on the method's operation speed, energy consumption, and device size [386]. Therefore, there is growing interest in the research of better-performing nonlinearities based on optics for the use in artificial neural networks using, e.g., warm atomic vapours of Rb [387] or Cs [5]. The latter experiment was conducted in our group by Mingwei Yang.

Furthermore, it is not only light that can be beneficial for certain machine learning architectures. Also (quantum) optical memories hold promise for applications in this field. Specifically in Reservoir Computing (RC) [388–390], which represents a highly successful approach for processing time-dependent information. A reservoir consists of some type of nonlinear dynamical system, which responds to a certain input in a given manner. This method was introduced to reduce the cost of training a large amount of network weights, as here only the output layer, i.e., the response of the dynamical system to the given inputs is trained. In RC, the exact structure of the reservoir is not crucial. Necessary characteristics are a high dimensionality, and that its response should depend not only on the present input, but also on past inputs, up to a given time. This latter point, also referred to as 'fading memory', means the reservoir should gradually forget old inputs as new ones come in. This feature aligns with the functionality of optical memories, which allow for more flexibility compared to simple optical delays, a well investigated architecture in the context of RC [391, 392]. In Ref. [393] it is shown that the performance of an unoptimised reservoir can be significantly improved by adding a time-delayed version of the input for a given task. The reservoir used here mirrors that of a multi-delay line reservoir, where an optical quantum memory, analogous to the one presented in Ch. 4, but operated in the realm of classical coherent pulses, stores information for different time periods. Here, part of the information is fed back into the system, and part of it is measured. The nonlinearity of the reservoir is provided by an semiconductor optical amplifier (SOA). This field of research is relatively new but highly interesting, and holds significant promise to offer near-future applications for our memory systems.

5.3 Synchronisation of (multi-)photon generation

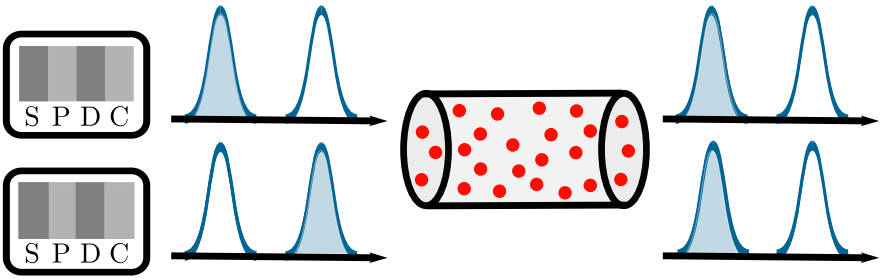

Figure 5.2: Schematic of the photon synchronisation scheme using a quantum memory. The probabilistic single photons (blue full pulses contain a photon and blue empty pulses are vacuum states) generated from, e.g., two SPDC sources in different time bins (heralding idler photons not shown for simplicity) are synchronised in time after being stored in the memory for different amounts of time.

Single photons constitute perhaps the most essential resource in discrete variable photonic quantum information processing (QIP). However, ideal single photon sources in terms of efficiency and deterministic generation remain elusive, as has been discussed in Ch. 1. Still to date, most experiments in quantum optics and experimental demonstrations of QIP algorithms are realised with non-deterministic heralded sources (such as SPDC), and commonly make use of post-selection. Unfortunately, the generation rates of multi-photon (entangled) states become very low as the number of photons N grows [138]. As an example, the generation rate for a 12-photon entangled state in Ref. [394] is 1 per hour, and in an experiment which employed five SPDC sources to generate 10 photons, it was necessary to maintain the mean photon number as low as $\mu < 0.05$, to effectively suppress multi-pair emissions [395], as explained in Ch. 1. Consequently, the resulting coincidence rate for 10 photons was only of a few events per hour. Quantum-dot sources perform better in this regard, and achieve $\sim$ 10-fold coincidences at rates of a few Hz [396, 397].

In this context, quantum memories find yet another application, as they are a potential solution for the so-called 'scaling catastrophe', by offering storage and on-demand retrieval of the photons, as shown schematically in Fig. 5.2. This combined time-multiplexing allows to synchronise probabilistic sources and thus increases the N-photon generation rate, allowing for higher probabilities in the generation of the multi-photon states required for QIP. Conversely, without memories, the N heralds would

have to fire simultaneously to achieve an N-fold coincidence. The scheme used for this is relatively simple (in theory but regrettably not experimentally). If M heralded parametric sources are generating M photons, where $M-1$ are being stored in QMs until the last photon is heralded, and thus triggers the read-out of all memories, then one can obtain a N^{M-1} enhancement factor for the M-fold coincidence probability, N being the number of storage time slots in a time-multiplexing scheme [100]. In Ref. [138], it is shown that even memories that do no yet achieve very high efficiencies are useful in this regard, when combined with post-selection schemes. The crucial figure of merit for synchronisation of single-photon events is determined to be the quantity $\eta_{\text{mem}}\text{TBP} = \eta_{\text{mem}}\,\Delta\omega_{\text{mem}}\cdot\tau$, the product of memory efficiency and the time-bandwidth product TBP. Their analysis highlights the importance of developing quantum memories for applications other than long-distance quantum communication. These types of experiments have been realised with fibre storage loops achieving enhancement factors up to 30-fold [100, 398, 399].
Using an atomic vapour ladder-type quantum memory, synchronisation of single photons from a warm vapour SPS based on FWM (using the same ladder-scheme) was realised in Ref. [400], achieving an end-to-end efficiency of $\eta_{e2e} = 25\%$, and high indistinguishability. Moreover, they observe a 10-fold increase in their photon-pair coincidence rate. Further experiments showing synchronisation of generated photons in atomic vapour memories (read-write or read-only, respectively) are presented in Refs. [401, 402].
Apart from synchronisation, memories could also serve as pulse shapers for the stored photons of, e.g., QD sources, as in Ref. [403].

5.4 Tests of fundamental physics in space

This section is based on Ref. [2]:
J.-M. Mol, **L. Esguerra**, M. Meister, D. E. Bruschi, A. W. Schell, J. Wolters, and L. Wörner, Quantum memories for fundamental science in space. *Quantum Sci. Technol.*, 8, 024006, 2023.

This section summarises the work presented as a white paper proposal for NASA, which was later published as a review paper in Quantum Science and Technology. Here we analysed possible applications of space-borne quantum memories in experiments that aim to investigate the correlations and connections between the foundations of quantum mechanics and general relativity, and therefore require extreme sensitivity. Since quantum memories preserve quantum entanglement and coherence in the storage process, they might aid to study Bell tests on astronomical distances, enhance measurement precision

on the effects of curved spacetime on quantum systems, or facilitate distributed quantum sensing networks and improve quantum clocks. The following subsections describe the aforementioned applications in a bit more detail, as presented in Ref. [2]. My primary contribution to this work was in the review of the state-of-the-art of the quantum memory realm. Nevertheless, for completeness, I include the proposals for applications in space-based fundamental physics experiments in the thesis, as they further expand the plethora of possible areas in which quantum memories may be of relevance in the future.

5.4.1 Long-range Bell tests

After Clauser's and Aspect's experimental demonstration of the violation of Bell's inequalities and the closing of the locality loophole (see Ch. 1, Sec. 1.1), many other such experiments have been carried out, even ruling out possible loopholes in fair-sampling and locality [404–407]. Investigations have even been performed on quantum many-body systems, such as BECs in Refs. [408–410], in order to better understand many-particle entanglement. Still, some possible (albeit controversial) loopholes may exist. One is the memory loophole, which states that under local realism there could be memory effects leading to statistical dependence between subsequent pairs of measurements. Furthermore, physical parameters might vary in time. Concrete experiments [411–413] have shown that, if each new measurement pair is conducted with a random pair of measurement settings, neither memory nor time inhomogeneity pose serious effects on the experiment. As in many experiments subsequent temporal measurements are averaged in order to achieve statistical significance, this memory loophole can be statistically mitigated, but it remains challenging to address it at a fundamental level. One possible solution to this problem involves extending the baseline of experiments by establishing genuine space-like separations between all measurements, effectively closing this loophole.
Although it is not absolutely necessary to perform Bell tests over large distances, quantum memories can here aid to enhance such experiments by storing a part of an entangled quantum state, and thus allowing synchronous measurements while satisfying the space-like separation criteria. A simple setup could involve an entangled photon-pair source and a quantum memory, which locally stores one of the created photons while the other is sent to a distant location. Upon arrival of the latter, a delayed measurement could be carried out. In this configuration, the need of a second long baseline is mitigated by reducing the requirement to one single extensive baseline.
Apart from closing potential loopholes, in order to demonstrate the technical realisability of such a proposal, one could think of using a ground-based entangled photon-pair source

combined with a memory, and sending the other photon to be detected on a satellite in low Earth orbit (LEO) at $200 - 2000\,\mathrm{km}$ height. The coherence times needed for the involved memory would be in the millisecond range, as realised already in some experiments [127, 200]. Moreover, positioning both source and memory on a LEO satellite or on the International Space Station (ISS), while the link is established to a detector orbiting the Moon, could be considered as an advanced experimental proposal. This type of setup would ease Bell tests investigating 'Freedom-of-Choice' loopholes, since two different experimenters on Earth and the Moon respectively, could independently choose their measurement basis during the travel time of the photon [414]. In this case, the needed storage or coherence times would reach one second. Although this has still not been seen at the single-photon level, it has been shown in memory experiments using weak coherent pulses containing many photons [218, 219], and can thus optimistically be envisioned to become a reality for single photon experiments in the near future.

5.4.2 Effects of curved spacetime on localised quantum systems

In a global quantum network, one could make use of entanglement between modes of a quantum field or other degrees of freedom, either within the same site and/or across sites. One or more of the nodes, carrying a quantum memory in which the information or state is stored, could undergo a physical process that affects the shared entanglement. Improved measurement sensitivity here would allow either for the discovery of novel physical effects, or for the development of new technologies, if these effects on entanglement can be engineered favourably.

Today, measurements on quantum states are routinely performed in the laboratory. However, new effects may exist on timescales where it is almost impossible to maintain the quantum coherence of a certain quantum system. It is in these cases where quantum memories may be of use, allowing to store a state long enough for such effects to be measurable.

A relevant case would be the dynamical creation of entanglement within moving cavities. (Relativistic) motion of a cavity that confines a quantum field has been shown to not only create particles through the dynamical Casimir effect [415], but also to create quantum correlations between field excitations [416–419]. In Refs. [420, 421], a systematic study of the effects of motion revealed how the properties of the involved transformations can be engineered to construct different (entangling) quantum gates. Work on the application of quantum metrology in a relativistic scenario, specifically in gravitational wave sensing by means of entangled states of phonons within a BEC, was developed in Ref. [422]. Hereby,

the assumption was made that the involved cavities are infinitely rigid. Nevertheless, in realistic studies going beyond proof-of-principle, the elastic properties of the cavities need to be taken into account. Preliminary attempts in this direction have been performed in Refs. [423, 424], but still more work is necessary to correctly characterise the system for concrete mission proposals. Similarly as before, for the promising path of highly sensitive measurements based on relativistic quantum fields, the problem of storing these fields for prolonged times for later processing arises. It becomes necessary to store the quantum states while the cavity is located in an isolated environment, hereby reducing mechanical vibrations and other constraints. Subsequently, if the state of the stored field is then affected by the motion of the setup containing the memory, this should affect any present entanglement as well. Specifically designed resonances have been proved to enhance the effects on the average particle number or the entanglement linearly or quadratically with time [421]. In the case that the characteristic frequencies involved in the memory are smaller than those of light, perturbations of, e.g., the phonons of a BEC, are affected by gravity and motion, and therefore, the discussed techniques apply. As a result, quantum memories with characteristic small frequencies should witness larger effects in a shorter time.

5.4.3 Entanglement dynamics due to motion

Entanglement measurements are another interesting type of experiment, which may benefit from precision improvement by means of quantum memories [425]. In order to test the effects of gravitational environment changes, quantum states need to be stored for prolonged times [426]. In Ref. [427] an experiment was proposed, in which two entangled cold atomic gases are used to test acceleration- or gravitation-induced decoherence effects. It makes use of two different spacecraft, each containing a quantum memory. The experiment begins by entangling both memories when the two spacecraft are located in the same orbit, e.g., in the same inertial frame, and accelerating one of the spacecraft to another orbit. Since, as discussed above, cavity motion has an effect on the states of localised systems confined within, such as the phononic modes of a BEC [422] or simple quantum field modes [416], the experiment anticipates some effect on the entanglement shared between these types of modes.
Necessary coherence times for the involved memories have been estimated to be in the order of 100 ms [427], going to seconds or minutes with more careful assumptions for precision. Depending on the achievable values for memory efficiency and fidelity, a possible requirement is again multimode capacity, in order to achieve a high enough SNR through statistics.

5.4.4 Quantum memories for improved clock precision

There are many relevant applications that require highly precise time measurements. Common ones are position accuracy in GPS systems, standardisation [428, 429], and conceivably gravitational potential mapping. Classically, the Allan deviation of each node can be reduced by sharing timing information and averaging within a network of clocks. In Ref. [430], a quantum clock network in space has been proposed. The N clocks in this configuration could share a quantum state, and measure and stabilise the average network frequency, as opposed to measuring and correcting nodes separately, as is done classically. Compared to these classical clock networks, going quantum could yield a maximum improvement of $\sqrt{N}$ in precision (best case scenario, i.e., Heisenberg limit), if the averaging times are kept short enough.
Quantum repeaters could aid entanglement propagation in such systems. Quantum memories offer flexibility by allowing the storage of quantum states for synchronisation between clock measurements, especially in complex larger networks. Multimode memories would be practical in this case, if it becomes necessary to store multiple photon pairs. Here, as the number of optimal modes for a clock scales as $(\log(n))^2$ [430], for a clock accommodating $n = 10^4$ qubits, 85 modes per channel would be required. This is already achievable with state-of-the-art quantum memories [202, 227, 431].
For the establishment of a global time reference, it becomes imperative that a sufficiently extensive clock network operates in space, owing to the aforementioned losses inherent to optical links limited to ground-based operations.

5.4.5 Distributed quantum sensing

Quantum sensing, one of the three pillars of quantum technologies and also the most advanced one, could also benefit greatly from the construction of such large space-based networks, as the ones described for clocks in the former section. In these space-borne distributed quantum sensor networks, at best the sensitivity scales as $1/N$, compared to a scaling of $1/\sqrt{N}$ in fully classical networks. This might enable sensitive measurements below the standard quantum limit [432–434], and precise detection of curved spacetime effects, that could lead to a deeper understanding of the relation between quantum physics and general relativity.
For these types of quantum-sensor networks, quantum memories, even deployed on ground-based stations or labs, are key devices. In the same manner as the development into

space-based networks is envisioned for improving quantum communication applications, in sensing applications it might yield comparable benefits for astronomy and geodesy. The construction of interferometric telescopes [435], or optical wavelength telescope arrays [436, 437] have recently been proposed as applications. For geodesic measurements, the practicability of employing quantum networks for the detection and localisation of seismic events has been shown in Ref. [438].

5.4.6 Summary

Space-borne quantum memories hold significant promise for advancing fundamental physics experiments [439]. They can aid in the realisation of Bell tests over astronomical distances, and possibly allow for tests of predictions of physics at the overlap of relativity and quantum mechanics. In the last sections, ideas that lie behind recent predictions of the effects of motion and dynamical gravitational fields on the quantum state of a localised system have been presented. Testing and validating these predictions will require storage of quantum states for extended times. Nevertheless, storage times and efficiencies in quantum memories are approaching a useful regime for space applications [130, 131]. Moreover, multimode capabilities are currently greatly investigated. Furthermore, the highly active research ongoing in the quantum technology and quantum memory communities grant an optimistic outlook for improvements in the next few years. For more specific details on the proposed ideas, I refer the reader to Ref. [2] and the references therein.

5.5 Alkali-noble gas memory

The QToRX (Quantum Token Based on Rubidium and Xenon) project [440] is a collaboration between the German Aerospace Center (DLR), the Physikalisch-Technische Bundesanstalt (PTB), and the Leibniz-Unversität Hannover (LUH) in the context of the so-called “Grand Challenge of Quantum Communication” [441], a funding challenge from the German Federal Ministry of Education and Research (BMBF). The aim of the challenge is the investigation and development of quantum communication technologies for applications besides from QKD, specifically for the secure authentication of IT system users by means of so-called quantum tokens. As in the exchange of quantum keys, quantum tokens are based on the principle that quantum information cannot be copied without being altered (no-cloning). The use of quantum states thus can, in certain contexts, guarantee physical protection against forgery. Quantum tokens represent a technical alternative to today’s security tokens and may also enable secure authentication

procedures in the future, not circumventable even by powerful quantum computers. In addition to authentication, possible future use cases include secure data storage while maintaining privacy, secure distributed computing, digital signatures, and forgery-proof documents [441].
An essential issue that must be overcome in order to develop quantum tokens is the currently still limited storage or coherence time achievable in optically interfaceable quantum memories, with state-of-the-art still in the millisecond range or lower. These are not yet sufficient for use in quantum token systems, for which storage of at least several minutes would be required, conditional on the application.
Exactly this extension of the available storage times in warm-alkali-vapour-based quantum memories constitutes the goal of the QToRX project. For this, long-lived but optically inaccessible collective states of noble-gas spins will be employed. The scheme relies in the coherent mapping of the spin excitation of the alkali atoms to the noble-gas spins via spin-exchange (SE) interaction, mediated by magnetic fields [442, 443]. This coherent and reversible mapping of nonclassical optical signals onto noble-gas spins via SE interaction has not been demonstrated to date (at the time of writing), and thus makes this project highly interesting.

Schemes to achieve the above mentioned mapping are outlined and characterised in more detail in Ref. [443]. In order to counteract the limited available storage time in alkali atoms resulting from the coupling of their valence electron spin to the environment, rare isotopes of noble gases are introduced in the cell. These isotopes, e.g., ^{3}He, have non-zero nuclear spins that are isolated from the environment due to the enclosing complete electronic shells. As a result, coherence times of hours or even days at room temperature or above are possible [444–446]. However, as they are not optically accessible using lasers, their preparation, interfacing, and monitoring is extremely complicated. Access to these spins is possible through collisions with optically active atoms (i.e., alkalis) via weak SE collisions [444, 447–451], involving the weak isotropic hyperfine interaction. Accordingly, only a small fraction of the spin orientation is transferred in one single collision [449]. Numerous collisions are thus needed to accumulate to a coherent and collective evolution of the two spin ensembles. This coherent coupling can be mediated and enhanced via external (magnetic) fields [452, 453]. In Ref. [443], different mixtures, experimental conditions, and parameters, including temperatures, coatings, and buffer gas pressures are investigated theoretically. Moreover, two distinct protocols are presented, namely a two-step sequential mapping, where the non-classical light is in a first step stored in the alkalis, and in a second step transferred to the noble gas spins via SE mediated via a magnetic field; and an adiabatic mapping, in which these two steps happen simultaneously.

Achievable efficiencies are calculated for both schemes. A schematic of the working principle of the alkali-noble-gas memory is depicted in Fig. 5.3.

For the QToRX memory, contrary to the name, cells containing a mixture of ^{133}Cs, ^{129}Xe, and N_2 buffer gas will be employed, due to our groups experience with caesium and since QToCsX would have been a bit more difficult to pronounce.
Notably, in Ref. [443], the necessity of using antirelaxation coatings was determined, as for this type of gas mixtures lower ^{129}Xe densities are required, in order to reduce the probability of short-lived molecule formation. Since long storage times are intended, wall collisions should no longer be neglected.
The QToRX memory is being built at the PTB at the time of writing, after the setup was moved from our lab at the DLR in December 2023. For this memory, a four-layer Twinleaf MS-2 magnetic shield with integrated coils to generate the external magnetic field will be used. This shield provides a shielding factor of 10^6. The cell will be heated by hot air using a 3D-printed PEEK oven. A side view of the shield and the oven is shown in Fig. 5.4.

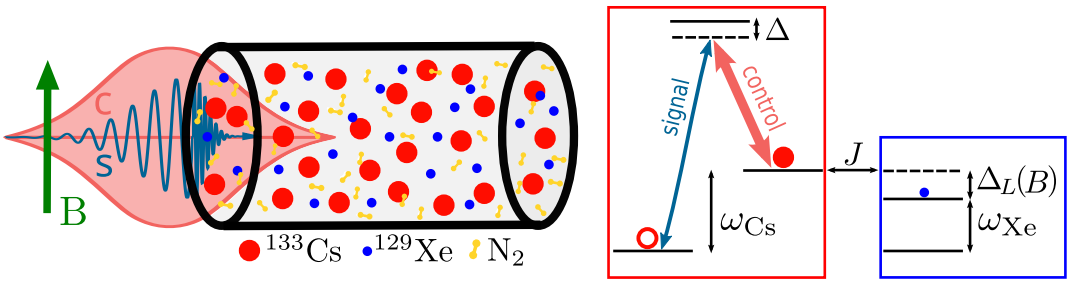

Figure 5.3: Schematic of the alkali-noble-gas memory working principle. The vapour cell contains ^{133}Cs (red), and a combination of ^{129}Xe (blue) and N_2 (yellow) as buffer gases (concentrations not to scale). A variable transverse magnetic field B is applied to the cell. Signal (s) and control (c) pulses enter the memory as usual. The storage in the alkali (^{133}Cs) is based on EIT/Raman storage (see Ch. 2), as indicated in the Λ-scheme in the red box. The level structure of ^{129}Xe is depicted in the blue box. Tuning the magnetic field changes the position of the upper energy level via the detuning $\Delta_L(B)$, such that the atoms can interact via the spin-exchange interaction, denoted by the interaction rate J (see Ref. [443]). ω_{Cs} and ω_{Xe} are the ground state energy splittings of Cs and Xe, respectively. Δ is the detuning from the excited state of Cs.

The Λ-scheme intended for storage in the alkali atoms will exploit the Zeeman substructure of the hyperfine states, as discussed in Ch. 4, Sec. 4.4.1. For this, the corresponding preparation of the system via Zeeman optical pumping will be conducted. Further,

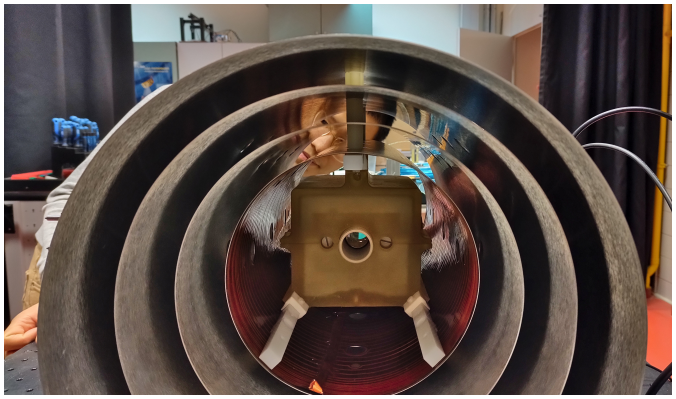

Figure 5.4: Side view of the four-layer Twinleaf MS-2 magnetic shield with integrated coils, containing the 3D-printed PEEK oven for heating the cell using hot air. In the back, our dear late colleague Tianhao Liu from the PTB, who unfortunately left us too soon.

improved control of the spin-states using guiding fields is intended, as discussed also in Sec. 4.4.1. The lasers systems for this project all consist of Toptica Lasers, which are subsequently amplified by Toptica tapered amplifiers (TAs), in order to increase the achievable powers (and Rabi frequencies) of the control and pump lasers. All of these improvements should lead to higher efficiencies, lower noise levels, and storage times (in the alkalis) in the millisecond range. Thereafter, the spin-exchange interaction and the coherent transfer of the excitation from the alkali atoms to the noble gas atoms can be investigated, with the goal of achieving minute- or hour-long storage times.

5.6 Quantum tokens for secure authentication

At the Conference of IT Security organised by the BMBF in March 2023 in Berlin, the developments of the "Grand Challenge of Quantum Communication" [441] were discussed, and the six competing experimental projects and one theory project presented their research after almost a year and a half of project duration. In this context, it was determined that each project should put more emphasis on the experimental demonstration of a quantum token, this being the main goal of the challenge. The theory group should thus aid in the creation of a general framework, applicable to all six different physical implementations, in order to determine relevant criteria to evaluate what comprises such a quantum token[1]. At this point it became clear to us that the definition and demonstration of the quantum token were not a straightforward matter.

[1] A theory to rule them all, so to say.

Since the QToRX memory presented above is not yet operational, it thus became my task to find out how we could demonstrate such a quantum token in the existing hyperfine memory we had, using weak coherent states at the SPL.
It turned out that the concept of a quantum token was not as established as other quantum concepts such as bits, memories, communication, computing, sensing, etc., and different meanings exist for the concept. Therefore, we first had to find a suitable definition. A token within the realm of classical security serves as an external mechanism utilised to obtain access to an electronically restricted resource. This token is employed either alongside or instead of a password [454]. Examples of security tokens include a banking token employed as a digital authenticator for accessing online banking services, wireless keycards used to open locked doors, etc. Security tokens allow to store information like passwords, cryptographic keys used to generate digital signatures, or biometric data (such as fingerprints). Let us thus define a token in general terms as a unique digital identifier or a one-time password. A quantum token is therefore a qubit-based token, which can serve for authentication purposes, and can be manipulated, transmitted, or stored [455]. One significant application of a quantum token is so-called unforgeable quantum money or quantum currency. In fact, unforgeable quantum money was the first ever proposed quantum cryptographic primitive by Wiesner already in the 70s, but first published in 1983 [33]. It uses conjugate quantum bases and works in a similar fashion to the BB84 QKD protocol. It was actually this idea of conjugate coding that inspired Bennett and Brassard to develop said protocol. However, since Wiesner's quantum money idea required long-term quantum storage devices or quantum memories, it did not obtain as much attention as QKD, which made its debut shortly after. The goal of a quantum money scheme is to achieve an efficient and authenticated transaction between a client, a vendor, and a bank via the use of a prepaid credit card, i.e., a device containing quantum information (private-key money scheme), or between a client and a vendor via the use of banknotes (public-key money scheme), with maximal security guarantees [456].

Because the development of quantum memories has seen a large impulse in the last two decades, the topic of unforgeable quantum money gained more attention again [457, 458]. Similar to QKD, not only approaches with single photons but also using attenuated coherent pulses have been developed [456, 459–461]. We were interested in these, as we have not yet paired our memory with a real single photon source. There has also been some development regarding quantum money schemes that circumvent the need of a quantum memory, e.g., in Ref. [462], but as these do not concern our research, I will not consider them further.

Among the mentioned references, the approach that seemed most experimentally straight-

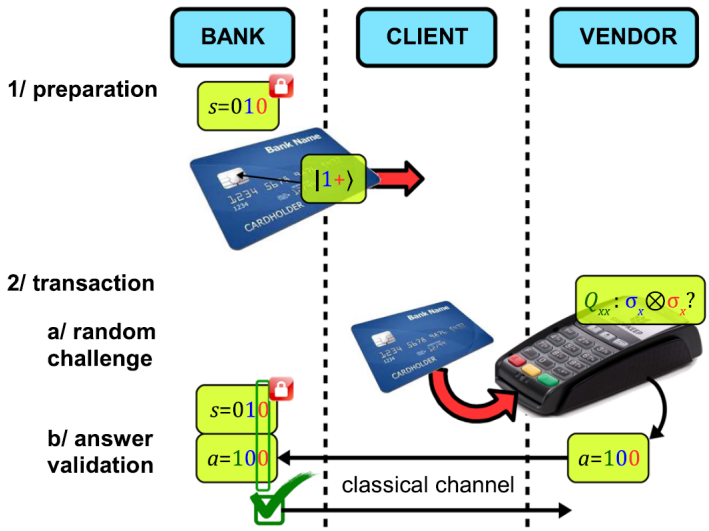

Figure 5.5: Schematic of a practical quantum money scheme, as presented in Ref. [456] by M. Bozzio (figure adapted from there). Depicted is a sequence of interactions between the client, the bank, and the vendor involved in the transaction. In a first preparation step, the bank makes use of a secret key, the bit string s, to prepare the quantum state to be stored on the card that is subsequently given to the client. For a given transaction with a vendor, the latter randomly selects one out of the two challenge questions $\hat{Q}_{zz}$ or $\hat{Q}_{xx}$, performs a measurement, and sends the outcome a back to the bank. The bank can now verify the validity of the card or, in the given case, detect a forgery attempt.

forward was the one presented by M. Bozzio in Ref. [456]. It is based on polarisation encoding of weak coherent states of light and classical verification mechanisms, and operates under conditions compatible with state-of-the-art ensemble-based QMs. The scheme is depicted in Fig. 5.5. Using two conjugate bases, $\{|0\rangle, |1\rangle\}$ and $\{|+\rangle, |-\rangle\}$, corresponding to the eigenvectors of the $\hat{\sigma}_z$ and $\hat{\sigma}_x$ matrices, the bank prepares a quantum state on the credit card using a secret key, consisting of a three-bit string $s = \{b, c_0, c_1\}$. Here, $b = 0\,(1)$ denotes that the first bit is encoded in the $\hat{\sigma}_z$ basis and the second in the $\hat{\sigma}_x$ basis (or vice versa), and c_0, c_1 are the corresponding bit values (0 for $\{|0\rangle, |+\rangle\}$ and 1 for $\{|1\rangle, |-\rangle\}$). The card, containing only the two-bit sequence, i.e., $|1, +\rangle$, is then handed to the client. Upon a transaction, the vendor randomly selects one out of two challenge questions $\hat{Q}_{zz} = \hat{\sigma}_z \otimes \hat{\sigma}_z$ or $\hat{Q}_{xx} = \hat{\sigma}_x \otimes \hat{\sigma}_x$, measures the qubits, and sends the outcome to the bank. There, the validity of the credit card is verified or a forgery attempt can be detected. If a dishonest client tries to duplicate the credit card, he will fail according to no-cloning. As the 2-qubit state is unknown, two copies of the credit card cannot ever pass both challenges with high probability. The maximal cheating

probability amounts to $\frac{3}{4}$. By using N of these qubit pairs, the cheating probability thus scales as $\left(\frac{3}{4}\right)^N$. The credit card should be able to preserve these states coherently for an extended amount of time, the point where quantum memories become a necessity. The above description corresponds to a case where true single qubit pairs are used, which I have chosen to explain for simplicity. The version using coherent states is analogous. The authors carry out a thorough security analysis of the protocol for this case, and further for the implementation using weak coherent pulses. In Ref. [461] this security analysis is developed further and extended to include noise and losses introduced by a dishonest party. Also, the case of a decohering QM is analysed. The calculation makes use of semidefinite programming (SDP). For further details on the security analysis and SDP see Ref. [126].

The implementation with coherent pulses from a telecom laser proposed in Ref. [456] makes use of polarisation degrees of freedom, in order to encode the quantum bits. They do not implement storage in a quantum memory, but directly send the qubits to the detection via polarisation analysers, corresponding to the vendor's role. In other words, they perform an on-the-fly quantum credit card generation and detection scheme. We use this scheme and a different encoding scheme using amplitude and phase degrees of freedom introduced in Ref. [460], as an inspiration to implement such a protocol, but making use of our quantum memory in order to store the quantum credit card.

Apart from all the different possible attacks that can be executed on a quantum money scheme (see Ref. [461]), in this context it is fundamental to consider the 50/50 Card Split [126]. In a lossy implementation of such a scheme, a dishonest client could be able to successfully extract twice the amount of money in two different banks without being detected. This would theoretically be possible in a case where the honest quantum channel, or the quantum memory, exhibit losses above 50%. In such a scenario, the client may simply replace the channel with a perfect one, split the money state in two, and send each to a different bank. If there have been no cloning attempts, both banks will confirm the validity the money. The dishonest client would then be able to spend twice the amount of money associated with the original state. Therefore, it becomes crucial to determine an upper bound on the losses of the memory and the quantum channel for secure quantum token (money) implementations.

5.6.1 Experimental proposal

Based on the implementation presented in the previous section, we needed to adapt the scheme to a version compatible with our hyperfine memory (see Ch. 4). The

use of polarisation degrees of freedom was problematic, since we would need to have a dual-rail memory that could store at least two perpendicular polarisations at the same time, similar to the one from Ref. [189]. The Bozzio scheme of Ref. [456] using two-qubit states can be carried out in an analogous manner with single qubit states or single coherent pulses, however requiring $2N$ states instead of N for the same security level. Our memory is highly suitable for a time-bin encoding, $\{|e\rangle, |l\rangle\}$ for early and late time bins, in which the subsequent qubit states may have scrambled global phases. The measurement step could be then achieved by interference of these pulses.

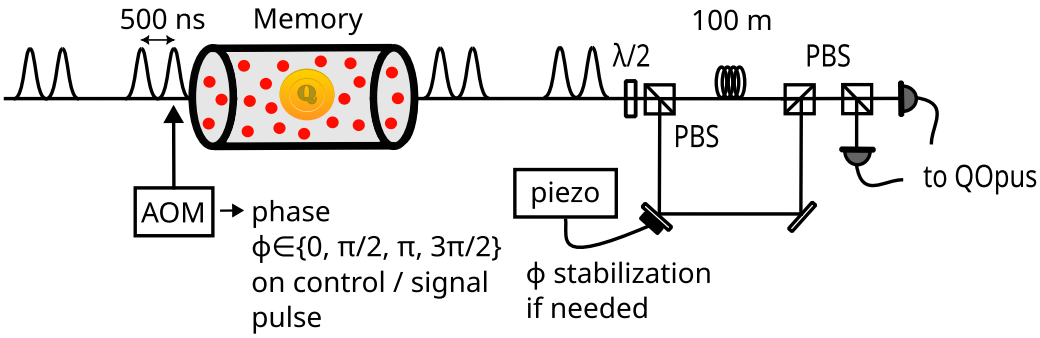

Figure 5.6: Schematic of the proposed experimental setup for the storage of quantum tokens ('qoins' Q) in time-bin encoding $\{|e\rangle, |l\rangle\}$ using our memory. AOM: acousto-optic modulator; $\lambda/2$: half-wave plate; piezo: piezoelectric chip and actuator; PBS: polarising beam splitter; Q; quantum token or quantum coin (qoin); QOpus: SNSPD detector.

The adapted quantum token (quantum money) protocol is schematically depicted in Fig. 5.6. Sequences of two attenuated pulses $\{|e\rangle, |l\rangle\}$ separated by $\sim 500\,\text{ns}$ are sent into the memory and subsequently stored, using the same EIT protocol presented in Ch. 4. The phase encoding is realised via the control pulse, which is generated using an AOM, as done in the later implementations of the memory. The AOM can be programmed to also imprint a phase on the storage control pulse. As the latter mediates the storage process, it should transfer the phase to the signal pulse during storage. Because the storage process is coherent, it should preserve the imprinted phase. The exact workings of this phase transfer will need to be investigated in detail. The same procedure can be repeated with the readout control pulse. The different phases are chosen from the set $\phi = \{0, \frac{\pi}{2}, \pi, \frac{3\pi}{2}\} + \phi_g$, where ϕ_g is a random global phase. Phase randomisation is a technique widely used in some QKD protocols with coherent states, in order to increase security [463]. At the interferometer, the phase setting corresponds to the measurement setting (basis) chosen for detection.

For the latter, the pair of pulses $\{|e\rangle, |l\rangle\}$ that have been retrieved from the memory are interfered using an unbalanced or asymmetric Mach-Zehnder interferometer (AMZI) and detected thereafter using two different detectors. The longer arm of the interferometer consists of a 100 m long fibre, a length corresponding to the pulse separation of 500 ns. Thus, the time delay between the pulses is matched to the time delay between the short and long paths of the interferometer, such that the component from the $|e\rangle$ pulse that takes the long path and the component of the $|l\rangle$ pulse taking the short path can interfere at the detector. The detected signal (at each detector) from the interferometer measured on a photodiode is then a series of three pulses, where the middle one corresponds to the one where $|e\rangle$ and $|l\rangle$ have interfered. Thus, depending on the phase imprinted by the AFG and the AMZI measurement setting, this middle pulse shows a varying amplitude between zero (destructive interference) and twice the initial pulse amplitude (constructive interference). The variation of the integrated area of this interference pulse over time can be used to determine a fringe visibility given as $V = \frac{(\max - \min)}{(\max + \min)}$, where max (min) correspond to the maximal (minimal) integrated pulse areas. This is analogous to the measurements performed in the second part of Ref. [136]. Thus, if the bases of the AFG and the AMZI match, the result is valid for constructive interference and invalid in the destructive case, while if the bases do not match, the result is discarded (as done in the quantum money protocol). A stable interferometer is in this case beneficial, such that the measurement setting is fixed and known, in order to carry out the protocol. In case of instability, a great deal of post processing would be required to determine the results where the used bases matched. It should be noted that, in order to store a single quantum token, the latter is 'divided into two parts' which are stored one after the other. Moreover, the protocol needs to be repeated thousands of times, which could be an argument against the usefulness of such a scheme.

5.6.2 First experimental tests

The first step towards this experimental realisation was building the AMZI and determining if phase stabilisation using a piezoelectric actuator on a mirror would be necessary. Some thought had to be put into how to program the AFG, such that it could imprint two different phases into subsequent pulses in a switching time below 500 ns. The phase implementation was coded by driving the AOM with an RF signal defined as a sine wave with a given phase (which would be randomised later), and multiplying this sine with a Gaussian envelope. This allows to implement the phase change in the code and thus overcome the slow switching time of the AFG. In order to test the interference

visibility and the stability of the AMZI, macroscopic control pulses without an extra imprinted phase and not involving storage were sent directly through it.
After analysing the data, the normalised integrated retrieval pulses over time showed much faster phase fluctuations than we had expected initially. This behaviour persisted even when interfering the control laser in cw. When changing the 100 m fibre for shorter ones (20 m and 5 m), the fast phase noise remained, only with a smaller amplitude. We considered its source to be optical feedback into the lasers, but this was ruled out after placing a Faraday isolator before the AMZI. All of this led to the conclusion that the fast phase noise we were observing had to come from the laser itself. When conducting the same measurement in cw with a Toptica laser, a nice phase oscillation is visible. Figure 5.7 (a) shows the fast phase noise from our control laser in cw compared to the smooth sinusoidal phase change from the Toptica laser in cw (b). The reason that the phase of the cw control laser stays in the lower range $(0 - 0.4)$ much more than in the upper range $(0.4 - 1.0)$ is not clear and requires more investigation. Unfortunately, these results meant the quantum token experiment is not feasible with the present memory setup and the current lasers.

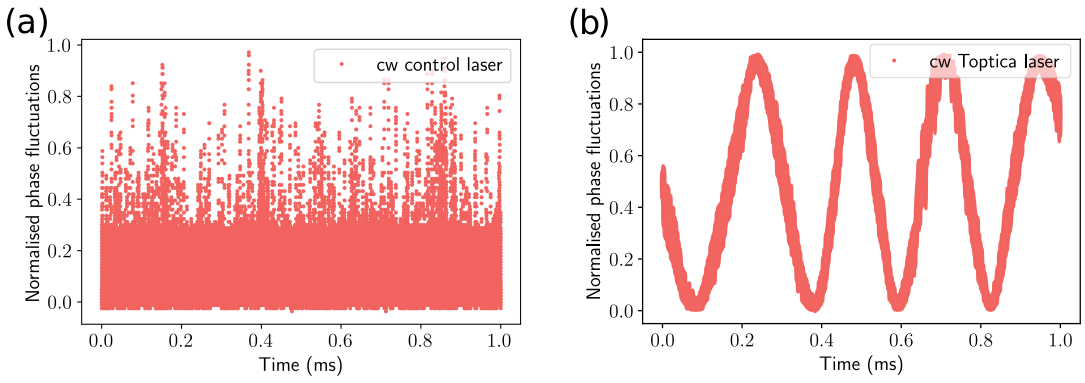

Figure 5.7: Phase behaviour of lasers interfering on the asymmetric Mach-Zehnder interferometer. (a) Control diode laser in cw. (b) Toptica laser in cw for comparison.

We wanted to find out possible reasons for this fast phase noise coming from the lasers. A qualitative measure for the phase stability can be determined from the frequency stability of the lasers. This, in turn, can be associated to the spectral width of the FFT of the beating signal of the offset lock (see Ch. 4). This led us to carry out the estimation of the laser linewidths from the offset lock performed in Ch. 4, Sec. 4.2.1. Observing the width of the beat signal on a spectrum analyser, we tried different measures that could possibly mitigate the noise, and thus reduce the spectral width. These comprised disconnecting the lasers from the RPs and using a low-noise power

supply for both signal and control lasers. However, none of these measures seemed to make a difference. Therefore, we have not been able, until the time of writing, to determine the reason for this extreme phase noise. Due to time reasons, I had to stop the project at this stage and continue writing the thesis you are reading. Thus, here is another endeavour I can pass on to my successor PhD student, hoping that it can soon be realised, e.g., with the QToRX setup currently in construction (see Sec. 5.5).

5.7 Portable rack-mounted memory-system demonstrator

As a preliminary step in the direction of testing quantum memories and quantum communication systems outside of laboratory environments, the QuMSeC (Quantum Memories for Secure Communication in Tomorrow's Society) project aimed to build a fully functional standalone rack demonstrator housing an optical quantum memory in a 19 inch rack. This project was a collaboration between the German Aerospace Center (DLR), the TU Berlin, the Humboldt-University Berlin, and the Ferdinand Braun Institute. From our group's side, Alexander Erl was the Master's student involved in building the memory package under supervision of Leon Meßner and myself, especially in the first stages of the project. He then went on to work together with Martin Jutisz from the HU Berlin, in order to integrate the memory with the laser systems built there. The knowledge and expertise gained by building the hyperfine memory presented in Ch. 4 was transferred into the memory and the filtering packages built by Alex in this project, and presented in his Master's thesis [11].

Specifically, the heater system used in this memory was designed after discovering the complications arising from the simple heating system based on Thorlabs HT10K flexible polyimide foil heating pads, implemented in the hyperfine memory. As a reminder, the non-vanishing magnetic fields inside the magnetic shielding led to lower pumping efficiencies, and thus to noise in memory operation, which had to be minimised by turning the heater off completely during storage experiments. This, however, led to $3-5$°C cooling off of the atoms during the measurements at SPL (60 s integration time), and thus to a non-negligible change in the optical depth of the system. Moreover, these magnetic fields can affect the spin orientation of the atoms and lead to faster degrading of the spinwave. Therefore, for the new heating system, we wanted the heating resistors to be placed outside of the shield and further away from the optical axis. Furthermore, we decided to use oxygen-free-high-thermal-conductivity (OFHC) copper, which is a premium grade of copper with a high level of conductivity and less susceptibility to magnetisation, due to its vanishing oxygen content, which can affect the electrical properties of the material. The

heating system consists of a half cylinder longer than the shielding, in which the Cs cell is positioned in the center, and two cylindrical covers that are placed on the top at the external ends using thermally conducting adhesive, such that there is enough space in the center for the capillary of the cell to be outside of the heater. This renders this the coolest part of the cell, such that the Cs will condense in that region, leaving the walls as clean as possible. A schematic and some pictures of the cell and this new heating system can be seen in Fig. 5.8. For this heating system, Cs cells with a smaller diameter were needed. From calculations carried out, as described in Ch. 3, focussing on diffusion, radiation trapping, and quenching, we decided to order different cells (from Precision Glassblowing) with a length of 7.5 cm and an inner (outer) diameter of 4 (6) mm, containing different buffer gas species and pressures: 5 torr N_2, 20 torr N_2, 5 torr Ar, and 20 torr Ar. The smaller diameter of the cells reduces the probability of radiation trapping in the radial direction. The cell used in the QuMSeC memory contains Cs and 5 torr N_2. The comparative analysis of the performance of these different cells still remains open for investigation.

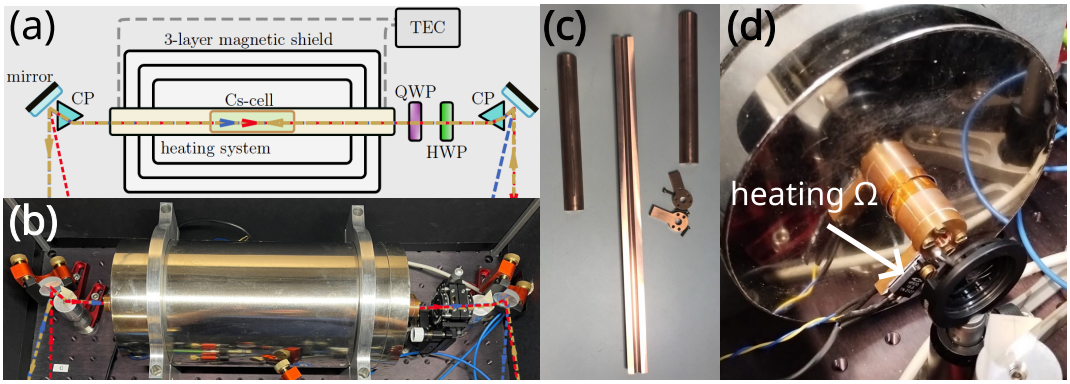

Figure 5.8: QuMSeC memory heating system. (a) Cut-out of the schematics of the memory cell with the OFHC-copper heating system containing the Cs cell. The blue and red arrows are the signal and control fields, respectively, and the mustard arrow represents the pump laser. CP: calcite prisms; HWP: half-wave plate, QWP: quarter-wave plate. (b) Picture of the same part of the actual memory setup as in (a). (c) Picture of the parts of the copper heating system. (d) Side-view of the heating system inside the cell. The heater resistors with NTC thermistors are glued from the outside and connected to the TEC. (Modified) from Ref. [11].

After thorough characterisation of the memory and filtering packages, the different setup packages were integrated into a compact and portable 19 inch rack, as depicted in Fig. 5.9. Various storage measurements using macroscopic coherent pulses and also at the SPL were realised in the rack. Achieved figures of merit are a $1/e$ storage time

Figure 5.9: Picture of the mobile demonstrator of an atomic quantum memory in a 19-inch rack built for the QuMSeC project by Martin Jutisz and Alexander Erl. Taken from Ref. [11].

of $\tau_{\text{mem}} = 3.3(1)\,\mu$s, and an end-to-end efficiency of $\eta_{e2e} = 7.4\%$, corresponding to an internal memory efficiency of $\eta_{\text{mem}} = 25\%$ at the SPL (average of 0.7 photons per pulse). The corresponding signal to noise ratio is SNR = 4.3, from which an upper bound on the conditional fidelity achievable by the memory of $\mathcal{F} = 92\%$ (see Ch. 2, Sec. 2.2.4) was determined. The efficiency and SNR results are below the ones presented in this thesis and show room for improvement.

The $1/e^2$ beam sizes used in the QuMSeC experiment for signal, control and pump beams are $241(2)\,\mu$m, $418(2)\,\mu$m, and $678(2)\,\mu$m, respectively. These are considerably larger than the ones used in the hyperfine memory presented in this thesis (see Ch. 4). The achieved longer storage time results from the larger interaction region, but also hints to the better performance of the heating system compared to the one used in this thesis. The

rack-implementation of the setup remains to be tested in out-of-laboratory environments, in order to subject it to real-world conditions. This will shed light into the robustness and feasibility of successful quantum storage in different environments. Nevertheless, this endeavour not only serves the purpose of practicality and portability, but also represents a transition from fundamental research to practical utility, demonstrating the system's potential for quantum information processing. For more details, I refer the reader to Ref. [11]. Furthermore, a publication about the mobile memory demonstrator is currently in the pipeline [464].

6 Conclusions

"One never notices what has been done; one can only see what remains to be done."

Marie Skłodowska-Curie

In this thesis, I have given a comprehensive description of the field of quantum memories, and have presented our group's first implementation of a warm vapour quantum memory based on EIT on the Cs D_1 line. We are primarily interested in possible applications of quantum memories onboard satellites, i.e., in space applications, although we also maintain keen interest in other fields. For this reason, our choice of memory system constitutes a warm vapour cell, a technically scalable and rather simple architecture, when compared to other possible experimental systems. Specifically, warm vapours do not require a considerable technical overhead, for example, consisting of cryostats, strong external fields, or vacuum chambers. Our main focus for memory operation was to achieve an optimisation of several figures of merit simultaneously, since to date no single memory system has been found to perform ideally with respect to all parameters essential for applications.

Our memory is operated using coherent pulses attenuated to the SPL and achieves an end-to-end efficiency of $\eta_{\mathrm{e2e}} = 13(2)\%$, which converted to an internal memory efficiency yields $\eta_{\mathrm{mem}} = 33(1)\%$. The simultaneously obtained SNR is 14(2), which translates to a noise level corresponding to $\mu_1 = 0.07(2)$ signal photons. We thus are on the right path to achieving values needed for practical implementations on QRs [130, 131, 377]. Our memory is not specifically optimised for long storage times, and we thus measure a maximal $1/e$ lifetime of $\tau_{\mathrm{mem}} = 0.89(5)\,\mu\mathrm{s}$. With the achieved memory bandwidth of $\Delta\omega_{\mathrm{mem}} = 220(30)\,\mathrm{MHz}$, this yields a time-bandwidth product of $\mathrm{TBP} = \Delta\omega_{\mathrm{mem}} \cdot \tau_{\mathrm{mem}} = 200(30)$.

For comparison, state-of-the-art values in warm vapours are a memory efficiency of $\eta_{\mathrm{mem}} = 82\%$ [186], a noise floor of $\mu_1 = 0.005$ and a time-bandwidth product

TBP = 250(20) (the latter two in the same experiment) [191], and a storage time of $\tau_{\mathrm{mem}} = 430(50)\,\mathrm{ms}$ [185]. These results are however achieved in independent experiments (apart from the above mentioned exception), and the last one is not obtained at the SPL, but with coherent pulses, and is thus not a 'quantum' memory per se. Moreover, these results imply trade-offs regarding further figures of merit.
We identify SRS and fluorescence as the limiting noise sources in our experiment . The control powers used in the experiment were comparatively low. However, much higher powers, on the order of hundreds of mW, will be needed in future experiments where larger beam sizes are planned. In contrast to similar experiments, we are not limited by FWM, which scales quadratically with pulse energy, rendering our memory ideal for use with stronger control pulses, in order to optimise the attainable efficiencies. To this end, the optical depth of the system should be increased as well. Regarding storage times, planned technical improvements will allow to extend these into the millisecond regime required in, i.e., QR implementations in future experiments, as the geometry with parallel signal and control beams allows for it. These improvements include the extension of the signal and control beam sizes and the implementation of better shielding against spurious magnetic fields. To this end, an improved heating system that aids in minimising the creation of unwanted currents inside the shield will also be employed. First investigations in this direction were performed in the context of the memory built for the QuMSeC project, using a heater made of OFHC copper, and are also planned for the alkali-noble gas memory currently under construction for the QToRX project. For the latter, a four-layer magnetic shielding (Twinleafs) and a 3D printed PEEK oven heated by hot air will be used. Moreover, to achieve the very large storage times, on the order of minutes or hours, intended in the aforementioned project, anti-relaxation coated cells will likely become necessary [185, 186]. Noise reduction is planned in future experiments by exploiting the Zeeman substructure of Cs, in order to prohibit SRS by selection rules. Furthermore, increased pumping efficiencies are essential for SRS reduction and storage time extension, and will be achieved by pumping with amplified pump lasers and larger beams. Even though first investigations on the attainable pumping lifetimes of the stretched state $|F = 4, m_F = \pm 4\rangle$ yielded values on the order of 1 ms, these can certainly be improved with the help of the new shield and heating system. These planned improvements to the memory system are described in detail in the intermediate conclusion of Chapter 4.

The experimental setup was used for additional experiments highly relevant for improving the memory for future applications. The first one was the operation as a spatially multimode memory, by addressing several modes with the use of AOMs. This experiment showed that the memory could be operated as a random access memory and achieved a

mean storage lifetime of $\tau_{\mathrm{mem}} = 3.2\,\mu$s, with an internal memory efficiency of $\eta_{\mathrm{mem}} = 36\,\%$ using macroscopic coherent pulses [3].
The next experiment conducted on the setup was the optimisation of the control pulses via a genetic algorithm. For this, some technical improvements were implemented, regarding the pulsing of the control laser, now performed with an AOM to yield better extinction rates. This method allows for an optimisation directly embedded in the experimental control and including all technical imperfections, which is thus agnostic to the underling physical theory. The obtained efficiencies with free-form control pulses are very similar to the case where Gaussian control pulses are used. The improvement of using free-form pulses amounts to 3(7)%. Furthermore, under the constraint of minimising the control pulse energy, we achieved a 30% reduction in the energy of the learned pulses with a minimal trade-off in efficiency of 4(6)% for specific signal pulse widths [4], although these results should be interpreted with caution and require further investigation.

Moreover, we performed theoretical simulations based on the theory developed in Refs. [123–125, 240, 241, 326]. The simulation predicted results comparable with our memory operation, even though it does not yet include many extensions, for instance, the inclusion of the excited state $F' = 4$ of the Cs D_1 manifold, the spatial distribution of the signal and control fields, the spinwave decay during storage and retrieval as a result from diffusion out of the interaction region or collisional effects, or any the of noise mechanisms. However, the good agreement has to be taken cautiously, since the parameter ranges of simulation and experiment are not exactly comparable. This results from the fact that the simulation yields very low efficiencies, when using the comparatively low values for the Doppler-broadening-corrected optical depth (when compared to optical depth values in cold atomic systems). It therefore, in its current state, serves more as a tool for a qualitative understanding of the processes occurring in the memory, and less to obtain concrete predictions. In order to quantitatively understand and predict the behaviour of future implementations of the system, the simulation would benefit from including the aforementioned extensions, as has been done in Ref. [95]. Nonetheless, as discussed already, the genetic algorithm has provided us with an alternative and improved manner of achieving control pulse optimisation.

In Chapter 5, I have given a general overview of possible future applications. As a first type, I have presented applications in the context of space deployment, such as for the realisation of intercontinental or global quantum communication via satellite-based QRs, and for tests of fundamental physics in space. Even though several advances have been made towards the construction of QRs consisting of quantum memories and single photon

sources onboard satellites with near-future available technology, the systems are not yet mature enough for efficient and reliable operation outside of laboratory environments. A first test towards this goal will be the operation of the 19 inch rack memory from the QuMSeC project outside of the lab. Nevertheless, incredible milestones, such as the MICIUS satellite demonstrating satellite-based QKD [373–376] or the CAL project [140], in which atomic BECs have been deployed on the ISS, have been achieved in the last years. These experiments were unthinkable 20-30 years ago. Perhaps, intercontinental satellite-based quantum communication will become a reality sooner than we think.
Furthermore, pairing of memory systems with single photon sources is an essential requirement for repeater functionality. A first realisation of single photon storage in a Λ-type warm atomic ensemble was performed in Ref. [191]. This is a remarkable achievement. However, the attained efficiencies are still very low for applications. Yet, they can be improved by further increasing the optical depth of the system. Surely, the next years will bring considerable improvements in this area. Specifically, in our group, interfacing SPS and memories is planned in several experiments. One experiment is aiming to store single photons from semiconductor QDs in a warm vapour ladder memory [287]. Another envisioned experiment intends to interface this same memory with a heralded photon from an SPDC source, also currently being built in our lab.
With respect to tests of fundamental physics regarding, e.g., long range Bell tests, gravitational effects on entanglement, distributed quantum sensing, etc., these ideas are, in many cases, very speculative and seem still very far away from being realised experimentally. However, they lay a roadmap for very interesting applications for the next decades.
The second type of applications I discuss are in the realm of ground-based realisations. The synchronisation of single photon generation suffers from the same issues of low efficiencies in the pairing of source and memories mentioned before. However, setting aside this issue, in this context, the obtained storage times in state-of-the art memories could already be sufficient for synchronisation of sources that are close to each other. Optical machine learning experiments with memories are in their initial stages, but since here the memories can be operated in the non-quantum regime, they should be technically simpler to achieve and thus realisable with current state-of-the art memories.

The achievement of ultra long storage times in warm vapour cells containing alkali and noble gas atoms has still not been realised experimentally. The intended coherent transfer of spin excitations from the alkali atoms to the noble gases, following the proposal of Ref. [443], promises to be experimentally arduous. The intended goal of secure long-time storage (hours to days) of a quantum token seems to lie relatively far in the future.

Nevertheless, the first experimental realisation of token storage conducted with attenuated coherent pulses in the alkali atoms, following the experimental proposal presented in Ch. 5, will be one of the first experiments performed on the QToRX memory, currently under construction. The lasers used in this experiment exhibit much better phase stability, which should facilitate the implementation of the token in time-bin encoding using subsequent pulses stored and retrieved from the memory. For the detection of the phases, the use of phase stabilisation on the interferometer should be implemented, in order to attain better control of the phase imprinted on the pulses at the detection stage. A realisation without this phase stabilisation could also be possible, but would make the postselection process highly complex.

Even if many of the envisioned applications presented in this thesis probably lie many years ahead in the future, in the case they are realised at all, all implementations and applications discussed here still offer a lot of highly interesting physics to explore in depth. The deep understanding of such complex many-particle systems and the exact interaction with light and other external fields, together with the pairing of heterogeneous quantum systems, are fields where a lot is still to be understood and discovered. Quantum information processing is still a rather young field, now turning 40 years, if we start counting from BB84. Therefore, much more lies ahead. If the ultimate goal, aside from a universal quantum computer, is a worldwide quantum internet, as envisioned in Refs. [53, 54], or maybe some other type of highly interesting application discovered along the way, we do not (and cannot) know with certainty. In my opinion, having such goals provides purpose and offers a sense of direction, even if they seem almost impossible to reach. However, I think it is essential that we, as scientific community, do not lose sight of the importance of rigour and accuracy when articulating bold statements, claims, and affirmations, especially when it comes to the field of QIP and the promises it holds. Moreover, history has taught us several times that groundbreaking scientific results can have atrocious consequences. I have, already in the introduction, mentioned the ominous tendency we humans have to forget. It is therefore never to early to begin to discuss the ethical use of the technologies we are helping to develop. Secure communication has many positive applications, but obviously the military and intelligence sectors will benefit enormously from it, and we should be prepared for what might come. In that sense, I want to reiterate the importance of scientific outreach in our society. As the internet once changed our reality completely, if these possible applications, including the dazzling quantum internet, do become a reality, the so-called second quantum revolution could again signify a complete change of paradigm. We, as scientists, also have the obligation; and for me personally, the pleasure, because it is a highly rewarding endeavour; to share

our knowledge in an understandable and exciting manner, and thus help to bridge the knowledge gap between the scientific community or academia, and the general public.

A Appendix

A.1 One-colour hyperfine (D_1) and two-colour Zeeman ($D_1 + D_2$) pumping experiment results

This Appendix contains some of the results achieved by David Becker in his Bachelor thesis "Time-Dependent Investigation of Optical Zeeman-Level Pumping in Cesium Vapor Cells" [10] under my supervision. All the figures in this section are taken from his thesis. The experimental setup he used for the measurements of optical pumping is depicted in Fig. A.1.

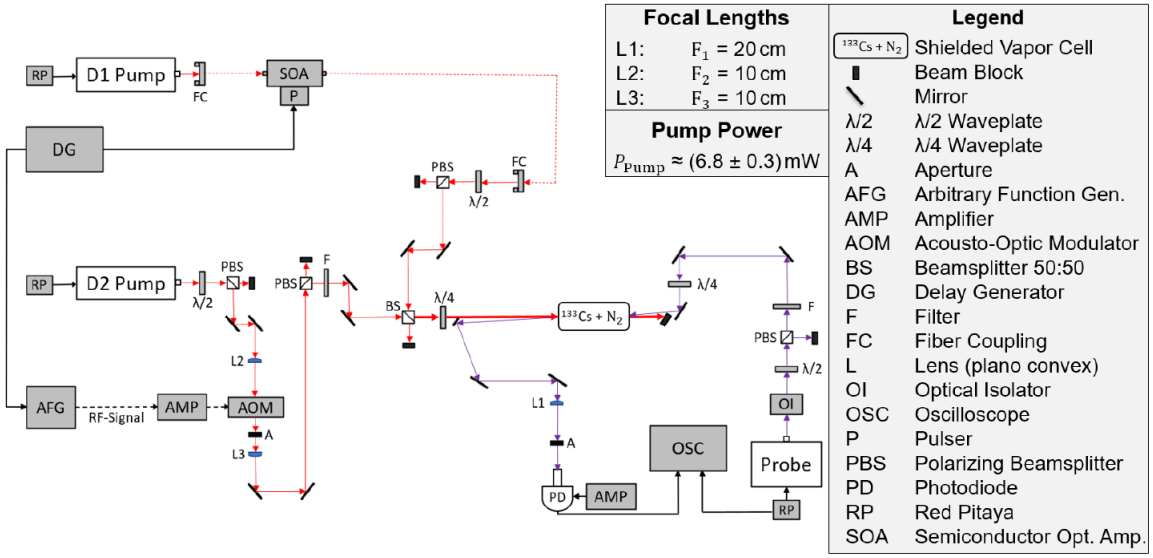

Figure A.1: Experimental setup for the two-colour Zeeman pumping experiment performed by David Becker for his Bachelor Thesis [10].

Optical pumping allows us to engineer changes to the absorptive capabilities of an atomic transition, without changing the vapour density. Through application of a sufficiently powerful unpolarised D_1 pump beam, it is theoretically possible to completely depopulate the $F = 4$ ground state, thus preventing the absorption of light at this transition frequency. The D_1 pump beam used in David's experiment, resonant with the $F = 4 \rightarrow F' = 4$

transition could be either circularly or linearly polarised. Therefore, it was impossible to achieve a complete depopulation of the $F = 4$ ground state, since the pump is unable to excite atoms in the $|F = 4, m_F = \pm 4\rangle$ and $|F = 4, m_F = 0\rangle$ state with circularly or linearly polarised light, respectively, due to the parasitic absorptive transitions always present because of optical selection rules (see Ch. 4, Sec. 4.2.2). This incomplete pumping, as well as a slight increase in absorption of the $F = 3 \rightarrow F' = (3, 4)$ transitions due to excited atoms relaxing into the $F = 3$ state, can be observed in the transmission spectra, where the absorption lines of the $F = 4 \rightarrow F' = (3, 4)$ transitions are still visible (see Fig. A.2).

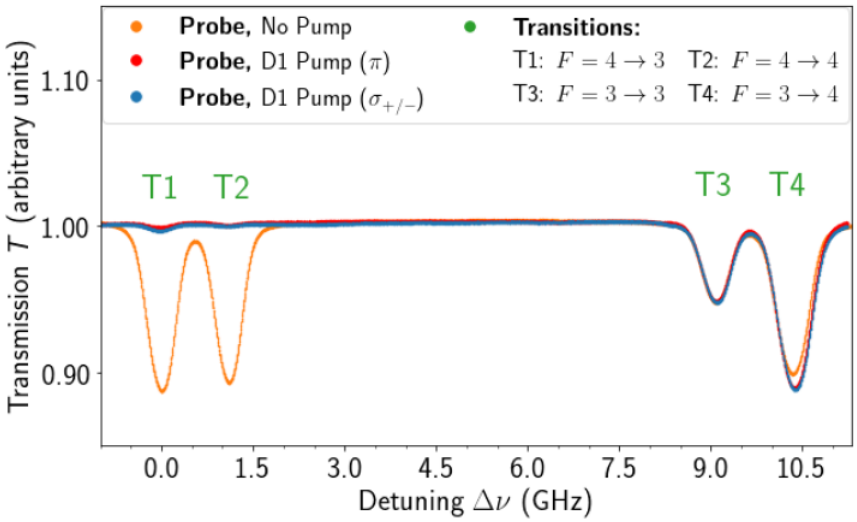

Figure A.2: Normalised Cs D_1 line transmission spectrum at $T = 21.5(5)$°C with no pump (yellow), after D_1 hyperfine pumping with linear polarisation (π, red), and after D_1 hyperfine pumping with circular polarisation ($\sigma^{\pm}$, blue). The probe power is $P_{\text{probe}} = 7.9(3)\,\mu$W and the maximal pump power is $P_{\text{pump}} = 6.8(3)$ mW.

Using either a one-colour hyperfine (D_1) or a two-colour Zeeman (D_1+D_2) pumping scheme, David was able to determine the pumping lifetimes of the respective transitions. These were obtained in pumping experiments consisting of a sequence of 12 ms pumping time, and a subsequent waiting time of 6 ms to let the system relax. From fitting the decay of the transmission of the signal laser on different transitions, and the optical depth (OD) exponential saturation curves determined from the data, he was able to obtain the $1/e$ lifetimes of the corresponding hyperfine state (in the D_1 pump case), and of the stretched state $|F = 4, m_F = \pm 4\rangle$ (in the Zeeman D_1+D_2 case), for different temperatures of the cell and various probing powers. Some of these results are collected here. The fit function used is given as

$$f(t) = (-1) \cdot b \cdot e^{\frac{-(t-a)}{\tau_{\mathrm{OD}}}} + c, \tag{A.1}$$

where where τ_{OD} is the lifetime and a, b, and c are other fit parameters with no explicit physical relevance. Here, several (5) relaxation phases are fitted by an exponential saturation function with the lifetime τ_{OD} as a fit parameter, and are then averaged to $\bar{\tau}_{\mathrm{OD}}$.

Fig. A.3 shows the OD saturation for the $F = 4 \rightarrow F' = 3$ transition measured at a cell temperature of $T = 21.5(5)$°C (a) and at a temperature $T = 56(6)$°C (b) for single color D_1 (hyperfine) pumping. The achieved average lifetimes $\bar{\tau}_{\mathrm{OD}}$ can be taken from the insets.

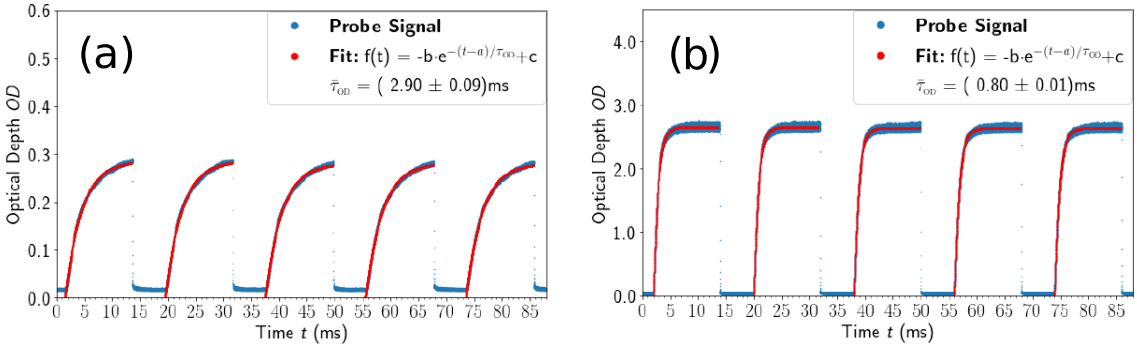

Figure A.3: OD rises for the $F = 4 \rightarrow F' = 3$ transition, measured at a cell temperature of (a) $T = 21.5(5)$°C, and (b) $T = 56(6)$°C, a probe power $P_{\mathrm{probe}} = 7.9(3)\,\mu$W, and with circularly polarized D_1 hyperfine pumping power of $P_{\mathrm{pump}} = 6.8(3)$ mW.

Fig. A.4 shows the OD saturation for the $F = 4 \rightarrow F' = 3$ transition measured at a cell temperature of $T = 21.5(5)$°C (a) and at a temperature of $T = 56(6)$°C (b) for the $D_1 + D_2$ two-color (Zeeman) pumping case. The achieved lifetimes can again be taken from the insets.

Figure A.5 shows the dependence of the achieved average lifetimes $\bar{\tau}_{\mathrm{OD}}$ for the $D_1 + D_2$ Zeeman two-colour pumping case on cell temperature (heating pad temperature) T and probe power P_{probe}. The lifetimes all lie in a range of $\bar{\tau}_{\mathrm{OD}} \sim (0.25 - 1.8)$ ms and, as expected, decrease with rising temperature, due to increased relaxation and dephasing processes, as explained in Ch. 3, Sec. 3.2.3. Regarding the measurements performed at $T = 56(6)$°C, and to a lesser extent measurements performed at $T = 38(3)$°C, it should be noted that the cooling down of the vapour cell throughout the duration of a series of measurements, which was usually a few minutes, led to a significant dependence of the lifetime on the order in which the various measurements were performed. The cooling

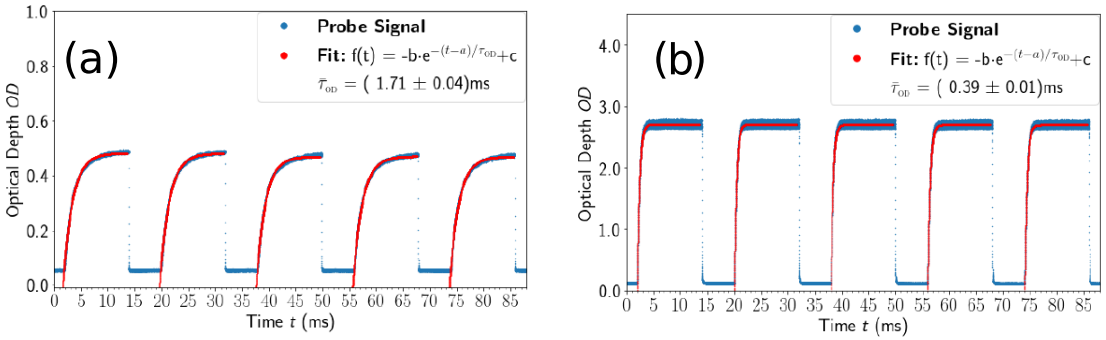

Figure A.4: OD rises for the $F = 4 \rightarrow F' = 3$ transition, measured at a cell temperature of (a) $T = 21.5(5)$°C, and (b) $T = 56(6)$°C, a probe power $P_{\text{probe}} = 7.9(3)\,\mu$W, and with circularly polarised D_1+ D_2 Zeeman pumping power of $P_{\text{pump}} = 6.8(3)$ mW (for both pump lasers).

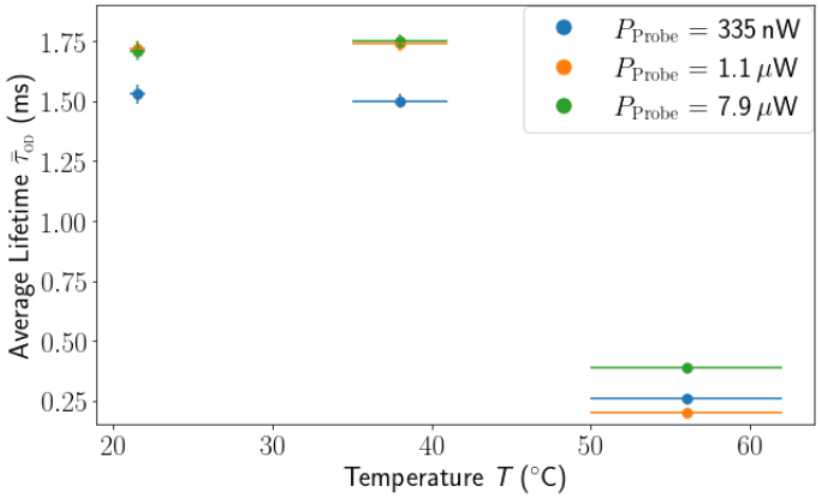

Figure A.5: Comparison of average lifetimes $\bar{\tau}_{\text{OD}}$ as a function of the vapour cell temperature T for the $F = 4 \rightarrow F' = 3$ transition. The measurements are conducted with a circularly polarised D_1+ D_2 Zeeman pumping power of $P_{\text{pump}} = 6.8(3)$ mW (for both pump lasers). The accuracy of the probe power amounts to ±3%.

off, as a reminder, was a consequence of the necessity of turning off the cell heaters, in order to minimise the presence of possible spurious magnetic field gradients. These resulted from the current flowing through the resistive heaters (Thorlabs HT10K flexible polyimide foil heaters with a 10 kΩ thermistor, controlled by a Meerstetter TEC 1091 temperature controller).

pump	$\bar{\tau}_{\mathrm{OD}}$ (ms)	
	$T = 21.5(5)$°C	$T = 56(6)$°C
D_1	2.90(9)	0.80(1)
$D_1 + D_2$	1.71(4)	0.39(1)

Table A.1: Comparison of average pumping lifetimes $\bar{\tau}_{\mathrm{OD}}$ for hyperfine one-colour pumping (D_1) vs. Zeeman two-colour pumping $D_1 + D_2$ at different temperatures.

Comparing the achieved Zeeman pumping lifetimes with the hyperfine pumping lifetimes (see Table A.1) yields the result that the former are consistently shorter than the latter, contrary to what we expected to see. This led us to the conclusion that there must be still some spurious magnetic fields inside the shield (even with turned off heaters), leading to relatively fast dephasing of the Zeeman coherence, since collisional processes and their resulting rates were not enough to explain this behaviour. From this result we were finally convinced of the necessity of implementing better shielding and guiding magnetic fields to attain a better control over the quantisation axis of the system in the case where no strong (control) light field is present. These improvements, as mentioned several times in the main text, are planned for the QToRX memory presented in Ch. 5, Sec. 5.5.

A.2 Filtering: Two etalon effects

The two etalons of the filtering system, Alice and Bob, are connected via a single mode fibre. If the mode matching is too good, an 'etaloning' effect between the end surface of Alice and the first surface of Bob becomes visible. This is depicted in Fig. A.6. In (a), the transmission frequency of both etalons is well matched, and the oscillations, although still present on the flanks of the Lorentzian, are minimal at the top. This was achieved at an exact temperature difference between Bob and Alice of $\Delta T = T_B - T_A = 0.5°\text{C}$. When the transmission maxima of both etalons is slightly shifted with respect to one another ($\Delta T = 0.17°\text{C}$) (b)[1], there are large oscillations at the top and the shape of the curve is no longer Lorentzian. (c) shows the behaviour when the shift corresponds to $\Delta T = -0.43°\text{C}$. To minimise these oscillations, it suffices to slightly diminish the alignment of the fibre coupling of Alice into Bob. This results in a more stable signal without significantly deteriorating the transmission.

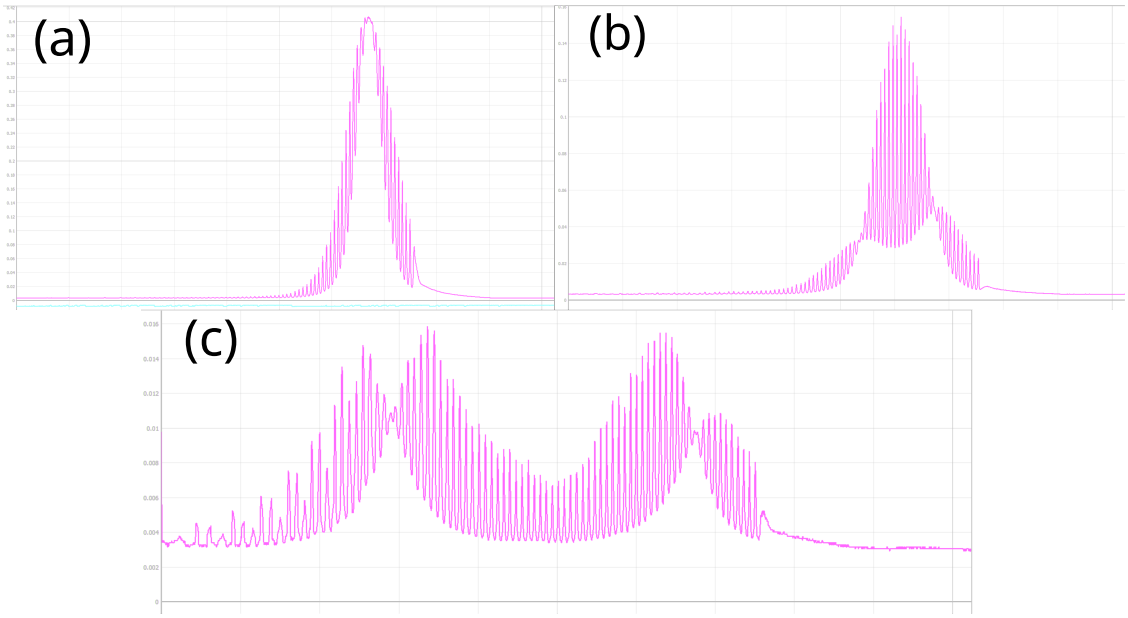

Figure A.6: Double etalon effect or 'etaloning' occurring between the etalons Alice and Bob at temperature differences of (a) $\Delta T = T_B - T_A = 0.5°\text{C}$, corresponding to the correct setting, (b) $\Delta T = 0.17°\text{C}$, and (c) $\Delta T = -0.43°\text{C}$, as measured on the RP oscilloscope function. This figure is only meant to show qualitative behaviour.

[1]The alert reader will maybe notice that Fig. A.6 (b) looks strikingly familiar and ghostly. This was indeed the first 'measurable' appearance of our dear lab ghost, Lord Etalon Eric.

Bibliography

[1] L. Esguerra, L. Meßner, E. Robertson, N. V. Ewald, M. Gündoğan, and J. Wolters. Optimization and readout-noise analysis of a warm-vapor electromagnetically-induced-transparency memory on the Cs D_1 line. *Phys. Rev. A*, 107(4):042607, 2023. xvii, 35, 44, 45, 109, 132, 139, 153

[2] J.-M. Mol, L. Esguerra, M. Meister, D. E. Bruschi, A. W. Schell, J. Wolters, and L. Wörner. Quantum memories for fundamental science in space. *Quantum Science and Technology*, 8(2):024006, 2023. xvii, 23, 175, 181, 182, 186

[3] L. Meßner, E. Robertson, L. Esguerra, K. Lüdge, and J. Wolters. Multiplexed random-access optical memory in warm cesium vapor. *Opt. Express*, 31(6):10150–10158, 2023. xvii, 35, 159, 160, 161, 173, 203

[4] E. Robertson, L. Esguerra, L. Meßner, G. Gallego, and J. Wolters. Machine learning optimal control pulses in an optical quantum memory experiment. *arXiv:2401.05077v1*, 2024. xvii, 147, 161, 162, 163, 170, 173, 203

[5] M. Yang, E. Robertson, L. Esguerra, K. Busch, and J. Wolters. Optical convolutional neural network with atomic nonlinearity. *Opt. Express*, 31(10):16451–16459, 2023. xvii, 179

[6] L. Esguerra Rodríguez, L. Meßner, E. Robertson, M. Gündoğan, and J. Wolters. Towards satellite-suited noise-free quantum memories. In *Conference on Lasers and Electro-Optics*, page JTh3A.55. Optica Publishing Group, 2021. xix

[7] L. Esguerra, L. Meßner, E. Robertson, M. Gündoğan, and J. Wolters. Towards satellite-suited noise-free quantum memories. In *2021 Conference on Lasers and Electro-Optics Europe and European Quantum Electronics Conference*, page eb_2_3. Optica Publishing Group, 2021. xix

[8] L. Esguerra, L. Messner, E. Robertson, M. Gündoğan, and J. Wolters. Optimization and noise study of a warm vapor EIT memory on the Cs D_1 line. In E. Diamanti, S. Ducci, N. Treps, and S. Whitlock, editors, *Quantum Technologies 2022*, volume PC12133, page PC121330P. SPIE, 2022. xix

[9] J. Wu. *Investigation of Optical Pumping and Spin Life-time in Cesium Vapor Cells*. Bachelor Thesis, TU Berlin, 2021. xx, 121

[10] D. Becker. *Time-Dependent Investigation of Optical Zeeman-Level Pumping in Cesium Vapor Cells*. Bachelor Thesis, TU Berlin, 2022. xx, 64, 121, 156, 207

[11] A. Erl. *A Mobile Demonstrator of an Atomic Quantum Memory for Secure Communication in Tomorrow's Societies*. Master Thesis, TU Berlin, 2023. xx, 32, 74, 133, 137, 138, 172, 196, 197, 198, 199

[12] L. Meßner. *Multi-cell quantum memory*. Master Thesis, TU Berlin, 2021. xx, 114, 115, 128, 160

[13] M. Yang. *Optical Convolutional Neural Network with Atomic Nonlinearity*. Master Thesis, Humboldt-Universität zu Berlin, 2021. xx

[14] ChatGPT. Available online at `https://chat.openai.com/`, 2024. 2

[15] J. E. Marsden and A. J. Tromba. *Vector Calculus*. W. H. Freeman, fifth edition edition, 2003. 3

[16] B. J. Hunt. Oliver Heaviside: A first-rate oddity. *Physics Today*, 65(11):48–54, 2012. 3

[17] G. N. Lewis. The conservation of photons. *Nature*, 118(2981):874–875, 1926. 3

[18] J. Nunn. *Quantum memory in atomic ensembles*. PhD Thesis, University of Oxford, 2008. 3, 9, 14, 23, 48

[19] J. Bardeen and W. H. Brattain. The transistor, a semi-conductor triode. *Phys. Rev.*, 74(2):230–231, 1948. 3

[20] T. H. Maiman. Stimulated optical radiation in ruby. *Nature*, 187(4736):493–494, 1960. 3

[21] M. Benyoucef. *Photonic Quantum Technologies: Science and Applications*. Wiley-VCH, 2023. 4, 5

[22] A. Einstein, B. Podolsky, and N. Rosen. Can a quantum-mechanical description of physical reality be considered complete? *Phys. Rev.*, 47(10):777–780, 1935. 4

[23] N. Bohr. Can quantum-mechanical description of physical reality be considered complete? *Phys. Rev.*, 48(8):696–702, 1935. 4

[24] J. S. Bell. On the Einstein Podolsky Rosen paradox. *Physics Physique Fizika*, 1(3): 195–200, 1964. 4

[25] A. Aspect. Closing the door on Einstein and Bohr's quantum debate. *Physics*, 8, 2015. 4

[26] S. J. Freedman and J. F. Clauser. Experimental test of local hidden-variable theories. *Phys. Rev. Lett.*, 28(14):938–941, 1972. 4

[27] J. F. Clauser, M. A. Horne, A. Shimony, and R. A. Holt. Proposed experiment to test local hidden-variable theories. *Phys. Rev. Lett.*, 23(15):880–884, 1969. 4, 12

[28] J. F. Clauser and A. Shimony. Bell's theorem. Experimental tests and implications. *Reports on Progress in Physics*, 41(12):1881, 1978. 4

[29] A. Aspect, J. Dalibard, and G. Roger. Experimental test of Bell's inequalities using time-varying analyzers. *Phys. Rev. Lett.*, 49(25):1804–1807, 1982. 4

[30] J. P. Dowling and G. J. Milburn. Quantum technology: The second quantum revolution. *Philosophical Transactions of the Royal Society of London. Series A: Mathematical, Physical and Engineering Sciences*, 361(1809):1655–1674, 2003. 5

[31] I. H. Deutsch. Harnessing the power of the second quantum revolution. *PRX Quantum*, 1(2):020101, 2020. 5

[32] R. P. Feynman. Simulating physics with computers. *International Journal of Theoretical Physics*, 21(6):467–488, 1982. 5

[33] S. Wiesner. Conjugate coding. *SIGACT News*, 15(1):78–88, 1983. 5, 190

[34] C. H. Bennett and G. Brassard. Quantum cryptography: Public key distribution and coin tossing. *Theor. Comput. Sci.*, 560:7–11, 2014. 5, 10, 176

[35] C. H. Bennett, G. Brassard, C. Crépeau, R. Jozsa, A. Peres, and W. K. Wootters. Teleporting an unknown quantum state via dual classical and Einstein-Podolsky-Rosen channels. *Phys. Rev. Lett.*, 70(13):1895–1899, 1993. 5, 6

[36] D. Deutsch. Quantum theory, the Church–Turing principle and the universal quantum computer. *Proc. R. Soc. Lond. A*, 400:97–117, 1985. 5

[37] D. P. DiVincenzo. Quantum computation. *Science*, 270(5234):255–261, 1995.

[38] D. P. DiVincenzo. The physical implementation of quantum computation. *Fortschritte der Physik*, 48(9-11):771–783, 2000. 6

[39] M. A. Nielsen and I. L. Chuang. *Quantum Computation and Quantum Information*. Cambridge University Press, 2000. 5, 6, 7, 12, 26, 29

[40] S. Lloyd. Universal quantum simulators. *Science*, 273(5278):1073–1078, 1996. 5

[41] N. Gisin, S. Pironio, and N. Sangouard. Proposal for implementing device-independent quantum key distribution based on a heralded qubit amplifier. *Phys. Rev. Lett.*, 105(7):070501, 2010. 5, 13

[42] V. Giovannetti, S. Lloyd, and L. Maccone. Quantum-enhanced measurements: Beating the standard quantum limit. *Science*, 306(5700):1330–1336, 2004. 5

[43] C. L. Degen, F. Reinhard, and P. Cappellaro. Quantum sensing. *Rev. Mod. Phys.*, 89(3):035002, 2017. 5

[44] B. Schumacher. Quantum coding. *Phys. Rev. A*, 51(4):2738–2747, 1995. 5

[45] R. Coffey. Forbes: Schrödinger's Pedophilia: The Cat Is Out Of The Bag (Box). Available online at `https://www.forbes.com/sites/rebeccacoffey/2022/01/24/schrdinger-pedophilia-the-cat-is-out-of-the-bag-box/`, Jan 24 2022. 5

[46] E. Schrödinger. Discussion of probability relations between separated systems. *Mathematical Proceedings of the Cambridge Philosophical Society*, 31(4):555–563, 1935. 5

[47] E. Knill, R. Laflamme, and G. J. Milburn. A scheme for efficient quantum computation with linear optics. *Nature*, 409(6816):46–52, 2001. 6

[48] J. M. Raimond, M. Brune, and S. Haroche. Manipulating quantum entanglement with atoms and photons in a cavity. *Rev. Mod. Phys.*, 73(3):565–582, 2001.

[49] N. Yoran and B. Reznik. Deterministic linear optics quantum computation with single photon qubits. *Phys. Rev. Lett.*, 91(3):037903, 2003.

[50] M. A. Nielsen. Optical quantum computation using cluster states. *Phys. Rev. Lett.*, 93(4):040503, 2004. 6

[51] A. Aspuru-Guzik and P. Walther. Photonic quantum simulators. *Nature Physics*, 8 (4):285–291, 2012. 6

[52] S.-H. Wei, B. Jing, X.-Y. Zhang, J.-Y. Liao, C.-Z. Yuan, B.-Y. Fan, C. Lyu, D.-L. Zhou, Y. Wang, G.-W. Deng, H.-Z. Song, D. Oblak, G.-C. Guo, and Q. Zhou. Towards real-world quantum networks: A review. *Laser & Photonics Reviews*, 16 (3):2100219, 2022. 7

[53] H. J. Kimble. The quantum internet. *Nature*, 453(7198):1023–1030, 2008. 7, 32, 205

[54] S. Wehner, D. Elkouss, and R. Hanson. Quantum internet: A vision for the road ahead. *Science*, 362(6412):eaam9288, 2018. 7, 205

[55] W. K. Wootters and W. H. Zurek. A single quantum cannot be cloned. *Nature*, 299: 802–803, 1982. 7

[56] R. L. Rivest, A. Shamir, and L. M. Adleman. A method for obtaining digital signatures and public-key cryptosystems. *Commun. ACM*, 26:96–99, 1978. 9

[57] P. W. Shor. Polynomial-time algorithms for prime factorization and discrete logarithms on a quantum computer. *SIAM Journal on Computing*, 26(5):1484–1509, 1997. 9

[58] A. K. Ekert. Quantum cryptography based on Bell's theorem. *Phys. Rev. Lett.*, 67 (6):661–663, 1991. 11, 12, 16

[59] H.-K. Lo and J. Preskill. Security of quantum key distribution using weak coherent states with nonrandom phases. *Quantum Info. Comput.*, 7(5):431–458, 2007. 12

[60] J. L. Duligall, M. S. Godfrey, K. A. Harrison, W. J. Munro, and J. G. Rarity. Low cost and compact quantum key distribution. *New Journal of Physics*, 8(10):249, 2006. 12

[61] F. Grosshans and P. Grangier. Continuous variable quantum cryptography using coherent states. *Phys. Rev. Lett.*, 88(5):057902, 2002. 12

[62] C. H. Bennett, G. Brassard, and N. D. Mermin. Quantum cryptography without Bell's theorem. *Phys. Rev. Lett.*, 68(5):557–559, 1992. 12, 176

[63] G. Brassard, N. Lütkenhaus, T. Mor, and B. C. Sanders. Limitations on practical quantum cryptography. *Phys. Rev. Lett.*, 85(6):1330–1333, 2000. 13

[64] E. Diamanti, H.-K. Lo, B. Qi, and Z. Yuan. Practical challenges in quantum key distribution. *npj Quantum Information*, 2(1):16025, 2016. 13

[65] A. Acín, N. Brunner, N. Gisin, S. Massar, S. Pironio, and V. Scarani. Device-independent security of quantum cryptography against collective attacks. *Phys. Rev. Lett.*, 98(23):230501, 2007. 13

[66] H.-K. Lo, M. Curty, and B. Qi. Measurement-device-independent quantum key distribution. *Phys. Rev. Lett.*, 108(13):130503, 2012. 13

[67] S. Abruzzo, H. Kampermann, and D. Bru. Measurement-device-independent quantum key distribution with quantum memories. *Phys. Rev. A*, 89(1):012301, 2014. 13

[68] N. Gisin, G. Ribordy, W. Tittel, and H. Zbinden. Quantum cryptography. *Rev. Mod. Phys.*, 74(1):145, 2002. 13, 16

[69] S. Pirandola, U. L. Andersen, L. Banchi, M. Berta, D. Bunandar, R. Colbeck, D. Englund, T. Gehring, C. Lupo, C. Ottaviani, J. L. Pereira, M. Razavi, J. S. Shaari, M. Tomamichel, V. C. Usenko, G. Vallone, P. Villoresi, and P. Wallden. Advances in quantum cryptography. *Adv. Opt. Photon.*, 12(4):1012–1236, 2020.

[70] F. Xu, X. Ma, Q. Zhang, H.-K. Lo, and J.-W. Pan. Secure quantum key distribution with realistic devices. *Rev. Mod. Phys.*, 92(2):025002, 2020. 13

[71] The Quantum Insider: 25 Quantum Cryptography & Encryption Companies. Available online at https://thequantuminsider.com/2021/01/11/25-companies-building-the-quantum-cryptography-communications-markets/, revised 2024, 2021. 13

[72] S. Pirandola, R. Laurenza, C. Ottaviani, and L. Banchi. Fundamental limits of repeaterless quantum communications. *Nature Communications*, 8(1):15043, 2017. 13

[73] S. Pirandola. End-to-end capacities of a quantum communication network. *Communications Physics*, 2(1):51, 2019.

[74] S. Pirandola. Limits and security of free-space quantum communications. *Phys. Rev. Res.*, 3(1):013279, 2021. 13

[75] C. H. Bennett, D. P. DiVincenzo, J. A. Smolin, and W. K. Wootters. Mixed-state entanglement and quantum error correction. *Phys. Rev. A*, 54(5):3824–3851, 1996. 13

[76] J.-W. Pan, C. Simon, Č. Brukner, and A. Zeilinger. Entanglement purification for quantum communication. *Nature*, 410(6832):1067–1070, 2001. 13, 14

[77] H.-J. Briegel, W. Dür, J. I. Cirac, and P. Zoller. Quantum repeaters: The role of imperfect local operations in quantum communication. *Phys. Rev. Lett.*, 81(26): 5932–5935, 1998. 13, 14

[78] W. Dür, H.-J. Briegel, J. I. Cirac, and P. Zoller. Quantum repeaters based on entanglement purification. *Phys. Rev. A*, 59(1):169–181, 1999. 14

[79] M. Zukowski, A. Zeilinger, M. A. Horne, and A. K. Ekert. "Event-ready-detectors" Bell experiment via entanglement swapping. *Physical Review Letters*, 71(26):4287–4290, 1993. 14

[80] F. Monteiro, V. C. Vivoli, T. Guerreiro, A. Martin, J.-D. Bancal, H. Zbinden, R. T. Thew, and N. Sangouard. Revealing genuine optical-path entanglement. *Phys. Rev. Lett.*, 114(17):170504, 2015. 14

[81] J.-W. Pan, D. Bouwmeester, H. Weinfurter, and A. Zeilinger. Experimental entanglement swapping: Entangling photons that never interacted. *Phys. Rev. Lett.*, 80 (18):3891–3894, 1998. 14

[82] L.-M. Duan, M. D. Lukin, J. I. Cirac, and P. Zoller. Long-distance quantum communication with atomic ensembles and linear optics. *Nature*, 414(6862):413–418, 2001. 14, 21, 32, 49

[83] C. H. Bennett, G. Brassard, S. Popescu, B. Schumacher, J. A. Smolin, and W. K. Wootters. Purification of noisy entanglement and faithful teleportation via noisy channels. *Phys. Rev. Lett.*, 76(5):722–725, 1996. 14

[84] C. Simon, H. de Riedmatten, M. Afzelius, N. Sangouard, H. Zbinden, and N. Gisin. Quantum repeaters with photon pair sources and multimode memories. *Phys. Rev. Lett.*, 98(19):190503, 2007. 16

[85] N. Sangouard, C. Simon, J. Minár, H. Zbinden, H. de Riedmatten, and N. Gisin. Long-distance entanglement distribution with single-photon sources. *Phys. Rev. A*, 76(5):050301, 2007. 16

[86] F. Flamini, N. Spagnolo, and F. Sciarrino. Photonic quantum information processing: a review. *Reports on Progress in Physics*, 82(1):016001, 2019. 16

[87] M. Razavi, M. Piani, and N. Lütkenhaus. Quantum repeaters with imperfect memories: Cost and scalability. *Phys. Rev. A*, 80(3):032301, 2009. 16

[88] N. Sangouard, C. Simon, H. de Riedmatten, and N. Gisin. Quantum repeaters based on atomic ensembles and linear optics. *Rev. Mod. Phys.*, 83(1):33–80, 2011. 16

[89] R. Loudon. *The Quantum Theory of Light*. Oxford University Press, 3rd edition edition, 2000. 17, 69, 82

[90] W. E. Lamb. Anti-photon. *Applied Physics B*, 60(2):77–84, 1995. 17

[91] C. Cohen-Tannoudji, J. Dupont-Roc, and G. Grynberg. *Photons and Atoms: Introduction to Quantum Electrodynamics*. Wiley-VCH, 1997. 17

[92] B. Lounis and M. Orrit. Single-photon sources. *Reports on Progress in Physics*, 68 (5):1129, 2005. 17, 18

[93] M. D. Eisaman, J. Fan, A. Migdall, and S. V. Polyakov. Invited Review Article: Single-photon sources and detectors. *Review of Scientific Instruments*, 82(7):071101, 2011. 17, 18

[94] G. C. Buser. *Storing single photons in broadband vapor cell quantum memories*. PhD Thesis, Universität Basel, 2023. 19, 23, 26, 29, 41, 46, 56, 105, 125, 126, 138, 153, 155

[95] R. Mottola. *Room Temperature Single Photon Sources and Atomic Quantum Memories for Broadband Quantum Networks*. PhD thesis, Universität Basel, 2023. 18, 19, 20, 164, 170, 203

[96] M. Gschrey, A. Thoma, P. Schnauber, M. Seifried, R. Schmidt, B. Wohlfeil, L. Krüger, J.-H. Schulze, T. Heindel, S. Burger, F. Schmidt, A. Strittmatter, S. Rodt, and S. Reitzenstein. Highly indistinguishable photons from deterministic quantum-dot microlenses utilizing three-dimensional in situ electron-beam lithography. *Nature Communications*, 6(1):7662, 2015. 18

[97] D. A. Vajner, L. Rickert, T. Gao, K. Kaymazlar, and T. Heindel. Quantum communication using semiconductor quantum dots. *Advanced Quantum Technologies*, 5(7):2100116, 2022. 18

[98] T. Heindel, J.-H. Kim, N. Gregersen, A. Rastelli, and R. Stephan. Quantum dots for photonic quantum information technology. *Adv. Opt. Photon.*, 15(3):613–738, 2023. 18

[99] T. Kroh, J. Wolters, A. Ahlrichs, A. W. Schell, A. Thoma, S. Reitzenstein, J. S. Wildmann, E. Zallo, R. Trotta, A. Rastelli, O. G. Schmidt, and O. Benson. Slow and fast single photons from a quantum dot interacting with the excited state hyperfine structure of the cesium D_1-line. *Scientific Reports*, 9(1):13728, 2019. 18

[100] F. Kaneda, F. Xu, J. Chapman, and P. G. Kwiat. Quantum-memory-assisted multi-photon generation for efficient quantum information processing. *Optica*, 4(9): 1034–1037, 2017. 18, 19, 38, 59, 181

[101] A. MacRae, T. Brannan, R. Achal, and A. I. Lvovsky. Tomography of a high-purity narrowband photon from a transient atomic collective excitation. *Phys. Rev. Lett.*, 109(3):033601, 2012. 19

[102] O. Davidson, R. Finkelstein, E. Poem, and O. Firstenberg. Bright multiplexed source of indistinguishable single photons with tunable GHz-bandwidth at room temperature. *New J. Phys.*, 23(7):073050, 2021. 19

[103] M. Afzelius, N. Gisin, and H. de Riedmatten. Quantum memory for photons. *Physics Today*, 68(12):42–47, 2015. 19

[104] C. W. Chou, S. V. Polyakov, A. Kuzmich, and H. J. Kimble. Single-photon generation from stored excitation in an atomic ensemble. *Phys. Rev. Lett.*, 92(21):213601, 2004. 19

[105] V. Balic, D. A. Braje, P. Kolchin, G. Y. Yin, and S. E. Harris. Generation of paired photons with controllable waveforms. *Physical Review Letters*, 94(18):183601, 2005.

[106] J. K. Thompson, J. Simon, H. Loh, and V. Vuletić. A high-brightness source of narrowband, identical-photon pairs. *Science*, 313(5783):74–77, 2006.

[107] C. Shu, P. Chen, T. K. A. Chow, L. Zhu, Y. Xiao, M. Loy, and S. Du. Subnatural-linewidth biphotons from a Doppler-broadened hot atomic vapour cell. *Nature Communications*, 7(1):12783, 2016.

[108] L. Zhu, X. Guo, C. Shu, H. Jeong, and S. Du. Bright narrowband biphoton generation from a hot rubidium atomic vapor cell. *Applied Physics Letters*, 110(16):161101, 2017.

[109] J. Mika and L. Slodička. High nonclassical correlations of large-bandwidth photon pairs generated in warm atomic vapor. *Journal of Physics B: Atomic, Molecular and Optical Physics*, 53(14):145501, 2020. 19

[110] R. W. Boyd. *Nonlinear Optics*. Academic Press, 3rd edition edition, 2008. 19, 65, 69, 85

[111] A. Ahlrichs. *Triply-Resonant Cavity-Enhanced Spontaneous Parametric Down-Conversion*. PhD Thesis, Humboldt-Universität zu Berlin, 2019. 20

[112] A. Ahlrichs and O. Benson. Bright source of indistinguishable photons based on cavity-enhanced parametric down-conversion utilizing the cluster effect. *Applied Physics Letters*, 108(2), 2016. 20

[113] R. Mottola, G. Buser, C. Müller, T. Kroh, A. Ahlrichs, S. Ramelow, O. Benson, P. Treutlein, and J. Wolters. An efficient, tunable, and robust source of narrow-band photon pairs at the ^{87}Rb D_1 line. *Opt. Express*, 28(3):3159, 2020. 20

[114] K. Heshami, D. G. England, P. C. Humphreys, P. J. Bustard, V. M. Acosta, J. Nunn, and B. J. Sussman. Quantum memories: emerging applications and recent advances. *J. Mod. Opt.*, 63(20):2005–2028, 2016. 20, 21, 35, 36, 48, 52, 102, 147

[115] B. M. Terhal. Quantum error correction for quantum memories. *Rev. Mod. Phys.*, 87(2):307–346, 2015. 21

[116] K. F. Reim. *Broadband optical quantum memory*. PhD Thesis, University of Oxford, 2011. 23, 48, 75, 119, 127

[117] C.-L. Cui, J.-K. Jia, J.-W. Gao, Y. Xue, G. Wang, and J.-H. Wu. Ultraslow and superluminal light propagation in a four-level atomic system. *Phys. Rev. A*, 76(3): 033815, 2007. 25

[118] A. Kaur and P. Kaur. Dressed state analysis of electromagnetically induced transparency in a five-level X-type atomic system with wavelength mismatching effects. *Physica Scripta*, 93(11):115101, 2018. 25

[119] B. Zhao, Y.-A. Chen, X.-H. Bao, T. Strassel, C.-S. Chuu, X.-M. Jin, J. Schmiedmayer, Z.-S. Yuan, S. Chen, and J.-W. Pan. A millisecond quantum memory for scalable quantum networks. *Nature Physics*, 5(2):95–99, 2009. 26, 102, 136

[120] K. T. Kaczmarek. *ORCA - Towards an integrated noise-free quantum memory*. PhD Thesis, University of Oxford, 2017. 26, 28, 31, 55

[121] A. I. Lvovsky, B. C. Sanders, and W. Tittel. Optical quantum memory. *Nat. Photonics*, 3(12):706–714, 2009. 29

[122] C. Simon, M. Afzelius, J. Appel, Boyer de la Giroday, A., S. J. Dewhurst, N. Gisin, C. Y. Hu, F. Jelezko, S. Kröll, J. H. Müller, J. Nunn, E. S. Polzik, J. G. Rarity, H. de Riedmatten, W. Rosenfeld, A. J. Shields, N. Sköld, R. M. Stevenson, R. Thew, I. A. Walmsley, M. C. Weber, H. Weinfurter, J. Wrachtrup, and R. J. Young. Quantum memories. *European Physical Journal D*, 58(1):1–22, 2010. 26, 52

[123] A. V. Gorshkov, A. André, M. Fleischhauer, A. S. Sørensen, and M. D. Lukin. Universal approach to optimal photon storage in atomic media. *Phys. Rev. Lett.*, 98 (12):1–4, 2007. 27, 39, 46, 50, 61, 87, 97, 146, 163, 171, 172, 203

[124] A. V. Gorshkov, A. André, M. D. Lukin, and A. S. Sørensen. Photon storage in Λ-type optically dense atomic media. I. Cavity model. *Phys. Rev. A*, 76(3):033804, 2007. 39, 88, 94, 96, 97, 98

[125] A. V. Gorshkov, A. André, M. D. Lukin, and A. S. Sørensen. Photon storage in Λ-type optically dense atomic media. II. Free-space model. *Phys. Rev. A*, 76(3): 033805, 2007. 27, 39, 61, 87, 88, 97, 99, 135, 146, 163, 167, 171, 172, 203

[126] M. Bozzio. *Security and implementation of advanced quantum cryptography: quantum money and quantum weak coin flipping*. PhD Thesis, Université Paris Saclay, 2021. 27, 192

[127] P. Jobez, C. Laplane, N. Timoney, N. Gisin, A. Ferrier, P. Goldner, and M. Afzelius. Coherent spin control at the quantum level in an ensemble-based optical memory. *Phys. Rev. Lett.*, 114(23):230502, 2015. 28, 37, 183

[128] M. Gündoğan. *Solid-State Quantum Memory for Photonic Qubits*. PhD Thesis, UPC - Universitat Politècnica de Catalunya, 2015. 28, 29, 52

[129] C. Mewes and M. Fleischhauer. Decoherence in collective quantum memories for photons. *Phys. Rev. A*, 72(2):022327, 2005. 28

[130] M. Gündoğan, J. S. Sidhu, V. Henderson, L. Mazzarella, J. Wolters, D. K. L. Oi, and M. Krutzik. Proposal for space-borne quantum memories for global quantum networking. *npj Quantum Information*, 7(1):128, 2021. 29, 31, 159, 171, 173, 176, 177, 186, 201

[131] J. Wallnöfer, F. Hahn, M. Gündoğan, J. S. Sidhu, F. Wiesner, N. Walk, J. Eisert, and J. Wolters. Simulating quantum repeater strategies for multiple satellites. *Communications Physics*, 5(1):169, 2022. 29, 31, 159, 171, 173, 176, 177, 186, 201

[132] S. Massar and S. Popescu. Optimal extraction of information from finite quantum ensembles. *Phys. Rev. Lett.*, 74(8):1259–1263, 1995. 29

[133] H. P. Specht, C. Nölleke, A. Reiserer, M. Uphoff, E. Figueroa, S. Ritter, and G. Rempe. A single-atom quantum memory. *Nature*, 473(7346):190–193, 2011. 29, 32

[134] M. Curty and N. Lütkenhaus. Intercept-resend attacks in the Bennett-Brassard 1984 quantum-key-distribution protocol with weak coherent pulses. *Phys. Rev. A*, 71(6):062301, 2005. 29

[135] M. Gündoğan, P. M. Ledingham, K. Kutluer, M. Mazzera, and H. de Riedmatten. Solid state spin-wave quantum memory for time-bin qubits. *Phys. Rev. Lett.*, 114 (23):230501, 2015. 29, 37, 59

[136] J. Wolters, G. Buser, A. Horsley, L. Béguin, A. Jöckel, J. P. Jahn, R. J. Warburton, and P. Treutlein. Simple atomic quantum memory suitable for semiconductor quantum dot single photons. *Phys. Rev. Lett.*, 119(6):1–5, 2017. 30, 35, 110, 194

[137] D. G. England, P. S. Michelberger, T. F. M. Champion, K. F. Reim, K. C. Lee, M. R. Sprague, X.-M. Jin, N. K. Langford, W. S. Kolthammer, J. Nunn, and I. A. Walmsley. High-fidelity polarization storage in a gigahertz bandwidth quantum memory. *Journal of Physics B: Atomic, Molecular and Optical Physics*, 45(12): 124008, 2012. 31

[138] J. Nunn, N. K. Langford, W. S. Kolthammer, T. F. M. Champion, M. R. Sprague, P. S. Michelberger, X.-M. Jin, D. G. England, and I. A. Walmsley. Enhancing multiphoton rates with quantum memories. *Phys. Rev. Lett.*, 110(13):133601, 2013. 31, 56, 171, 180, 181

[139] D. Becker, M. D. Lachmann, S. T. Seidel, H. Ahlers, A. N. Dinkelaker, J. Grosse, O. Hellmig, H. Müntinga, V. Schkolnik, T. Wendrich, A. Wenzlawski, B. Weps, R. Corgier, T. Franz, N. Gaaloul, W. Herr, D. Lüdtke, M. Popp, S. Amri, H. Duncker, M. Erbe, A. Kohfeldt, A. Kubelka-Lange, C. Braxmaier, E. Charron, W. Ertmer, M. Krutzik, C. Lämmerzahl, A. Peters, W. P. Schleich, K. Sengstock, R. Walser, A. Wicht, P. Windpassinger, and E. M. Rasel. Space-borne Bose–Einstein condensation for precision interferometry. *Nature*, 562(7727):391–395, 2018. 31, 36

[140] D. C. Aveline, J. R. Williams, E. R. Elliott, C. Dutenhoffer, J. R. Kellogg, J. M. Kohel, N. E. Lay, K. Oudrhiri, R. F. Shotwell, N. Yu, and R. J. Thompson. Observation of Bose–Einstein condensates in an Earth-orbiting research lab. *Nature*, 582(7811): 193–197, 2020. 36, 204

[141] K. Frye, S. Abend, W. Bartosch, A. Bawamia, D. Becker, H. Blume, C. Braxmaier, S.-W. Chiow, M. A. Efremov, W. Ertmer, P. Fierlinger, T. Franz, N. Gaaloul, J. Grosse, C. Grzeschik, O. Hellmig, V. A. Henderson, W. Herr, U. Israelsson, J. Kohel, M. Krutzik, C. Kürbis, C. Lämmerzahl, M. List, D. Lüdtke, N. Lundblad, J. P. Marburger, M. Meister, M. Mihm, H. Müller, H. Müntinga, A. M. Nepal, T. Oberschulte, A. Papakonstantinou, J. Perovšek, A. Peters, A. Prat, E. M. Rasel, A. Roura, M. Sbroscia, W. P. Schleich, C. Schubert, S. T. Seidel, J. Sommer, C. Spindeldreier, D. Stamper-Kurn, B. K. Stuhl, M. Warner, T. Wendrich, A. Wenzlawski,

A. Wicht, P. Windpassinger, N. Yu, and L. Wörner. The Bose-Einstein Condensate and Cold Atom Laboratory. *EPJ Quantum Technology*, 8(1):1, 2021. 31, 36

[142] M. Steger, K. Saeedi, M. L. W. Thewalt, J. J. L. Morton, H. Riemann, N. V. Abrosimov, P. Becker, and H.-J. Pohl. Quantum information storage for over 180s using donor spins in a ^{28}Si "semiconductor vacuum". *Science*, 336(6086):1280–1283, 2012. 32

[143] N. Sangouard, R. Dubessy, and C. Simon. Quantum repeaters based on single trapped ions. *Phys. Rev. A*, 79(4):042340, 2009. 32

[144] A. Reiserer and G. Rempe. Cavity-based quantum networks with single atoms and optical photons. *Rev. Mod. Phys.*, 87(4):1379–1418, 2015. 32

[145] S. Langenfeld, S. Welte, L. Hartung, S. Daiss, P. Thomas, O. Morin, E. Distante, and G. Rempe. Quantum teleportation between remote qubit memories with only a single photon as a resource. *Phys. Rev. Lett.*, 126(13):130502, 2021. 32

[146] H. J. Kimble. Strong interactions of single atoms and photons in cavity QED. *Physica Scripta*, 1998(T76):127, 1998. 32

[147] Tatjana Wilk, Simon C. Webster, Axel Kuhn, and Gerhard Rempe. Single-atom single-photon quantum interface. *Science*, 317(5837):488–490, 2007.

[148] C. Junge, D. O'Shea, J. Volz, and A. Rauschenbeutel. Strong coupling between single atoms and nontransversal photons. *Phys. Rev. Lett.*, 110(21):213604, 2013.

[149] H. Takahashi, E. Kassa, C. Christoforou, and M. Keller. Strong coupling of a single ion to an optical cavity. *Phys. Rev. Lett.*, 124(1):013602, 2020. 32

[150] S. Olmschenk, D. N. Matsukevich, P. Maunz, D. Hayes, L.-M. Duan, and C. Monroe. Quantum teleportation between distant matter qubits. *Science*, 323(5913):486–489, 2009. 33

[151] V. Krutyanskiy, M. Meraner, J. Schupp, V. Krcmarsky, H. Hainzer, and B. P. Lanyon. Light-matter entanglement over 50 km of optical fibre. *npj Quantum Information*, 5(1):72, 2019.

[152] T. van Leent, M. Bock, F. Fertig, R. Garthoff, S. Eppelt, Y. Zhou, P. Malik, M. Seubert, T. Bauer, W. Rosenfeld, W. Zhang, C. Becher, and H. Weinfurter. Entangling single atoms over 33 km telecom fibre. *Nature*, 607(7917):69–73, 2022.

[153] V. Krutyanskiy, M. Galli, V. Krcmarsky, S. Baier, D. A. Fioretto, Y. Pu, A. Mazloom, P. Sekatski, M. Canteri, M. Teller, J. Schupp, J. Bate, M. Meraner, N. Sangouard, B. P. Lanyon, and T. E. Northup. Entanglement of trapped-ion qubits separated by 230 meters. *Phys. Rev. Lett.*, 130(5):050803, 2023.

[154] V. Krutyanskiy, M. Canteri, M. Meraner, J. Bate, V. Krcmarsky, J. Schupp, N. Sangouard, and B. P. Lanyon. Telecom-wavelength quantum repeater node based on a trapped-ion processor. *Phys. Rev. Lett.*, 130(21):213601, 2023. 33

[155] J. Schupp, V. Krcmarsky, V. Krutyanskiy, M. Meraner, T. E. Northup, and B. P. Lanyon. Interface between trapped-ion qubits and traveling photons with close-to-optimal efficiency. *PRX Quantum*, 2(2):020331, 2021. 33

[156] M. Körber, O. Morin, S. Langenfeld, A. Neuzner, S. Ritter, and G. Rempe. Decoherence-protected memory for a single-photon qubit. *Nature Photonics*, 12(1): 18–21, 2018. 33

[157] N. Kalb, A. Reiserer, S. Ritter, and G. Rempe. Heralded storage of a photonic quantum bit in a single atom. *Phys. Rev. Lett.*, 114(22):220501, 2015. 33

[158] T. Wilk, A. Gaëtan, C. Evellin, J. Wolters, Y. Miroshnychenko, P. Grangier, and A. Browaeys. Entanglement of two individual neutral atoms using Rydberg blockade. *Phys. Rev. Lett.*, 104(1):010502, 2010. 33

[159] J. I. Cirac and P. Zoller. Quantum computations with cold trapped ions. *Phys. Rev. Lett.*, 74(20):4091–4094, 1995.

[160] S. Daiss, S. Langenfeld, S. Welte, E. Distante, P. Thomas, L. Hartung, O. Morin, and G. Rempe. A quantum-logic gate between distant quantum-network modules. *Science*, 371(6529):614–617, 2021. 33

[161] P. Kobel, M. Breyer, and M. Köhl. Deterministic spin-photon entanglement from a trapped ion in a fiber Fabry–Perot cavity. *npj Quantum Information*, 7(1):6, 2021. 33

[162] N. T. Son, C. P. Anderson, A. Bourassa, K. C. Miao, C. Babin, M. Widmann, M. Niethammer, J. Ul Hassan, N. Morioka, I. G. Ivanov, F. Kaiser, J. Wrachtrup, and D. D. Awschalom. Developing silicon carbide for quantum spintronics. *Applied Physics Letters*, 116(19):190501, 2020. 33

[163] C. E. Bradley, J. Randall, M. H. Abobeih, R. C. Berrevoets, M. J. Degen, M. A. Bakker, M. Markham, D. J. Twitchen, and T. H. Taminiau. A ten-qubit solid-state

spin register with quantum memory up to one minute. *Phys. Rev. X*, 9(3):031045, 2019. 34

[164] S. Yang, Y. Wang, D. D. B. Rao, T. Hien Tran, A. S. Momenzadeh, M. Markham, D. J. Twitchen, P. Wang, W. Yang, R. Stöhr, P. Neumann, H. Kosaka, and J. Wrachtrup. High-fidelity transfer and storage of photon states in a single nuclear spin. *Nature Photonics*, 10(8):507–511, 2016. 34

[165] G. Balasubramanian, P. Neumann, D. Twitchen, M. Markham, R. Kolesov, N. Mizuochi, J. Isoya, J. Achard, J. Beck, J. Tissler, V. Jacques, P. R. Hemmer, F. Jelezko, and J. Wrachtrup. Ultralong spin coherence time in isotopically engineered diamond. *Nature Materials*, 8(5):383–387, 2009. 34

[166] A. Reiserer, N. Kalb, M. S. Blok, K. J. M. van Bemmelen, T. H. Taminiau, R. Hanson, D. J. Twitchen, and M. Markham. Robust quantum-network memory using decoherence-protected subspaces of nuclear spins. *Phys. Rev. X*, 6(2):021040, 2016.

[167] Y.-I. Sohn, S. Meesala, B. Pingault, H. A. Atikian, J. Holzgrafe, M. Gündoğan, C. Stavrakas, M. J. Stanley, A. Sipahigil, J. Choi, M. Zhang, J. L. Pacheco, J. Abraham, E. Bielejec, M. D. Lukin, M. Atatüre, and M. Lončar. Controlling the coherence of a diamond spin qubit through its strain environment. *Nature Communications*, 9 (1):2012, 2018. 34

[168] M. Pompili, S. L. N. Hermans, S. Baier, H. K. C. Beukers, P. C. Humphreys, R. N. Schouten, R. F. L. Vermeulen, M. J. Tiggelman, L. dos Santos Martins, B. Dirkse, S. Wehner, and Hanson R. Realization of a multinode quantum network of remote solid-state qubits. *Science*, 372(6539):259–264, 2021. 34

[169] R. Debroux, C. P. Michaels, C. M. Purser, N. Wan, M. E. Trusheim, J. Arjona Martínez, R. A. Parker, A. M. Stramma, K. C. Chen, L. de Santis, E. M. Alexeev, A. C. Ferrari, D. Englund, D. A. Gangloff, and M. Atatüre. Quantum control of the tin-vacancy spin qubit in diamond. *Phys. Rev. X*, 11(4):041041, 2021. 34

[170] D. D. Sukachev, A. Sipahigil, C. T. Nguyen, M. K. Bhaskar, R. E. Evans, F. Jelezko, and M. D. Lukin. Silicon-vacancy spin qubit in diamond: A quantum memory exceeding 10 ms with single-shot state readout. *Phys. Rev. Lett.*, 119(22):223602, 2017. 34

[171] A. Sipahigil, K. D. Jahnke, L. J. Rogers, T. Teraji, J. Isoya, A. S. Zibrov, F. Jelezko, and M. D. Lukin. Indistinguishable photons from separated silicon-vacancy centers in diamond. *Phys. Rev. Lett.*, 113(11):113602, 2014. 34

[172] M. K. Bhaskar, R. Riedinger, B. Machielse, D. S. Levonian, C. T. Nguyen, E. N. Knall, H. Park, D. Englund, M. Lončar, D. D. Sukachev, and M. D. Lukin. Experimental demonstration of memory-enhanced quantum communication. *Nature*, 580 (7801):60–64, 2020. 34

[173] J. Wolters, A. W. Schell, G. Kewes, N. Nüsse, M. Schoengen, H. Döscher, T. Hannappel, B. Löchel, M. Barth, and O. Benson. Enhancement of the zero phonon line emission from a single nitrogen vacancy center in a nanodiamond via coupling to a photonic crystal cavity. *Applied Physics Letters*, 97(14):141108, 2010. 34

[174] B. Machielse, S. Bogdanovic, S. Meesala, S. Gauthier, M. J. Burek, G. Joe, M. Chalupnik, Y. I. Sohn, J. Holzgrafe, R. E. Evans, C. Chia, H. Atikian, M. K. Bhaskar, D. D. Sukachev, L. Shao, S. Maity, M. D. Lukin, and M. Loncar. Quantum interference of electromechanically stabilized emitters in nanophotonic devices. *Phys. Rev. X*, 9(3):031022, 2019. 34

[175] N. H. Wan, T.-J. Lu, K. C. Chen, M. P. Walsh, M. E. Trusheim, L. de Santis, E. A. Bersin, I. B. Harris, S. L. Mouradian, I. R. Christen, E. S. Bielejec, and D. Englund. Large-scale integration of artificial atoms in hybrid photonic circuits. *Nature*, 583 (7815):226–231, 2020. 34

[176] J. Kitching. Chip-scale atomic devices. *Applied Physics Reviews*, 5(3):031302, 2018. 34

[177] A. Horsley. *High resolution field imaging with atomic vapor cells*. PhD Thesis, Universität Basel, 2015. 35, 75, 76, 77, 78, 79, 80, 81, 82, 104, 111, 120, 134, 135, 155

[178] P. S. Michelberger. *Room temperature caesium quantum memory for quantum information applications*. PhD Thesis, University of Oxford, 2015. 35, 48, 102, 104, 105, 147

[179] N. B. Phillips, A. V. Gorshkov, and I. Novikova. Optimal light storage in atomic vapor. *Physical Review A*, 78(2):1–9, 2008. 35, 44, 105, 129, 161

[180] S. E. Thomas, J. H. Munns, K. T. Kaczmarek, C. Qiu, B. Brecht, A. Feizpour, P. M. Ledingham, I. A. Walmsley, J. Nunn, and D. J. Saunders. High efficiency Raman memory by suppressing radiation trapping. *New Journal of Physics*, 19(6):0–7, 2017. 49, 79

[181] S. E. Thomas, T. M. Hird, J. H. D. Munns, B. Brecht, D. J. Saunders, J. Nunn, I. A. Walmsley, and P. M. Ledingham. Raman quantum memory with built-in

suppression of four-wave-mixing noise. *Phys. Rev. A*, 100(3):033801, 2019. 35, 49, 59, 151

[182] J. L. Rubio, D. Viscor, J. Mompart, and V. Ahufinger. Atomic-frequency-comb quantum memory via piecewise adiabatic passage. *Phys. Rev. A*, 98(4):043834, 2018. 35, 54

[183] K. T. Kaczmarek, P. M. Ledingham, B. Brecht, S. E. Thomas, G. S. Thekkadath, O. Lazo-Arjona, J. H. D. Munns, E. Poem, A. Feizpour, D. J. Saunders, J. Nunn, and I. A. Walmsley. High-speed noise-free optical quantum memory. *Phys. Rev. A*, 97(4):042316, 2018. 35, 56

[184] R. Finkelstein, E. Poem, O. Michel, O. Lahad, and O. Firstenberg. Fast, noise-free memory for photon synchronization at room temperature. *Sci. Adv.*, 4(1):eaap8598, 2018. 35, 56

[185] O. Katz and O. Firstenberg. Light storage for one second in room-temperature alkali vapor. *Nat. Commun.*, 9(1):2074, 2018. 35, 59, 78, 105, 155, 158, 173, 202

[186] J. Guo, X. Feng, P. Yang, Z. Yu, L. Q. Chen, C.-h. Yuan, and W. Zhang. High-performance Raman quantum memory with optimal control in room temperature atoms. *Nat. Commun.*, 10(1):148, 2019. 35, 49, 59, 78, 161, 201, 202

[187] M. Hosseini, B. M. Sparkes, G. Campbell, P. K. Lam, and B. C. Buchler. High efficiency coherent optical memory with warm rubidium vapour. *Nat. Commun.*, 2 (1):174, 2011. 35, 52, 59

[188] M. Hosseini, G. Campbell, B. M. Sparkes, P. K. Lam, and B. C. Buchler. Unconditional room-temperature quantum memory. *Nature Physics*, 7(10):794–798, 2011. 35

[189] M. Namazi, C. Kupchak, B. Jordaan, R. Shahrokhshahi, and E. Figueroa. Ultralow-noise room-temperature quantum memory for polarization qubits. *Phys. Rev. Appl.*, 8(3):034023, 2017. 35, 193

[190] D. J. Saunders, J. H. D. Munns, T. F. M. Champion, C. Qiu, K. T. Kaczmarek, E. Poem, P. M. Ledingham, I. A. Walmsley, and J. Nunn. Cavity-enhanced room-temperature broadband Raman memory. *Phys. Rev. Lett.*, 116(9):090501, 2016. 35, 49, 105, 151

[191] G. Buser, R. Mottola, B. Cotting, J. Wolters, and P. Treutlein. Single-photon storage in a ground-state vapor cell quantum memory. *PRX Quantum*, 3(2):020349, 2022. 35, 59, 155, 171, 202, 204

[192] P. S. Michelberger, T. F. M. Champion, M. R. Sprague, K. T. Kaczmarek, M. Barbieri, X. M. Jin, D. G. England, W. S. Kolthammer, D. J. Saunders, J. Nunn, and I. A. Walmsley. Interfacing GHz-bandwidth heralded single photons with a warm vapour Raman memory. *New J. Phys.*, 17(4):043006, 2015. 35, 49

[193] J. Appel, E. Figueroa, D. Korystov, M. Lobino, and A. I. Lvovsky. Quantum memory for squeezed light. *Phys. Rev. Lett.*, 100(9):093602, 2008. 35

[194] S. Riedl, M. Lettner, C. Vo, S. Baur, G. Rempe, and S. Dürr. Bose-Einstein condensate as a quantum memory for a photonic polarization qubit. *Phys. Rev. A*, 85(2):022318, 2012. 36

[195] E. Saglamyurek, T. Hrushevskyi, A. Rastogi, L. W. Cooke, B. D. Smith, and L. J. Leblanc. Storing short single-photon-level optical pulses in Bose–Einstein condensates for high-performance quantum memory. *New Journal of Physics*, 23(4): 043028, 2021. 36, 50, 59

[196] Y.-F. Hsiao, P.-J. Tsai, H.-S. Chen, S.-X. Lin, C.-C. Hung, C.-H. Lee, Y.-H. Chen, Y.-F. Chen, I. A. Yu, and Y.-C. Chen. Highly efficient coherent optical memory based on electromagnetically induced transparency. *Phys. Rev. Lett.*, 120(18):183602, 2018. 36, 44, 59, 144

[197] Y.-W. Cho, G. T. Campbell, J. L. Everett, J. Bernu, D. B. Higginbottom, M. T. Cao, J. Geng, N. P. Robins, P. K. Lam, and B. C. Buchler. Highly efficient optical quantum memory with long coherence time in cold atoms. *Optica*, 3(1):100–107, 2016. 36, 38, 52, 59

[198] E. Bimbard, R. Boddeda, N. Vitrant, A. Grankin, V. Parigi, J. Stanojevic, A. Ourjoumtsev, and P. Grangier. Homodyne tomography of a single photon retrieved on demand from a cavity-enhanced cold atom memory. *Phys. Rev. Lett.*, 112(3):033601, 2014. 36

[199] S.-J. Yang, X.-J. Wang, X.-H. Bao, and J.-W. Pan. An efficient quantum light–matter interface with sub-second lifetime. *Nat. Photonics*, 10(6):381–384, 2016. 36

[200] X.-H. Bao, A. Reingruber, P. Dietrich, J. Rui, A. Dück, T. Strassel, L. Li, N.-L. Liu, B. Zhao, and J.-W. Pan. Efficient and long-lived quantum memory with cold atoms inside a ring cavity. *Nat. Phys.*, 8(7):517–521, 2012. 36, 183

[201] D.-S. Ding, Z.-Y. Zhou, B.-S. Shi, and G.-C. Guo. Single-photon-level quantum image memory based on cold atomic ensembles. *Nature Communications*, 4(1):2527, 2013. 36

[202] Y.-F. Pu, N. Jiang, W. Chang, H.-X. Yang, C. Li, and L.-M. Duan. Experimental realization of a multiplexed quantum memory with 225 individually accessible memory cells. *Nat. Commun.*, 8(1):15359, 2017. 36, 159, 185

[203] N. Jiang, Y.-F. Pu, W. Chang, C. Li, S. Zhang, and L.-M. Duan. Experimental realization of 105-qubit random access quantum memory. *npj Quantum Information*, 5(1):28, 2019. 36, 159

[204] Y. Yu, F. Ma, X.-Y. Luo, B. Jing, P.-F. Sun, R.-Z. Fang, C.-W. Yang, H. Liu, M.-Y. Zheng, X.-P. Xie, W.-J. Zhang, L.-X. You, Z. Wang, T.-Y. Chen, Q. Zhang, X.-H. Bao, and J.-W. Pan. Entanglement of two quantum memories via fibres over dozens of kilometres. *Nature*, 578(7794):240–245, 2020. 36

[205] Y.-C. Tseng, Y.-C. Wei, and Y.-C. Chen. Efficient quantum memory for photonic polarization qubits generated by cavity-enhanced spontaneous parametric downconversion. *Opt. Express*, 30(11):19944–19960, 2022. 36, 44, 111

[206] D. M. Farkas, K. M. Hudek, E. A. Salim, S. R. Segal, M. B. Squires, and D. Z. Anderson. A compact, transportable, microchip-based system for high repetition rate production of Bose–Einstein condensates. *Applied Physics Letters*, 96(9):093102, 2010. 36

[207] E. A. Salim, J. DeNatale, D. M. Farkas, K. M. Hudek, S. E. McBride, J. Michalchuk, R. Mihailovich, and D. Z. Anderson. Compact, microchip-based systems for practical applications of ultracold atoms. *Quantum Information Processing*, 10(6):975, 2011.

[208] C. J. E. Straatsma, M. K. Ivory, J. Duggan, J. Ramirez-Serrano, D. Z. Anderson, and E. A. Salim. On-chip optical lattice for cold atom experiments. *Opt. Lett.*, 40 (14):3368–3371, 2015. 36

[209] J. A. Rushton, M. Aldous, and M. D. Himsworth. Contributed Review: The feasibility of a fully miniaturized magneto-optical trap for portable ultracold quantum technology. *Review of Scientific Instruments*, 85(12):121501, 2014. 36

[210] E. Da Ros, S. Kanthak, E. Saglamyürek, M. Gündogan, and M. Krutzik. Proposal for a long-lived quantum memory using matter-wave optics with Bose-Einstein condensates in microgravity. *Phys. Rev. Res.*, 5(3):033003, 2023. 36

[211] R. L. Ahlefeldt, M. R. Hush, and M. J. Sellars. Ultranarrow optical inhomogeneous linewidth in a stoichiometric rare-earth crystal. *Phys. Rev. Lett.*, 117(25):250504, 2016. 36

[212] S. Welinski, A. Tiranov, M. Businger, A. Ferrier, M. Afzelius, and P. Goldner. Coherence time extension by large-scale optical spin polarization in a rare-earth doped crystal. *Phys. Rev. X*, 10(3):031060, 2020.

[213] M. F. Askarani, A. Das, J. H. Davidson, G. C. Amaral, N. Sinclair, J. A. Slater, S. Marzban, C. W. Thiel, R. L. Cone, D. Oblak, and W. Tittel. Long-lived solid-state optical memory for high-rate quantum repeaters. *Phys. Rev. Lett.*, 127(22):220502, 2021. 36

[214] B. Lauritzen, J. Minár, H. de Riedmatten, M. Afzelius, N. Sangouard, C. Simon, and N. Gisin. Telecommunication-wavelength solid-state memory at the single photon level. *Phys. Rev. Lett.*, 104(8):080502, 2010. 36, 50

[215] I. Craiciu, M. Lei, J. Rochman, J. M. Kindem, J. G. Bartholomew, E. Miyazono, T. Zhong, N. Sinclair, and A. Faraon. Nanophotonic quantum storage at telecommunication wavelength. *Phys. Rev. Appl.*, 12(2):024062, 2019. 36

[216] C. W. Thiel, T. Böttger, and R. L. Cone. Rare-earth-doped materials for applications in quantum information storage and signal processing. *Journal of Luminescence*, 131(3):353–361, 2011. 37

[217] E. Fraval, M. J. Sellars, and J. J. Longdell. Dynamic decoherence control of a solid-state nuclear-quadrupole qubit. *Phys. Rev. Lett.*, 95(3):030506, 2005. 37

[218] M. Zhong, M. P. Hedges, R. L. Ahlefeldt, J. G. Bartholomew, S. E. Beavan, S. M. Wittig, J. J. Longdell, and M. J. Sellars. Optically addressable nuclear spins in a solid with a six-hour coherence time. *Nature*, 517(7533):177–180, 2015. 37, 183

[219] Y. Ma, Y.-Z. Ma, Z.-Q. Zhou, C.-F. Li, and G.-C. Guo. One-hour coherent optical storage in an atomic frequency comb memory. *Nat. Commun.*, 12(1):2381, 2021. 37, 54, 183

[220] M. P. Hedges, J. J. Longdell, Y. Li, and M. J. Sellars. Efficient quantum memory for light. *Nature*, 465(7301):1052–1056, 2010. 37, 50

[221] M. Sabooni, Q. Li, S. Kröll, and L. Rippe. Efficient quantum memory using a weakly absorbing sample. *Phys. Rev. Lett.*, 110(13):133604, 2013. 37, 54, 59

[222] G. Heinze, C. Hubrich, and T. Halfmann. Stopped light and image storage by electromagnetically induced transparency up to the regime of one minute. *Phys. Rev. Lett.*, 111(3):033601, 2013. 37

[223] D. Schraft, M. Hain, N. Lorenz, and T. Halfmann. Stopped light at high storage efficiency in a Pr^{3+}:Y_2SiO_5 crystal. *Phys. Rev. Lett.*, 116(7):073602, 2016. 37, 59

[224] T.-S. Yang, Z.-Q. Zhou, Y.-L. Hua, X. Liu, Z.-F. Li, P.-Y. Li, Y. Ma, C. Liu, P.-J. Liang, X. Li, Y.-X. Xiao, J. Hu, C.-F. Li, and G.-C. Guo. Multiplexed storage and real-time manipulation based on a multiple degree-of-freedom quantum memory. *Nat. Commun.*, 9(1):3407, 2018. 37

[225] D. Lago-Rivera, S. Grandi, J. V. Rakonjac, A. Seri, and H. de Riedmatten. Telecom-heralded entanglement between multimode solid-state quantum memories. *Nature*, 594(7861):37–40, 2021. 37

[226] A. Seri, A. Lenhard, D. Rieländer, M. Gündogan, P. M. Ledingham, M. Mazzera, and H. de Riedmatten. Quantum correlations between single telecom photons and a multimode on-demand solid-state quantum memory. *Phys. Rev. X*, 7(2):021028, 2017. 37

[227] A. Seri, D. Lago-Rivera, A. Lenhard, G. Corrielli, R. Osellame, M. Mazzera, and H. de Riedmatten. Quantum storage of frequency-multiplexed heralded single photons. *Phys. Rev. Lett.*, 123(8):080502, 2019. 37, 185

[228] N. Maring, P. Farrera, K. Kutluer, M. Mazzera, G. Heinze, and H. de Riedmatten. Photonic quantum state transfer between a cold atomic gas and a crystal. *Nature*, 551(7681):485–488, 2017. 37

[229] A. Holzäpfel, J. Etesse, K. T. Kaczmarek, A. Tiranov, N. Gisin, and M. Afzelius. Optical storage for 0.53s in a solid-state atomic frequency comb memory using dynamical decoupling. *New Journal of Physics*, 22(6):063009, 2020. 37, 59

[230] A. Ortu, A. Holzäpfel, J. Etesse, and M. Afzelius. Storage of photonic time-bin qubits for up to 20ms in a rare-earth doped crystal. *npj Quantum Information*, 8 (1):29, 2022.

[231] G. Corrielli, A. Seri, M. Mazzera, R. Osellame, and H. de Riedmatten. Integrated optical memory based on laser-written waveguides. *Phys. Rev. Appl.*, 5(5):054013, 2016. 37

[232] L. You, J. Quan, Y. Wang, Y. Ma, X. Yang, Y. Liu, H. Li, J. Li, J. Wang, J. Liang, Z. Wang, and X. Xie. Superconducting nanowire single photon detection system for space applications. *Opt. Express*, 26(3):2965–2971, 2018. 37

[233] M. Gündoğan, J. S. Sidhu, M. Krutzik, and D. K. L. Oi. Time-delayed single satellite quantum repeater node for global quantum communications. *arXiv:2303.04174*, 2023. 37, 178

[234] T. B. Pittman and J. D. Franson. Cyclical quantum memory for photonic qubits. *Phys. Rev. A*, 66(6):062302, 2002. 38

[235] T. B. Pittman, B. C. Jacobs, and J. D. Franson. Single photons on pseudodemand from stored parametric down-conversion. *Phys. Rev. A*, 66(4):042303, 2002. 38

[236] J.-I. Yoshikawa, K. Makino, S. Kurata, P. van Loock, and A. Furusawa. Creation, storage, and on-demand release of optical quantum states with a negative Wigner function. *Phys. Rev. X*, 3(4):041028, 2013. 38

[237] M. Bouillard, G. Boucher, J. Ferrer Ortas, B. Pointard, and R. Tualle-Brouri. Quantum storage of single-photon and two-photon Fock states with an all-optical quantum memory. *Phys. Rev. Lett.*, 122(21):210501, 2019. 38

[238] C. J. Evans, C. M. Nunn, S. W. L. Cheng, J. D. Franson, and T. B. Pittma. Experimental storage of photonic polarization entanglement in a broadband loop-based quantum memory. *arXiv:2306.09986*, 2023. 38, 59

[239] X.-L. Pang, A.-L. Yang, J.-P. Dou, H. Li, C.-N. Zhang, E. Poem, D. J. Saunders, H. Tang, J. Nunn, I. A. Walmsley, and X.-M. Jin. A hybrid quantum memory-enabled network at room temperature. *Science Advances*, 6(6), 2020. 38

[240] A. V. Gorshkov, A. André, M. D. Lukin, and A. S. Sørensen. Photon storage in Λ-type optically dense atomic media. III. Effects of inhomogeneous broadening. *Phys. Rev. A*, 76(3):033806, 2007. 39, 61, 87, 97, 101, 146, 163, 164, 171, 172, 203

[241] A. V. Gorshkov, T. Calarco, M. D. Lukin, and A. S. Sørensen. Photon storage in Λ-type optically dense atomic media. IV. Optimal control using gradient ascent. *Phys. Rev. A*, 77(4):043806, 2008. 39, 40, 61, 87, 97, 98, 100, 129, 146, 161, 163, 165, 171, 172, 203

[242] I. Novikova, A. V. Gorshkov, D. F. Phillips, A. S. Sørensen, M. D. Lukin, and R. L. Walsworth. Optimal control of light pulse storage and retrieval. *Physical Review Letters*, 98(24):1–4, 2007. 40, 129

[243] S. A. Moiseev and S. Kröll. Complete reconstruction of the quantum state of a single-photon wave packet absorbed by a Doppler-broadened transition. *Phys. Rev. Lett.*, 87(17):173601, 2001. 40, 50

[244] E. Saglamyurek, T. Hrushevskyi, A. Rastogi, K. Heshami, and L. J. Leblanc. Coherent storage and manipulation of broadband photons via dynamically controlled Autler–Townes splitting. *Nature Photonics*, 12(12):774–782, 2018. 49, 59

[245] O. Davidson, O. Yogev, E. Poem, and O. Firstenberg. Fast, noise-free atomic optical memory with 35-percent end-to-end efficiency. *Communications Physics*, 6(1):131, 2023. 56, 57, 59

[246] K. F. Reim, P. Michelberger, K. C. Lee, J. Nunn, N. K. Langford, and I. A. Walmsley. Single-photon-level quantum memory at room temperature. *Physical Review Letters*, 107(5):1–4, 2011. 45, 59

[247] W. Zhi, R. Guobin, L. Shuqin, and J. Shuisheng. Loss properties due to Rayleigh scattering in different types of fiber. *Opt. Express*, 11(1):39–47, 2003. 41

[248] F. Yu, P. Song, D. Wu, T. Birks, D. Bird, and J. Knight. Attenuation limit of silica-based hollow-core fiber at mid-IR wavelengths. *APL Photonics*, 4(8):080803, 2019. 41

[249] K.-J. Boller, A. Imamoglu, and S. E. Harris. Observation of electromagnetically induced transparency. *Phys. Rev. Lett.*, 66(20):2593–2596, 1991. 42

[250] S. E. Harris, J. E. Field, and A. Imamoglu. Nonlinear optical processes using electromagnetically induced transparency. *Phys. Rev. Lett.*, 64(10):1107–1110, 1990. 42

[251] S. E. Harris. Electromagnetically induced transparency. *Physics Today*, 50(7):36–42, 1997.

[252] J. P. Marangos. Electromagnetically induced transparency. *Journal of Modern Optics*, 45(3):471–503, 1998. 42

[253] S. H. Autler and C. H. Townes. Stark effect in rapidly varying fields. *Phys. Rev.*, 100(2):703–722, 1955. 43, 46, 49

[254] A. Kasapi, M. Jain, G. Y. Yin, and S. E. Harris. Electromagnetically induced transparency: Propagation dynamics. *Phys. Rev. Lett.*, 74(13):2447–2450, 1995. 43

[255] L. V. Hau, S. E. Harris, Z. Dutton, and C. H. Behroozi. Light speed reduction to 17 metres per second in an ultracold atomic gas. *Nature*, 397(6720):594–598, 1999. 43

[256] S. E. Harris, J. E. Field, and A. Kasapi. Dispersive properties of electromagnetically induced transparency. *Phys. Rev. A*, 46(1):R29–R32, 1992. 44

[257] M. Fleischhauer and M. D. Lukin. Dark-state polaritons in electromagnetically induced transparency. *Physical Review Letters*, 84(22):5094–5097, 2000. 44

[258] M. Fleischhauer, S. F. Yelin, and M. D. Lukin. How to trap photons? Storing single-photon quantum states in collective atomic excitations. *Optics Communications*, 179(1):395–410, 2000. 44

[259] C. Liu, Z. Dutton, C. H. Behroozi, and L. V. Hau. Observation of coherent optical information storage in an atomic medium using halted light pulses. *Nature*, 409 (6819):490–493, 2001. 44

[260] M. Bajcsy, S. Hofferberth, V. Balic, T. Peyronel, M. Hafezi, A. S. Zibrov, V. Vuletic, and M. D. Lukin. Efficient all-optical switching using slow light within a hollow fiber. *Phys. Rev. Lett.*, 102(20):203902, 2009. 44

[261] B. S. Ham, P. R. Hemmer, and M. S. Shahriar. Efficient electromagnetically induced transparency in a rare-earth doped crystal. *Optics Communications*, 144(4):227–230, 1997. 44

[262] E. Baldit, K. Bencheikh, P. Monnier, J. A. Levenson, and V. Rouget. Ultraslow light propagation in an inhomogeneously broadened rare-earth ion-doped crystal. *Phys. Rev. Lett.*, 95(14):143601, 2005. 44

[263] D. F. Phillips, A. Fleischhauer, A. Mair, R. L. Walsworth, and M. D. Lukin. Storage of light in atomic vapor. *Phys. Rev. Lett.*, 86(5):783–786, 2001. 44

[264] M. D. Eisaman, A. André, F. Massou, M. Fleischhauer, A. S. Zibrov, and M. D. Lukin. Electromagnetically induced transparency with tunable single-photon pulses. *Nature*, 438(7069):837–841, 2005.

[265] S. Manz, T. Fernholz, J. Schmiedmayer, and J. W. Pan. Collisional decoherence during writing and reading quantum states. *Physical Review A*, 75(4):1–4, 2007. 44, 45

[266] M. Fleischhauer and M. D. Lukin. Quantum memory for photons: Dark-state polaritons. *Phys. Rev. A*, 65(2):022314, 2002. 45, 46, 87

[267] M. T. Hsu, G. Hétet, O. Glöckl, J. J. Longdell, B. C. Buchler, H. A. Bachor, and P. K. Lam. Quantum study of information delay in electromagnetically induced transparency. *Physical Review Letters*, 97(18):1–4, 2006. 45

[268] M. D. Lukin, M. Fleischhauer, A. S. Zibrov, H. G. Robinson, V. L. Velichansky, L. Hollberg, and M. O. Scully. Spectroscopy in dense coherent media: Line narrowing and interference effects. *Phys. Rev. Lett.*, 79(16):2959–2962, 1997. 45, 87

[269] I. Novikova, R. L. Walsworth, and Y. Xiao. Electromagnetically induced transparency-based slow and stored light in warm atoms. *Laser and Photonics Reviews*, 6(3):333–353, 2012. 46, 87, 153

[270] M. Fleischhauer, A. Imamoglu, and J. P. Marangos. Electromagnetically induced transparency: Optics in coherent media. *Rev. Mod. Phys.*, 77(2):633–673, 2005. 46, 84, 87

[271] P. M. Anisimov, J. P. Dowling, and B. C. Sanders. Objectively discerning Autler-Townes splitting from electromagnetically induced transparency. *Phys. Rev. Lett.*, 107(16):163604, 2011. 46

[272] C. V. Raman and K. S. Krishnan. A new type of secondary radiation. *Nature*, 121 (3048):501–502, 1928. 46

[273] A. E. Kozhekin, K. Mlmer, and E. Polzik. Quantum memory for light. *Phys. Rev. A*, 62(3):033809, 2000. 47

[274] J. Nunn, I. A. Walmsley, M. G. Raymer, K. Surmacz, F. C. Waldermann, Z. Wang, and D. Jaksch. Mapping broadband single-photon wave packets into an atomic memory. *Phys. Rev. A*, 75(1):011401, 2007. 47, 48

[275] A. Rastogi, E. Saglamyurek, T. Hrushevskyi, S. Hubele, and L. J. Leblanc. Discerning quantum memories based on electromagnetically-induced-transparency and Autler-Townes-splitting protocols. *Physical Review A*, 100(1):1–15, 2019. 50

[276] M. Nilsson and S. Kröll. Solid state quantum memory using complete absorption and re-emission of photons by tailored and externally controlled inhomogeneous absorption profiles. *Optics Communications*, 247(4):393–403, 2005. 50

[277] A. L. Alexander, J. J. Longdell, M. J. Sellars, and N. B. Manson. Photon echoes produced by switching electric fields. *Phys. Rev. Lett.*, 96(4):043602, 2006.

[278] B. Kraus, W. Tittel, N. Gisin, M. Nilsson, S. Kröll, and J. I. Cirac. Quantum memory for nonstationary light fields based on controlled reversible inhomogeneous broadening. *Phys. Rev. A*, 73(2):020302, 2006.

[279] M. U. Staudt, S. R. Hastings-Simon, M. Nilsson, M. Afzelius, V. Scarani, R. Ricken, H. Suche, W. Sohler, W. Tittel, and N. Gisin. Fidelity of an optical memory based on stimulated photon echoes. *Phys. Rev. Lett.*, 98(11):113601, 2007. 50

[280] B. M. Sparkes, J. Bernu, M. Hosseini, J. Geng, Q. Glorieux, P. A. Altin, P. K. Lam, N. P. Robins, and B. C. Buchler. Gradient echo memory in an ultra-high optical depth cold atomic ensemble. *New Journal of Physics*, 15(8):085027, 2013. 50, 52

[281] G. Hétet, J. J. Longdell, A. L. Alexander, P. K. Lam, and M. J. Sellars. Electro-optic quantum memory for light using two-level atoms. *Phys. Rev. Lett.*, 100(2):023601, 2008. 50

[282] M. Afzelius, C. Simon, H. d. Riedmatten, and N. Gisin. Multimode quantum memory based on atomic frequency combs. *Phys. Rev. A*, 79(5):052329, 2009. 52, 53, 54

[283] J. Nunn, K. Reim, K. C. Lee, V. O. Lorenz, B. J. Sussman, I. A. Walmsley, and D. Jaksch. Multimode memories in atomic ensembles. *Phys. Rev. Lett.*, 101(26): 260502, 2008. 53

[284] R. Finkelstein, O. Lahad, O. Michel, O. Davidson, E. Poem, and O. Firstenberg. Power narrowing: Counteracting Doppler broadening in two-color transitions. *New Journal of Physics*, 21(10):103024, 2019. 56

[285] K. F. Reim, J. Nunn, V. O. Lorenz, B. J. Sussman, K. C. Lee, N. K. Langford, D. Jaksch, and I. A. Walmsley. Towards high-speed optical quantum memories. *Nat. Photonics*, 4(4):218–221, 2010. 56

[286] S. E. Thomas, S. Sagona-Stophel, Z. Schofield, I. A. Walmsley, and P. M. Ledingham. Single-photon-compatible telecommunications-band quantum memory in a hot atomic gas. *Phys. Rev. Appl.*, 19(3):L031005, 2023. 57

[287] B. Maaß, N. V. Ewald, A. Barua, S. Reitzenstein, and J. Wolters. Room-temperature ladder-type optical memory compatible with single photons from InGaAs quantum dots. *arXiv:2402.14686v1*, 2024. 57, 204

[288] D. A. Steck. Cesium D line data. Available online at `http://steck.us/alkalidata` (revision 2.3.2), 2023. 62, 63, 64, 65, 68, 69, 70, 74, 75, 78, 101, 132, 155, 158

[289] R. Mottola, G. Buser, and P. Treutlein. Electromagnetically induced transparency and optical pumping in the hyperfine Paschen-Back regime. *Phys. Rev. A*, 108(6): 062820, 2023. 63

[290] R. Mottola, G. Buser, and P. Treutlein. Optical memory in a microfabricated rubidium vapor cell. *Phys. Rev. Lett.*, 131(26):260801, 2023. 63

[291] D. A. Steck. Quantum and Atom Optics. Available online at `http://steck.us/teaching` (revision 0.14), 2023. 64, 65, 66, 68, 70, 73, 88

[292] M. A. Zentile, J. Keaveney, L. Weller, D. J. Whiting, C. S. Adams, and I. G. Hughes. ElecSus: A program to calculate the electric susceptibility of an atomic ensemble. *Computer Physics Communications*, 189:162–174, 2015. 64

[293] J. Keaveney, C. S. Adams, and I. G. Hughes. ElecSus: Extension to arbitrary geometry magneto-optics. *Computer Physics Communications*, 224:311–324, 2018. 64

[294] B. Cordero, V. Gómez, A. E. Platero-Prats, M. Revés, J. Echeverría, E. Cremades, F. Barragán, and S. Alvarez. Covalent radii revisited. *Dalton Transactions*, pages 2832–2838, 2008. 66

[295] R. Paschotta. RP Photonics Encyclopedia: Effective mode area. Available online at `https://www.rp-photonics.com/effective_mode_area.html`, 2006, 2006. 67

[296] C. Cohen-Tannoudji, J. Dupont-Roc, and G. Grynberg. *Atom-Photon Interactions*. Wiley-VCH, 2004. 69, 82, 93

[297] K. DeRose, K. Jiang, J. Li, M. Julius, L. Zhuo, S. Wenner, and S. Bali. Producing slow light in warm alkali vapor using electromagnetically induced transparency. *American Journal of Physics*, 91(3):193–205, 2023. 71

[298] M. Fox. *Quantum Optics: An Introduction*. Oxford University Press, 2006. 71, 73

[299] J. J. Olivero and R. L. Longbothum. Empirical fits to the Voigt line width: A brief review. *Journal of Quantitative Spectroscopy and Radiative Transfer*, 17(2):233–236, 1977. 72

[300] M. Danos and S. Geschwind. Broadening of microwave absorption lines due to wall collisions. *Phys. Rev.*, 91(5):1159–1162, 1953. 72, 79

[301] W. Happer. Optical pumping. *Rev. Mod. Phys.*, 44(2):169–249, 1972. 75, 120

[302] W. Happer, Y.-Y. Jau, and T. Walker. *Optically Pumped Atoms*. Wiley-VCH, 2010. 75, 120, 134, 135

[303] L. Ma, O. Slattery, and X. Tang. Optical quantum memory based on electromagnetically induced transparency. *Journal of Optics*, 19(4), 2017. 77

[304] R. Finkelstein, S. Bali, O. Firstenberg, and I. Novikova. A practical guide to electromagnetically induced transparency in atomic vapor. *New Journal of Physics*, 25(3):035001, 2023. 77

[305] M. Parniak and W. Wasilewski. Direct observation of atomic diffusion in warm rubidium ensembles. *Applied Physics B*, 116(2):415–421, 2014. 77

[306] D. J. Croucher and J. L. Clark. Total collision cross sections and van der Waals constants for alkali atom interactions with atoms and non-reactive diatomic molecules at thermal energies. *Journal of Physics B*, 2(5):603–623, 1969. 78, 80, 135

[307] R. Chrapkiewicz, W. Wasilewski, and C. Radzewicz. How to measure diffusional decoherence in multimode rubidium vapor memories? *Optics Communications*, 317: 1–6, 2014. 78

[308] F. A. Franz and C. E. Sooriamoorthi. Spin relaxation within the $^6P_2$ and $^6S_2$ states of cesium measured by white-light optical pumping. *Physical Review A*, 10(1): 126–140, 1974. 78, 79

[309] S. Legowski. Relaxation of optically pumped cesium atoms by different buffer gases. *The Journal of Chemical Physics*, 41(5):1313–1317, 1964. 79

[310] N. Beverini, P. Minguzzi, and F. Strumia. Foreign-gas-induced cesium hyperfine relaxation. *Physical Review A*, 4(2):550–555, 1971. 79

[311] D. Giel, Hinz G., D. Nettels, and A. Weis. Diffusion of Cs atoms in Ne buffer gas measured by optical magnetic resonance tomography. *Opt. Express*, 6(13):251–256, 2000. 79

[312] N. Beverini, P. Violino, and F. Strumia. Optical pumping of caesium in the presence of heavy noble gases. *Zeitschrift für Physik*, 265(2):189–196, 1973. 79

[313] A. A. Medvedev, V. V. Meshkov, A. V. Stolyarov, and M. C. Heaven. Ab initio interatomic potentials and transport properties of alkali metal (M = Rb and Cs)–rare gas (Rg = He, Ne, Ar, Kr, and Xe) media. *Phys. Chem. Chem. Phys.*, 20(40): 25974–25982, 2018. 79

[314] M. V. Balabas, K. Jensen, W. Wasilewski, H. Krauter, L. S. Madsen, J. H. Müller, T. Fernholz, and E. S. Polzik. High quality anti-relaxation coating material for alkali atom vapor cells. *Opt. Express*, 18(6):5825–5830, 2010. 78

[315] J. Vanier, J.-F. Simard, and J.-S. Boulanger. Relaxation and frequency shifts in the ground state of ^{85}Rb. *Phys. Rev. A*, 9(3):1031–1040, 1974. 79

[316] S. Micalizio, A. Godone, F. Levi, and C. Calosso. Pulsed optically pumped ^{87}Rb vapor cell frequency standard: A multilevel approach. *Phys. Rev. A*, 79(1):013403, 2009. 79

[317] Y. Shi, T. Scholtes, Z. D. Grujic, V. Lebedev, V. Dolgovskiy, and A. Weis. Quantitative study of optical pumping in the presence of spin-exchange relaxation. *Phys. Rev. A*, 97(1):013419, 2018. 80

[318] J. Singh, P. A. M. Dolph, and W. A. Tobias. Alkali metal vapor pressures and number densities for hybrid spin exchange optical pumping. Available online at `https://people.nscl.msu.edu/~singhj/docs/vp195.pdf`, 2008. 81, 134

[319] D. Budker and D. F. Jackson Kimball. *Optical Magnetometry*. Cambridge University Press, 2013. 81

[320] Z. J. Jabbour, J. Sagle, R. K. Namiotka, and J. Huennekens. Measurement of the self-broadening rate coefficients of the cesium resonance lines. *Journal of Quantitative Spectroscopy and Radiative Transfer*, 54(5):767–778, 1995. 81, 135

[321] G. A. Pitz, D. E. Wertepny, and G. P. Perram. Pressure broadening and shift of the cesium D_1 transition by the noble gases and N_2, H_2, HD, D_2, CH_4, C_2H_6, CF_4, and ^{3}He. *Physical Review A*, 80(6):1–8, 2009. 81, 134, 135

[322] D. A. McGillis and L. Krause. Inelastic collisions between excited alkali atoms and molecules. IV. Sensitized fluorescence and quenching in Cs-N_2, Cs-H_2, Cs-HD, Cs-D_2 systems. *Canadian Journal of Physics*, 46(1):1051–1057, 1968. 82

[323] P. W. Milonni. *Fast Light, Slow Light and Left-Handed Light*. Institute of Physics (IoP), Bristol and Philadelphia, 2005. 82, 84, 86, 87

[324] B. Lounis and C. Cohen-Tannoudji. Coherent population trapping and Fano profiles. *Journal de Physique II*, 2(4):579–592, 1992. 85

[325] M. D. Lukin. Colloquium: Trapping and manipulating photon states in atomic ensembles. *Reviews of Modern Physics*, 75(2):457–472, 2003. 87, 93

[326] M. T. Rakher, R. J. Warburton, and P. Treutlein. Prospects for storage and retrieval of a quantum-dot single photon in an ultracold ^{87}Rb ensemble. *Phys. Rev. A*, 88(5): 053834, 2013. 88, 146, 161, 164, 165, 167, 171, 203

[327] J. Hald and E. S. Polzik. Mapping a quantum state of light onto atoms. *Journal of Optics B*, 3(1):83, 2001. 93

[328] J. Simon, H. Tanji, J. K. Thompson, and V. Vuletic. Interfacing collective atomic excitations and single photons. *Phys. Rev. Lett.*, 98(18):183601, 2007. 98

[329] P. R. S. Carvalho, L. E. E. de Araujo, and J. W. R. Tabosa. Angular dependence of an electromagnetically induced transparency resonance in a Doppler-broadened atomic vapor. *Phys. Rev. A*, 70(6):063818, 2004. 102

[330] P.-C. Guan, Y.-F. Chen, and I. A. Yu. Role of degenerate Zeeman states in the storage and retrieval of light pulses. *Phys. Rev. A*, 75(1):013812, 2007. 105, 155, 173

[331] Z. Xu, Y. Wu, L. Tian, L. Chen, Z. Zhang, Z. Yan, S. Li, H. Wang, C. Xie, and K. Peng. Long lifetime and high-fidelity quantum memory of photonic polarization qubit by lifting Zeeman degeneracy. *Phys. Rev. Lett.*, 111(24):240503, 2013. 105, 155, 173

[332] J. Nunn, J. H. Munns, S. Thomas, K. T. Kaczmarek, C. Qiu, A. Feizpour, E. Poem, B. Brecht, D. J. Saunders, P. M. Ledingham, D. V. Reddy, M. G. Raymer, and I. A. Walmsley. Theory of noise suppression in Λ-type quantum memories by means of a cavity. *Physical Review A*, 96(1):1–11, 2017. 105

[333] G. S. Agarwal, T. N. Dey, and D. J. Gauthier. Competition between electromagnetically induced transparency and Raman processes. *Phys. Rev. A*, 74(4):043805, 2006. 105

[334] K.-I. Harada, T. Kanbashi, M. Mitsunaga, and K. Motomura. Competition between electromagnetically induced transparency and stimulated Raman scattering. *Phys. Rev. A*, 73(1):013807, 2006. 105

[335] N. Lauk, C. O'Brien, and M. Fleischhauer. Fidelity of photon propagation in electromagnetically induced transparency in the presence of four-wave mixing. *Physical Review A*, 88(1), 2013. 105

[336] N. B. Phillips, A. V. Gorshkov, and I. Novikova. Light storage in an optically thick atomic ensemble under conditions of electromagnetically induced transparency and four-wave mixing. *Phys. Rev. A*, 83(6):063823, 2011. 105

[337] P. Palittapongarnpim, A. MacRae, and A. I. Lvovsky. Note: A monolithic filter cavity for experiments in quantum optics. *Review of Scientific Instruments*, 83(6): 066101, 2012. 106, 107

[338] W. Zinth and U. Zinth. *Optik: Lichtstrahlen-Wellen-Photonen, 3. Auflage*. Oldenbourg Verlag München, 2011. 106

[339] B. Wiegand, B. Leykauf, R. Jördens, and M. Krutzik. Linien: A versatile, user-friendly, open-source FPGA-based tool for frequency stabilization and spectroscopy parameter optimization. *Review of Scientific Instruments*, 93(6):063001, 2022. 115, 117

[340] U. Schünemann, H. Engler, R. Grimm, M. Weidemüller, and M. Zielonkowski. Simple scheme for tunable frequency offset locking of two lasers. *Review of Scientific Instruments*, 70:242–243, 1999. 115

[341] J.-P. Ruske. Wellenleitermodulatoren für neue Einsatzgebiete. *Optik & Photonik*, 1: 49–52, 2010. 125

[342] Jenoptik: Electro optical modulators. Available online at `https://www.jenoptik.com/products/optoelectronic-systems/light-modulation/integrated-optical-modulators-fiber-coupled`, 2023. 125

[343] S. M. Kostritskii, P. Bourson, R. Mouras, and M. D. Fontana. Optical fatigue of undoped lithium niobate crystals caused by irreversible photorefractive damage at high-intensity illumination. *Optical Materials*, 29(6):732–737, 2007. 126

[344] R. Paschotta. RP Photonics Encyclopedia: Acousto-optic modulators. Available online at `https://www.rp-photonics.com/acousto_optic_modulators.html`, 2008, 2008. 127

[345] F. Sarreshtedari, A. Rashedi, F. Ghashghaei, and M. Sabooni. Engineering of the cesium Zeeman sublevel populations using sequences of laser pulses and RF excitation. *Physica Scripta*, 96(1):015401, 2021. 155

[346] K. Zhang, J. Guo, L. Q. Chen, C. Yuan, Z. Y. Ou, and W. Zhang. Suppression of the four-wave-mixing background noise in a quantum memory retrieval process by channel blocking. *Physical Review A*, 90(3), 2014. 156

[347] M. Faraday. I. Experimental researches in electricity. Nineteenth series. *Philosophical Transactions of the Royal Society of London*, 136:1–20, 1846. 158

[348] W. Hanle. Über magnetische Beeinflussung der Polarisation der Resonanzfluoreszenz. *Zeitschrift für Physik*, 30(1):93–105, 1924. 158

[349] I. Usmani, M. Afzelius, H. de Riedmatten, and N. Gisin. Mapping multiple photonic qubits into and out of one solid-state atomic ensemble. *Nature Communications*, 1 (1):12, 2010. 159

[350] D.-S. Ding, W. Zhang, Z.-Y. Zhou, S. Shi, G.-Y. Xiang, X.-S. Wang, Y.-K. Jiang, B.-S. Shi, and G.-C. Guo. Quantum storage of orbital angular momentum entanglement in an atomic ensemble. *Phys. Rev. Lett.*, 114(5):050502, 2015. 159

[351] S. Langenfeld, O. Morin, M. Körber, and G. Rempe. A network-ready random-access qubits memory. *npj Quantum Information*, 6(1):86, 2020. 159

[352] C. Li, S. Zhang, Y.-K. Wu, N. Jiang, Y.-F. Pu, and L.-M. Duan. Multicell atomic quantum memory as a hardware-efficient quantum repeater node. *PRX Quantum*, 2 (4):040307, 2021. 159

[353] I. Novikova, N. B. Phillips, and A. V. Gorshkov. Optimal light storage with full pulse-shape control. *Phys. Rev. A*, 78(2):021802, 2008. 161

[354] K. Shinbrough, B. D. Hunt, and V. O. Lorenz. Optimization of broadband Λ-type quantum memory using Gaussian pulses. *Phys. Rev. A*, 103(6):062418, 2021. 163

[355] K. Shinbrough and V. O. Lorenz. Variance-based sensitivity analysis of Λ-type quantum memory. *Phys. Rev. A*, 107(3):033703, 2023. 163

[356] QDYN: Library. Available online at `https://qdyn-library.net/`, 2020. 165

[357] Numba. Available online at `https://numba.pydata.org/`, 2023. 165

[358] E. Gomez Lopez. *Tunable delay of photons using electromagnetically induced transparency in cesium vapor*. Master Thesis, Humboldt-Universität zu Berlin, 2019. 172

[359] A. M. Akulshin, A. Lezama, A. I. Sidorov, R. J. McLean, and P. Hannaford. 'Storage of light' in an atomic medium using electromagnetically induced absorption. *Journal of Physics B: Atomic, Molecular and Optical Physics*, 38(23):L365, 2005. 172

[360] A. Lezama, A. M. Akulshin, A. I. Sidorov, and P. Hannaford. Storage and retrieval of light pulses in atomic media with "slow" and "fast" light. *Phys. Rev. A*, 73(3): 033806, 2006.

[361] W. S. Martins, D. M. Conrado, V. Ádony, S. Barreiro, M. Oriá, M. Chevrollier, and R. A. de Oliveira. Efficient atomic memory using electromagnetically induced absorption. *Physics Open*, 9:100081, 2021. 172

[362] V. B. Braginsky, Y. I. Vorontsov, and K. S. Thorne. Quantum nondemolition measurements. *Science*, 209(4456):547–557, 1980. 176

[363] C. S. Unnikrishnan. Quantum non-demolition measurements: concepts, theory and practice. *Current Science*, 109(11):2052–2060, 2015. 176

[364] B. Korzh, C. C. W. Lim, R. Houlmann, N. Gisin, M. J. Li, D. Nolan, B. Sanguinetti, R. Thew, and H. Zbinden. Provably secure and practical quantum key distribution over 307 km of optical fibre. *Nature Photonics*, 9(3):163–168, 2015. 175

[365] T. Jennewein, J. P. Bourgoin, Higgins. B., C. Holloway, E. Meyer-Scott, C. Erven, Heim B., Z. Yan, H. Hübel, G. Weihs, E. Choi, I. D'Souza, D. Hudson, and R. Laflamme. QEYSSAT: A mission proposal for a quantum receiver in space. In Zameer U. Hasan, Philip R. Hemmer, Hwang Lee, and Charles M. Santori, editors, *Advances in Photonics of Quantum Computing, Memory, and Communication VII*, volume 8997, page 89970A. SPIE, 2014. 176

[366] D. K. L. Oi, A. Ling, G. Vallone, P. Villoresi, S. Greenland, E. Kerr, M. Macdonald, H. Weinfurter, H. Kuiper, E. Charbon, and R. Ursin. CubeSat quantum communications mission. *EPJ Quantum Technology*, 4(1):6, 2017.

[367] E. Kerstel, A. Gardelein, M. Barthelemy, M. Fink, S. K. Joshi, R. Ursin, and The CSUG Team. Nanobob: A CubeSat mission concept for quantum communication experiments in an uplink configuration. *EPJ Quantum Technology*, 5(1):6, 2018.

[368] L. Mazzarella, C. Lowe, D. Lowndes, S. K. Joshi, S. Greenland, D. McNeil, C. Mercury, M. Macdonald, J. Rarity, and D. K. L. Oi. QUARC: Quantum Research Cubesat - a constellation for quantum communication. *Cryptography*, 4(1), 2020.

[369] A. Villar, A. Lohrmann, X. Bai, T. Vergoossen, R. Bedington, C. Perumangatt, H. Y. Lim, T. Islam, A. Reezwana, Z. Tang, R. Chandrasekara, S. Sachidananda, K. Durak, C. F. Wildfeuer, D. Griffin, D. K. L. Oi, and A. Ling. Entanglement demonstration on board a nano-satellite. *Optica*, 7(7):734–737, 2020. 176

[370] S. Khatri, A. J. Brady, R. A. Desporte, M. P. Bart, and J. P. Dowling. Spooky action at a global distance: Analysis of space-based entanglement distribution for the quantum internet. *npj Quantum Information*, 7(1), 2021. 176

[371] J. S. Sidhu, T. Brougham, D. McArthur, R. G. Pousa, and D. K. L. Oi. Finite key effects in satellite quantum key distribution. *npj Quantum Information*, 8(1):18, 2022.

[372] C. C.-W. Lim, F. Xu, J.-W. Pan, and A. Ekert. Security analysis of quantum key distribution with small block length and its application to quantum space communications. *Phys. Rev. Lett.*, 126(10):100501, 2021. 176

[373] J.-G. Ren, P. Xu, H.-L. Yong, L. Zhang, S.-K. Liao, J. Yin, W.-Y. Liu, W.-Q. Cai, M. Yang, L. Li, K.-X. Yang, X. Han, Y.-Q. Yao, J. Li, H.-Y. Wu, S. Wan, L. Liu, D.-Q. Liu, Y.-W. Kuang, Z.-P. He, P. Shang, C. Guo, R.-H. Zheng, K. Tian, Z.-C. Zhu, N.-L. Liu, C.-Y. Lu, R. Shu, Y.-A. Chen, C.-Z. Peng, J.-Y. Wang, and J.-W. Pan. Ground-to-satellite quantum teleportation. *Nature*, 549(7670):70–73, 2017. 176, 204

[374] S.-K. Liao, W.-Q. Cai, W.-Y. Liu, L. Zhang, Y. Li, J.-G. Ren, J. Yin, Q. Shen, Y. Cao, Z.-P. Li, F.-Z. Li, X.-W. Chen, L.-H. Sun, J.-J. Jia, J.-C. Wu, X.-J. Jiang, J.-F. Wang, Y.-M. Huang, Q. Wang, Y.-L. Zhou, L. Deng, T. Xi, L. Ma, T. Hu, Q. Zhang, Y.-A. Chen, N.-L. Liu, X.-B. Wang, Z.-C. Zhu, C.-Y. Lu, R. Shu, C.-Z. Peng, J.-Y. Wang, and J.-W. Pan. Satellite-to-ground quantum key distribution. *Nature*, 549(7670):43–47, 2017. 176

[375] J. Yin, Y.-H. Li, S.-K. Liao, M. Yang, Y. Cao, L. Zhang, J.-G. Ren, W.-Q. Cai, W.-Y. Liu, S.-L. Li, R. Shu, Y.-M. Huang, L. Deng, L. Li, Q. Zhang, N.-L. Liu, Y.-A. Chen, C.-Y. Lu, X.-B. Wang, F. Xu, J.-Y. Wang, C.-Z. Peng, A. K. Ekert, and J.-W. Pan. Entanglement-based secure quantum cryptography over 1,120 kilometres. *Nature*, 582(7813):501–505, 2020. 176, 177

[376] S.-K. Liao, W.-Q. Cai, J. Handsteiner, B. Liu, J. Yin, L. Zhang, D. Rauch, M. Fink, J.-G. Ren, W.-Y. Liu, Y. Li, Q. Shen, Y. Cao, F.-Z. Li, J.-F. Wang, Y.-M. Huang, L. Deng, T. Xi, L. Ma, T. Hu, L. Li, N.-L. Liu, F. Koidl, P. Wang, Y.-A. Chen, X.-B. Wang, M. Steindorfer, G. Kirchner, C.-Y. Lu, R. Shu, R. Ursin, T. Scheidl, C.-Z. Peng, J.-Y. Wang, A. Zeilinger, and J.-W. Pan. Satellite-relayed intercontinental quantum network. *Phys. Rev. Lett.*, 120(3):030501, 2018. 176, 204

[377] C. Liorni, H. Kampermann, and D. Bruß. Quantum repeaters in space. *New J. Phys.*, 23(5):053021, 2021. 177, 201

[378] C. Panayi, M. Razavi, X. Ma, and N. Lütkenhaus. Memory-assisted measurement-device-independent quantum key distribution. *New Journal of Physics*, 16(4):043005, 2014. 177

[379] D. Luong, L. Jiang, J. Kim, and N. Lütkenhaus. Overcoming lossy channel bounds using a single quantum repeater node. *Applied Physics B*, 122(4):96, 2016. 177

[380] K. Boone, J.-P. Bourgoin, E. Meyer-Scott, K. Heshami, T. Jennewein, and C. Simon. Entanglement over global distances via quantum repeaters with satellite links. *Phys. Rev. A*, 91(5):052325, 2015. 177

[381] J. Wallnöfer, F. Hahn, F. Wiesner, N. Walk, and J. Eisert. Faithfully simulating near-term quantum repeaters. *PRX Quantum*, 5(1):010351, 2024. 178

[382] H. J. Caulfield and S. Dolev. Why future supercomputing requires optics. *Nature Photonics*, 4(5):261–263, 2010. 179

[383] D. A. B. Miller. The role of optics in computing. *Nature Photonics*, 4(7):406, 2010.

[384] P. L. McMahon. The physics of optical computing. *Nature Reviews Physics*, 5(12): 717–734, 2023. 179

[385] X. Lin, Y. Rivenson, N. T. Yardimci, M. Veli, Y. Luo, M. Jarrahi, and A. Ozcan. All-optical machine learning using diffractive deep neural networks. *Science*, 361 (6406):1004–1008, 2018. 179

[386] S. Zarei and A. Khavasi. Realization of optical logic gates using on-chip diffractive optical neural networks. *Scientific Reports*, 12(1):15747, 2022. 179

[387] A. Ryou, J. Whitehead, M. Zhelyeznyakov, P. Anderson, C. Keskin, M. Bajcsy, and A. Majumdar. Free-space optical neural network based on thermal atomic nonlinearity. *Photon. Res.*, 9(4):B128–B134, 2021. 179

[388] H. Jaeger. The 'echo state' approach to analysing and training recurrent neural networks. Technical Report GMD Report 148, German National Research Institute for Computer Science, 2001. 179

[389] W. Maass, T. Natschläger, and H. Markram. Real-time computing without stable states: A new framework for neural computation based on perturbations. *Neural computation*, 14(11):2531–2560, 2002.

[390] G. van der Sande, D. Brunner, and M. C. Soriano. Advances in photonic reservoir computing. *Nanophotonics*, 6(3):561–576, 2017. 179

[391] Y. Paquot, F. Duport, A. Smerieri, J. Dambre, B. Schrauwen, M. Haelterman, and S. Massar. Optoelectronic reservoir computing. *Scientific Reports*, 2(1):287, 2012. 179

[392] D. Brunner, M. C. Soriano, C. R. Mirasso, and I. Fischer. Parallel photonic information processing at gigabyte per second data rates using transient states. *Nature Communications*, 4(1):1364, 2013. 179

[393] L. Jaurigue, E. Robertson, J. Wolters, and K. Lüdge. Reservoir computing with delayed input for fast and easy optimisation. *Entropy*, 23(12), 2021. 179

[394] H.-S. Zhong, Y. Li, W. Li, L.-C. Peng, Z.-E. Su, Y. Hu, Y.-M. He, X. Ding, W. Zhang, H. Li, L. Zhang, Z. Wang, L. You, X.-L. Wang, X. Jiang, L. Li, Y.-A. Chen, N.-L. Liu, C.-Y. Lu, and J.-W. Pan. 12-photon entanglement and scalable scattershot boson sampling with optimal entangled-photon pairs from parametric down-conversion. *Phys. Rev. Lett.*, 121(25):250505, 2018. 180

[395] X.-L. Wang, L.-K. Chen, W. Li, H.-L. Huang, C. Liu, C. Chen, Y.-H. Luo, Z.-E. Su, D. Wu, Z.-D. Li, H. Lu, Y. Hu, X. Jiang, C.-Z. Peng, L. Li, N.-L. Liu, Y.-A. Chen, C.-Y. Lu, and J.-W. Pan. Experimental ten-photon entanglement. *Phys. Rev. Lett.*, 117(21):210502, 2016. 180

[396] H. Wang, J. Qin, X. Ding, M.-C. Chen, S. Chen, X. You, Y.-M. He, X. Jiang, L. You, Z. Wang, C. Schneider, J. J. Renema, S. Höfling, C.-Y. Lu, and J.-W. Pan. Boson sampling with 20 input photons and a 60-mode interferometer in a 10^{14}-dimensional Hilbert space. *Phys. Rev. Lett.*, 123(25):250503, 2019. 180

[397] N. Maring, A. Fyrillas, M. Pont, E. Ivanov, P. Stepanov, N. Margaria, W. Hease, A. Pishchagin, A. Lemaître, I. Sagnes, T. H. Au, S. Boissier, E. Bertasi, A. Baert, M. Valdivia, M. Billard, O. Acar, A. Brieussel, R. Mezher, S. C. Wein, A. Salavrakos, P. Sinnott, D. A. Fioretto, P.-E. Emeriau, N. Belabas, S. Mansfield, P. Senellart, J. Senellart, and N. Somaschi. A versatile single-photon-based quantum computing platform. *Nature Photonics*, 2024. 180

[398] F. Kaneda and P. G. Kwiat. High-efficiency single-photon generation via large-scale active time multiplexing. *Science Advances*, 5(10):eaaw8586, 2019. 181

[399] E. Meyer-Scott, N. Prasannan, I. Dhand, C. Eigner, V. Quiring, S. Barkhofen, B. Brecht, M. B. Plenio, and C. Silberhorn. Scalable generation of multiphoton entangled states by active feed-forward and multiplexing. *Phys. Rev. Lett.*, 129(15): 150501, 2022. 181

[400] O. Davidson, O. Yogev, E. Poem, and O. Firstenberg. Single-photon synchronization with a room-temperature atomic quantum memory. *Phys. Rev. Lett.*, 131(3):033601, 2023. 181

[401] K. Su, Y. Wang, S. Zhang, Z. Kong, Y. Zhong, J. Li, H. Yan, and S.-L. Zhu. Synchronization and phase shaping of single photons with high-efficiency quantum memory. *Chinese Physics Letters*, 38(9):094202, 2021. 181

[402] C.-N. Zhang, H. Li, J.-P. Dou, F. Lu, H.-Z. Yang, X.-L. Pang, and X.-M. Jin. Hong–Ou–Mandel interference linking independent room-temperature quantum memories. *Photon. Res.*, 10(10):2388–2393, 2022. 181

[403] S. E. Thomas, L. Wagner, R. Joos, R. Sittig, C. Nawrath, P. Burdekin, T. Huber-Loyola, S. Sagona-Stophel, S. Höfling, M. Jetter, P. Michler, I. A. Walmsley, S. L. Portalupi, and P. M. Ledingham. Deterministic storage and retrieval of telecom quantum dot photons interfaced with an atomic quantum memory. *arXiv:2303.04166v1*, 2023. 181

[404] B. Hensen, H. Bernien, A. E. Dréau, A. Reiserer, N. Kalb, M. S. Blok, J. Ruitenberg, R. F. L. Vermeulen, R. N. Schouten, C. Abellán, W. Amaya, V. Pruneri, M. W. Mitchell, M. Markham, D. J. Twitchen, D. Elkouss, S. Wehner, T. H. Taminiau, and R. Hanson. Loophole-free Bell inequality violation using electron spins separated by 1.3 kilometres. *Nature*, 526(7575):682–686, 2015. 182

[405] M. Giustina, M. A. M. Versteegh, S. Wengerowsky, J. Handsteiner, A. Hochrainer, K. Phelan, F. Steinlechner, J. Kofler, J.-Å. Larsson, C. Abellán, W. Amaya, V. Pruneri, M. W. Mitchell, J. Beyer, T. Gerrits, A. E. Lita, L. K. Shalm, S. W. Nam, T. Scheidl, R. Ursin, B. Wittmann, and A. Zeilinger. Significant-loophole-free test of Bell's theorem with entangled photons. *Phys. Rev. Lett.*, 115(25):250401, 2015.

[406] T. Scheidl, R. Ursin, J. Kofler, Ramelow, Sven, X.-S. Ma, T. Herbst, L. Ratschbacher, A. Fedrizzi, N. K. Langford, T. Jennewein, and A. Zeilinger. Violation of local realism with freedom of choice. *Proceedings of the National Academy of Sciences*, 107(46):19708–19713, 2010.

[407] L. K. Shalm, E. Meyer-Scott, B. G. Christensen, P. Bierhorst, M. A. Wayne, M. J. Stevens, T. Gerrits, S. Glancy, D. R. Hamel, M. S. Allman, K. J. Coakley, S. D. Dyer, C. Hodge, A. E. Lita, V. B. Verma, C. Lambrocco, E. Tortorici, A. L. Migdall, Y. Zhang, D. R. Kumor, W. H. Farr, F. Marsili, M. D. Shaw, J. A. Stern, C. Abellán, W. Amaya, V. Pruneri, T. Jennewein, M. W. Mitchell, P. G. Kwiat, J. C. Bienfang, R. P. Mirin, E. Knill, and S. W. Nam. Strong loophole-free test of local realism. *Phys. Rev. Lett.*, 115(25):250402, 2015. 182

[408] R. Schmied, J.-D. Bancal, B. Allard, M. Fadel, V. Scarani, P. Treutlein, and N. Sangouard. Bell correlations in a Bose-Einstein condensate. *Science*, 352(6284): 441–444, 2016. 182

[409] M. Fadel, T. Zibold, B. Décamps, and P. Treutlein. Spatial entanglement patterns and Einstein-Podolsky-Rosen steering in Bose-Einstein condensates. *Science*, 360 (6387):409–413, 2018.

[410] P. Colciaghi, Y. Li, P. Treutlein, and T. Zibold. Einstein-Podolsky-Rosen experiment with two Bose-Einstein condensates. *Phys. Rev. X*, 13(2):021031, 2023. 182

[411] J. Barrett, D. Collins, L. Hardy, A. Kent, and S. Popescu. Quantum nonlocality, Bell inequalities, and the memory loophole. *Phys. Rev. A*, 66(4):042111, 2002. 182

[412] R. D. Gill. Accardi contra Bell (cum mundi): The impossible coupling. *arXiv:quant-ph/0110137v4*, 2002.

[413] R. D. Gill. Time, finite statistics, and Bell's fifth position. *arXiv:quant-ph/0301059*, 2018. 182

[414] M. Mohageg, L. Mazzarella, D. V. Strekalov, N. Yu, A. Zhai, S. Johnson, C. Anastopoulos, J. Gallicchio, B. L. Hu, T. Jennewein, S.-Y. Lin, A. Ling, C. Marquardt, M. Meister, A. Roura, L. Wörner, W. P. Schleich, R. Newell, C. Schubert, G. Vallone, P. Villoresi, and P. Kwiat. The deep space quantum link: Prospective fundamental physics experiments using long-baseline quantum optics. *EPJ Quantum Technology*, 9(1):3039, 2022. 183

[415] V. V. Dodonov. Current status of the dynamical Casimir effect. *Physica Scripta*, 82 (3):038105, 2010. 183

[416] D. E. Bruschi, I. Fuentes, and J. Louko. Voyage to Alpha Centauri: Entanglement degradation of cavity modes due to motion. *Phys. Rev. D*, 85(6):061701, 2012. 183, 184

[417] N. Friis, A. R. Lee, D. E. Bruschi, and J. Louko. Kinematic entanglement degradation of fermionic cavity modes. *Phys. Rev. D*, 85(2):025012, 2012.

[418] N. Friis, D. E. Bruschi, J. Louko, and I. Fuentes. Motion generates entanglement. *Phys. Rev. D*, 85(8):081701, 2012.

[419] D. E. Bruschi, A. Dragan, A. R. Lee, I. Fuentes, and J. Louko. Relativistic motion generates quantum gates and entanglement resonances. *Phys. Rev. Lett.*, 111(9): 090504, 2013. 183

[420] N. Friis, M. Huber, I. Fuentes, and D. E. Bruschi. Quantum gates and multipartite entanglement resonances realized by nonuniform cavity motion. *Phys. Rev. D*, 86 (10):105003, 2012. 183

[421] D. E. Bruschi, J. Louko, D. Faccio, and I. Fuentes. Mode-mixing quantum gates and entanglement without particle creation in periodically accelerated cavities. *New Journal of Physics*, 15(7):073052, 2013. 183, 184

[422] C. Sabín, D. E. Bruschi, M. Ahmadi, and I. Fuentes. Phonon creation by gravitational waves. *New Journal of Physics*, 16(8):085003, 2014. 183, 184

[423] D. Rätzel, F. Schneiter, D. Braun, T. Bravo, R. Howl, M. P. E. Lock, and I. Fuentes. Frequency spectrum of an optical resonator in a curved spacetime. *New Journal of Physics*, 20(5):053046, 2018. 184

[424] T. Bravo, D. Rätzel, and I. Fuentes. Gravitational time dilation in extended quantum systems: The case of light clocks in Schwarzschild spacetime. *AVS Quantum Science*, 5(1):014401, 2023. 184

[425] R. Barzel, M. Gündoğan, M. Krutzik, D. Rätzel, and C. Lämmerzahl. Entanglement dynamics of photon pairs and quantum memories in the gravitational field of the earth. *Quantum*, 8:1273, 2024. 184

[426] D. Rideout, T. Jennewein, G. Amelino-Camelia, T. F. Demarie, B. L. Higgins, A. Kempf, A. Kent, R. Laflamme, X. Ma, R. B. Mann, E. Martín-Martínez, N. C. Menicucci, J. Moffat, C. Simon, R. Sorkin, L. Smolin, and D. R. Terno. Fundamental quantum optics experiments conceivable with satellites - reaching relativistic distances and velocities. *Classical and Quantum Gravity*, 29(22):224011, 2012. 184

[427] D. E. Bruschi, C. Sabín, A. White, V. Baccetti, D. K. L. Oi, and I. Fuentes. Testing the effects of gravity and motion on quantum entanglement in space-based experiments. *New Journal of Physics*, 16(5):053041, 2014. 184

[428] B. Guinot and E. F. Arias. Atomic time-keeping from 1955 to the present. *Metrologia*, 42(3):S20, 2005. 185

[429] C. W. Chou, D. B. Hume, T. Rosenband, and D. J. Wineland. Optical clocks and relativity. *Science*, 329(5999):1630–1633, 2010. 185

[430] P. Kómár, E. M. Kessler, M. Bishof, L. Jiang, A. S. Sørensen, J. Ye, and M. D. Lukin. A quantum network of clocks. *Nature Physics*, 10(8):582–587, 2014. 185

[431] M. Lipka, M. Mazelanik, A. Leszczyński, W. Wasilewski, and M. Parniak. Massively-multiplexed generation of Bell-type entanglement using a quantum memory. *Communications Physics*, 4(1):46, 2021. 185

[432] Q. Zhuang, Z. Zhang, and J. H. Shapiro. Distributed quantum sensing using continuous-variable multipartite entanglement. *Phys. Rev. A*, 97(3):032329, 2018. 185

[433] X. Guo, C. R. Breum, J. Borregaard, S. Izumi, M. V. Larsen, T. Gehring, M. Christandl, J. S. Neergaard-Nielsen, and U. L. Andersen. Distributed quantum sensing in a continuous-variable entangled network. *Nature Physics*, 16(3):281–284, 2020.

[434] Zheshen Zhang and Quntao Zhuang. Distributed quantum sensing. *Quantum Science and Technology*, 6(4):043001, 2021. 185

[435] D. Gottesman, T. Jennewein, and S. Croke. Longer-baseline telescopes using quantum repeaters. *Phys. Rev. Lett.*, 109(7):070503, 2012. 186

[436] E. T. Khabiboulline, J. Borregaard, K. de Greve, and M. D. Lukin. Optical interferometry with quantum networks. *Phys. Rev. Lett.*, 123(7):070504, 2019. 186

[437] E. T. Khabiboulline, J. Borregaard, K. de Greve, and M. D. Lukin. Quantum-assisted telescope arrays. *Phys. Rev. A*, 100(2):022316, 2019. 186

[438] J.-P. Chen, C. Zhang, Y. Liu, C. Jiang, D.-F. Zhao, W.-J. Zhang, F.-X. Chen, H. Li, L.-X. You, Z. Wang, Y. Chen, X.-B. Wang, Q. Zhang, and J.-W. Pan. Quantum key distribution over 658 km fiber with distributed vibration sensing. *Phys. Rev. Lett.*, 128(18):180502, 2022. 186

[439] A. Belenchia, M. Carlesso, Ö. Bayraktar, D. Dequal, I. Derkach, G. Gasbarri, W. Herr, Y. L. Li, M. Rademacher, J. Sidhu, D. K. Oi, S. T. Seidel, R. Kaltenbaek, C. Marquardt, H. Ulbricht, V. C. Usenko, L. Wörner, A. Xuereb, M. Paternostro, and A. Bassi. Quantum physics in space. *Physics Reports*, 951:1–70, 2022. 186

[440] Q-ToRX: Quantentoken auf Basis von Rubidium und Xenon. Available online at `https://www.forschung-it-sicherheit-kommunikationssysteme.de/projekte/q-torx`, 2021. 186

[441] Grand Challenge der Quantenkommunikation. Available online at `https://www.forschung-it-sicherheit-kommunikationssysteme.de/foerderung/bekanntmachungen/gcq`, 2021. 186, 187, 189

[442] O. Katz, E. Reches, R. Shaham, A. V. Gorshkov, and O. Firstenberg. Optical quantum memory with optically inaccessible noble-gas spins. *arXiv:2007.08770v2*, 2020. 187

[443] O. Katz, R. Shaham, E. Reches, A. V. Gorshkov, and O. Firstenberg. Optical quantum memory for noble-gas spins based on spin-exchange collisions. *Phys. Rev. A*, 105(4):042606, 2022. 187, 188, 204

[444] C. Gemmel, W. Heil, S. Karpuk, K. Lenz, C. Ludwig, Y. Sobolev, K. Tullney, M. Burghoff, W. Kilian, S. Knappe-Grüneberg, W. Müller, A. Schnabel, F. Seifert, L. Trahms, and St. Baeßler. Ultra-sensitive magnetometry based on free precession of nuclear spins. *European Physical Journal D*, 57(3):303–320, 2010. 187

[445] W. C. Chen, T. R. Gentile, C. B. Fu, S. Watson, G. L. Jones, J. W. McIver, and D. R. Rich. Polarized ^{3}He cell development and application at NIST. *Journal of Physics: Conference Series*, 294(1):012003, 2011.

[446] T. R. Gentile, P. J. Nacher, B. Saam, and T. G. Walker. Optically polarized ^{3}He. *Rev. Mod. Phys.*, 89(4):045004, 2017. 187

[447] M. A. Bouchiat, T. R. Carver, and C. M. Varnum. Nuclear polarization in ^{3}He gas induced by optical pumping and dipolar exchange. *Phys. Rev. Lett.*, 5(8):373–375, 1960. 187

[448] N. D. Bhaskar, W. Happer, and T. McClelland. Efficiency of spin exchange between rubidium spins and ^{129}Xe nuclei in a gas. *Phys. Rev. Lett.*, 49(1):25–28, 1982.

[449] T. G. Walker and W. HAPPER. Spin-exchange optical pumping of noble-gas nuclei. *Rev. Mod. Phys.*, 69(2):629–642, 1997. 187

[450] S. Appelt, A. B.-A. Baranga, C. J. Erickson, M. V. Romalis, A. R. Young, and W. Happer. Theory of spin-exchange optical pumping of ^{3}He and ^{129}Xe. *Phys. Rev. A*, 58(2):1412–1439, 1998.

[451] O. Katz, R. Shaham, and O. Firstenberg. Quantum interface for noble-gas spins based on spin-exchange collisions. *PRX Quantum*, 3(1):010305, 2022. 187

[452] T. W. Kornack and M. V. Romalis. Dynamics of two overlapping spin ensembles interacting by spin exchange. *Phys. Rev. Lett.*, 89(25):253002, 2002. 187

[453] R. Shaham, O. Katz, and O. Firstenberg. Strong coupling of alkali-metal spins to noble-gas spins with an hour-long coherence time. *Nature Physics*, 18(5):506–510, 2022. 187

[454] M. Schink, A. Wagner, F. Unterstein, and J. Heyszl. Security and trust in open source security tokens. *IACR Transactions on Cryptographic Hardware and Embedded Systems*, 2021(3):176–201, 2021. 190

[455] S. Ben-David and O. Sattath. Quantum tokens for digital signatures. *Quantum*, 7: 901, 2023. 190

[456] M. Bozzio, A. Orieux, L. Trigo Vidarte, I. Zaquine, I. Kerenidis, and E. Diamanti. Experimental investigation of practical unforgeable quantum money. *npj Quantum Information*, 4(1):5, 2018. 190, 191, 192, 193

[457] F. Pastawski, N. Y. Yao, L. Jiang, M. D. Lukin, and J. I. Cirac. Unforgeable noise-tolerant quantum tokens. *Proceedings of the National Academy of Sciences*, 109(40):16079–16082, 2012. 190

[458] K. Bartkiewicz, A. Černoch, G. Chimczak, K. Lemr, A. Miranowicz, and F. Nori. Experimental quantum forgery of quantum optical money. *npj Quantum Information*, 3(1):7, 2017. 190

[459] R. Amiri and J. M. Arrazola. Quantum money with nearly optimal error tolerance. *Phys. Rev. A*, 95(6):062334, 2017. 190

[460] J.-Y. Guan, J. M. Arrazola, R. Amiri, W. Zhang, H. Li, L. You, Z. Wang, Q. Zhang, and J.-W. Pan. Experimental preparation and verification of quantum money. *Phys. Rev. A*, 97(3):032338, 2018. 192

[461] M. Bozzio, E. Diamanti, and F. Grosshans. Semi-device-independent quantum money with coherent states. *Phys. Rev. A*, 99(2):022336, 2019. 190, 192

[462] P. Schiansky, J. Kalb, E. Sztatecsny, M.-C. Roehsner, T. Guggemos, A. Trenti, M. Bozzio, and P. Walther. Demonstration of quantum-digital payments. *Nature Communications*, 14(1):3849, 2023. 190

[463] Y. Zhao, B. Qi, and H.-K. Lo. Experimental quantum key distribution with active phase randomization. *Applied Physics Letters*, 90(4):044106, 2007. 193

[464] M. Jutisz et al. Stand alone mobile quantum memory demonstrator. *in preparation*, 2024. 199